JPTM
Journal of Pathology and Translational Medicine

Journal of Pathology and Translational Medicine

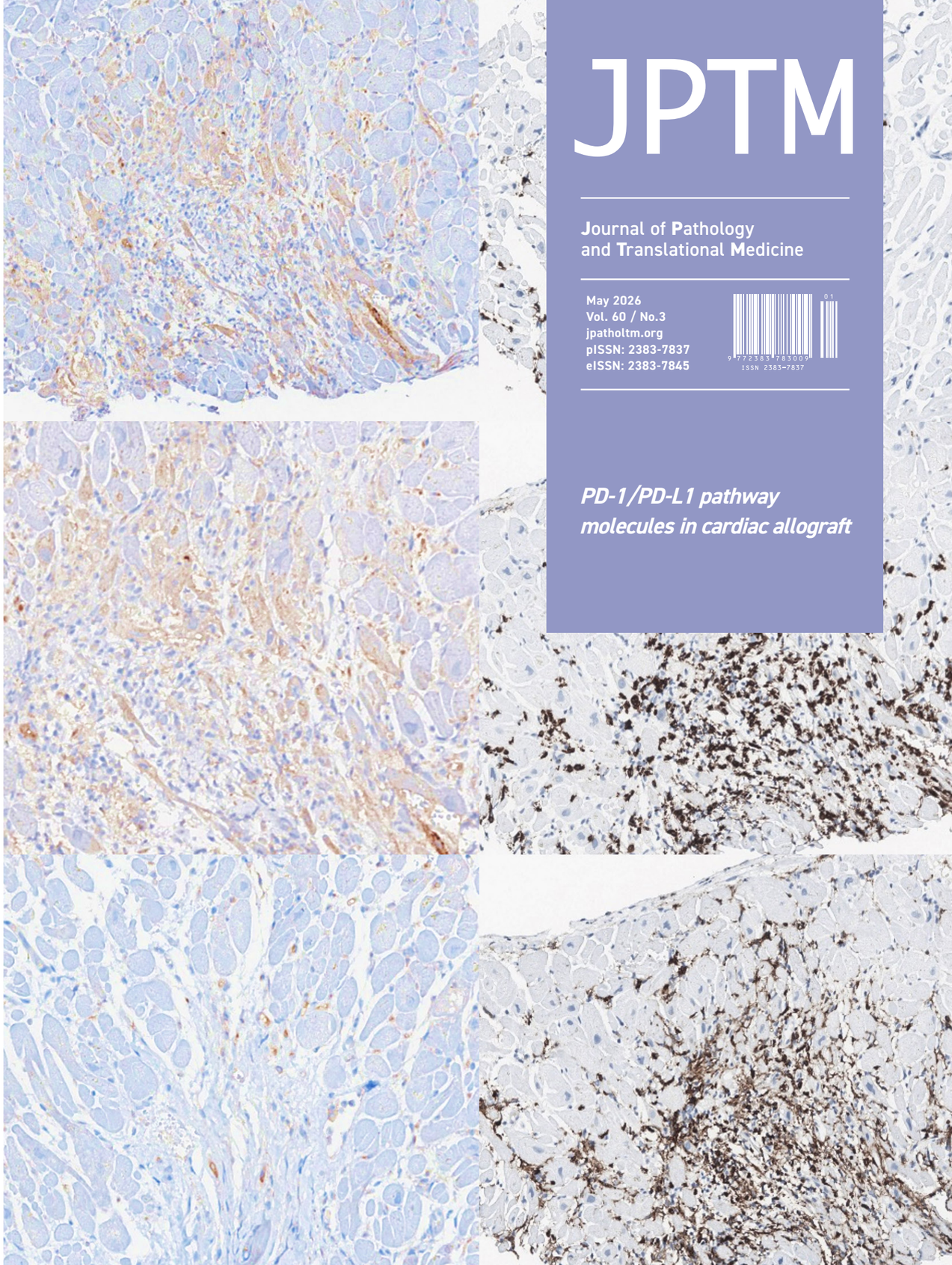

JPTM

Journal of Pathology and Translational Medicine

May 2026
Vol. 60 / No.3
jpatholtm.org
pISSN: 2383-7837
eISSN: 2383-7845

PD-1/PD-L1 pathway molecules in cardiac allograft

Vol. 60, No.3, pp 285-370, May 2026

JPTM

jpatholtm.org
pISSN 2383-7837 · eISSN 2383-7845

Vol. 60, No.3, May 2026

Published on 15 May 2026

Aims & Scope

The Journal of Pathology and Translational Medicine is an open venue for the rapid publication of major achievements in various fields of pathology, cytopathology, and biomedical and translational research. The Journal aims to share new insights into the molecular and cellular mechanisms of human diseases and to report major advances in both experimental and clinical medicine, with a particular emphasis on translational research. The investigations of human cells and tissues using high-dimensional biology techniques such as genomics and proteomics will be given a high priority. Articles on stem cell biology are also welcome. The categories of manuscript include original articles, review and perspective articles, case studies, brief case reports, and letters to the editor.

Subscription Information

To subscribe to this journal, please contact the Korean Society of Pathologists/the Korean Society for Cytopathology. Full text PDF files are also available at the official website (https://jpatholtm.org). *Journal of Pathology and Translational Medicine* is indexed by Emerging Sources Citation Index (ESCI), PubMed, PubMed Central, Scopus, KoreaMed, KoMCI, WPRIM, Directory of Open Access Journals (DOAJ), and CrossRef. Circulation number per issue is 50.

Contact the Korean Society of Pathologists/the Korean Society for Cytopathology

Publishers: Ha, Seung Yeon, MD; Choi, Yoon Jung, MD
Editors-in-Chief: Jung, Chan Kwon, MD; Park, So Yeon, MD
Published by the Korean Society of Pathologists/the Korean Society for Cytopathology

Editorial Office
Suite 706, 217 Saechang-ro, Yongsan-gu, Seoul 04376, Korea
Tel: +82-2-795-3094 Fax: +82-2-790-6635 E-mail: office@jpatholtm.org
#1508 Renaissancetower, 14 Mallijae-ro, Mapo-gu, Seoul 04195, Korea
Tel: +82-2-593-6943 Fax: +82-2-593-6944 E-mail: office@jpatholtm.org

Printed by M2PI
#805, 26 Sangwon 1-gil, Seongdong-gu, Seoul 04779, Korea
Tel: +82-2-6966-4930 Fax: +82-2-6966-4945 E-mail: support@m2-pi.com

Manuscript Editing by InfoLumi Co.
210-202, 421 Pangyo-ro, Bundang-gu, Seongnam 13522, Korea
Tel: +82-70-8839-8800 E-mail: infolumi.chang@gmail.com

Front cover image: Immunohistochemical staining for PD-L1, PD-1, CD8, and CD4 in endomyocardial biopsies after heart transplantation (p. 324)

Editorial Board

JPTM

jpatholtm.org
pISSN 2383-7837 · eISSN 2383-7845

Contents

Vol. 60, No.3, May 2026

REVIEW ARTICLE

ORIGINAL ARTICLES

CASE STUDY

NEWSLETTER

JPTM

REVIEW ARTICLE

pISSN 2383-7837 · eISSN 2383-7845

Journal of Pathology and Translational Medicine 2026; 60: 285-306
https://doi.org/10.4132/jptm.2026.03.11

Gene fusions in melanocytic lesions: an updated comprehensive review

Volha Lenskaya[1], Larisa Erikson[2], Victor G. Prieto[1], Woo Cheal Cho[1]

[1]Department of Pathology and Laboratory Medicine, The University of Texas MD Anderson Cancer Center, Houston, TX, USA
[2]Department of Pathology, Children's Hospital, University of Colorado School of Medicine, Aurora, CO, USA

The scope of gene fusions in melanocytic neoplasms is broader than previously recognized, extending well beyond the Spitz-lineage neoplasms where kinase fusions involving *ALK*, *ROS1*, *NTRK1/2/3*, *RET*, *MET*, *BRAF*, and *MAP3K8* define biologically and morphologically distinct tumors. Emerging studies demonstrate that a meaningful proportion of conventional non-Spitz lineage melanomas harbor oncogenic fusions. Such fusions may impact clinical behavior, histopathologic presentation and provide opportunities for targeted therapy. The World Health Organization classification of skin tumors, 5th edition, now incorporates fusion status into taxonomy and risk stratification, yet some important questions remain for further investigation: fusion-associated neoplasms can mimic non-melanocytic neoplasm; Spitz-type fusions appear in non-Spitz lesions; and melanocytic differentiation may occur in some other fusion-driven lesions. Broad-panel next-generation sequencing (including RNA-seq), together with targeted fluorescence in situ hybridization and immunohistochemistry enhances detection of known and novel fusion partners. Early clinical evidence of TRK, ALK, and ROS1 inhibitor efficacy underscores the translational promise of fusion testing and opens avenues for personalized therapy. This review synthesizes current knowledge on the genomics, histopathology, diagnosis, and therapeutic implications of fusion-driven melanocytic neoplasms, highlighting consensus points and remaining controversies.

Keywords: Gene fusions; Melanocytic lesions; Spitz neoplasms

INTRODUCTION

Recent advancements in molecular techniques, such as next-generation sequencing (NGS) and whole-transcriptome sequencing, have significantly enhanced our understanding of the tumorigenic mechanisms underlying melanocytic neoplasms, particularly through the identification of novel gene fusions. While gene fusions are commonly associated with Spitz melanocytic neoplasms, new evidence suggests that these fusion events are not limited to Spitz neoplasms. The scope of gene fusions in melanocytic tumors is broader than previously recognized. Therefore, it is increasingly important that molecular findings complement, rather than replace, the pathologist's morphological assessment to avoid diagnostic bias and ensure accurate tumor classification. This review aims to provide a comprehensive, up-to-date overview of fusion-associated melanocytic neoplasms, emphasizing the importance of properly interpreting molecular data, which are context-dependent, as well as exploring the potential prognostic and therapeutic significance of gene fusions in these tumors (Supplementary Tables S1, S2).

ROLE OF GENE FUSIONS AND METHODS OF DETECTION

Gene fusions are hybrid genes resulting from structural genomic rearrangements that juxtapose coding or regulatory regions of distinct genes, often resulting in aberrant transcriptional or functional activity. Most oncogenic fusions are in-frame fusions involving exonic regions of protein-coding genes that are crucial for the functioning of those proteins [1]. The most affected gene

Received: November 28, 2025 **Revised:** March 11, 2026 **Accepted:** March 11, 2026
Corresponding Author: Volha Lenskaya, MD
Department of Pathology and Laboratory Medicine, The University of Texas MD Anderson Cancer Center, 1515 Holcombe Blvd, Unit 85, Houston, TX 77030, USA
Tel: +1-8323505873, Fax: +1-713-745-8228, E-mail: vlenskaya@mdanderson.org

groups involved in a majority of human cancers are protein kinases (PKs) and transcription factors (TFs) [2]. The mutational dysregulation of these gene groups significantly impacts tumorigenesis due to the innate function of PKs to mediate most cellular signal transduction events by phosphorylation of specific substrates, thus modifying their activity, cellular localization, and/or association with other proteins. TFs are the "transistors" of the cellular signaling circuits, controlling the transcriptional outcome of activated signaling by binding to regulative elements of their corresponding target genes and driving or suppressing their expression [1]. Not only conventional gene fusion but precisely kinase fusions are fairly common in melanocytic lesions and seen within approximately half of all spitzoid neoplasms [3,4]. The kinase gene fusions are defined as chimeric oncogenes generated by structural rearrangements that fuse a PK domain to a heterologous partner, leading to constitutive activation of signaling pathways such as mitogen-activated protein kinase (MAPK) or phosphoinositide 3-kinase (PI3K)/AKT/mammalian target of rapamycin (mTOR). The current understanding on how gene fusions drive cancer favors the aberrant gene function model rather than promoter-induced overexpression model; in other words, gene fusions act by altering protein function rather than just increasing how much of the protein is produced by the novel-fused gene [1].

Detection of gene fusions and other genomic rearrangements involves multiple methodologies, categorized by sequencing and non-sequencing approaches. Non-sequencing techniques, such as fluorescence in situ hybridization (FISH) and immunohistochemistry (IHC), offer rapid turnaround time, cost efficiency, and allow morphologic confirmation of which cells contain the target, making them widely adopted in clinical practice. However, these methods have intrinsic limitations: FISH cannot reliably detect small intrachromosomal rearrangements or define fusion partners, and IHC provides only semi-quantitative data [5,6]. Reverse transcriptase polymerase chain reaction, though highly sensitive, depends on prior knowledge of fusion partners due to its reliance on gene-specific primers, limiting its utility for genes with numerous fusion variants [7]. NGS, encompassing both DNA- and RNA-based strategies, addresses many of these limitations by allowing simultaneous identification of multiple fusion events [8]. DNA-based NGS interrogates both exonic and intronic regions, but carries a risk of false negatives, necessitating confirmation with RNA-based assays, which focus specifically on expressed transcripts [9]. RNA-based NGS, particularly through targeted fusion panels, has become an essential complementary technique due to its high sensitivity for fusion transcripts [10,11]. Liquid biopsy–based detection, primarily via circulating tumor DNA analyzed by DNA-based NGS, is promising but also challenged due to DNA fragmentation, low concentrations, and technical artifacts that reduce sensitivity compared to tissue analyses [12,13]. Given these complexities, optimal diagnostic accuracy often requires the integration of orthogonal sequencing methods—using DNA and RNA sequencing in parallel—to achieve comprehensive fusion detection [14]. When a novel gene fusion is identified, functional characterization is necessary to assess its clinical significance. A recently introduced functional genomic strategy systematically evaluates the cellular impact of gene fusions, incorporating an integrated, evidence-based classification framework to prioritize their relevance [15]. Importantly, a recent retrospective analysis demonstrated improved clinical outcomes among patients harboring actionable gene fusions who received fusion-targeted therapies (n = 25) compared with those treated with just systemic therapies not matched to their fusions (n = 42) [16]. These findings underscore the clinical value of fusion testing and highlight the therapeutic potential.

Non-Spitz melanocytic nevi

To date most of the gene fusions in benign non-Spitz melanocytic nevi, although rare, were reported in congenital nevi, known to harbor missense pathogenic variants in *NRAS* and *BRAF* and with a remaining 25% being unknown mutation status [17]. Gene fusions were identified in wild-type and mutant for *NRAS*/*BRAF*/*KRAS* nevi.

BRAF

In 2007, Dessars et al. [18] reported two cases of congenital melanocytic nevi with *BRAF* fusions: first was *FCHSD1::BRAF* and a second one where the partner to *BRAF* was not determined. Neither of two cases had a *BRAF* or *NRAS* mutation [18]. In 2019, Mir et al. [19] reported potentially actionable *AKAP9::BRAF* fusion in a giant congenital melanocytic nevus subsequently successfully targeted by trametinib [19]. In 2022, Molho-Pessach et al. [20] reported a *CUX1::BRAF* fusion in a case of another giant congenital melanocytic nevus. A *ZNF777::BRAF* was fusion identified in a congenital nevus from a patient with multiple melanomas where one of the prior patient's melanomas demonstrated the same fusion along with a *TERT* promoter mutation and *MET* copy gain [21]. In a cohort of 19 cases with wild type for *NRAS* and *BRAF* congenital nevi, gene fusions were identified in 12

https://doi.org/10.4132/jptm.2026.03.11

cases (7% of the total 169 patient cohort), where *BRAF* fusions significantly outperformed *RAF1* fusions. Ten different partner genes were identified (*AGAP3*, *AKAP9*, *EEA1*, *GOLGA4*, *LCA5*, *MIER3*, *PHIP*, *QKI*, *SEC31A*, and *STRN3*), where only *EEA1* and *GOLGA4* were recurrent partners. Clinically *BRAF*/*RAF1* fusions are significantly associated with a hyperproliferative phenotype of the nevi ($p < .001$), chronic intractable pruritus, requirement for surgical intervention for tumor overgrowth and high sensitivity to MEK inhibitors [22]. Histopathology of *BRAF*-fusion driven non-Spitz nevi demonstrated variable patterns of desmoplasia and fibrosis. Two of the mentioned cases of congenital nevi harboring *EVI5::BRAF* and *QKI::BRAF* fusions were successfully treated with MEK inhibitors [22]. The study from Botton et al. [23] revealed another *BRAF* fusion partner, *ZKSCAN5* (a zinc finger protein), in an intradermal melanocytic lesion from the buttock. Agrawal and Guo [24] reported another dermal melanocytic lesion with congenital features and bland nevoid cytomorphology also from a buttock of 44-year-old female with an *EPS15*:*BRAF* fusion. Recently Roy et al. [25] reported a case series of five giant congenital melanocytic nevi with *BRAF* fusions (two cases with *AKAP9::BRAF*, *ATAD2::BRAF*, *ST13::BRAF*, and *TRIM4::BRAF*) demonstrating the same hyperproliferative phenotype, pruritus, multiple satellite nevi, and desmoplastic stroma. Interestingly, one patient with *ATAD2::BRAF* fusion developed neurocutaneous melanosis. El-Rayes et al. [26] reported another case of congenital melanocytic nevus with *SH2B1::BRAF* fusion and associated neurocristic cutaneous hamartoma.

RAF1

In 2019, Baltres et al. [27] reported a case of rapidly growing mass from the lumbosacral giant congenital nevus, showing melanoma with myxoid and rhabdomyosarcomatous transformation, and harboring an in-frame *SASS6::RAF1* fusion by RNA-based sequencing in both the melanoma and nevus components. Neither component had *NRAS* or *BRAF* mutations by sequencing. A *RAF1* break-apart FISH assay revealed a balanced rearrangement in the nevus and an unbalanced one in the malignant component [27]. In 2019, Martins da Silva et al. [28] in study of twenty-one congenital melanocytic nevi reported two novel gene fusions in *NRAS*-wild type nevi - *ZEB2::ALK* and *SOX5::RAF1* and one *GGNBP2::MYO19* in *NRAS*-mutant nevus. The *ZEB2::ALK* and *SOX5::RAF1* fusions were identified only in nevi and not in the unaffected skin, supporting the oncogenic potential of those two fusions. On the other hand, the *GGNBP2::MYO19* fusion was also detected in the unaffected skin and was considered non-actionable [28]. Vinyals et al. [29] found the same *SOX5::RAF1* fusion in a *NRAS*/*BRAF*-wild type congenital nevus. That study revealed that *SOX5::RAF1* fusion transcript expression led to *MAPK* activation through increased levels of phosphorylated ERK protein in the cytosol of transduced cells; induced growth factor-independent cell growth in murine hematopoietic Ba/F3 cells and Melan-A immortalized melanocytes; and promoted tumor growth and lung metastasis in mice. It was suggested that *SOX5::RAF1* fusion is an oncogenic functional fusion with heightened possibility to malignant transformation and potentially targetable with RAF1 kinase inhibitors or those targeting MAPK pathways [29].

These studies show that *BRAF* and *RAF1* kinase fusions represent recurrent genetic alterations in congenital and non-Spitz melanocytic nevi that usually lack mutations in *BRAF*, *KRAS*, or *NRAS*. These fusion events activate the MAPK pathway, frequently demonstrate fibrotic background on histopathology, should undergo close follow up and may be amenable to targeted therapy with RAF or MEK inhibitors.

RASGRF2

In 2021, the group of Houlier et al. [30] reported five cases harboring *RASGRF2* fusions, in particular *ATP2B4::RASGRF2* and *ERBIN::RASGRF2* fusions, with a variety of clinical presentations ranging from large congenital nevus to melanoma ex-nevus as well as intermediate grade melanocytic lesions (melanocytomas). Most cases were present at birth, including a large congenital nevus, supporting a postzygotic origin of the *RASGRF2* fusion, similar to *BRAF* and *RAF1* gene fusions in nevi. Interestingly, in the reported malignant transformed case of that series, the melanoma demonstrated a peculiar histomorphology of mainly dermal expansion of dense sheets of epithelioid atypical melanocytes. In addition, this malignant case demonstrated *BAP1* inactivation and authors hypothesized that *RASGRF2* fusion induced the overexpression of a chimeric RasGRF2 protein leading to an oncogenic activation of the *MAPK* pathway, considering that all cases demonstrated RasGRF2 overexpression [30]. The *RASGRF2* expression was reported in multiple other carcinomas including rapidly growing triple-negative breast cancer [31], invasive colorectal cancers [32] and lung carcinomas associated with poor prognosis [33]. The fusion partner *ATP2B4*, that was found three out of five cases, was also repeatedly reported as *ATP2B4::PRKCA* in pigmented epithelioid melanocytomas including congenital cases [34,35]. No gene fusions involving another gene partner *ERBIN* (ERBB2

interacting protein) have been previously reported in melanocytic lesions. Overall, melanocytic lesions harboring *RASGRF2* fusions display unusual dermal morphological features and can progress to malignancy although more data is needed to prove it as an oncogenic driver.

Other

Perron et al. [36] reported four cases of melanocytic myxoid spindle cell tumor with *ALK* rearrangement (MMySTAR) including *FBXO28::ALK*, *NPAS2::ALK*, *TPM3::ALK*, and *PPFIBP1::ALK*. These lesions lose at least partially Melan-A expression and were interpreted as a potentially new variant of compound nevi linked to a kinase fusion [36].

Conventional non-Spitz melanoma

Unlike driver somatic mutations, such as *BRAF*, *KIT*, *NRAS*, *NF1*, *GNAQ*, or *GNA11*, gene fusions are rare in conventional non-Spitz melanomas with recently reported data indicating that only 2% of melanomas harbor it. Among melanomas with gene fusions, *BRAF* fusions were the most common, present in 0.8% (6/750) of cases, followed by *RAF1* fusions in 0.7% (5/750), and *ALK* fusions in 0.3% (2/750). Melanomas with gene fusions were typically triple wild-type, lacking somatic mutations in *BRAF*, *NRAS*, or *KIT*. A recent study from Moran et al. [37] reported that all *BRAF*-fused melanomas (100%; 5/5) also consistently harbored *TERT* promoter mutations. Our study showed that only 44% (4/9) of *BRAF*-fused melanomas had *TERT* promoter mutations [38].

BRAF

The *AGK* is the most frequent fusion partner of *BRAF* in melanomas [37,39,40]. Other less common fusion partners include *AGAP3*, *AGT7*, *ARMC10*, *CDH3*, *CHCDH3*, *CCT8*, *CCDC91*, *GTF2IRD1*, *DIP2B*, *FMN1*, *GTF21*, *MKRN1*, *PAPSS1*, *RAD18*, *SEPT3*, *TRIM24*, *TAX1BP1*, and *MYO5A* [37-45]. Menzies et al. [46] reported *PPFIBP2::BRAF* fusion on a superficial spreading melanoma metastatic to brain and a *KIAA1549::BRAF* fusion on a metastatic acral lentiginous melanoma, both included in a trametinib and pembrolizumab trial. Kim et al. [47] added other new *BRAF* gene partners in mucosal non-Spitz melanomas such as *ZNF767*, *NFIC*, *TNEM178B*, and *DGKI*. Perron et al. [48] reported two cases of deeply infiltrative melanomas with sclerosing/desmoplastic features and an *AKAP9::BRAF* fusion where one of the cases also had *MDM2* amplification. We have recently reported a case of fatal melanoma with *RNF11:BRAF* fusion also containing a *TERT* promoter mutation and showing peculiar epithelioid and rhabdoid morphologies, occasional giant pleomorphic cells and multinucleation, progressed with multiple metastases and reported non-responsive to therapy [49]. We also presented another case of melanoma with rhabdoid cytomorphology, multinucleation and occasional Reed-Sternberg–like cells resembling alveolar soft part sarcoma, that harbored a *SBF1::BRAF* fusion and a *TERT* promoter mutation [50]. The histopathologic features of *BRAF*-fused conventional bona fide melanomas seem to differ from those of Spitz melanocytic neoplasms with *BRAF* fusions.

The recent data have shown variability in treatment responses for these tumors, with *BRAF* fusion potentially indicating a poorer prognosis and/or more aggressive behavior [37,39,49,51].

RAF1

RAF1-fused conventional melanomas are extremely rare and comprise only 0.6% of cases [52,53]. Available data shows *RAF1* gene fusion partners such as *ANO10*, *CCDC85A*, *CDH3*, *GCC2*, *GOLGA4*, *EFNB1*, *EFCC1*, *FCGRT*, *FYCO1*, *LRCH3*, *MAD1L1*, *MAP4*, *NF2*, *RUFY1*, and *SLC4A7* [37,53-58]. The study of Williams et al. [52] added additional *RAF1* 5′ fusion partners: *MAP4* (n=3), *CTNNA1* (n=2), *LRCH3* (n=2), *GOLGA4* (n=2), *CTDSPL* (n=2), and *PRKAR2A* (n=2), where 62% (23/37) of cases had *TERT* promoter mutation and 60% (24/40) had *CDKN2A* activating mutation [52]. We have encountered a case on the ankle in a 24-year-old female, resistant to therapy and fatal, triple wild-type melanoma with a *MAP4::RAF1* fusion and *TERT* promoter mutation [59]. The study from Stransky et al. [60] reported 4 additional *RAF1* gene fusion partners in conventional melanoma including *LMNA*, *MPRIP*, *TRAK1*, and *CLCN6*.

Most of the reported *RAF1*-fused melanomas responded to targeted therapy and available in vitro studies also demonstrated sensitivity of *RAF1* fusions to the multi-kinase inhibitor sorafenib and variably responsiveness to the MEK inhibitors [53,55,61,62].

NTRK

The study from Lezcano et al. [63] reported *NTRK1* fusion partners including *TRIM63*, *DDR2* and *GON4L*, and one *NTRK2::TRAF2*, where all lesions were immunoreactive for pan-TRK.

ALK

Couts et al. [64] reported a mucosal melanoma case with an

https://doi.org/10.4132/jptm.2026.03.11

EML4::ALK fusion that was sensitive to ALK inhibitors. The study from Moran et al. [37] also reported two melanomas with *EML4::ALK* and *MLPH::ALK*. Perkins et al. [65] presented two cases of pediatric melanoma with *ZEB2::ALK* fusion arising within a congenital melanocytic nevus. There is a recent case of *BAP1*-inactivated melanoma associated with *ALK* fusion with unknown partner [66].

FGFR

The novel *FGFR3::TACC3* fusion was reported by Lee et al. [67] in a case of conventional melanoma with plasmacytoid features from the orbit.

MAPK

Beyond Spitz lineage, *MAP3K8* rearrangements occur in ~1.5%–1.7% of conventional melanomas in The Cancer Genome Atlas/other datasets, but most are C-terminal truncations, intronic region, rather than named fusions. *MAP3K8*-rearranged melanomas tend to have a low mutational burden and significant decrease of typical ultraviolet (UV)-mutational patterns, with frequency of UV-associated mutations (C>T and G>A) in comparison to *MAP3K8* wild melanoma of 40% vs. 74% (p = .0023) [68]. The break-apart FISH strategy and sequencing-based approaches have the potential to identify patients with *MAP3K8* truncating rearrangements. There are data of acral melanomas with *MAP3K8*:*DEK* fusion [69]. There is a recent case of a fatal mucosal melanoma with focal spitzoid features and *MAP3K8::PAK2* fusion, *CRKL* amplification and hemizygous *TP53* R280T mutation [70]. Although immune checkpoint therapy combinations are unlikely to benefit patients with melanomas carrying *MAP3K8* truncations, these melanomas have displayed sensitivity to both MEK and ERK inhibitors, providing rationale for a dual combination approach [68].

Similar to *MAP3K8*, the *MAP2K1* gene in conventional, acral, and mucosal melanomas is commonly reported to be mutated or truncated rather than fused [45,71-73]. In the largest cohort of *MAP2K1*-mutated primary cutaneous melanocytic tumors. Ebbelaar et al. [73] reported these alterations occur across the melanocytic spectrum (common and congenital nevi, melanocytomas, spitzoid tumors, desmoplastic melanomas) and can be grouped in three classes: I (RAF-dependent), II (RAF-regulated), and III (RAF-independent). Class I appeared almost exclusively in melanomas with co-driver *BRAF* or *NRAS* alterations and correlated with aggressive behavior. Classes II and III often acted as sole drivers across nevi, melanocytomas, and melanomas and carried substantial metastatic risk—especially when associated with *TERT*-promoter mutations [73].

Other

Other infrequent fusions included *CANT1::ETV4*, *CCDC6::RET*, *CLPTM1L:ADCY2*, *NOTCH1::GNB1*, *ADCY2::TERT*, *NAGS::MAST2*, *MDM2::GNS*, *MDM2::CCT2*, *PTEN::RPL11*, *TERT:ADCY2*, *TERT*:*PDCD1LG2*, and *PAK2::LOC646214* [37,69,74]. A recent study of acral melanomas reported another cohort of recurrently fused kinase genes included *TRIO* (11 fusions in 3 tumors), *PAK1* (9 fusions in 6 tumors), *DGKB* (7 fusions in 4 tumors), and *DCLK1* (3 fusions in 2 tumors) [45].

We also recently added two cases of *BCR*-fused melanoma *BCR::ZNF711* (zinc finger protein 711) and *BCR::CYLC2* (cylicin 2), where mutations in *BRAF*, *KIT*, or *NRAS*, both cases underwent immunotherapy and remained without evidence of disease although functional significance of *BCR* fusions in melanomas remains unclear at this point [75].

Spitz neoplasms

Historically Spitz neoplasms represent a diagnostic "gray zone" in dermatopathology mainly due to low inter-observer agreement in terminology—such as 'true Spitz lineage' versus 'Spitz-like'—and inconsistent classification across a spectrum that includes benign Spitz nevi, lesions of uncertain malignant potential (atypical Spitz tumors or melanocytomas), and Spitz melanomas. The diagnostic complexity is further complicated by their variable biological behavior and potential for locoregional lymph node involvement. Spitz neoplasms can be classified into four groups: (1) mutations (*HRAS* mutations [with or without 11p amplification] and 6q23 deletions); (2) receptor tyrosine kinase fusions (*ALK*, *ROS1*, *NTRK1*, *NTRK3*, *RET*, *MET*, *MERTK*, *LCK*, and *FGFR1*); (3) serine/threonine kinase fusions and mutations (*BRAF*, *RAF1*, *ERBB4*, *MAP3K8*, *MAP3K3*, and *PRKDC*); and (4) other rare genomic aberrations [76-78]. All these driver gene alterations so far are considered mutually exclusive. In the receptor tyrosine kinase fusions group, the 3′ end intact kinase domain is placed under the control of the promoter of 5′ end partner gene followed by generation of a chimeric protein with functional kinase with constant overexpression of the RTK in melanocytes. The cellular localization of the chimeric protein—whether at the cytoplasmic membrane, within the cytoplasm, or in the nucleus—is determined by the biological properties of the 5′ fusion partner [79]. The serine threonine kinase fusions are less frequent and demonstrate similar mechanism to

RTK fusions with *BRAF* partner while in *MAP3K8* fusions, the 5′ partner retains the first eight exons of *MAP3K8*, with the fusion breakpoint occurring downstream. This results in the loss of the 3′ sequence encoding the regulatory tail that normally occludes the kinase domain [80]. The new oncogenic model was recently described with *MAP2K1* micro-deletions and fusions involving *RASGRF1* and *RASGRF2* where the main driver is kinase modulator rather than the kinase itself [30,81,82].

The current problem of Spitz neoplasms lies in the presence of clearly malignant tumors with spitzoid morphology and fatal outcomes, where growing data on oncogenic gene fusions may help segregate these "Spitz-like" tumors from "true Spitz lineage" and thus allow a different patient management. Truly malignant, fusion-driven Spitz neoplasms do occur but they remain relatively rare. In such cases, molecular alterations such as homozygous deletions of 9p21 (*CDKN2A*), 6p25 copy number gain, *TP53* mutations or loss, *PREX* p.S658 L mutation, *Rb* gain or *TERT* promoter mutations may provide useful prognostic information and consideration of a diagnosis of Spitz melanoma [77,83-85]. Further understanding of gene fusions in Spitz neoplasms may aid in their diagnostic classification, risk stratification, and therapeutic decision-making.

HRAS

Up to 20% of Spitz nevi harbor copy number gains and/or activating mutations in HRAS, located at chromosome 11p15.5 [86]. Spitz nevi with this genomic alteration often exhibit desmoplastic features and/or gain of 11p as the only detectable copy number aberrations (isolated gain of 11p); however, this phenotype is not consistently present in all cases [87].

Tyrosine kinase fusion–associated Spitz neoplasms

ALK

ALK gene rearrangements have been identified in approximately 10%–20% of Spitz nevi, 15% of atypical Spitz tumors, and about 3% of Spitz melanomas [79,88,89]. The most frequent fusion partners include *TPM3* and *DCTN1*, followed by *NPM1*, *TPR*, *CLIP1*, *GTF3C2*, *MLPH*, *EEF2*, *MYO5A*, *EHBP1*, and *KANK1* [88,90-93]. The chimeric fusion protein upregulates *MAPK* and PI3K/AKT/mTOR pathway and can be inhibited by *ALK* inhibitors [79]. *ALK*-rearranged spitzoid tumors are well characterized in the literature: they occur in a wide age range, usually involve lower limbs and usually clinically are amelanotic and polypoid [90,94]. These *ALK*-rearranged Spitz melanocytic neoplasms demonstrate distinct histopathology: exophytic or polypoid tumors with fusiform-to-epithelioid melanocytes arranged in a nested, fascicular, or plexiform growth pattern with wedge-shaped base architecture and infiltrative border at the periphery, or rarely a bulbous to nodular 'dumbbell' growth pattern [90]. Angiomatoid histomorphology is also seen in *ALK* fusions [80]. Several authors reported a total 11 cases of Spitz neoplasms harboring *MLPH::ALK* and diagnosed them as Spitz nevi or atypical Spitz tumors (ASTs) with only one case of Spitz melanoma [91,92,95,96]. *MLPH::ALK*-driven Spitz lesions tend to occur in younger population (<40 years old) with slight female predominance, manifest as an exophytic or polypoid nodule characterized by a proliferation of fusiform-to-epithelioid melanocytes with consistent dermal mitotic activity and diffuse expression of cytoplasmic *ALK* by IHC except of one case [91,92,95,96]. We also encountered a case of *MLPH::ALK*-fused atypical Spitz tumor with perineural invasion. Interestingly, in case of *EHBP1::ALK* fusion the ALK IHC demonstrated a peculiar membranous pattern of staining. It is important to remember that although ALK IHC is available along with ROS1 and pan-TRK, the positive result is only a reflection of overexpression and is not confirmative for fusion [97]. The type of labeling (membranous, cytoplasmic, or nuclear) is also should not be considered diagnostic Spitz nevi vs AST vs melanoma since it is fully dependable to the 5′ end fusion partner.

There are only a few documented cases of Spitz melanoma featuring *ALK* fusions [79,91,98]. Spitz melanoma with *SLC20A1::ALK* fusion, negative for *BRAF*, *KIT*, *NRAS*, *TERT* but harboring *GRM3* that is known to upregulate the MAPK pathway [99]. Frederico et al. [100] reported a *C2orf42::ALK* fusion Spitz melanoma in a 5-year-old girl with lymph node metastasis as well as diffuse membranous staining for ALK. Raghavan et al. [98] reported two Spitz melanomas, both with fascicular cytomorphology, one with a *DCTN1::ALK* fusion and second with a fusion of the 3′ portion of *ALK* to an intergenic region of chromosome 11q. This resulted in a gain of the distal portion of *ALK* encoding the kinase domain, suggesting that a complex rearrangement resulted in an *ALK* kinase fusion as the oncogene in this case [98]. Neither gene fusion is diagnostic for Spitz melanoma although fusions involving *ALK* and *MAP3K8* are among the most common rearrangements associated with progression to Spitz melanoma [97,101]. *TERT* promoter mutations rather than other factors such as deletions of the *CDKN2A* gene are highly predictive of an aggressive clinical course characterized by the development of distant metastases and a fatal outcome [101].

https://doi.org/10.4132/jptm.2026.03.11

ROS1

Wiesner et al. [79] reported *ROS1* fusions in 17% of Spitz neoplasms where 25.3% from detected fusions comprised benign Spitz nevi, 6.3% AST/melanocytomas, and 9% Spitz melanomas [85,102]. Therefore, *ROS1* fusions in Spitz neoplasms have a tendency for favorable outcome [102,103]. Furthermore, only few reported cases of *ROS1* fused Spitz melanomas reported to date, none of which resulted in distant metastases or death from disease [79,104]. *ROS1* fusions have been reported to have several partner genes, including most prevalent *PWWP2A* (37% of cases) and *TPM3* (31% of cases), followed by *PPFIBP1*, *CAPRIN1*, *MYO5A*, *CLIP1*, *ERC1*, *FIP1L1*, *HLA-A*, *KIAA1598*, *MYH9*, *ZCCHC8*, and *GOPC* [79,98,103,105,106]. The chimeric fusion product demonstrates constitutively increased phosphorylation activity, with increased activation of downstream MAPK and PI3K/AKT/mTOR signaling cascades [4,79]. We also encountered a classic Spitz nevus with *PPFIBP1::ROS1*-fused atypical Spitz tumor (Fig. 1A, B). There are also reports of *ROS1* fusions in desmoplastic Spitz nevi [79,102], pigmented spindle cell nevi of Reed and one eruptive Spitz nevus [107].

The clinical presentation of *ROS1*-fused Spitz lesions was well described by Gerami et al. [102]: age range of 3 to 58 years (mean of 19 years), no particular anatomical site predisposition, presented as pink to red papules. Although *ROS1*-fused Spitz neoplasms generally lack specific histopathologic characteristics in comparison to *ALK*-fused lesions, lesions with *ROS1* fusions displayed a well-circumscribed epidermal and dermal proliferation of epithelioid and spindled melanocytes with mild to moderate atypia, low mitotic activity (~1.3/mm^2) and Kamino bodies [102]. There was also transepidermal elimination of melanocytic nests and myxoid/mucinous stroma [103]. Immunohistochemically, the anti-*ROS1* monoclonal antibody is quite specific but at the same

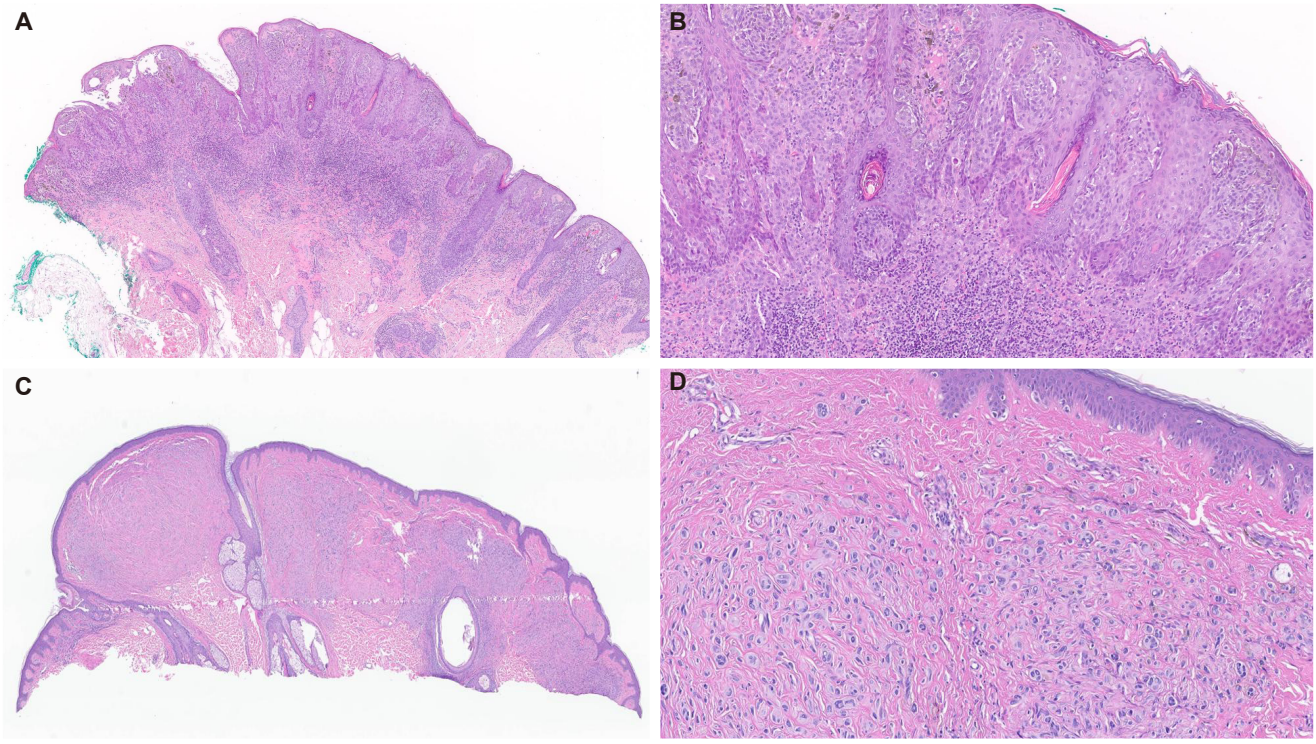

Fig. 1. *PPFIBP1::ROS1*-fused Spitz nevus. A shave biopsy shows symmetrical compound melanocytic proliferation with spitzoid morphology (A). The cytomorphology is significant for large melanocytes, single and nested, with focal Kamino bodies, clefting, ample amphophilic cytoplasm, and prominent nucleoli. There was no expression for *BRAF*V600E, ALK, and pan-TRK, while molecular studies detect the presence of a *PPFIBP1::ROS1* gene fusion and CCND1 was borderline amplified (B). *MYO5A::FGFR1*-fused atypical Spitz tumor. A shave biopsy shows atypical compound melanocytic proliferation with spitzoid cytomorphology and associated desmoplastic stroma (C). The lesional cells are large epithelioid and spindled melanocytes with vesicular or hyperchromatic chromatin and scattered nucleoli with moderate amounts of amphophilic cytoplasm. Molecular studies reveal *MYO5A::FGFR1* fusion; however, additional molecular alterations including TERT promoter mutations were not identified (D).

time is typically weak; therefore it is recommended to confirm *ROS1* rearrangement by FISH, polymerase chain reaction, or NGS [77]. Various immunohistochemical staining patterns have been reported, including diffuse granular cytoplasmic, dot-like, and nuclear expression; however, no consistent correlation has been established between these patterns and the subcellular localization of the different *ROS1* fusion variants identified to date [108]. The implementation of NGS recently yielded a novel and potentially actionable *ROS1* p.S1986P mutation, which has not been previously reported in Spitz nevus [85]. The group of Delsupehe et al. [78] reported two new fusions: *LIMA1::ROS1*, in a 17-year-old male with hypertrophic buccal lesion, histologically composed of epithelioid and fusiform melanocytes, that was subsequently classified as Spitz nevus; and *LRRFIP2::ROS1*, in a 73-year-old female with rapidly growing lesion on the ankle, composed of conspicuous epithelial component of single melanocytes with architectural disarray and epithelioid dermal component, later categorized as AST/Spitz melanocytoma. As was mentioned before, *ROS1* fusions in melanoma and "favor melanoma" lesions are rare and include: *GOPC::ROS1* in acral lentiginous conventional melanoma [109] and a case of unresectable Spitz tumor [105] with dramatic response to *ROS1* targeting tyrosine kinase inhibitors—entrectinib and crizotinib in both cases; and a *ROS1* fusions were also reported in 9.1% of spitzoid melanomas [79]; as well as *ROS1* rearrangement was reported in a superficial spreading conventional melanoma but was likely nonfunctional [4].

NTRK 1/2/3

The *NTRK1*, *NTRK2*, and *NTRK3* genes encode TrkA, TrkB, and TrkC receptors, which mediate melanocyte responses to neurotrophic signals [110,111]. *NTRK* gene fusions lead to Trk overexpression or activation, triggering MAPK, PI3K, and PLCγ pathways [112]. The frequency of *NTRK* fusions in Spitz neoplasms is approximately 10%–17% with NTRK1 being most prevalent followed by *NTRK3* [113]. It is important to mention that pan-TRK and NTRK1 antibodies are widely used and cost-effective for screening for *NTRK* fusion, including available clones A7H66R and EPR173441 [114-118]. Pan-TRK immunostaining patterns differ by *NTRK* fusion type, with *NTRK1* fusions typically showing strong cytoplasmic staining and *NTRK3* fusions presenting as weak, granular, or nuclear-cytoplasmic staining. Molecular analyses (e.g., FISH, RNA sequencing) are necessary to confirm the specific fusion partner [97].

NTRK1

NTRK1 encodes the TRKA receptor, a key oncogenic driver and promising target for cancer therapy due to its pivotal role in tumorigenesis. *NTRK1* activation triggers cell signaling through pathways such as PI3K/AKT and MAPK [79]. *NTRK1* fusions have been found across the entire Spitz spectrum including Spitz nevi, AST/melanocytoma, and Spitz melanomas [79,114]. Most reported partner genes include *LMNA*, *PRDX1*, *TPM3*, *TP53*, and *KHDRBS1* [119] where *LMNA* was predominantly reported in Spitz nevi followed by atypical Spitz tumors and some spitzoid melanomas that harbor additional findings such homozygous *CDKN2A* deletion without known recurrence [111]; *PRDX1* was reported in atypical Spitz tumor [120]; *TPM3* in atypical Spitz tumor with associated heterozygous loss of *CDKN2A* and recurrence; *TP53* and *KHDRBS1* both were also reported in atypical Spitz tumors [111]. Histopathologically, *NTRK1* fusion–positive tumors often display classic spitzoid morphology, with rare cases reported to show some rosettes, filigree-like epidermal rete ridges, lobulated nests or exhibit prominent maturation [121], though no specific histopathologic features reliably predict their presence. Unlike *ALK*-rearranged neoplasms, which more commonly exhibit plexiform or fascicular growth, *NTRK1*-positive lesions more frequently contain epithelioid-to-spindled cell cytomorphology [117].

NTRK1 fusions were also reported in non-Spitz melanomas: *NTRK1::TRIM63* in nodular melanoma, *NTRK1::DDR2* in nodular melanoma from umbilical region with metastasis to colon, and a *NTRK1::GON4L* in nodular melanoma from back with metastasis in the duodenum co-occurred with *NRAS* Q61L mutation [63]. Lee et al. [122] reported *NTRK1* translocation in another spitzoid melanoma which co-occurred with homozygous deletion of chromosomal 9p21 by FISH with positive lymph node and no recurrence. Raghavan et al. [98] reported another melanoma case with *TPM3::NTRK1* fusion along with gain of chromosome 17 and loss of chromosome 5p upstream of *TERT* which possibly altered *TERT* promoter or enhancer sequences.

NTRK2

While *NTRK2* fusions are relatively rare compared to other fusions like *NTRK1* and *NTRK3*, their identification in melanocytic lesions is important due to the possibility of targeted cancer therapies. The *NTRK2::TFG* fusion was reported in Spitz nevus which histopathology reminded pigmented spindle cell nevus of Reed with diffuse pan-TRK cytoplasmic immunoreactivity and negative for ALK, ROS1, and BRAFV600E [123]. Mansour et

https://doi.org/10.4132/jptm.2026.03.11

al. [124] reported a series of five Spitz tumors with *SQSTM1::NTRK2* where all patients were female, all cases demonstrated diffuse pan-TRK staining and peculiar, prominent dendritic processes, highlighted with Melan-A immunohistochemistry, as well as conspicuous solitary or clustered hyaline. The junctional component showed horizontally oriented junctional nests and conspicuous lentiginous, single-cell growth in the follicular epithelium [124]. A *NTRK2::TRAF2* fusion was also reported in a primary spitzoid melanoma, superficial spreading type, arising from perianal skin [63].

NTRK3

NTRK3 fusions can be detected in 0.7% of Spitz tumors. They are observed in pigmented spindle cell nevus of Reed and in a subset of Spitz nevi with schwannomatous morphology with MYO5A being the most frequent partner, commonly affecting children [125]. Wang et al. [126] also reported this frequent occurrence in younger-age patients. *NTRK3* gene fusions were reported by Yeh et al. [121] with fusion partners including *ETV6*, *MYO5A*, and *MYH9*, with a median age of 10 years. de la Fouchardiere et al. [127] described different features depending on the gene partner. *NTRK3::ETV6* occurred in younger patients and had epithelioid or classic Spitz cytomorphology while *NTRK3::MYO5A* lesions contained spindled cells arranged in fascicles with neuroid features such as pseudo-Verocay bodies. They detected a chimeric product from *NTRK3::ETV6* localization in the nucleus and cytoplasm, followed by intense nuclear and less intense cytoplasmic pan-TRK immunohistochemistry; and localization of *NTRK3::MYO5A* chimeric product in dendrites, followed by linear pan-TRK immunopositivity [127]. The *MYH9::NTRK3*-fused tumors are composed of syncytial epithelioid cells, with central desmoplastic stroma and peripheral collagen trapping [115,127]. The most recent *NTRK3* gene fusion partner was reported by Della Mura et al. [128] as *VIM::NTRK3* in a 10-year-old girl in atypical Spitz tumor/Spitz melanocytoma showing peculiar granular cytoplasmic and perinuclear dot-like pattern on pan-TRK IHC. While occasional involvement of regional lymph nodes has been observed, distant metastases and poor prognoses have not been documented to date.

RET

About 3%–4% of Spitz neoplasms were found to have *RET* fusions with *CCDC6*, *KIF5B*, *LMNA*, *GOLGA5*, and *MYO5A* [37,79,129,130]. Additionally, Donati et al. [129] reported other partners: *OPTN* in three cases, and *AGAP3*, *NCOA4*, *ERC1*, and *MYH9*. These *RET*-fused Spitz neoplasms do not demonstrate a definitive characteristic tumor cytomorphology, although nevoid cytomorphology may be associated with *KIF5B*, neuroid-like with *MYO5A*, epithelioid with *LMNA* and *CCDC6* and transepidermal elimination/floating intraepithelial nests of pigmented melanocytes with *OPTN* [129]. Kim et al. [130] reported a case series where all *RET*-fused Spitz neoplasms demonstrated similar morphological features, i.e. plaque-like silhouette with expansile and dyshesive nests of monotonous predominantly epithelioid melanocytes without high grade atypia or pleomorphism. Although these *RET* fusions have been identified in all three Spitz nevi, atypical Spitz tumors, and Spitzoid melanomas, the available follow-up data indicate a favorable prognosis. The therapeutic potential for vandetanib and cabozantinib in these lesions is under investigation [131].

MET

MET-fused Spitz neoplasms have been rarely reported, harboring a diverse range of fusion partners, including *TRIM4*, *ZKSCAN1*, *LRRFIP1*, *PPFIBP1*, *EPS15*, and *DCTN1* [85,88,132,133]. The chimeric fusion product activates the MAPK, PI3K/AKT, and PLCg1 pathways [88]. The most recent study from Roy et al. [134] discovered a significant addition to the novel *MET* gene fusion partners cohort: *CPSF7*, *DCTN1*, *KIF5B*, *KLHL7*, *LRRFIP1*, *TRIM4*, and *ZKSCAN1*, being diagnosed in low grade melanocytomas or nevi, and *EPS15*, *MLPH*, *PPFIBP1*, and *TRIM4* in high grade melanocytomas or melanomas [134]. This study identified three main histopathologic patterns in *MET*-fused melanocytic neoplasms: "plexiform maturing fascicles", "Reed-like" pattern, and "BAP1-deficient-like" pattern [134]. All cases with available follow-up have demonstrated indolent clinical behavior.

Serine-threonine kinase-rearranged Spitz tumors

BRAF

BRAF-fused Spitz neoplasms along with *MAP3K8* fusions are among the fusion driven Spitz subtypes that are likely to be diagnosed as Spitz melanoma. Activating point mutations of *BRAF* are not characteristic for Spitz neoplasm while BRAF fusions are relatively common with overall prevalence of 5%–5.7% with 14% reported as Spitz nevi, 45% as AST, and 41% as Spitz melanoma [3,79,89,98,132,135,136]. *BRAF*, a proto-oncogene on chromosome 7q encoding a serine/threonine kinase, when fused, loses its autoinhibitory CR1 and CR2 domains, retaining only the active CR3 kinase domain, thereby driving MEK-ERK pathway activation [41].

The most reported *BRAF* gene fusion partners include *CLIP2*, *AKAP9*, *EML4*, *AGK*, *BAIAP2L1*, *CEP89*, *CUX1*, *DYNC1/2*, *LSM14A*, *MAD1L1*, *MLANA*, *MYO5A*, *MZT1*, *NRF1*, *SKAP2*, *SLC12A7*, *SOX6*, *TRIM24*, *NUDCD3*, *PLIN3*, *KCTD7*, and *ZKSCAN5* [23,43,48,79,98,135-138]. The *AGK* and *AKAP9* are the most frequent partners. Roy et al. [139] reported two desmoplastic Spitz nevi with *TMEM106B::BRAF* in one patient with a ring chromosome 7. Sorino et al. [140] reported an atypical Spitz tumor on the left outer ear in 13-year-old boy with *TAX1BP1::BRAF*, a finding that was previously reported only in non-Spitz melanomas. In the study by Sharma et al. [141] there were additional *BRAF* gene fusion partners: AST with *TRIM33*, *TRIM24*, *RAB3GAP2*, *ZNF777*, *CDC42BPB*, *COBL*, *GOLGA4*, *KLC1*, *AGAP3*, *GTF2I*, *OSBPL1A*, *SND1*, *BIDC1*, and Spitz melanoma with *ERC1* [141]. Roy et al. [142] reported additional novel *BRAF* partners such as *WDR91*, *ERC1*, *GTF2I*, *KIFAP3*, *RECQL*, *RNF11*, *RP2*, and *TMEM178B* in "favor benign" Spitz neoplasms and *EEA1*, *TRIM33*, *NRF1*, *ZKSCAN1* in "favor or concerning for melanoma" Spitz neoplasms.

Clinically, the *BRAF*-fused Spitz lesions usually present as a pink papule on the extremities of young patients, predominantly females [136]. Histopathologically, in 2023, Roy et al. [142] reported a series of 58 cases with *BRAF* gene fusions and described three main histopathological presentations: (1) large epithelioid melanocytes arrayed as single cells embedded in a markedly fibrotic stroma ("buckshot" pattern); (2) polypoid growth with a whorled arrangement of cords and single melanocytes within a desmoplastic stroma ("cords in whorled fibrosis" pattern); and (3) fascicular growth of spindled melanocytes ("spindle-cell fascicles" pattern). These morphologic patterns did not distinguish benign and malignant melanocytic tumors with *BRAF* fusion [142]. In general, *BRAF*-fused Spitz neoplasms often lack well-organized nest formation and are primarily composed of large epithelioid cells with marked cytologic atypia and sclerotic stroma [89]. Marked fibrosis was more frequently present in *BRAF*-rearranged cases than in other fusions ($p = 5 \times 10^{-5}$) [116].

In the large study of 38 cases and a meta-analysis performed by Sharma et al. [141], the *BRAF*-fused Spitz neoplasms lacked PRAME expression (24/24) and maintained p16 expression (16/21) with wild-type *TERT* promoter. Two of the cases developed lymph node metastasis although no recurrence or distant metastasis (mean follow-up time 26.1 months) [141]. Additional data for sentinel lymph node metastases were reported [104,135,142]. On the other hand, there is a case of 14-year-old boy with an *EML4::BRAF* fusion Spitz melanoma who developed lung, liver, and brain metastases while on ipilimumab and temozolomide and expired 18 months after diagnosis; the tumor also harbored a hotspot TPM [135]. There is another reported *MAD1L1::BRAF* fusion in fatal case of Spitz melanoma with *TERT* promoter mutation, CDKN2A/B deletions, *MTAP* deletion, *MITF* amplification, and *PIK3CB* amplification, who developed multiple distant metastasis [143].

RAF1

Donati et al. [144] reported two Spitz nevi and 1 Spitz melanoma with *RAF1* rearrangement with the following gene fusion partners: *CTDSPL* and *ATP2B4* in nevi cases and *PPAP2B* in melanoma case with associated homozygous deletion of 9p21 (*CDKN2A*) in greater than 80 % of enumerated cells. Serine–threonine kinase–rearranged Spitz tumors appear to acquire additional chromosomal aberrations more readily than receptor tyrosine kinase–rearranged Spitz neoplasms, with earlier malignant transformation that may be driven by *CDKN2A* alterations [47,145].

MAPK

The *MAP3K8* is a serine-threonine kinase that directly phosphorylates MEK and activates ERK1/2. The truncating mutations and fusions of *MAP3K8* eliminate the autoinhibitory C-terminal domain from the translated protein then leading to increased catalytic activity of the kinase and increased functioning of MEK1/2-ERK1/2 pathway, which is involved in cell proliferation, division, and differentiation [146]. Recent studies, using transcriptome sequencing, found structural initiating oncogenic alterations such as *MAP2K1* in-frame deletions, *MAP3K3* fusions, and *MAP3K8* kinase fusions or truncations, in 9%–33% of Spitz neoplasms where non-*BRAF MAPK* gene alterations represented the most frequent driver in Spitz melanomas (22%) [147,148].

MAP3K8

Of the reported *MAP3K8*-fused Spitz neoplasms, 8% were classified as Spitz nevi, 40% as AST, and 52% as Spitz melanomas [98,145,148]. Among other serine–threonine kinase as well as tyrosine kinase fusions, the *MAP3K8* fusion was the most common alteration observed in AST or Spitz melanoma (n = 25, 33%), while such alteration was quite rare in the group of Spitz nevi (n = 6, 2%) [116]. *MAP3K8* gene fusion partners include *ATP2A2*, *CCNY*, *CDC42EP3*, *CUBN*, *DIP2C*, *GNG2*, *LINC00703*, *LYZL2*, *MIR3681HG*, *PCDH7*, *PIP4K2A*, *PRKACB*,

https://doi.org/10.4132/jptm.2026.03.11

RSU1, *SFMBT2*, *SLC4A4*, *SPECC1*, *STX7*, *SVIL*, *UBL3*, and *ZFP36L1* [85,98,138,145,148]. Sibira et al. [149] also recently reported a case of Spitz melanoma with *MAP3K8::ABLIM1* with associated *GRIN2A*, *TP53*, and *TERT* promoter mutations with rapid distant metastasis to lung. *MAP3K8*-fused Spitz neoplasms frequently harbor additional prognostically important genomic alterations such as biallelic inactivation or deletion of *CDKN2A/B* [85,98,116,145,148]. We encountered a case of *MAP3K8*-rearranged Spitz melanoma with unknown fusion partner, inactivating mutations involving *CDKN2A* and *CDKN2B*, and a *TERT* promoter mutation, with a Breslow thickness of 14.0 mm and lymph node metastasis (Fig. 2).

Clinically, Spitz neoplasms harboring *MAP3K8* fusions usually present as asymmetric, exophytic, pigmented lesions on the lower extremities, affecting patients of all ages with a slight female predominance [145,147]. Multiple other studies reported that *MAP3K8*-fused Spitz neoplasms presented as a dome-shaped or nodular lesion with overlying epidermal hyperplasia, and were associated with predominant epithelioid morphology, high-grade cytological atypia, multinucleated giant cells, and p16 loss [98,116,145,147,148].

Although lymph node metastases are frequently reported, widespread metastatic disease is rare [145]. The data are limited but appeared to be a short-lived response to MEK inhibitor in a Spitz melanoma with a *GNG2::MAP3K8* fusion [138].

MAP2K1

The proto-oncogene *MAP2K1*, situated at 15q and encoding a serine–threonine kinase integral to the RAF-MEK1/2-ERK1/2 signaling axis, exhibits recurrent mutations in Spitz neoplasms, mostly in-frame deletions involving exon 2 and 3, predominantly in atypical and malignant Spitz tumors which, similar to *MAP3K8* fusion events, disrupt the autoinhibitory MEK domain and result in constitutive downstream pathway activation [81].

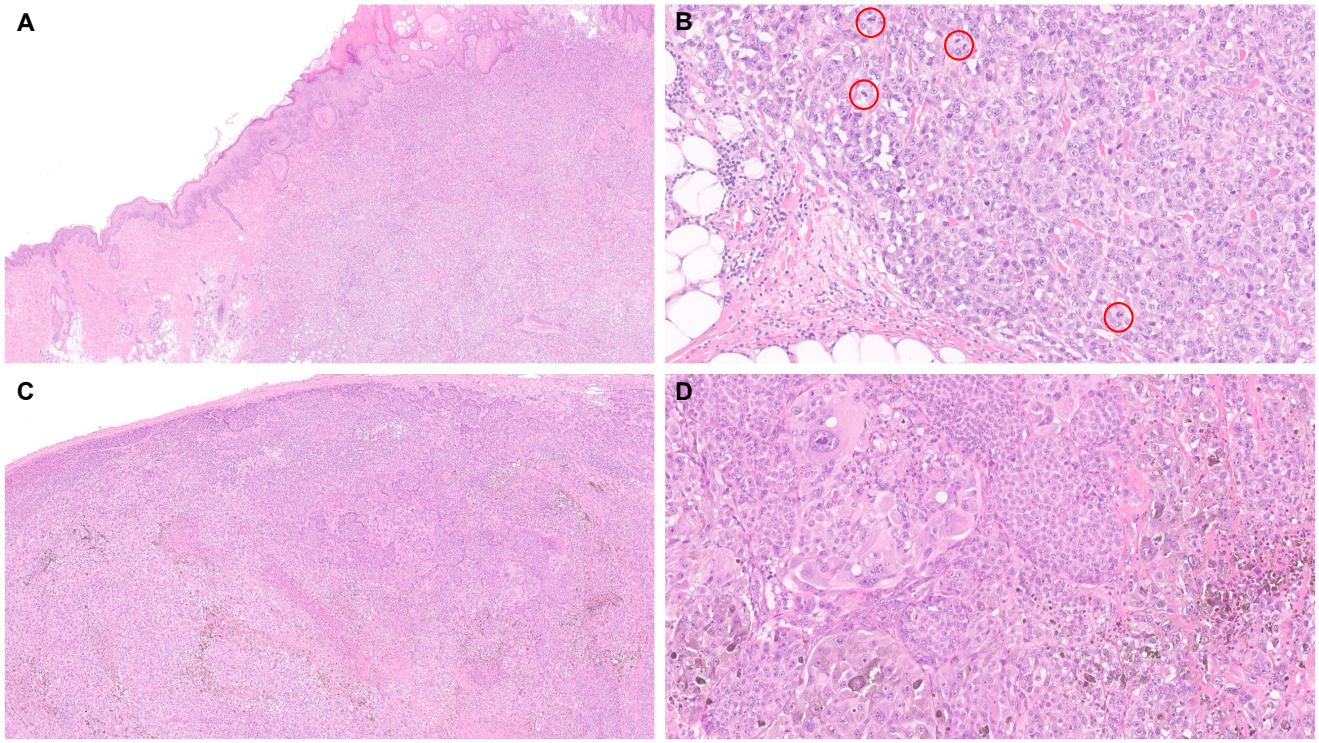

Fig. 2. *MAP3K8*-rearranged Spitz melanoma. The tumor exhibits a nodular growth pattern predominantly involving the dermis and subcutis (A), with a Breslow thickness of 14 mm. Mitotic figures (up to 20/mm^2) are readily identified (red circles), even in the deep dermis and subcutis. The tumor cells exhibit an epithelioid morphology with abundant eosinophilic cytoplasm and conspicuous nucleoli (B). A regional lymph node shows metastatic melanoma with focal tumor necrosis and regression (C). Marked cytologic atypia and pleomorphism, as well as occasional intracytoplasmic pigmentation, are more evident in metastatic tumor deposits (D). Molecular studies revealed inactivating mutations involving *CDKN2A* and *CDKN2B*, a *TERT* promoter mutation, and a *MAP3K8* rearrangement (with its fusion partner being unknown).

These mutations are fairly rare in Spitz neoplasms, with limited data available to date [116,148,150,151]. Whether *MAP2K1*-altered Spitz neoplasm harbor a distinctive histopathologic feature is questionable due to a high prevalence of additional genomic alterations [81]. Based on the available literature, *MAP2K1*-mutated Spitz neoplasms clinically present as small, pigmented, flat to slightly elevated lesions, predominantly on the lower extremities of young females. They tend to be wedge-shaped, compound or intradermal, with large epithelioid cells showing moderate to severe nuclear pleomorphism arranged in nests and showing a plexiform growth pattern, poor maturation and a tendency to converge around adnexal structures and neurovascular bundles [116,148,150,151]. In contrast to *MAP3K8*-fused Spitz neoplasms, these lesions often fail to demonstrate epidermal hyperplasia while frequently containing melanophages [81,150].

Other gene fusions in Spitz neoplasms

Kervarrec et al. [152] reported an exophytic-shaped Spitz nevus without architectural or cytological atypia and a *LMNA::MST1R* fusion, where *MST1R* (macrophage stimulating 1 receptor) is a transmembrane tyrosine kinase receptor homologue of *MET* receptor, a known gene in Spitz tumors pathogenesis. The complex three-way translocation *TRPM1::PUM::LCK* inducing *LCK* mRNA overexpression was reported in case of agminated Spitz nevi occurring in a giant congenital, hyperpigmented macule without any other known translocation; authors suggested the possibility of additional "second hit" mutation beyond the initial gene fusion [153]. Quan et al. [85] reported another novel gene fusions, *MYO5A::FGFR1*, *MYO5A::ERBB4*, and *PRKDC::CTNNB1*, as well as a novel potentially oncogenic *ROS1* p.S1986P mutation. We encountered another *MYO5A::FGFR1*-fused atypical Spitz tumor with desmoplastic stroma and prominent plump melanocytes (Fig. 1C, D). We recently also received a case of melanoma with Spitzoid features with locoregional metastasis and brain metastasis with a novel *LOC107984974::RARA* fusion (Fig. 3). Lastly, we want to report our new case of invasive melanoma with Spitzoid features and Breslow thickness of 8.8 mm from the right knee in 8-year-old girl, with *ETV6::ZNF784*

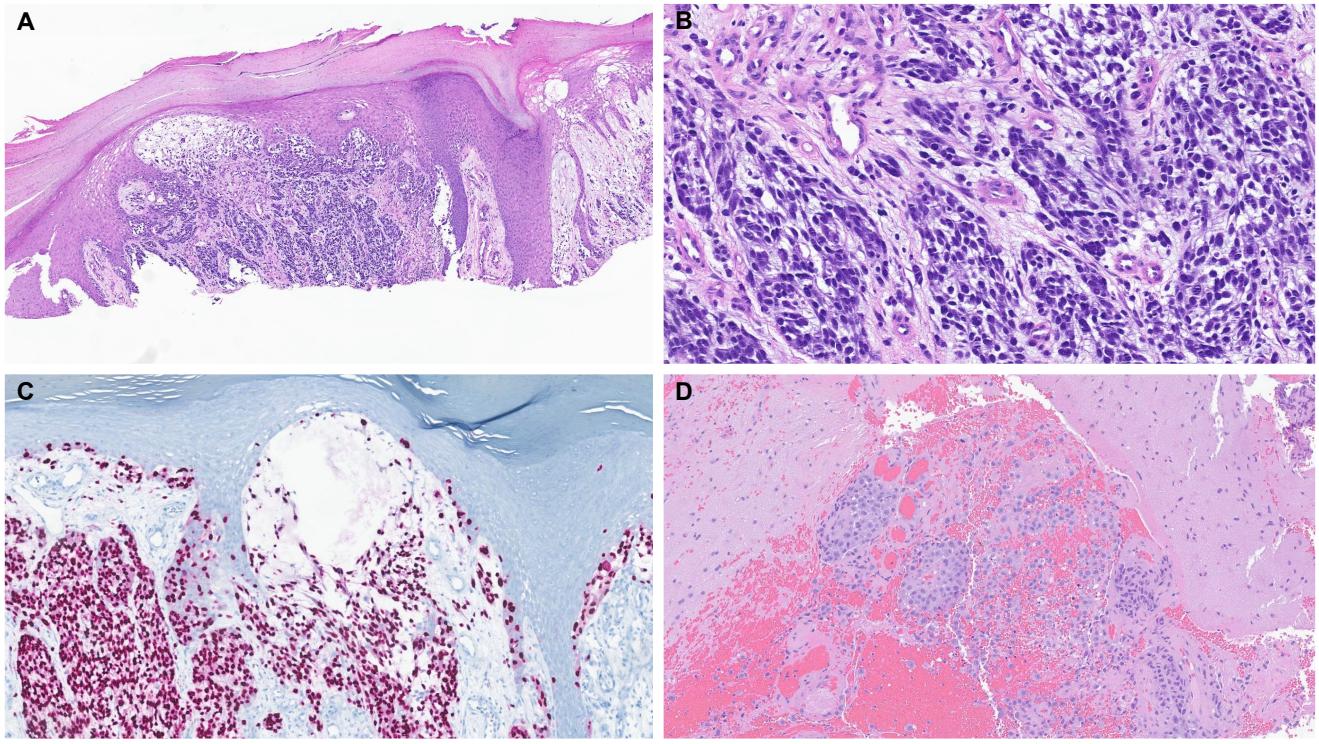

Fig. 3. *RARA*-rearranged melanoma. A shave biopsy specimen shows a non-ulcerated invasive melanoma with a Breslow thickness of at least 1.2 mm (A). The tumor cells exhibit epithelioid and focally spindled morphologies while lacking histopathologic features of a Spitz neoplasm (B). The cells are diffusely positive for SOX10 (C). The melanoma was clinically aggressive, causing locoregional and distant metastases, including a brain metastasis (D), despite systemic therapies. Molecular studies showed this melanoma to be triple wild-type (i.e., lacking *BRAF*, *NRAS*, *NF1* [or *KIT*] mutations), with a tumor mutational burden of 6 mutations/Mb, harboring a *LOC107984974::RARA* fusion.

https://doi.org/10.4132/jptm.2026.03.11

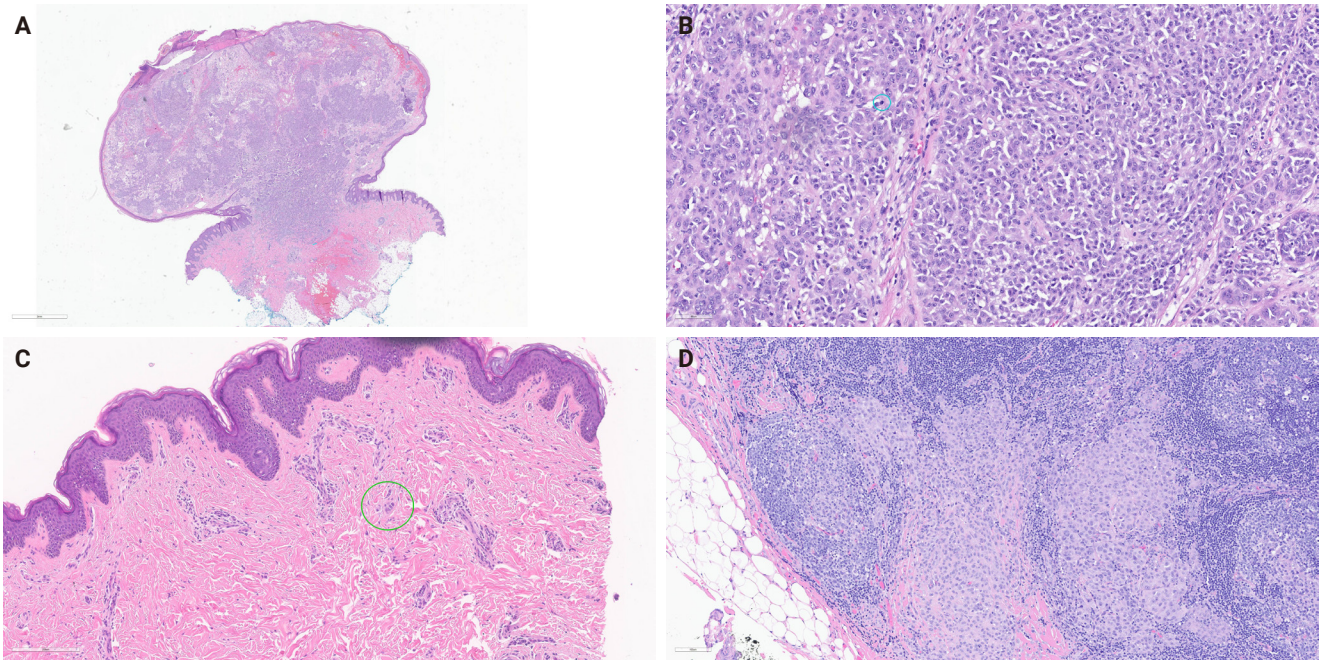

Fig. 4. *ETV6::ZNF784*-fused melanoma with Spitzoid features of the right knee. A polypoid-shaped ulcerated atypical compound melanocytic lesion with spitzoid morphology (A). The tumor cells exhibit epithelioid and Spitzoid morphologies with abundant mitotic figures, up to 9 figures/mm^2 (blue circle) (B). The subsequent excision specimen and tip margin demonstrates multiple microsatellites (green circle) (C). The sentinel lymph node lymphadenectomy demonstrates metastatic tumor (D). Molecular studies reveal *ETV6::ZNF784* fusion; three copy number alterations: gain of chromosome 5, loss of chromosome 9 including *CDKN2A/2B* genes and segmental loss of chromosome 10 (10p15.3–p14 and 10p11.23–p11.21); and two mutations: *ERG* p.A368V and *SPRTN* p.R140C mutations; the neoplastic cells were negative *BRAF*V600E, p16, ALK1, ROS1, and panNTK immunohistochemical studies. Interestingly, the patient demonstrated a synchronous atypical compound melanocytic neoplasm with Spitzoid features with the same genetic alteration on the left fifth finger, suggesting for a two synchronous or agminated presentation of fusion-driven melanocytic neoplasms.

fusion, characterized by multiple microsatellitosis and lymph node metastases; the patient also had and a synchronous/or agminated compound melanocytic lesion with the same genetic alteration on the left fifth finger (Fig. 4).

Pigmented spindle cell nevus of Reed

VandenBoom et al. [125] analyzed twenty-three pigmented spindle cell nevi (PSCNs) and found that 78% harbored gene fusions being *NTRK3* most frequent with *ETV6* and *MYO5A* being the most common 5′ partners. Other fusions included *MYO5A::MERTK* (2), *MYO5A::ROS1*, *MYO5A::RET*, and *ETV6::PITX3* [125]. Giubellino et al. [154] added two additional cases of PSCN of Reed with *MYO5A::NTRK3* fusion. In 2021, Goto et al. [123] reported a *TFG::NTRK2* fusion in PSCN. Those Spitz lesions with *NTRK3* fusions develop in younger patients [121]. Predominantly on the extremities and show expansile nests of heavily pigmented spindle-shaped melanocytes with a plaque-like silhouette [125,126]. There is a recent PSCN in 61-year-old male with a *SQSTM1::NTRK2* fusion and lacking alterations of *ALK*, *ROS1*, *RET*, *NTRK1*, and *NTRK3* genes [155]. The observed *BRAF* V600E expression and older age may suggest the diagnosis of PSCN [156].

Pigmented epithelioid melanocytoma

Pigmented epithelioid melanocytoma (PEM) is an intermediate grade lesion with relatively frequent involvement of regional lymph nodes but rare distant metastasis [157,158]. There are two main molecular pathways for PEM: (1) fusions involving *PRKCA*, usually in young patients, with solid sheets of monomorphic, pigmented epithelioid melanocytes [34,35,159]; and (2) inactivating alterations in *PRKAR1A* with a preexisting mutation of *BRAF* or *NRAS* which demonstrate variable histomorphology and often demonstrate a conventional nevus component [3]. In addition, some lesions have alterations in *GNA11* and *GNAQ*, changes

commonly seen in blue-nevus-type neoplasm [159]. The reported *PRKCA* partners include *ATP2B4*, *RNF13*, *SCARB1*, *CD63*, *MAP3K3*, and *ITGB5* [34,35,159,160]. The other rare gene fusions reported are *MYO5A::NTRK3*, *TPR::NTRK1*, *NTRK3::SCAPER*, *CD63::PRKCB*, and *HTT::PKN1* [159,161-163].

Blue nevi group melanocytic neoplasms

PRKC-fusion melanocytic tumors have now been reclassified into the blue-nevus family with mostly benign course after excision and occasional cases of melanoma, often with *BAP1* loss [164]. The study of 51 cases from de la Fouchardiere et al. [165] identified that *PRKC*-fused melanocytic neoplasms involve *PRKCA* in 35 cases, *PRKCB* in 15 cases, and *PRKCG* in one case. The reported gene fusions among *PRKC*-fused lesions include *PTPRJ::PRKCB*, *ATP2B4::PRKCA*, *PTPRJ::PRKCA*, *SLC44A1::PRKCA*, *RNF13::PRKCA*, *LAMTOR1::PRKCA*, *HM13-PRKCA*, *EDNRB-PRKCA*, *SCARB1::PRKCA*, *PTTG1IP-PRKCB*, *EMP1-PRKCB*, *MLNA-PRKCG*, and *CD44-PRKCB* [164,165]. *PTPRJ* and *SLC11A2* were involved in both *PRKCA* and *PRKCB* fusions [165]. In two of the melanoma cases harboring *PRKC* fusions there was a *BAP1* loss [60,165,166]. *PRKC*-fused cases are dermal-based lesions composed of medium-sized, epithelioid/oval cells with distinct hypercellular areas and a sheet-like pattern alternating with areas with less compact oval/spindled melanocytes and fibrotic stroma, and overall minimal to light pigmentation [164,165].

While activating mutations in *GNAQ*, *GNA11*, *CYSLTR2*, and *PLCB4* genes are considered the main oncogenic drivers of blue nevi and blue malignant melanocytic tumors, the recent study reported an alternative oncogenic pathway involving *GRM1* fusions such as *MYO10::GRM1* and *ZEB2::GRM1* fusions as well *GRM1* rearrangement with an unknown partner identified by FISH [167]. Of note, both blue nevi-like melanomas demonstrate *MYO10::GRM1* fusion with SF3B1 co-mutation.

Deep penetrating melanocytic neoplasms/WNT-activated melanocytomas

Yeh et al. [168] showed that deep penetrating melanocytic nevi/melanocytomas harbor activating mutations in the β-catenin and MAPK pathways, with a single reported *AKAP9::BRAF* fusion; progression to malignant counterparts appears to require additional alterations such as *TERT*-promoter mutations and *CDKN2A* loss.

Other melanocytic neoplasms

Gene fusions have also been reported as oncogenic drivers in other tumors that demonstrate melanocytic differentiation.

The cutaneous melanocytic tumor with *CRTC1::TRIM11* fusion, present as slowly growing, well-circumscribed dermal nodule on adults across a broad age range and with no consistent anatomic distribution. It is composed of spindle and epithelioid melanocytes organized in nests, fascicles, or bundles and separated by delicate collagenous septa. IHC reveals consistent expression of S100, SOX10, and MiTF, with variable positivity for other melanocytic markers such as Melan-A, PRAME, and HMB-45, and nearly universal nuclear TRIM11 expression [169,170]. Initially reported with rare regional metastasis but recently reported to demonstrate more aggressive behavior [171-175].

Subsequently, the three pediatric dermal tumors resembling *CRTC1::TRIM11* tumor were described driven by a *MED15::ATF1* [176]. They typically occur as dermal nodules on the head and neck (arm, cheek, scalp), some with epidermal involvement or ulceration, and may show early regional lymph nodes spread. They are highly cellular, composed of monomorphic oval-to-round epithelioid cells arranged in vague nests and short fascicles within a fibrotic stroma, with high mitotic activity (6–12/mm^2). They demonstrate strong, diffuse nuclear SOX10 and MITF expression, variable S100 positivity, and focal reactivity for Melan-A, HMB-45, and pan-melanoma markers [176].

There are two additional types of lesions driven by *ACTIN::MITF* (*ACTB::MITF*, *ACTG1::MITF*) and *MITF::CREM*. They also typically present as dermal nodules—often occurring on the extremities or head and neck—in predominantly adult female patients. They both exhibit clear cell features on histopathology and consistent MITF expression and melanocytic markers (such as HMB-45 antigen and Melan-A), variable S100 protein, and typically negative SOX10 in most *ACTIN::MITF* cases, whereas *MITF::CREM* tumors tend to mirror the phenotype of *CRTC1::TRIM11* neoplasms with more frequent SOX10 and S100 expression [177-182].

CONCLUSION

Gene fusions define and drive distinct, clinically meaningful subsets across all melanocytic tumors. Recognizing fusion-associated histomorphologies and using screening immunohistochemistry, if applicable, with confirmation by FISH or RNA-based sequencing improves diagnosis, classification, and possible selection for targeted therapy.

https://doi.org/10.4132/jptm.2026.03.11

Supplementary Information
The Data Supplement is available with this article at https://doi.org/10.4132/jptm.2026.03.11.

Ethics Statement
Not applicable.

Availability of Data and Material
All data generated or analyzed during the study are included in this published article (and its supplementary information files).

Code Availability
Not applicable.

ORCID
Volha Lenskaya https://orcid.org/0000-0002-0852-7187
Larisa Erikson https://orcid.org/0009-0008-2881-7123
Victor G. Prieto https://orcid.org/0000-0001-9204-7161
Woo Cheal Cho https://orcid.org/0000-0001-5867-1403

Author Contributions
Conceptualization: VL, WCC. Data curation: VL. Formal analysis: VL. Investigation: VL, LE. Methodology: VL. Project administration: VL. Resources: VGP, WCC. Supervision: VL, WCC. Validation: VL. Visualization: VL. Writing—original draft: VL, LE. Writing—review & editing: VL, VGP, WCC. Approval of final manuscript: all authors.

Conflicts of Interest
The authors declare that they have no potential conflicts of interest.

Funding Statement
No funding to declare.

REFERENCES

1. Salokas K, Weldatsadik RG, Varjosalo M. Human transcription factor and protein kinase gene fusions in human cancer. Sci Rep 2020; 10: 14169.
2. Forbes SA, Beare D, Boutselakis H, et al. COSMIC: somatic cancer genetics at high-resolution. Nucleic Acids Res 2017; 45: D777-83.
3. Quan VL, Panah E, Zhang B, Shi K, Mohan LS, Gerami P. The role of gene fusions in melanocytic neoplasms. J Cutan Pathol 2019; 46: 878-87.
4. Shalin SC. A review of kinase fusions in melanocytic tumors. Lab Invest 2017; 97: 158-65.
5. Solomon JP, Hechtman JF. Detection of *NTRK* fusions: merits and limitations of current diagnostic platforms. Cancer Res 2019; 79: 3163-8.
6. Pecciarini L, Brunetto E, Grassini G, et al. Gene fusion detection in NSCLC routine clinical practice: targeted-NGS or FISH? Cells 2023; 12: 1135.
7. Zito Marino F, Buono S, Montella M, et al. *NTRK* gene aberrations in triple-negative breast cancer: detection challenges using IHC, FISH, RT-PCR, and NGS. J Pathol Clin Res 2023; 9: 367-77.
8. Nakagawa H, Fujita M. Whole genome sequencing analysis for cancer genomics and precision medicine. Cancer Sci 2018; 109: 513-22.
9. Heydt C, Wolwer CB, Velazquez Camacho O, et al. Detection of gene fusions using targeted next-generation sequencing: a comparative evaluation. BMC Med Genomics 2021; 14: 62.
10. Szurian K, Kashofer K, Liegl-Atzwanger B. Role of next-generation sequencing as a diagnostic tool for the evaluation of bone and soft-tissue tumors. Pathobiology 2017; 84: 323-38.
11. Vendrell JA, Grand D, Rouquette I, et al. High-throughput detection of clinically targetable alterations using next-generation sequencing. Oncotarget 2017; 8: 40345-58.
12. Bartels S, Persing S, Hasemeier B, Schipper E, Kreipe H, Lehmann U. Molecular analysis of circulating cell-free DNA from lung cancer patients in routine laboratory practice: a cross-platform comparison of three different molecular methods for mutation detection. J Mol Diagn 2017; 19: 722-32.
13. Underhill HR. Leveraging the fragment length of circulating tumour DNA to improve molecular profiling of solid tumour malignancies with next-generation sequencing: a pathway to advanced non-invasive diagnostics in precision oncology? Mol Diagn Ther 2021; 25: 389-408.
14. Song Z, Lu C, Xu CW, Zheng Z. Noncanonical gene fusions detected at the DNA level necessitate orthogonal diagnosis methods before targeted therapy. J Thorac Oncol 2021; 16: 344-8.
15. Li J, Lu H, Ng PK, et al. A functional genomic approach to actionable gene fusions for precision oncology. Sci Adv 2022; 8: eabm2382.
16. Nikanjam M, Okamura R, Barkauskas DA, Kurzrock R. Targeting fusions for improved outcomes in oncology treatment. Cancer 2020; 126: 1315-21.
17. Polubothu S, McGuire N, Al-Olabi L, et al. Does the gene matter? Genotype-phenotype and genotype-outcome associations in con-

genital melanocytic naevi. Br J Dermatol 2020; 182: 434-43.
18. Dessars B, De Raeve LE, El Housni H, et al. Chromosomal translocations as a mechanism of BRAF activation in two cases of large congenital melanocytic nevi. J Invest Dermatol 2007; 127: 1468-70.
19. Mir A, Agim NG, Kane AA, Josephs SC, Park JY, Ludwig K. Giant congenital melanocytic nevus treated with trametinib. Pediatrics 2019; 143: e20182469.
20. Molho-Pessach V, Hartshtark S, Merims S, et al. Giant congenital melanocytic naevus with a novel *CUX1-BRAF* fusion mutation treated with trametinib. Br J Dermatol 2022; 187: 1052-4.
21. Sampath AJ, Ruffolo AM, Miedema J, Googe PB, Thomas NE. Genetic abnormalities in congenital melanocytic nevi and their associated melanomas. JAAD Case Rep 2024; 45: 94-7.
22. Martin SB, Polubothu S, Bruzos AL, et al. Mosaic *BRAF* fusions are a recurrent cause of congenital melanocytic nevi targetable by MAPK pathway inhibition. J Invest Dermatol 2024; 144: 593-600.
23. Botton T, Yeh I, Nelson T, et al. Recurrent BRAF kinase fusions in melanocytic tumors offer an opportunity for targeted therapy. Pigment Cell Melanoma Res 2013; 26: 845-51.
24. Agrawal S, Guo R. Melanocytic neoplasm with novel *EPS15*:*BRAF* fusion and congenital features. Hum Pathol 2025; 165: 105790.
25. Roy SF, Agim NG, Mir A, et al. Congenital melanocytic naevi initiated by *BRAF* fusion oncogene with firmness, pruritus and desmoplastic stroma. Br J Dermatol 2025; 193: 232-9.
26. El-Rayes D, Wilson K, Maguiness S, Miller D, Cazzato G, Giubellino A. Congenital melanocytic nevus with neurocristic cutaneous hamartoma: a case report. Dermatopathology (Basel) 2025; 12: 12.
27. Baltres A, Salhi A, Houlier A, et al. Malignant melanoma with areas of rhabdomyosarcomatous differentiation arising in a giant congenital nevus with *RAF1* gene fusion. Pigment Cell Melanoma Res 2019; 32: 708-13.
28. Martins da Silva V, Martinez-Barrios E, Tell-Marti G, et al. Genetic abnormalities in large to giant congenital nevi: beyond *NRAS* mutations. J Invest Dermatol 2019; 139: 900-8.
29. Vinyals A, Ferreres JR, Calbet-Llopart N, et al. Oncogenic properties via MAPK signaling of the *SOX5-RAF1* fusion gene identified in a wild-type NRAS/BRAF giant congenital nevus. Pigment Cell Melanoma Res 2022; 35: 450-60.
30. Houlier A, Pissaloux D, Tirode F, et al. *RASGRF2* gene fusions identified in a variety of melanocytic lesions with distinct morphological features. Pigment Cell Melanoma Res 2021; 34: 1074-83.
31. Korolkova OY, Widatalla SE, Whalen DS, et al. Reciprocal expression of annexin A6 and RasGRF2 discriminates rapidly growing from invasive triple negative breast cancer subsets. PLoS One 2020; 15: e0231711.
32. Lu P, Chen J, Yan L, et al. RasGRF2 promotes migration and invasion of colorectal cancer cells by modulating expression of MMP9 through Src/Akt/NF-κB pathway. Cancer Biol Ther 2019; 20: 435-43.
33. Nakagawa T, Kim Y, Kano J, et al. High expression of Ras-specific guanine nucleotide-releasing factor 2 (RasGRF2) in lung adenocarcinoma is associated with tumor invasion and poor prognosis. Pathol Int 2021; 71: 255-60.
34. Bahrami A, Lee S, Wu G, et al. Pigment-synthesizing melanocytic neoplasm with protein kinase C alpha (*PRKCA*) fusion. JAMA Dermatol 2016; 152: 318-22.
35. Cohen JN, Joseph NM, North JP, Onodera C, Zembowicz A, LeBoit PE. Genomic analysis of pigmented epithelioid melanocytomas reveals recurrent alterations in *PRKAR1A*, and *PRKCA* genes. Am J Surg Pathol 2017; 41: 1333-46.
36. Perron E, Pissaloux D, Charon Barra C, et al. Melanocytic myxoid spindle cell tumor with *ALK* rearrangement (MMySTAR): report of 4 cases of a nevus variant with potential diagnostic challenge. Am J Surg Pathol 2018; 42: 595-603.
37. Moran JM, Le LP, Nardi V, et al. Identification of fusions with potential clinical significance in melanoma. Mod Pathol 2022; 35: 1837-47.
38. Ibrahim E, Yang R, Nagarajan P, Sweeney K, Chen H, Roy-Chowdhuri S, et al. Clinicopathologic and molecular characterization of *BRAF*-fused melanomas: a retrospective analysis of 9 cases with 8 novel fusions detected by next-generation sequencing. Lab Invest 2025; 105(3 Suppl): 102669.
39. Turner JA, Bemis JGT, Bagby SM, et al. *BRAF* fusions identified in melanomas have variable treatment responses and phenotypes. Oncogene 2019; 38: 1296-308.
40. Botton T, Talevich E, Mishra VK, et al. Genetic heterogeneity of BRAF fusion kinases in melanoma affects drug responses. Cell Rep 2019; 29: 573-88.
41. Hutchinson KE, Lipson D, Stephens PJ, et al. *BRAF* fusions define a distinct molecular subset of melanomas with potential sensitivity to MEK inhibition. Clin Cancer Res 2013; 19: 6696-702.
42. Clark HE, Huang YY, Vance GH, Alomari AK. Fatal melanoma with a novel *MYO5A-BRAF* fusion and small associated conventional nevus: a case report and review of literature. J Cutan Pathol 2022; 49: 808-12.
43. Ross JS, Wang K, Chmielecki J, et al. The distribution of *BRAF*

https://doi.org/10.4132/jptm.2026.03.11

gene fusions in solid tumors and response to targeted therapy. Int J Cancer 2016; 138: 881-90.
44. Busam KJ, Shah KN, Gerami P, Sitzman T, Jungbluth AA, Kinsler V. Reduced H3K27me3 expression is common in nodular melanomas of childhood associated with congenital melanocytic nevi but not in proliferative nodules. Am J Surg Pathol 2017; 41: 396-404.
45. Newell F, Wilmott JS, Johansson PA, et al. Whole-genome sequencing of acral melanoma reveals genomic complexity and diversity. Nat Commun 2020; 11: 5259.
46. Menzies AM, Yeh I, Botton T, Bastian BC, Scolyer RA, Long GV. Clinical activity of the MEK inhibitor trametinib in metastatic melanoma containing BRAF kinase fusion. Pigment Cell Melanoma Res 2015; 28: 607-10.
47. Kim HS, Jung M, Kang HN, et al. Oncogenic *BRAF* fusions in mucosal melanomas activate the MAPK pathway and are sensitive to MEK/PI3K inhibition or MEK/CDK4/6 inhibition. Oncogene 2017; 36: 3334-45.
48. Perron E, Pissaloux D, Neub A, et al. Unclassified sclerosing malignant melanomas with *AKAP9-BRAF* gene fusion: a report of two cases and review of *BRAF* fusions in melanocytic tumors. Virchows Arch 2018; 472: 469-76.
49. Gao Y, Yang RK, Curry JL, Torres-Cabala CA, Cho WC. Melanoma with *RNF11::BRAF* fusion: a novel fusion previously undescribed in melanoma. Am J Dermatopathol 2025; 47: 391-4.
50. Cho WC, Yang RK, Lenskaya V, Prieto VG. *SBF1::BRAF*-fused melanoma with prominent rhabdoid morphology and Reed-Sternberg-like cells: potential morphologic clues to *BRAF*-fused melanomas of non-Spitz lineage? Am J Dermatopathol 2025; 47: 733-5.
51. Johnson DB, Nebhan CA, Noel MS. MEK inhibitors in non-V600 *BRAF* mutations and fusions. Oncotarget 2020; 11: 3900-3.
52. Williams EA, Shah N, Montesion M, et al. Melanomas with activating *RAF1* fusions: clinical, histopathologic, and molecular profiles. Mod Pathol 2020; 33: 1466-74.
53. Khaddour K, Haq R, Buchbinder EI, et al. Targeting *RAF1* gene fusions with MEK inhibition in metastatic melanoma. Oncologist 2025; 30: oyae297.
54. Kim KB, Semrad T, Schrock AB, et al. Significant clinical response to a MEK inhibitor therapy in a patient with metastatic melanoma harboring an *RAF1* fusion. JCO Precis Oncol 2018; 2: 1-6.
55. McEvoy CR, Xu H, Smith K, et al. Profound MEK inhibitor response in a cutaneous melanoma harboring a *GOLGA4-RAF1* fusion. J Clin Invest 2019; 129: 1940-5.
56. Boileau M, Descarpentries C, Delzenne G, et al. Clinical response under MEK inhibitor alone in metastatic melanoma with a novel fusion involving the *RAF1* gene. Melanoma Res 2023; 33: 247-51.
57. Hayward NK, Wilmott JS, Waddell N, et al. Whole-genome landscapes of major melanoma subtypes. Nature 2017; 545: 175-80.
58. Pacaud A, Amintas S, Boussemart L, Cappellen D, Gerard E. A case of multi-metastatic melanoma with *RAF1* fusion: a surprising response to anti-MEK therapy. Eur J Cancer 2021; 147: 161-3.
59. Do J, Yang RK, Curry JL, Cho WC. Fatal melanoma with *MAP4::RAF1* fusion: expanding the clinicopathologic and prognostic spectrum of *RAF1*-fused melanomas. Am J Dermatopathol 2026; 48: 135-9.
60. Stransky N, Cerami E, Schalm S, Kim JL, Lengauer C. The landscape of kinase fusions in cancer. Nat Commun 2014; 5: 4846.
61. Palanisamy N, Ateeq B, Kalyana-Sundaram S, et al. Rearrangements of the RAF kinase pathway in prostate cancer, gastric cancer and melanoma. Nat Med 2010; 16: 793-8.
62. Jain P, Fierst TM, Han HJ, et al. *CRAF* gene fusions in pediatric low-grade gliomas define a distinct drug response based on dimerization profiles. Oncogene 2017; 36: 6348-58.
63. Lezcano C, Shoushtari AN, Ariyan C, Hollmann TJ, Busam KJ. Primary and metastatic melanoma with *NTRK* fusions. Am J Surg Pathol 2018; 42: 1052-8.
64. Couts KL, Bemis J, Turner JA, et al. ALK inhibitor response in melanomas expressing *EML4-ALK* fusions and alternate ALK isoforms. Mol Cancer Ther 2018; 17: 222-31.
65. Perkins IU, Tan SY, McCalmont TH, et al. Melanoma in infants, caused by a gene fusion involving the anaplastic lymphoma kinase (ALK). Pigment Cell Melanoma Res 2024; 37: 6-14.
66. Shaker N, Phelps R, Niedt G, et al. BRCA1-associated protein-1 inactivated melanoma arising in a pre-existing nevus with *ALK* fusion and low tumor mutational burden. Am J Dermatopathol 2025; 47: 264-8.
67. Lee J, Lee J, Hong SD, Jang KT, Lee SJ. *FGFR3-TACC3*: a novel gene fusion in malignant melanoma. Precis Future Med 2018; 2: 71-5.
68. Lehmann BD, Shaver TM, Johnson DB, et al. Identification of targetable recurrent *MAP3K8* rearrangements in melanomas lacking known driver mutations. Mol Cancer Res 2019; 17: 1842-53.
69. Liang WS, Hendricks W, Kiefer J, et al. Integrated genomic analyses reveal frequent TERT aberrations in acral melanoma. Genome Res 2017; 27: 524-32.
70. Wang J, Algarin YA, El-Sayed I, Bastian B, Yeh I. Mucosal melanoma with *MAP3K8* gene rearrangement. In: The American So-

ciety of Dermatopathology, 61st Annual Meeting; 2024 Nov 4-10; Chicago, IL, USA.
71. Wang M, Banik I, Shain AH, Yeh I, Bastian BC. Integrated genomic analyses of acral and mucosal melanomas nominate novel driver genes. Genome Med 2022; 14: 65.
72. Williams EA, Montesion M, Shah N, et al. Melanoma with in-frame deletion of *MAP2K1*: a distinct molecular subtype of cutaneous melanoma mutually exclusive from *BRAF*, *NRAS*, and *NF1* mutations. Mod Pathol 2020; 33: 2397-406.
73. Ebbelaar CF, Jansen AM, Speet LC, et al. Clinical outcomes and genomic profiles of *MAP2K1*-mutated primary cutaneous melanocytic tumours. EBioMedicine 2025; 114: 105643.
74. Furney SJ, Turajlic S, Stamp G, et al. The mutational burden of acral melanoma revealed by whole-genome sequencing and comparative analysis. Pigment Cell Melanoma Res 2014; 27: 835-8.
75. Ibrahim E, Yang RK, Curry JL, Cho WC. *BCR::ZNF711* and *BCR::CYLC2* fusions: novel *BCR* fusions expanding the molecular spectrum of gene fusions in melanoma. Am J Dermatopathol 2024; 46: 797-9.
76. Elder DE, Bastian BC, Cree IA, Massi D, Scolyer RA. The 2018 World Health Organization classification of cutaneous, mucosal, and uveal melanoma: detailed analysis of 9 distinct subtypes defined by their evolutionary pathway. Arch Pathol Lab Med 2020; 144: 500-22.
77. Hagstrom M, Fumero-Velazquez M, Dhillon S, Olivares S, Gerami P. An update on genomic aberrations in Spitz naevi and tumours. Pathology 2023; 55: 196-205.
78. Delsupehe L, Steelandt T, Lemahieu J, et al. Novel gene fusion discovery in Spitz tumours and its relevance in diagnostics. Virchows Arch 2024; 485: 269-79.
79. Wiesner T, He J, Yelensky R, et al. Kinase fusions are frequent in Spitz tumours and spitzoid melanomas. Nat Commun 2014; 5: 3116.
80. de la Fouchardiere A, Mazzei ME, Pastor M, Forster AM, Prieto VG. Spitz tumours and mimickers. Virchows Arch 2025; 486: 143-64.
81. Sunshine JC, Kim D, Zhang B, et al. Melanocytic neoplasms with *MAP2K1* in frame deletions and Spitz morphology. Am J Dermatopathol 2020; 42: 923-31.
82. Goto K, Pissaloux D, Fraitag S, et al. *RASGRF1*-rearranged cutaneous melanocytic neoplasms with spitzoid cytomorphology: a clinicopathologic and genetic study of 3 cases. Am J Surg Pathol 2022; 46: 655-63.
83. Urso C. Melanocytic skin neoplasms: what lesson from genomic aberrations? Am J Dermatopathol 2019; 41: 623-9.
84. Huang FW, Hodis E, Xu MJ, Kryukov GV, Chin L, Garraway LA. Highly recurrent *TERT* promoter mutations in human melanoma. Science 2013; 339: 957-9.
85. Quan VL, Zhang B, Zhang Y, et al. Integrating next-generation sequencing with morphology improves prognostic and biologic classification of Spitz neoplasms. J Invest Dermatol 2020; 140: 1599-608.
86. Barr RJ, Morales RV, Graham JH. Desmoplastic nevus: a distinct histologic variant of mixed spindle cell and epithelioid cell nevus. Cancer 1980; 46: 557-64.
87. Lezcano CM, Yeh I, Eslamdoost N, et al. Expanding the spectrum of microscopic and cytogenetic findings associated with Spitz tumors with 11p gains. Am J Surg Pathol 2021; 45: 277-85.
88. Yeh I, Botton T, Talevich E, et al. Activating MET kinase rearrangements in melanoma and Spitz tumours. Nat Commun 2015; 6: 7174.
89. Amin SM, Haugh AM, Lee CY, et al. A comparison of morphologic and molecular features of *BRAF*, *ALK*, and *NTRK1* fusion spitzoid neoplasms. Am J Surg Pathol 2017; 41: 491-8.
90. Busam KJ, Kutzner H, Cerroni L, Wiesner T. Clinical and pathologic findings of Spitz nevi and atypical Spitz tumors with *ALK* fusions. Am J Surg Pathol 2014; 38: 925-33.
91. Salah HT, Yang RK, Roy-Chowdhuri S, et al. Spitz melanocytic neoplasms with *MLPH::ALK* fusions: report of two cases with previously unreported features and literature review. J Cutan Pathol 2024; 51: 407-14.
92. Kastnerova L, Martinek P, Grossmann P, et al. A clinicopathological study of 29 spitzoid melanocytic lesions with *ALK* fusions, including novel fusion variants, accompanied by fluorescence in situ hybridization analysis for chromosomal copy number changes, and both *TERT* promoter and next-generation sequencing mutation analysis. Am J Dermatopathol 2020; 42: 578-92.
93. Bahrani E, Kunder CA, Teng JM, et al. Spitz nevus with *EHBP1-ALK* fusion and distinctive membranous localization of *ALK*. J Cutan Pathol 2022; 49: 584-8.
94. Yeh I, de la Fouchardiere A, Pissaloux D, et al. Clinical, histopathologic, and genomic features of Spitz tumors with *ALK* fusions. Am J Surg Pathol 2015; 39: 581-91.
95. Chung CT, Marrano P, Swanson D, Dickson BC, Thorner PS. Fusion of *ALK* to the melanophilin gene *MLPH* in pediatric Spitz nevi. Hum Pathol 2019; 87: 57-64.
96. Fujimoto M, Togashi Y, Matsuzaki I, et al. A case report of atypical Spitz tumor harboring a novel *MLPH-ALK* gene fusion with discordant ALK immunohistochemistry results. Hum Pathol 2018; 80: 99-103.

https://doi.org/10.4132/jptm.2026.03.11

97. Schoelinck J, Pissaloux D, Mouthon M, Vergara R, de la Fouchardiere A. Clinical, histological and genetic correlations in melanocytic tumours with chromosomal rearrangements. Ann Pathol 2025; 45: 3-14.
98. Raghavan SS, Peternel S, Mully TW, et al. Spitz melanoma is a distinct subset of spitzoid melanoma. Mod Pathol 2020; 33: 1122-34.
99. Cho WC, Prieto VG, Yang RK. Spitz melanoma with *SLC20A1::ALK* fusion: a novel fusion previously undescribed in Spitz melanocytic neoplasm. Am J Dermatopathol 2024; 46: 700-3.
100. Frederico IK, Mesbah Ardakani N, Ryan AL, Cowley MJ, Wood BA. Spitz melanoma of childhood with a novel promoter hijacking anaplastic lymphoma kinase (C2orf42-ALK) rearrangement. Am J Dermatopathol 2021; 43: 972-5.
101. Pappo AS, McPherson V, Pan H, et al. A prospective, comprehensive registry that integrates the molecular analysis of pediatric and adolescent melanocytic lesions. Cancer 2021; 127: 3825-31.
102. Gerami P, Kim D, Compres EV, et al. Clinical, morphologic, and genomic findings in *ROS1* fusion Spitz neoplasms. Mod Pathol 2021; 34: 348-57.
103. Donati M, Kastnerova L, Martinek P, et al. Spitz tumors with *ROS1* fusions: a clinicopathological study of 6 cases, including FISH for chromosomal copy number alterations and mutation analysis using next-generation sequencing. Am J Dermatopathol 2020; 42: 92-102.
104. Lee S, Barnhill RL, Dummer R, et al. *TERT* promoter mutations are predictive of aggressive clinical behavior in patients with spitzoid melanocytic neoplasms. Sci Rep 2015; 5: 11200.
105. Robertson SJ, Orme L, Teixeira R, et al. Evaluation of crizotinib treatment in a patient with unresectable *GOPC-ROS1* fusion agminated Spitz nevi. JAMA Dermatol 2021; 157: 836-41.
106. Church AJ, Moustafa D, Pinches RS, Hawryluk EB, Schmidt BA. Genomic comparison of malignant melanoma and atypical Spitz tumor in the pediatric population. Pediatr Dermatol 2022; 39: 409-19.
107. Raghavan SS, Kapler ES, Dinges MM, Bastian BC, Yeh I. Eruptive Spitz nevus, a striking example of benign metastasis. Sci Rep 2020; 10: 16216.
108. Cesinaro AM, Gallo G, Manfredini S, Maiorana A, Bettelli SR. ROS1 pattern of immunostaining in 11 cases of spitzoid tumour: comparison with histopathological, fluorescence in-situ hybridisation and next-generation sequencing analysis. Histopathology 2021; 79: 966-74.
109. Couts KL, McCoach CE, Murphy D, et al. Acral lentiginous melanoma harboring a *ROS1* gene fusion with clinical response to entrectinib. JCO Precis Oncol 2017; 1: 1-7.
110. Amatu A, Sartore-Bianchi A, Bencardino K, Pizzutilo EG, Tosi F, Siena S. Tropomyosin receptor kinase (TRK) biology and the role of *NTRK* gene fusions in cancer. Ann Oncol 2019; 30: viii5-15.
111. Yeh I, Busam KJ, McCalmont TH, et al. Filigree-like rete ridges, lobulated nests, rosette-like structures, and exaggerated maturation characterize Spitz tumors with *NTRK1* fusion. Am J Surg Pathol 2019; 43: 737-46.
112. Khotskaya YB, Holla VR, Farago AF, Mills Shaw KR, Meric-Bernstam F, Hong DS. Targeting TRK family proteins in cancer. Pharmacol Ther 2017; 173: 58-66.
113. Cappellesso R, Nozzoli F, Zito Marino F, et al. *NTRK* gene fusion detection in atypical Spitz tumors. Int J Mol Sci 2021; 22: 12332.
114. Yin L, Shi C, He X, et al. *NTRK*-rearranged spindle cell neoplasms: a clinicopathological and molecular study of 13 cases with peculiar characteristics at one of the largest institutions in China. Pathology 2023; 55: 362-74.
115. Dal Pozzo CA, Cappellesso R. The morpho-molecular landscape of Spitz neoplasms. Int J Mol Sci 2022; 23: 4211.
116. Kervarrec T, Pissaloux D, Tirode F, et al. Morphologic features in a series of 352 Spitz melanocytic proliferations help predict their oncogenic drivers. Virchows Arch 2022; 480: 369-82.
117. Kiuru M, Jungbluth A, Kutzner H, Wiesner T, Busam KJ. Spitz Tumors: Comparison of histological features in relationship to immunohistochemical staining for ALK and NTRK1. Int J Surg Pathol 2016; 24: 200-6.
118. Sekoranja D, Pizem J, Luzar B. An update on molecular genetic aberrations in Spitz melanocytic proliferations: correlation with morphological features and biological behavior. Acta Med Acad 2021; 50: 157-74.
119. Forschner A, Forchhammer S, Bonzheim I. *NTRK* gene fusions in melanoma: detection, prevalence and potential therapeutic implications. J Dtsch Dermatol Ges 2020; 18: 1387-92.
120. Cazzato G, Colagrande A, Resta L, et al. *LMNA::NTRK1* and *PRDX1::NTRK1* atypical Spitz tumor: a report of two additional cases with histological, immunohistochemical, and molecular insights. Am J Dermatopathol 2025; 47: 22-4.
121. Yeh I, Tee MK, Botton T, et al. *NTRK3* kinase fusions in Spitz tumours. J Pathol 2016; 240: 282-90.
122. Lee CY, Sholl LM, Zhang B, et al. Atypical spitzoid neoplasms in childhood: a molecular and outcome study. Am J Dermatopathol 2017; 39: 181-6.

123. Goto K, Pissaloux D, Tirode F, de la Fouchardiere A. Spitz nevus with a novel *TFG-NTRK2* fusion: the first case report of *NTRK2*-rearranged Spitz/Reed nevus. J Cutan Pathol 2021; 48: 1193-6.
124. Mansour B, Vanecek T, Kastnerova L, Nosek D, Kazakov DV, Donati M. Spitz tumor with *SQSTM1::NTRK2* fusion: a clinicopathological study of 5 cases. Am J Dermatopathol 2023; 45: 306-10.
125. VandenBoom T, Quan VL, Zhang B, et al. Genomic fusions in pigmented spindle cell nevus of reed. Am J Surg Pathol 2018; 42: 1042-51.
126. Wang L, Busam KJ, Benayed R, et al. Identification of *NTRK3* fusions in childhood melanocytic neoplasms. J Mol Diagn 2017; 19: 387-96.
127. de la Fouchardiere A, Tee MK, Peternel S, et al. Fusion partners of NTRK3 affect subcellular localization of the fusion kinase and cytomorphology of melanocytes. Mod Pathol 2021; 34: 735-47.
128. Della Mura M, Sorino J, Colagrande A, et al. Atypical Spitz tumor/Spitz melanocytoma revealing a *VIM::NTRK3* gene fusion: clinicopathological correlation of a unique molecular finding. Am J Dermatopathol 2025; 47: 886-90.
129. Donati M, Goutas D, Pissaloux D, et al. Clinical, morphologic, and genomic findings in Spitz tumors with *RET* fusion: a series of 31 cases. Mod Pathol 2025; 38: 100740.
130. Kim D, Compres EV, Zhang B, et al. A series of *RET* fusion Spitz neoplasms with plaque-like silhouette and dyscohesive nesting of epithelioid melanocytes. Am J Dermatopathol 2021; 43: 243-51.
131. Yakes FM, Chen J, Tan J, et al. Cabozantinib (XL184), a novel MET and VEGFR2 inhibitor, simultaneously suppresses metastasis, angiogenesis, and tumor growth. Mol Cancer Ther 2011; 10: 2298-308.
132. Zarabi SK, Azzato EM, Tu ZJ, et al. Targeted next generation sequencing (NGS) to classify melanocytic neoplasms. J Cutan Pathol 2020; 47: 691-704.
133. Feldman T, Zaaroura H, Abaya HH, Zohar Y, Bergman R. Congenital Spitz melanocytoma with activating *ZKSCAN1::MET* kinase fusion. J Cutan Pathol 2025; 52: 617-21.
134. Roy S, Milante R, Busam K, de la Fouchardiere A, Yeh I. *MET*-fused melanocytic Spitz tumors: 18 cases with identifiable histomorphological and genetic features. Lab Invest 2025; 105(3 Suppl): 102693.
135. Wu G, Barnhill RL, Lee S, et al. The landscape of fusion transcripts in spitzoid melanoma and biologically indeterminate spitzoid tumors by RNA sequencing. Mod Pathol 2016; 29: 359-69.
136. Kim D, Khan AU, Compres EV, et al. *BRAF* fusion Spitz neoplasms: clinical morphological, and genomic findings in six cases. J Cutan Pathol 2020; 47: 1132-42.
137. Donati M, Kastnerova L, Ptakova N, Michal M, Kazakov DV. Polypoid atypical Spitz tumor with a fibrosclerotic stroma, *CLIP2-BRAF* fusion, and homozygous loss of 9p21. Am J Dermatopathol 2020; 42: 204-7.
138. Newman S, Fan L, Pribnow A, et al. Clinical genome sequencing uncovers potentially targetable truncations and fusions of *MAP3K8* in spitzoid and other melanomas. Nat Med 2019; 25: 597-602.
139. Roy SF, Bastian BC, Maguiness S, et al. Multiple desmoplastic Spitz nevi with *BRAF* fusions in a patient with ring chromosome 7 syndrome. Pigment Cell Melanoma Res 2021; 34: 987-93.
140. Sorino J, Della Mura M, Ingravallo G, Colagrande A, Cazzato G. *TAX1BP1::BRAF* fusion in *BRAF*-mutated atypical Spitz tumor/Spitz melanocytoma: a novel molecular finding with histopathological insights. Am J Dermatopathol 2025; 47: 568-9.
141. Sharma N, Patel P, Chen A, et al. The clinical, morphologic, and molecular spectrum of *BRAF* fusion Spitz tumors. Am J Surg Pathol 2024; 48: 1588-99.
142. Roy SF, Milante R, Pissaloux D, et al. Spectrum of melanocytic tumors harboring *BRAF* gene fusions: 58 cases with histomorphologic and genetic correlations. Mod Pathol 2023; 36: 100149.
143. Hiraki T, Hirakawa S, Otsuki Y, Kajimoto K, Goto K, Serizawa M. Fatal Spitz melanoma with *MAD1L1::BRAF* fusion: a case report and literature review. J Cutan Pathol 2025; 52: 199-205.
144. Donati M, Nosek D, Olivares S, et al. Spitz tumor with *RAF1* fusion: a report of 3 cases. Ann Diagn Pathol 2023; 67: 152215.
145. Houlier A, Pissaloux D, Masse I, et al. Melanocytic tumors with *MAP3K8* fusions: report of 33 cases with morphological-genetic correlations. Mod Pathol 2020; 33: 846-57.
146. Johannessen CM, Boehm JS, Kim SY, et al. COT drives resistance to RAF inhibition through MAP kinase pathway reactivation. Nature 2010; 468: 968-72.
147. Newman S, Pappo A, Raimondi S, Zhang J, Barnhill R, Bahrami A. Pathologic characteristics of Spitz melanoma with *MAP3K8* fusion or truncation in a pediatric cohort. Am J Surg Pathol 2019; 43: 1631-7.
148. Quan VL, Zhang B, Mohan LS, et al. Activating structural alterations in MAPK genes are distinct genetic drivers in a unique subgroup of Spitzoid neoplasms. Am J Surg Pathol 2019; 43: 538-48.
149. Sibira R, Vu A, Giubellino A, Murugan P. Spitz melanoma with

https://doi.org/10.4132/jptm.2026.03.11

MAP3K8::ABLIM1 rearrangement: a case report with review of the literature. Diagn Pathol 2024; 19: 133.
150. Donati M, Nosek D, Waldenback P, et al. *MAP2K1*-mutated melanocytic neoplasms with a SPARK-like morphology. Am J Dermatopathol 2021; 43: 412-7.
151. Kerckhoffs KG, Aallali T, Ambarus CA, Sigurdsson V, Jansen AM, Blokx WA. Expanding spectrum of "spitzoid" lesions: a small series of 4 cases with *MAP2K1* mutations. Virchows Arch 2021; 479: 195-202.
152. Kervarrec T, Pissaloux D, Chokri I, Tirode F, de la Fouchardiere A. *MST1R*/*RON* fusion as a potential oncogenic driver in Spitz tumours. Pathology 2024; 56: 1051-3.
153. Goto K, Pissaloux D, Durand L, Tirode F, Guillot B, de la Fouchardiere A. Novel three-way complex rearrangement of *TRPM1-PUM1-LCK* in a case of agminated Spitz nevi arising in a giant congenital hyperpigmented macule. Pigment Cell Melanoma Res 2020; 33: 767-72.
154. Giubellino A, He Y, Munro SA, et al. Gene expression profile of benign, intermediate, and malignant Spitz and spitzoid melanocytic lesions. Cancers (Basel) 2024; 16: 1798.
155. Scarfo F, Brunetto E, Magliacane G, Pecciarini L, Ferrara G, Rizzo N. Spitz spindle cell/reed nevus with *SQSTM1::NTRK2* fusion and atypical features in an older male patient: a case report and review of literature. J Cutan Pathol 2025; 52: 367-73.
156. Mohan LS, Khan AU, Zhang B, et al. Retrospective cohort: genomic differences between pigmented spindle cell nevi of reed and reed-like melanomas. Am J Dermatopathol 2020; 42: 641-7.
157. Zembowicz A, Carney JA, Mihm MC. Pigmented epithelioid melanocytoma: a low-grade melanocytic tumor with metastatic potential indistinguishable from animal-type melanoma and epithelioid blue nevus. Am J Surg Pathol 2004; 28: 31-40.
158. Zembowicz A, Knoepp SM, Bei T, et al. Loss of expression of protein kinase a regulatory subunit 1alpha in pigmented epithelioid melanocytoma but not in melanoma or other melanocytic lesions. Am J Surg Pathol 2007; 31: 1764-75.
159. Isales MC, Mohan LS, Quan VL, et al. Distinct genomic patterns in pigmented epithelioid melanocytoma: a molecular and histologic analysis of 16 cases. Am J Surg Pathol 2019; 43: 480-8.
160. Zaaroura H, Cyrenne B, Somers GR, et al. Two congenital cases of pigmented epithelioid melanocytoma with unique clinical and genetic features. Dermatol Online J 2023; 29: 3.
161. Friedman BJ, Hernandez S, Fidai C, et al. A pediatric case of pigmented epithelioid melanocytoma with chromosomal copy number alterations in 15q and 17q and a novel *NTRK3-SCAPER* gene fusion. J Cutan Pathol 2020; 47: 70-5.
162. Scollan ME, Yamashiro DJ, Niedt GW, Garzon MC. Novel *CD63-PRKCB* fusion in a case of pigmented epithelioid melanocytoma. Pediatr Dermatol 2022; 39: 322-3.
163. Donati M, Kastnerova L, Cempirkova D, Vanecek T, Michal M, Kazakov DV. Vulvar pigmented epithelioid melanocytoma with a novel *HTT-PKN1* fusion: a case report. Am J Dermatopathol 2020; 42: 544-6.
164. Li A, Umphress B, Dehner C, et al. Genomic and transcriptomic characterization of protein kinase C fusion melanocytic neoplasms with distinctive hypopigmented histomorphology: a single-institution study. J Cutan Pathol 2025; 52: 432-41.
165. de la Fouchardiere A, Pissaloux D, Houlier A, et al. Histologic and genetic features of 51 melanocytic neoplasms with protein kinase C fusion genes. Mod Pathol 2023; 36: 100286.
166. Zhao J, Lampley N, Benton S, et al. Next-generation sequencing reveals a new class of melanocytic neoplasms with hybrid genomic features of PEM including protein kinase R 1 alpha gene inactivation and Spitz tumor-defining protein kinase fusions. Am J Dermatopathol 2022; 44: 568-74.
167. Kervarrec T, Lo Bello G, Pissaloux D, et al. *GRM1* gene fusions as an alternative molecular driver in blue nevi and related melanomas. Mod Pathol 2023; 36: 100264.
168. Yeh I, Lang UE, Durieux E, et al. Combined activation of MAP kinase pathway and β-catenin signaling cause deep penetrating nevi. Nat Commun 2017; 8: 644.
169. Parra O, Linos K. Cutaneous melanocytic tumor with *CRTC1::TRIM11* fusion: review of the literature of a potentially novel entity. Biology (Basel) 2021; 10: 1286.
170. Cellier L, Perron E, Pissaloux D, et al. Cutaneous melanocytoma with *CRTC1-TRIM11* fusion: report of 5 cases resembling clear cell sarcoma. Am J Surg Pathol 2018; 42: 382-91.
171. Miyagi Y, Senzaki H, Kato I, Kakuda Y, Goto K. A case of a *CRTC1::TRIM11* cutaneous tumor with venous and lymphatic invasion and lymph node metastasis. Cureus 2025; 17: e83821.
172. Tseng C, Hein EC, Smith SM, King I, Saibil S, Saeed Kamil Z. Ulcerated *CRTC1::TRIM11* cutaneous tumor with metastases. J Cutan Pathol 2024; 51: 735-41.
173. Bontoux C, Baroudjian B, Le Maignan C, et al. *CRTC1-TRIM11* fusion in a case of metastatic clear cell sarcoma: are *CRTC1-TRIM11* fusion-bearing tumors melanocytomas or clear cell sarcomas? Am J Surg Pathol 2019; 43: 861-3.
174. Kashima J, Motoi T, Nishimaki M, et al. A case report of cutaneous melanocytoma with *CRTC1-TRIM11* fusion: Is CMCT distinct from clear cell sarcoma of soft tissue? Pathol Int 2019; 69: 496-501.

175. Ko JS, Wang L, Billings SD, et al. *CRTC1-TRIM11* fusion defined melanocytic tumors: a series of four cases. J Cutan Pathol 2019; 46: 810-8.
176. Ko JS, Lemahieu J, Billings SD, et al. *MED15::ATF1*-rearranged tumor: a novel cutaneous tumor with melanocytic differentiation. Mod Pathol 2024; 37: 100438.
177. de la Fouchardiere A, Pissaloux D, Tirode F, Karanian M, Fletcher CD, Hanna J. Clear cell tumor with melanocytic differentiation and *ACTIN-MITF* translocation: report of 7 cases of a novel entity. Am J Surg Pathol 2021; 45: 962-8.
178. Kalmykova AV, Baranovska-Andrigo V, Michal M. Update on cutaneous mesenchymal tumors in the 5th edition of WHO classification of skin tumors with an emphasis on new fusion-associated neoplasms. Virchows Arch 2024; 485: 777-92.
179. Kalmykova A, Mosaieby E, Kacerovska D, et al. *MITF::CREM*-rearranged tumor: a novel group of cutaneous tumors with melanocytic differentiation. Virchows Arch 2023; 483: 569-75.
180. Bigot NJ, Neyaz A, Naous R, et al. Rapidly enlarging *ACTIN::MITF* rearranged clear cell tumour with melanocytic differentiation. Histopathology 2025; 86: 829-32.
181. Alexandrescu S, Imamovic-Tuco A, Janeway K, Hanna J. Clear cell tumor with melanocytic differentiation and *MITF::CREM* translocation. J Cutan Pathol 2023; 50: 619-22.
182. de la Fouchardiere A, Pissaloux D, Tirode F, Hanna J. Clear cell tumor with melanocytic differentiation and *MITF-CREM* translocation: a novel entity similar to clear cell sarcoma. Virchows Arch 2021; 479: 841-6.

https://doi.org/10.4132/jptm.2026.03.11

JPTM

ORIGINAL ARTICLE

pISSN 2383-7837 · eISSN 2383-7845

Journal of Pathology and Translational Medicine 2026; 60: 307-318
https://doi.org/10.4132/jptm.2026.01.01

Aquaporin 1 promotes proliferation and migration of tumor by up-regulating claudin-1 expression in colon cancer

Wei Wei Xie*, Lin Xu*, Qian Li, Dao Quan Zhang, Yu Bao Zhou

Department of Digestive Medicine, The Second Affiliated Hospital of Anhui Medical University, Hefei, China

Graphical abstract

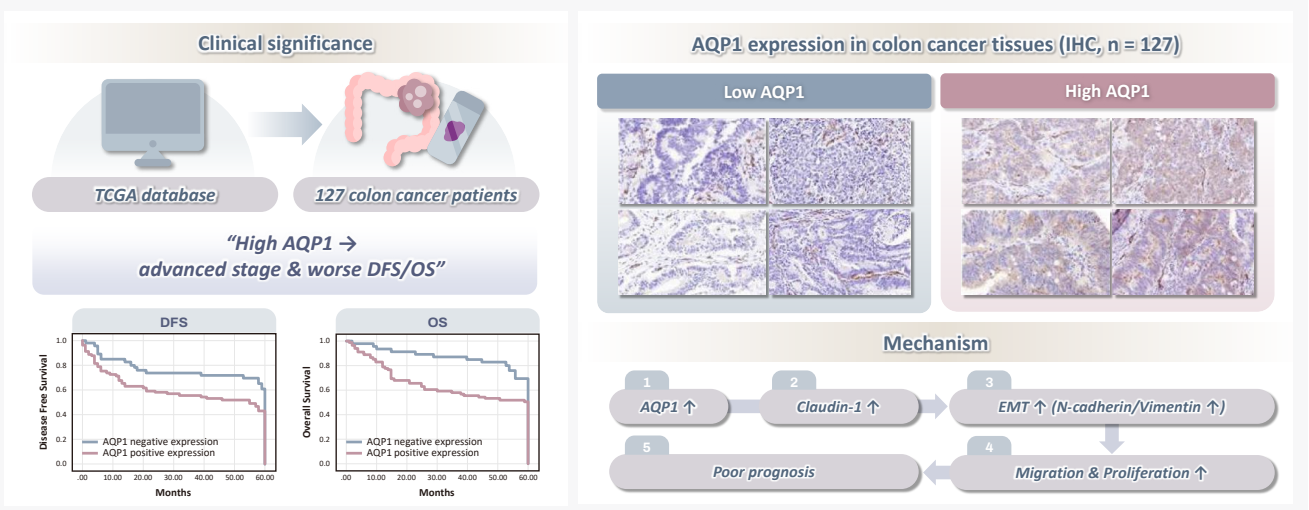

CONCLUSION AQP1 correlates with unfavorable prognosis in colon cancer and potentially enhances the proliferation and migration of colon cancers by up-regulating Claudin-1 expression.

Xie W et al. Journal of Pathology and Translational Medicine

JPTM

ORIGINAL ARTICLE

pISSN 2383-7837 · eISSN 2383-7845

Journal of Pathology and Translational Medicine 2026; 60: 307-318
https://doi.org/10.4132/jptm.2026.01.01

Aquaporin 1 promotes proliferation and migration of tumor by up-regulating claudin-1 expression in colon cancer

Wei Wei Xie*, Lin Xu*, Qian Li, Dao Quan Zhang, Yu Bao Zhou

Department of Digestive Medicine, The Second Affiliated Hospital of Anhui Medical University, Hefei, China

Background: With the rising incidence of colon cancer, several studies have indicated that aquaporin 1 (AQP1) expression is associated with the development of colon cancer. This study aims to elucidate the potential molecular mechanisms between them. **Methods:** We screened data from The Cancer Genome Atlas (TCGA) database and retrospectively examined AQP1 protein expression in 127 colon cancer patients to analyze the relationship between AQP1 expression and pathological stages, prognosis. We created stable colon cancer cell lines with differential AQP1 expression, the effect of AQP1 expression on the proliferation and migration of colon cancer cells was assessed by in vitro and in vivo studies, and explored potential molecular mechanisms through Western blotting. **Results:** High AQP1 expression was associated with poorer survival (overall survival [OS], p = .028) in colon cancer patients from the TCGA database. Similarly, retrospective clinical data indicated that high AQP1 expression was associated with reduced disease-free survival and OS (p = .036 and p = .017, respectively). The low-expressing AQP1 colon cancer cells exhibited a decrease in proliferation and migration ability of colon cancer cells compared to the overexpressing AQP1 group (p < .05) in vitro and in vivo. Immunohistochemistry and western blotting experiments validated heightened expression of N-cadherin, vimentin, and claudin-1 in the tumor tissues of the overexpressing AQP1 group. Conversely, reduced AQP1 expression resulted in decreased expression of claudin-1. **Conclusions:** AQP1 correlates with unfavorable prognosis in colon cancer and potentially enhances the proliferation and migration of colon cancer by up-regulating claudin-1 expression.

Keywords: Aquaporin 1; Claudin-1; Colon neoplasms; Epithelial-mesenchymal transition

INTRODUCTION

Colorectal cancer (CRC) stands as the most prevalent malignant tumor within the digestive system and is the third most common malignant tumor globally [1]. According to the 2022 Global Cancer Observatory (GLOBOCAN) data, CRC specifically accounts for 9.7% of total new cancer cases, and 9.4% of total cancer-related deaths [2]. Surgical resection remains the primary treatment for stages I–III colon cancer, while stage IV disease requires individualized therapeutic approaches [3]. Nevertheless, up to 50% of patients after treatment develop liver metastases, contributing to a poor prognosis [4]. Therefore, there is a necessity to identify a novel therapeutic target for long-term use in treating colon cancer.

The aquaporin family (AQPs) comprises small-molecule membrane proteins that promote cell migration, expansion and adhesion [5]. AQP1 expression is elevated in various tumor types, which can increase the risk of death in some cancer patients. In diseases such as lung adenocarcinoma, pleural mesothelioma, colorectal cancer, breast cancer, and prostate cancer, the hazard ratios for AQP1 are 4.0, 2.7, 2.6 to 3.4, 2.85, and 3.35, respectively [6,7]. AQP1 is expressed in colon cancer tissues

Received: September 9, 2025 **Revised:** December 31, 2025 **Accepted:** December 31, 2025

Corresponding Author: Yu-Bao Zhou, MSc
Department of Digestive Medicine, The Second Affiliated Hospital of Anhui Medical University, No.678 Furong Road, Economic and Technological Development Zone, Hefei City, Anhui Province 230000, China
Tel: +86-15215513030, Fax: +86-551-63869400, E-mail: zhouyubao@fy.ahmu.edu.cn

*Wei Wei Xie and Lin Xu contributed equally to this work.

but not in normal colon mucosa. Furthermore, its expression undergoes upregulation from the early to advanced stages of colon cancer development [8,9]. Evidence has been presented illustrating a correlation between the severity of the disease and the increased expression of AQP1 in colon cancer [10]. Increasing evidence suggests that AQP1 can influence cancer cell migration, invasion, and angiogenesis, potentially contributing to the development and progression of various cancers via tumor cell proliferation. Nevertheless, the precise signaling pathways remain elusive. Therefore, the aim of this study is to explore the effect of AQP1 on the clinicopathology and prognosis of colon cancer patients by database analysis and retrospective clinical study, and elucidate the potential molecular mechanisms through which AQP1 modulates the biological behaviors of colon cancer cells, providing potential novel therapeutic targets for colon cancer.

MATERIALS AND METHODS

Materials

Human colon cancer cell lines RKO and SW620 were procured from Procell Life Science and Technology Co. (Wuhan, China). Dulbecco's modified Eagle's medium (DMEM) culture medium and bovine serum were procured from Gibco (Grand Island, NY, USA). Antibodies against AQP1 (cat No. 20333-1-AP), actin (cat No. 66009-1-Ig), claudin-1 (cat No. 13050-1-AP), N-cadherin (cat No. 22018-1-AP), vimentin (cat No. 10366-1-AP), and Ki-67 (cat No. 27309-1-AP) were purchased from Proteintech (Wuhan, China).

The Cancer Genome Atlas database analysis

The relationship between AQPs and pathological stages of colon cancer patients was analyzed from The Cancer Genome Atlas (TCGA) database, and the correlation between AQP1 with different degrees of expression and the prognosis of colon cancer patients was observed.

Patients, samples, and clinicopathological data

A retrospective cohort study of 127 colon cancer patients who underwent first surgical resection from December 2017 to March 2020 at the Second Affiliated Hospital of Anhui Medical University was included in this study. Inclusion criteria are as follows: (1) patients aged between 18 and 80 years; (2) pathologically confirmed colon cancer patients undergoing initial radical resection; (3) availability of complete clinicopathological data and follow-up information, along with signed informed consent for this study. Exclusion criteria are as follows: (1) presence of other primary malignant tumors or severe systemic diseases; (2) incomplete clinical data; (3) unwillingness to participate in this study. All colon cancer patients were tested for AQP1 protein expression data by immunohistochemistry. Demographic and clinicopathologic information was retrospectively obtained from patients' medical records.

Cell culture

RKO and SW620 cells were cultivated in DMEM medium enriched with 10% (v/v) fetal bovine serum (Gibco) and 1% (v/v) antibiotic/antifungal solution (Beijing Beyotime Biotech Co. Inc, Beijing, China). All these cells underwent incubation in a 37°C environment with humidified air containing 5% CO_2. Adherent cultured cells were passaged every 1–2 days. And cells in the logarithmic growth phase were utilized for the experiments.

Lentiviral infection

Lentiviral delivery of low-expressing AQP1, overexpressing AQP1, and negative control viral RNA were constructed by Genechem Co. Ltd. (Shanghai, China). RKO and SW620 cell lines were transduced with lentiviruses, plated in 6-well plates at a density of 4×10^5 cells/mL 24 hours before transfection, and then rinsed with serum-free, antibiotic-free DMEM medium. Low-expressing AQP1, overexpressing AQP1, and negative control viral RNA, along with the viral transfection solution, were appropriately diluted in serum-free, antibiotic-free DMEM medium following reagent instructions. These two dilutions were combined to create a transfection complex. The multiplicity of infection was set at 20, and infection was carried out with polybrene (6 μg/mL) for 8 hours.

Western blotting assays

Protein lysate (RIPA lysate:protease inhibitor:phosphatase inhibitor at 100:1:1) was added to each group of cells to be lysed on ice for 30 minutes to obtain whole-cell extracts and centrifuged in a centrifuge at 13,200 rpm for 25 minutes at 4°C. Supernatants were collected and protein concentrations were measured using the BCA Protein Assay Kit (Beijing Beyotime Biotech Co. Inc.), and proteins were denatured at 100°C for 10 minutes of denaturation. Equal amounts of proteins were electrophoresed by 10% sodium dodecyl sulfate polyacrylamide gel electrophoresis for 90 minutes, membrane transfer for 80 minutes, blocking solution was blocked and incubated with specific

https://doi.org/10.4132/jptm.2026.01.01

primary antibody overnight. Membrane was washed with TBST and incubated with secondary antibody then secondary antibody (Affinit Goat Anti-Rabbit IgG (H+L) HRP S0001, Goat Anti-Mouse IgG (H+L) HRP S0002) were incubated to form immune complexes, then the membranes were photographed with a gel imager and the results were analyzed. Quantification was performed using Image-J (1.53k, National Institutes of Health, Bethesda, MD, USA).

Cell migration assay

Wound healing assay

The AQP1 differentially expressing RKO and SW620 cell lines were plated into 6-well plates and allowed to reach confluence. Linear wounds were gently created using the tip of a 200 μL sterile yellow pipette. After rinsing with phosphate buffered saline (PBS) to remove debris, the cells were incubated with fetal bovine serum-free medium at 37°C and 5% CO_2 for 48 hours. Images of the wound area were obtained using phase contrast microscopy, and the images were then analyzed to quantify migration, quantifying wound closure for each sample as the area covered by cells over 48 hours.

Migration assay

A total of 1×10^4 cells were mixed with 200 μL of serum-free DMEM and added homogeneously to the inner chamber of a transwell and the lower chamber was loaded with 800 μL of medium containing 30% fetal bovine serum. The cells were incubated in 5% CO_2 at 37°C for 48 hours. After incubation, the cells were removed from the upper surface of the membrane with a cotton swab, fixed with 10% paraformaldehyde for 10 minutes, and stained with 1% crystal violet for 30 minutes to count the migrating cells left on the bottom surface, which were analyzed by microscopic observation.

Cell proliferation experiment

Plate cloning assay

Cells in logarithmic growth phase were inoculated into 6-well plates, each experimental group was inoculated with 1,000 cells/well. And the culture was continued until the number of cells was greater than 50 for 14 days or until the number of cells was greater than 50 in the majority of individual clones, and then fixation staining and photographs were taken. The rate of clone formation was calculated using Image-J software.

Cell Counting Kit-8 assay

Colon cancer cells in the logarithmic growth stage were seeded into 96-well plates at a density of $1–2 \times 10^3$ cells and cultured in 100 μL of DMEM per well. After the cells were attached to the wall, respectively, continue to incubate for 0, 12, 24, 48, 60, 72 hours to add the Cell Counting Kit-8 (CCK8) reagent (5 mg/mL) (Beijing Beyotime Biotech Co. Inc.) 10 μL/well, continue to incubate for 2 hours and then measure the cell formation rate with the spectrophotometer. The absorbance values at 450 nm were measured by spectrophotometer, respectively.

In vivo studies

All animal experiments were performed in accordance with the National Institutes of Health (NIH) Guide for the Care and Use of Laboratory Animals and approved by the Institutional Animal Care and Use Committee of Anhui Medical University (Hefei, China) (approval number: LLSC20241736). Four-week-old male nude mice were purchased from Hangzhou Ziyuan Laboratory Animal Science and Technology Co. (Hangzhou, China). Mice were housed in a pathogen-free animal facility with controlled temperature and humidity. About 1×10^7 SW620-shAQP1, SW620-control and SW620-ovAQP1 cells were suspended in 0.1 mL of PBS. And the above cell lines were injected subcutaneously into the mice, which were euthanized four weeks later, and all the tumors were carefully excised, their sizes were recorded, and the tumors were embedded in 10% formalin and paraffin for immunohistochemical staining.

Immunohistochemistry

Tumor tissue specimens from mice were fixed in formalin for 12 hours and dehydrated. After paraffin embedding, the tissues were cut into 4-μm microsections. Tissue sections were dewaxed, rehydrated, and then soaked in methanol containing 0.3% hydrogen peroxide for 30 minutes to block endogenous peroxidase activity. The sections were then heated in a pressure cooker containing 10 mM ethylenediaminetetraacetic acid buffer (pH 8.0) for 2 minutes. After cooling, the sections were incubated in 1% blocking serum for 30 minutes to reduce nonspecific binding. The primary anti-AQP1 polyclonal antibody was diluted 1:250 and incubated with the sections overnight at 4°C. The sections were then incubated with the biotinylated secondary antiserum followed by horseradish peroxidase–conjugated streptavidin-biotin complex. Finally, the sections were developed with diaminobenzidine and restained with haematoxylin.

Using the German Immune Response Score, the immune response score (IRS) evaluates stained sections in an uninformative manner without prior information. The IRS scores the distribution (0–4) and intensity (0–3) of the immune response, which are then multiplied to produce an IRS score. The percentage of positive cells was scored as follows: "0" (<5%), "1" (5%–25%), "2" (25%–50%), "3" (50%–75%), and "4" (>75%). The intensity of staining was scored as follows: "0" (no staining), "1" (weak staining), "2" (moderate staining), and "3" (strong staining). The final AQP1 expression score was calculated using the percentage of positivity score multiplied the staining intensity score, ranging from 0 to 12. We estimated the IRS by averaging the values of eight fields of view for each sample at 400× magnification. AQP1 expression was defined as follows: low expression (0–6/0–3 score) and high expression (>6/4–6 score). Immunohistochemical analysis and scoring were performed by two independent investigators.

Statistical analysis

Disease-free survival (DFS) was measured from the date of surgery to the date of recurrence. Overall survival (OS) time was defined as the period from the date of colectomy to the date of death. Follow-up of patients was continued until death or 5 years after surgery, whichever occurred first. Statistical analyses were performed using SPSS ver. 25.0 for Windows (IBM Corp., Armonk, NY, USA). Qualitative variables were analyzed using the Pearson χ^2 test or Fisher's exact test. OS and DFS were calculated using the Kaplan-Meier method and Life Table method. A comparison between groups was conducted using Student's t-test and the Mann-Whitney test. A value of $p < .05$ was considered statistically significant.

The experimental data were analyzed statistically using GraphPad Prism 9.0 (GraphPad Software Inc., San Diego, CA, USA), and the data were expressed as mean ± standard deviation. Differences between two groups were analyzed using t-test, and comparisons between multiple groups were made using one-way ANOVA. All experiments were repeated 3 times, and the difference was considered statistically significant at $p < .05$.

RESULTS

AQP1 expression correlates with an unfavorable prognosis in colon patients

Analysis of the relationship between the AQPs and pathological staging of colon cancer patients by the TCGA database revealed that only AQP1 expression levels were associated with pathological staging ($p < .001$), and high AQP1 expression means a later pathological staging (Table 1) and lymphatic vessel invasion in colon cancer ($p = .046$) (AQP1 expression levels were graded by median). Survival analysis showed that the OS of patients with high AQP1 expression were statistically different from those of the low expression group ($p = .028$) (Fig. 1A).

Table 1. TNM stage of colon cancer patients according to the expression of AQPs by TCGA

	No.	TNM stage				F value	p-value
		I	II	III	IV		
AQP1	298	9.73 ± 1.17	10.02 ± 1.37	10.17 ± 1.17	10.77 ± 1.03	7.935	<.001
AQP2	176	0.87 ± 0.49	1.35 ± 0.90	1.41 ± 1.20	1.47 ± 0.84	2.364	.073
AQP3	298	8.46 ± 1.87	8.19 ± 1.68	8.35 ± 1.86	8.43 ± 1.76	0.373	.773
AQP4	142	0.94 ± 0.72	1.05 ± 0.72	1.11 ± 0.77	1.42 ± 1.67	1.196	.314
AQP5	276	2.84 ± 2.80	3.14 ± 2.86	3.62 ± 3.21	3.02 ± 2.91	0.762	.516
AQP6	286	2.74 ± 1.33	2.77 ± 1.36	3.05 ± 1.47	2.98 ± 1.36	0.844	.471
AQP7	298	4.19 ± 1.22	4.27 ± 1.65	4.54 ± 1.51	4.84 ± 1.68	2.378	.070
AQP8	270	4.78 ± 3.40	5.07 ± 3.87	5.32 ± 3.78	4.94 ± 3.70	0.206	.892
AQP9	298	4.91 ± 2.43	5.41 ± 2.35	5.37 ± 2.33	5.58 ± 2.04	0.790	.501
AQP10	156	1.32 ± 1.15	1.19 ± 0.89	1.43 ± 0.92	1.10 ± 0.79	0.916	.435
AQP11	298	5.66 ± 0.73	5.73 ± 0.91	5.56 ± 0.81	5.55 ± 0.83	0.925	.429
AQP12	288	3.58 ± 1.61	3.81 ± 1.81	4.01 ± 1.73	4.07 ± 1.59	0.933	.425

Values are presented as mean ± SD.
AQP, aquaporin; TCGA, The Cancer Genome Atlas; SD, standard deviation.

https://doi.org/10.4132/jptm.2026.01.01

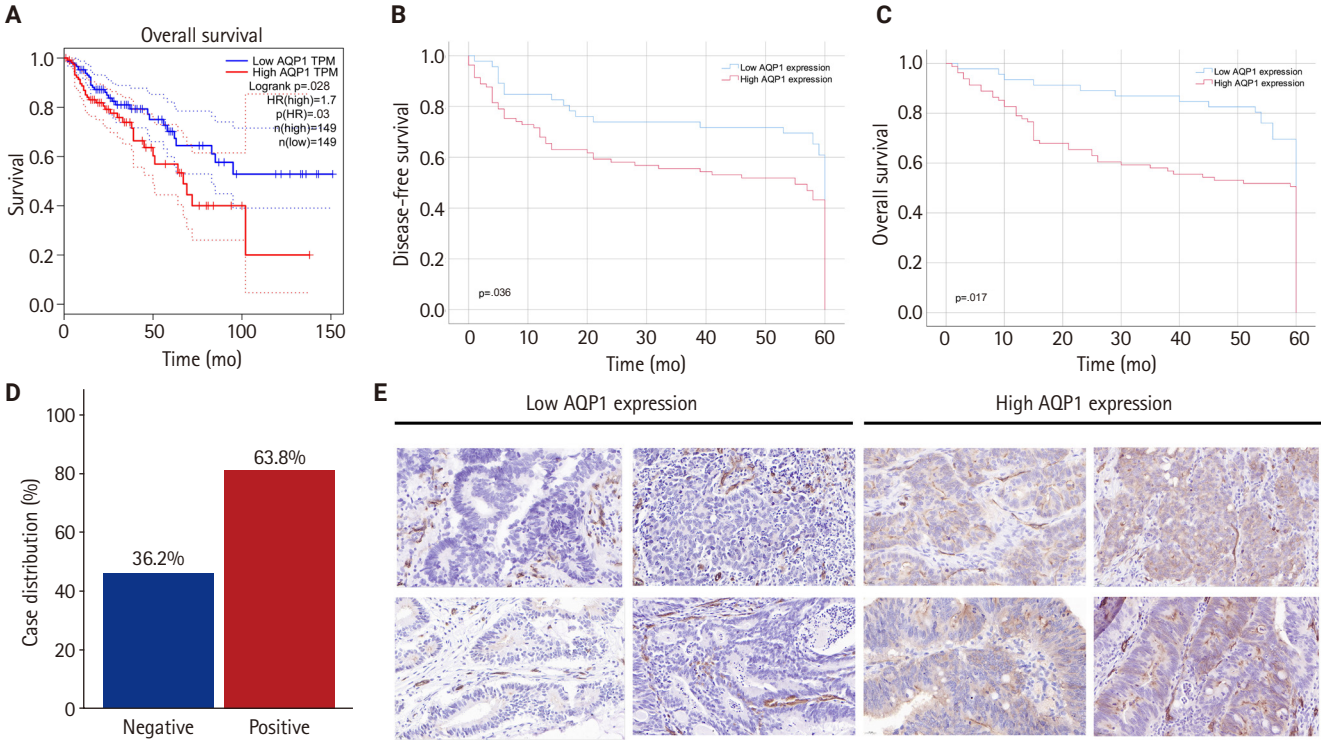

Fig. 1. Aquaporin 1 (AQP1) is differentially expressed in colon cancer and its high expression is associated with poorer prognosis. (A) Overall survival (OS) of colon cancer patients from The Cancer Genome Atlas database. (B, C) Disease-free survival (DFS), OS of 127 colon cancer patients from the Second Affiliated Hospital of Anhui Medical University based on AQP1 expression. (D) Quantitative mapping of AQP1 expression. (E) A total of 127 colon cancer tissues were obtained showing representative images of immunohistochemical AQP1 staining.

Association of AQP1 protein expression with demographic characteristics, clinicopathological features, and survival of colon cancer patients

Demographic, clinical and pathological data of 127 patients with colon cancer are shown in Table 2. The median age was 65.0 years old (range, 21 to 88 years). The male-to-female ratio was comparable. Of the 127 patients, 17 (13.4%) had intestinal obstruction, 86 (67.7%) had intestinal stenosis, 17 (13.4%) had hydroperitoneum, and 71 (55.9%) had lesions located in the right colon. According to the 8th edition of the American Joint Committee on Cancer/Union for International Cancer Control staging system, the tumor stages were distributed as follows: stage I in six cases (4.7%); stage II in 70 cases (55.1%); stage III in 41 cases (32.3%); and stage IV in 10 cases (7.9%) (Table 2).

High AQP1 expression was found in 63.8% (81/127) of the patients (Fig. 1D). The association between high AQP1 expression and tumor location in the right colon (p = .034), poorly differentiated (p = .020), neurological invasion (p = .001), lymph node metastasis (p = .021), vascular embolism (p = .004), and pathologic tumor stage (p = .027) (Table 2) were significant. The mean follow-up was 44.2 months (range, 1 to 60 months), with recurrence occurring in 61 (43.6%) of the cases. Statistical analysis of survival data showed that high AQP1 expression was associated with poorer DFS and OS (p = .036 and p = .017, respectively) (Fig. 1B, C).

Effect of AQP1 on migration of RKO and SW620 cells

To clarify the role of AQP1 in colon cancer metastasis, we constructed stably transfected RKO and SW620 cell lines with low and overexpressing of AQP1. Western blotting results showed that RKO and SW620 cells had been successfully transfected with lentivirus.

Wound healing assay showed that the percentage of wound healing was decreased in low-expressing AQP1 cells compared to overexpressing AQP1 cells (p < .05) (Fig. 2A–D). Migration assay of RKO and SW620 also showed that the decrease in the number of transmembrane cells in the low-expressing AQP1 cells inhibited the metastasis of colon cancer cells, whereas the

Table 2. Clinicopathological features of colon cancer patients according to the expression of AQP1

Factor	Total (n = 127)	AQP1 expression		p-value
		High (n = 81)	Low (n = 46)	
Sex (M/F)	66/61	44/37	22/24	.481
Age (yr)	127	60.57 ± 12.59	63.41 ± 12.38	.220
Hemoglobin (g/L)	127	105.80 ± 24.05	104.37 ± 25.79	.754
CEA	102 (68/34)[a]	13.37 ± 36.06	11.57 ± 21.62	.790
CA19-9	99 (65/34)[a]	23.29 ± 35.26	19.85 ± 20.61	.602
CA72-4	98 (65/33)[a]	5.82 ± 9.77	4.07 ± 5.57	.345
Intestinal obstruction				.087
No	110 (86.6)	67 (82.7)	43 (93.5)	
Yes	17 (13.4)	14 (17.3)	3 (6.5)	
Intestinal stenosis				.128
No	41 (32.3)	30 (37.0)	11 (23.9)	
Yes	86 (67.7)	51 (63.0)	35 (76.1)	
Hydroperitoneum				.242
No	110 (86.8)	68 (84.0)	42 (91.3)	
Yes	17 (13.4)	13 (16.0)	4 (8.7)	
Location				.034
Right colon	71 (55.9)	51 (63.0)	20 (43.5)	
Left colon	56 (44.1)	30 (37.0)	26 (56.5)	
Tumor differentiation				.020[b]
Poorly	19 (15.0)	17 (21.0)	2 (4.3)	
Moderately	106 (83.5)	63 (77.8)	43 (93.5)	
Well	2 (1.6)	1 (1.2)	1 (2.2)	
Perineural invasion				.001
No	43 (33.9)	19 (23.5)	24 (52.2)	
Yes	84 (66.1)	62 (76.5)	22 (47.8)	
Lymphatic invasion				.021
No	80 (63.0)	45 (55.6)	35 (76.1)	
Yes	47 (37.0)	36 (44.4)	11 (23.9)	
Vascular thrombosis				.004
No	56 (44.1)	28 (34.6)	28 (60.9)	
Yes	71 (55.9)	53 (65.4)	18 (39.1)	
TNM stage				.027[b]
I	6 (4.7)	3 (3.7)	3 (6.5)	
II	70 (55.1)	38 (46.9)	32 (69.6)	
III	41 (32.3)	31 (38.3)	10 (21.7)	
IV	10 (7.9)	9 (11.1)	1 (2.2)	

Values are presented as mean ± SD or number (%).
AQP1, aquaporin 1; CEA, carcinoembryonic antigen; CA19-9, glycoconjugate antigen 19-9; CA72-4, glycoconjugate antigen 72-4; SD, standard deviation.
[a]Numbers in parentheses indicate cases with high AQP1 expression/low AQP1 expression; [b]Fisher's exact test; statistically significant differences ($p < .05$).

increase in the number of transmembrane cells in the overexpressing AQP1 cells promoted the colon cancer migration (Fig. 2E–G). These results suggest that elevated AQP1 in colon cancer cells promotes colon cancer cell migration in vitro.

Effect of AQP1 on proliferation of RKO and SW620 cells

Plate cloning assays showed a reduction in the number of clones of low-expressing AQP1 cells compared to overexpress-

https://doi.org/10.4132/jptm.2026.01.01

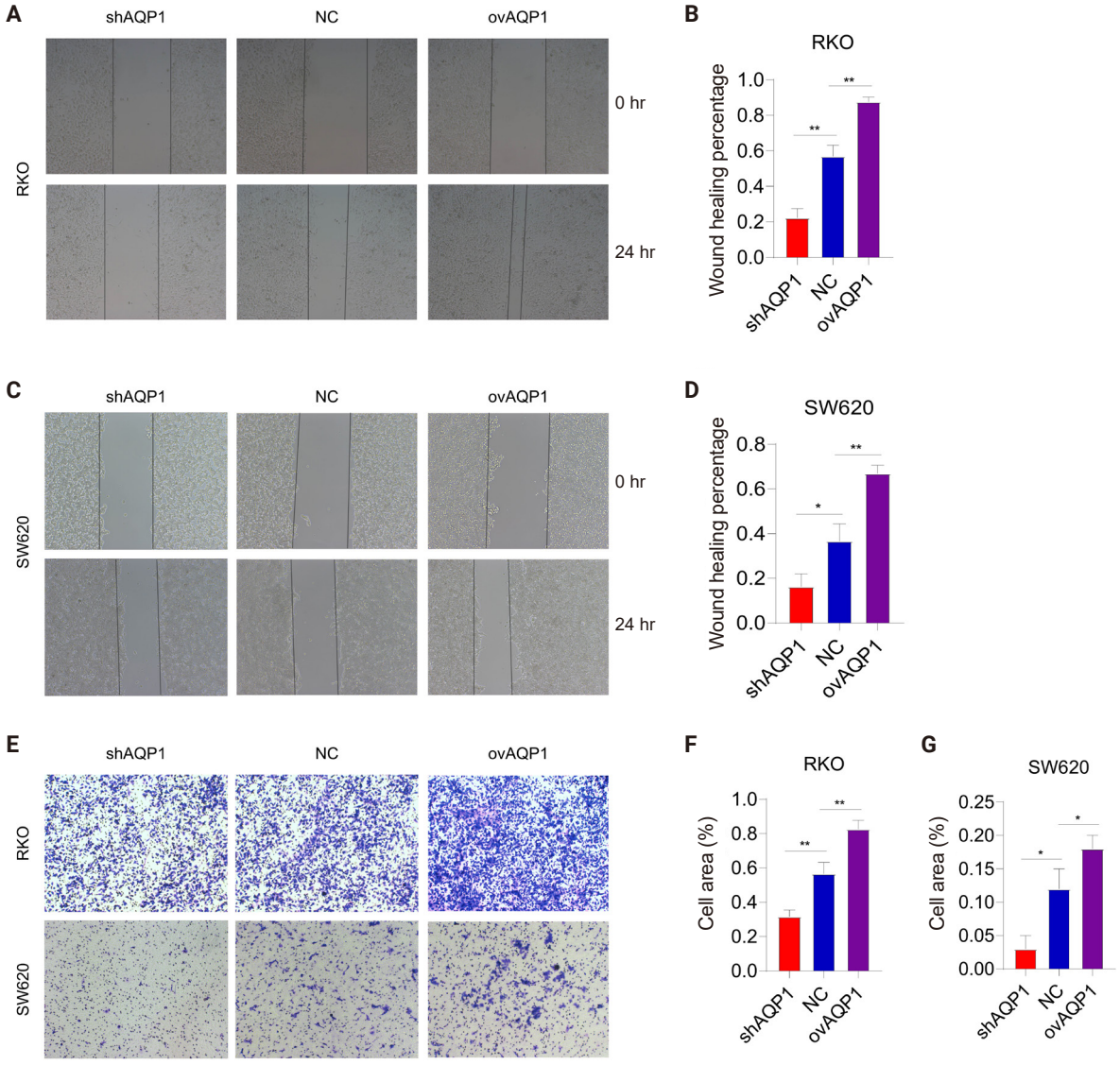

Fig. 2. Aquaporin 1 (AQP1) promoted colon cancer cell migration in vitro. (A–D) Wound healing assay showed that the percentage of wound healing was reduced in low-expressing AQP1 cells compared to overexpressing AQP1 ($p < .05$). (E–G) Differences in migration ability of RKO and SW620 cells with different expression of AQP1, E is a representative image and histograms of F and G are quantitative. NC, negative control. *$p < .05$, **$p < .01$.

ing AQP1 cells ($p < .05$) (Fig. 3A–C). We used CCK8 reagent to assess the effect of different expression levels of AQP1 on the proliferative ability of colon cancer cells (Fig. 3D, E). The cell proliferation curves showed elevated AQP1 expression at the same time and increased cell number, representing enhanced cell proliferation ability. These results suggest that AQP1 promotes the proliferation of colon cancer cells in vitro.

Effect of AQP1 on colon cancer cell proliferation ability in vivo

To confirm the role of AQP1 in growth and proliferation in vivo, we injected tumor cells (SW620-shAQP1, SW620-NC, and SW620-ovAQP1) into the subcutaneous tissue of nude mice and established a subcutaneous tumorigenic model. After 30 days, we found that the nude mice in the SW620-ovAQP1 group had a larger volume of subcutaneous tumors when compared to the SW620-NC group; on the contrary, subcutaneous

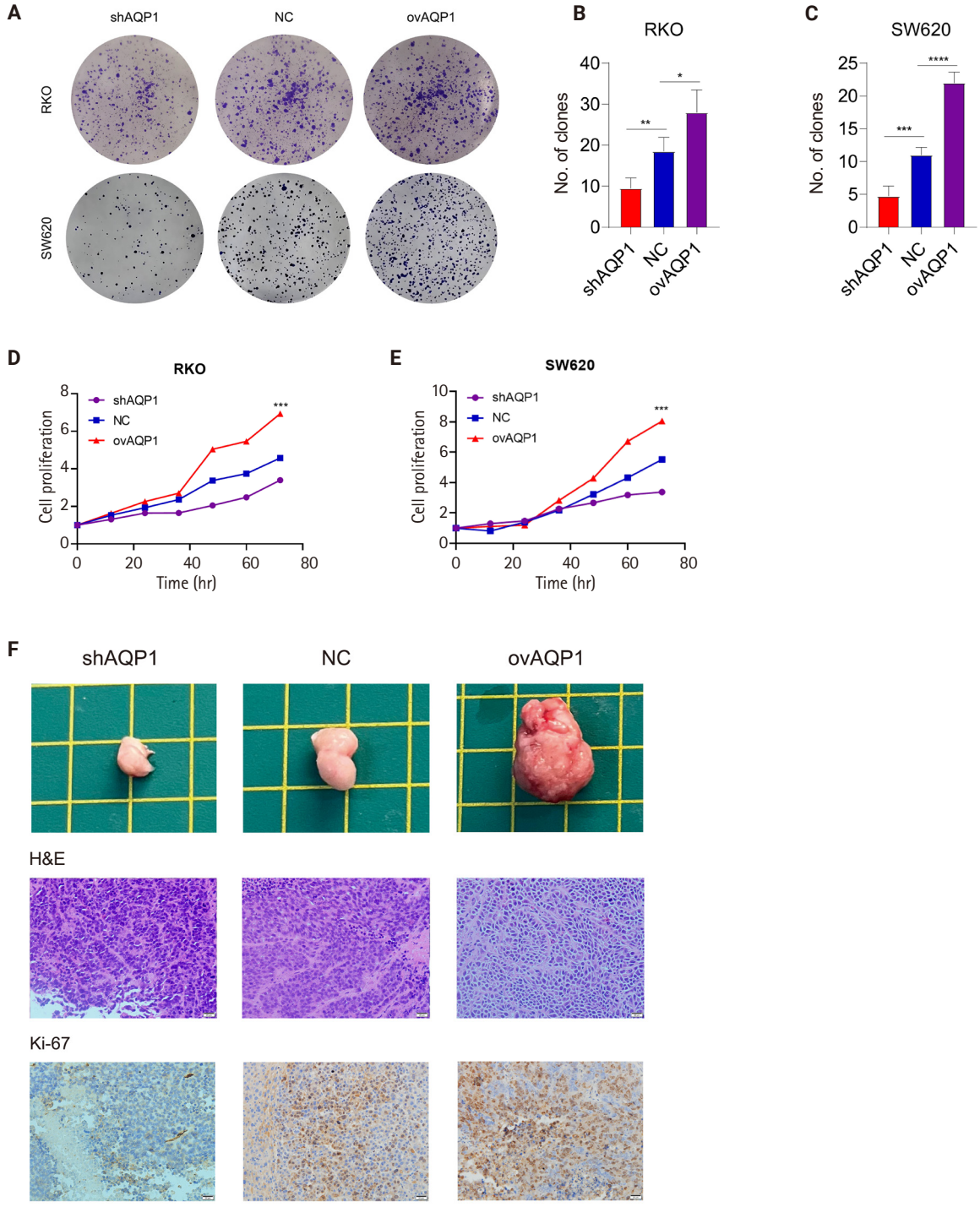

Fig. 3. Effect of aquaporin 1 (AQP1) on proliferative capacity of colon cancer cells in vitro and in vivo. (A–C) Plate cloning assay demonstrated a decrease in the number of clones of low-expressing AQP1 cells compared to overexpressing AQP1 cells ($p < .05$). (D, E) Cell proliferation curves of Cell Counting Kit-8 assay showed enhanced proliferation of colon cancer cells with elevated AQP1 expression at the same time points. *$p < .05$, **$p < .01$, ***$p < .001$. (F) Subcutaneous tumorigenic model in nude mice was constructed by subcutaneous injection of SW620-shAQP1, SW620-NC, and SW620-ovAQP1 cells, and representative images of subcutaneous tumors were obtained, stained by hematoxylin and eosin (H&E) and tumor tissues of the three groups were examined by immunohistochemistry, indicating that the expression levels of Ki-67. NC, negative control.

https://doi.org/10.4132/jptm.2026.01.01

tumor volume was smaller in nude mice injected with SW620-shAQP1 group compared with SW620-NC group (Fig. 3F). And the expression levels of Ki-67 in the subcutaneous tumor tissues of nude mice were examined by immunohistochemistry, results demonstrate that Ki-67 levels are higher in the ovAQP1 group compared to the shAQP1 group (Fig. 3F). These results suggest that increased AQP1 expression promotes the proliferative capacity of colon cancer in vivo.

Next, the expression levels of AQP1, N-cadherin, vimentin, and claudin-1 in the subcutaneous tumor tissues of nude mice were examined by immunohistochemistry. The expression levels of N-cadherin, vimentin, and claudin-1 were higher in the ovAQP1 group than in the shAQP1 group (Fig. 4A). Therefore, we hypothesized that AQP1 may promote epithelial-mesenchymal transition (EMT) by promoting the expression of claudin-1.

AQP1 may promote EMT by up-regulating claudin-1 expression

Based on the above results, we hypothesized that AQP1 may regulate tumor proliferation and metastasis through EMT. To determine the possible mechanism of action of AQP1 on colon cancer cell migration, we examined the expression of EMT-related genes by Western blotting experiments. With elevated AQP1 expression, the expression of claudin-1 was upregulated, as was the expression level of the epithelial cell marker, N-cadherin, whereas the low-expressing AQP1 resulted in the opposite (Fig. 4B). These results suggest that AQP1 may promote the EMT process by up-regulating the expression of claudin-1.

DISCUSSION

Colon cancer frequently invades neighboring tissues and metastasizes via lymphatic and blood vessels [11], with distant metastases present in 25% of patients at diagnosis and high recurrence rates post-surgery [12]. Although screening has reduced the overall incidence rate, the incidence rate among young people and the mortality rate among patients under 65 years of age are still rising [13]. Despite therapies targeting proliferation, angiogenesis, and the tumor microenvironment, metastasis remains a major cause of death, with a 5-year survival rate below 15% for advanced cases [14,15]. Understanding the molecular mechanisms driving progression is critical for developing more effective treatments.

AQP1 elevation is more pronounced in middle and advanced, poorly differentiated colon cancer tissues [16]. The expression of AQP1 is linked to lymph node metastasis, lymphovascular infiltration, and vascular infiltration in colon cancer, establishing it as an independent predictor of poor prognosis [17]. Similar to these findings, we derived that among the AQPs, only AQP1 was associated with pathological stage of colon cancer patients ($p < .001$) and lymphovascular invasion ($p = .046$) ac-

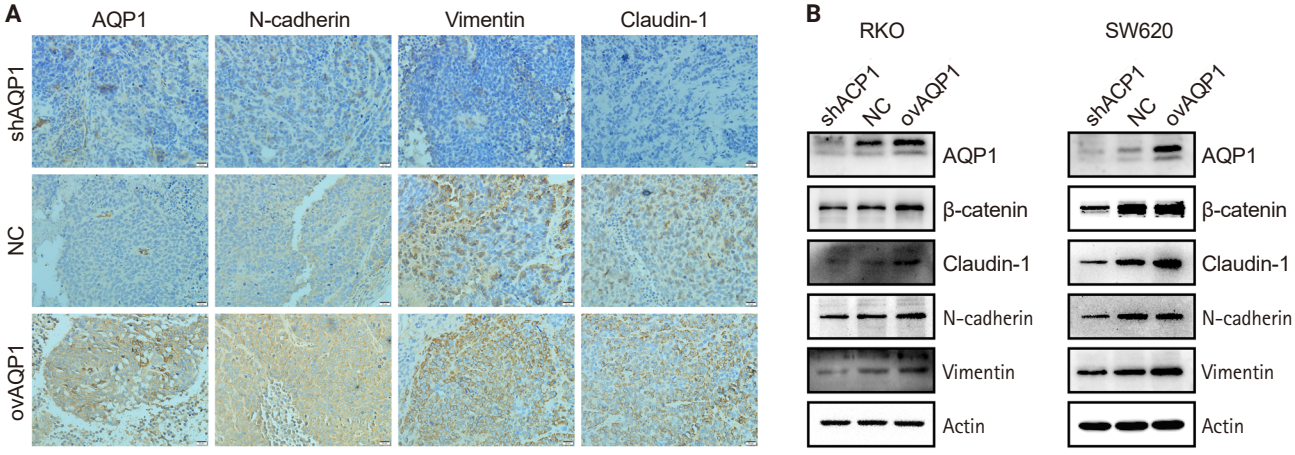

Fig. 4. Aquaporin 1 (AQP1) promotes epithelial-mesenchymal transition by upregulating claudin-1 expression. (A) Tumor tissues of the three groups were examined by immunohistochemistry, indicating that the expression levels of N-cadherin, vimentin, and claudin-1 were higher in ovAQP1 group than in shAQP1 group. (B) Lentiviruses delivering low-expressing AQP1, overexpressing AQP1 and negative control (NC) were transfected into RKO and SW620 cells, and the effect of transfection was determined by Western blotting. The expression of AQP1, β-catenin, claudin-1, N-cadherin, and vimentin in RKO and SW620 cells with low-expressing and overexpressing of AQP1.

cording to TCGA. Survival analysis showed that patients with high AQP1 expression had shorter OS (p = .028). In this study, 63.8% of cases were high AQP1 expression, which was significantly correlated with aggressive tumor characteristics including degree of differentiation, perineural invasion, lymphatic invasion, choroidal cancer embolism, and tumor stage. Patients with high AQP1 expression had shorter DFS and OS than those with low AQP1 expression. These findings suggest that AQP1 plays a tumor-promoting role in colon cancer.

Numerous studies demonstrate that the dual-channel functionality of AQP1, involving water and ions, enhances the migration and invasion of cancer cells in vitro [18,19]. Ion channel inhibitors like 5HMF and AqB011, along with water pore channel inhibitors like Bacopaside II and AqB013, have demonstrated the ability to impair the in vitro migration of colon cancer cells. When employed in combination, AQP1 blockers exhibit a synergistic effect, efficiently decelerating the progression of cancer. Hence, they are regarded as a promising tool for enhancing cancer treatment [19-21]. In the realm of medical possibilities, AQP1 blockers show promise for treating congestive heart failure, refractory edema associated with cirrhosis, and specific cancer therapies [22].

Colon cancer employ various mechanisms for spreading, with the most central being the transition of cells from a non-motile, quiescent epithelial phenotype to a mesenchymal cell-like form characterized by traits such as migration, invasion, and resistance—commonly known as EMT [23]. Throughout EMT, there is typically a reduction in the levels of epithelial cell markers, coupled with an upregulation of mesenchymal cell-associated markers [24]. To unravel the specific mechanism, we constructed colon cancer cell lines exhibiting varied expression of AQP1. Within this study, it was demonstrated that AQP1 promotes the proliferative and metastatic ability of colon cancer in vitro and in vivo. Western blotting revealed a gradual increase in the expression of N-cadherin as the content of AQP1 increased. Recognizing N-cadherin as a promoter of tumor metastasis and a major intracellular marker of EMT, its heightened expression correlates directly with tumor invasiveness, spread, and resistance to cell death. Elevated N-cadherin levels are considered an independent prognostic factor for poor outcomes in solid tumor cells, including colon cancer [25,26]. Therefore, our conclusion is that the metastatic capability of colon cancer cells escalates in tandem with the increased expression of AQP1, affirming the promotional role of AQP1 in colon cancer metastasis. Simultaneously, we observed an elevation in claudin-1 expression with heightened AQP1 expression. In normal epithelial cells, claudin-1 plays a role in preserving the mucosal barrier of the normal colon epithelium [27,28]; nevertheless, in the context of colon cancer, its overexpression promotes the transformation, invasion, and metastasis of cancer cells [29]. Given the alteration in transcription factors linked to EMT, we hypothesized that AQP1 influences the EMT process in colon cancer by up-regulating claudin-1 expression.

AQP1 is expressed in various gastrointestinal tumors, but studies indicate its functions vary across different contexts. For instance, reports indicate AQP1 exhibits tumor-suppressing effects in intrahepatic cholangiocarcinoma, potentially regulating tumor growth by modulating Snail expression [30]. Conversely, it promotes tumorigenesis in gastric, pancreatic, and hepatocellular carcinomas [31-33]. This study further demonstrates its oncogenic role in colorectal cancer. Thus, we conclude that AQP1 exhibits distinct biological behaviors across different gastrointestinal malignancies. No studies have yet elucidated the potential reasons for this discrepancy. Future research will investigate whether AQP1 mutations exist in different gastrointestinal tumors and further explore the causes of these mutations.

The precise mechanism by which AQP1 regulates claudin-1 in colon cancer progression remains unclear. Current evidence primarily relies on in vitro and single-center retrospective studies, which lack robust mechanistic depth. Future studies should employ multicenter prospective cohorts, AQP1-knockout/transgenic mouse models, and metastatic xenograft models to clarify its role in tumor invasion and metastasis. Additionally, advanced molecular techniques are needed to dissect the AQP1–claudin-1 interaction, including upstream regulators and downstream effectors to identify potential therapeutic targets.

In conclusion, the findings of this study propose that AQP1 potentially stimulates the proliferation, metastasis, and EMT of colon cancer cells by upregulating claudin-1 expression, indicating an association with unfavorable outcomes in colon cancer. The reduction in AQP1 expression hindered the proliferation and migration abilities of colon cancer cells. AQP1 emerges as a potential molecular marker for predicting the prognosis of colon cancer patients and serves as a potential target for the treatment of colon cancer.

Ethics Statement

All procedures performed in the current study were approved by Institutional Review Board (IRB) of the Second Affiliated Hospital of Anhui Medical University (approval number:

https://doi.org/10.4132/jptm.2026.01.01

YX2024-213) in accordance with the 1964 Helsinki declaration and its later amendments. Informed consent was obtained from all individual participants included in the study. The data did not contain any patient-identifiable information.

Availability of Data and Material

The datasets generated or analyzed during the study are available from the corresponding author on reasonable request.

Code Availability

Not applicable.

ORCID

Wei Wei Xie	https://orcid.org/0000-0002-4584-4544
Lin Xu	https://orcid.org/0009-0008-6851-8304
Qian Li	https://orcid.org/0009-0003-6989-2721
Dao Quan Zhang	https://orcid.org/0009-0000-3931-8460
Yu Bao Zhou	https://orcid.org/0009-0006-6115-5788

Author Contributions

Conceptualization: WWX, DQZ, YBZ. Data curation: LX, QL. Formal analysis: WWX, LX, QL. Funding acquisition: YBZ. Investigation: WWX, LX, QL. Methodology: WWX, LX, DQZ, YBZ. Project administration: DQZ, YBZ. Resources: YBZ. Software: WWX, LX. Supervision: DQZ, YBZ. Validation: WWX, LX, QL. Visualization: LX, QL. Writing—original draft: WWX, LX, QL. Writing—review & editing: YBZ, DQZ. Approval of final manuscript: all authors.

Conflicts of Interest

The authors declare that they have no potential conflicts of interest.

Funding Statement

This project was supported by Clinical Research Cultivation Program of the Second Affiliated Hospital of Anhui Medical University (2020LCZD13) and Scientific Research Program of Higher Education Institutions in Anhui Province (Natural Science) (2024AH050791).

REFERENCES

1. Liu S, Peng X, Wu X, et al. Construction of a new immune-related lncRNA model and prediction of treatment and survival prognosis of human colon cancer. World J Surg Oncol 2022; 20: 71.
2. Bray F, Laversanne M, Sung H, et al. Global cancer statistics 2022: GLOBOCAN estimates of incidence and mortality worldwide for 36 cancers in 185 countries. CA Cancer J Clin 2024; 74: 229-63.
3. Benson AB, Venook AP, Al-Hawary MM, et al. NCCN guidelines insights: colon cancer, version 2.2018. J Natl Compr Canc Netw 2018; 16: 359-69.
4. Brown KG, Koh CE. Surgical management of recurrent colon cancer. J Gastrointest Oncol 2020; 11: 513-25.
5. Wang L, Zhang Y, Wu X, Yu G. Aquaporins: new targets for cancer therapy. Technol Cancer Res Treat 2016; 15: 821-8.
6. Mobasheri A, Airley R, Hewitt SM, Marples D. Heterogeneous expression of the aquaporin 1 (AQP1) water channel in tumors of the prostate, breast, ovary, colon and lung: a study using high density multiple human tumor tissue microarrays. Int J Oncol 2005; 26: 1149-58.
7. Chow PH, Bowen J, Yool AJ. Combined systematic review and transcriptomic analyses of mammalian aquaporin classes 1 to 10 as biomarkers and prognostic indicators in diverse cancers. Cancers (Basel) 2020; 12: 1911.
8. Moon C, Soria JC, Jang SJ, et al. Involvement of aquaporins in colorectal carcinogenesis. Oncogene 2003; 22: 6699-703.
9. Smith E, Tomita Y, Palethorpe HM, et al. Reduced aquaporin-1 transcript expression in colorectal carcinoma is associated with promoter hypermethylation. Epigenetics 2019; 14: 158-70.
10. El Hindy N, Bankfalvi A, Herring A, et al. Correlation of aquaporin-1 water channel protein expression with tumor angiogenesis in human astrocytoma. Anticancer Res 2013; 33: 609-13.
11. Pretzsch E, Bosch F, Neumann J, et al. Mechanisms of metastasis in colorectal cancer and metastatic organotropism: hematogenous versus peritoneal spread. J Oncol 2019; 2019: 7407190.
12. Young PE, Womeldorph CM, Johnson EK, et al. Early detection of colorectal cancer recurrence in patients undergoing surgery with curative intent: current status and challenges. J Cancer 2014; 5: 262-71.
13. Siegel RL, Wagle NS, Cercek A, Smith RA, Jemal A. Colorectal cancer statistics, 2023. CA Cancer J Clin 2023; 73: 233-54.
14. Van Cutsem E, Cervantes A, Adam R, et al. ESMO consensus guidelines for the management of patients with metastatic colorectal cancer. Ann Oncol 2016; 27: 1386-422.
15. Khan S, Ricciardelli C, Yool AJ. Targeting aquaporins in novel therapies for male and female breast and reproductive cancers. Cells 2021; 10: 215.
16. Hong Y, Chen Z, Li N, Zhang M. Prognostic value of serum aquaporin-1, aquaporin-3 and galectin-3 for young patients with colon cancer. Ann Clin Biochem 2020; 57: 404-11.

17. Yoshida T, Hojo S, Sekine S, et al. Expression of aquaporin-1 is a poor prognostic factor for stage II and III colon cancer. Mol Clin Oncol 2013; 1: 953-8.
18. Pei JV, Kourghi M, De Ieso ML, et al. Differential inhibition of water and ion channel activities of mammalian aquaporin-1 by two structurally related bacopaside compounds derived from the medicinal plant *Bacopa monnieri*. Mol Pharmacol 2016; 90: 496-507.
19. De Ieso ML, Pei JV, Nourmohammadi S, et al. Combined pharmacological administration of AQP1 ion channel blocker AqB011 and water channel blocker Bacopaside II amplifies inhibition of colon cancer cell migration. Sci Rep 2019; 9: 12635.
20. Chow PH, Kourghi M, Pei JV, Nourmohammadi S, Yool AJ. 5-Hydroxymethyl-furfural and structurally related compounds block the ion conductance in human aquaporin-1 channels and slow cancer cell migration and invasion. Mol Pharmacol 2020; 98: 38-48.
21. Dorward HS, Du A, Bruhn MA, et al. Pharmacological blockade of aquaporin-1 water channel by AqB013 restricts migration and invasiveness of colon cancer cells and prevents endothelial tube formation in vitro. J Exp Clin Cancer Res 2016; 35: 36.
22. Verkman AS, Anderson MO, Papadopoulos MC. Aquaporins: important but elusive drug targets. Nat Rev Drug Discov 2014; 13: 259-77.
23. Skarkova V, Vitovcova B, Matouskova P, et al. Role of N-cadherin in epithelial-to-mesenchymal transition and chemosensitivity of colon carcinoma cells. Cancers (Basel) 2022; 14: 5146.
24. Wang J, Zhang N, Han Q, et al. Pin1 inhibition reverses the acquired resistance of human hepatocellular carcinoma cells to Regorafenib via the Gli1/Snail/E-cadherin pathway. Cancer Lett 2019; 444: 82-93.
25. Yan X, Yan L, Liu S, Shan Z, Tian Y, Jin Z. N-cadherin, a novel prognostic biomarker, drives malignant progression of colorectal cancer. Mol Med Rep 2015; 12: 2999-3006.
26. Ye Z, Zhou M, Tian B, Wu B, Li J. Expression of lncRNA-CCAT1, E-cadherin and N-cadherin in colorectal cancer and its clinical significance. Int J Clin Exp Med 2015; 8: 3707-15.
27. Gunzel D, Yu AS. Claudins and the modulation of tight junction permeability. Physiol Rev 2013; 93: 525-69.
28. Singh AB, Uppada SB, Dhawan P. Claudin proteins, outside-in signaling, and carcinogenesis. Pflugers Arch 2017; 469: 69-75.
29. Bhat AA, Ahmad R, Uppada SB, Singh AB, Dhawan P. Claudin-1 promotes TNF-alpha-induced epithelial-mesenchymal transition and migration in colorectal adenocarcinoma cells. Exp Cell Res 2016; 349: 119-27.
30. Zhuang MQ, Jiang XL, Liu WD, et al. Aquaporin 1 is a prognostic marker and inhibits tumour progression through downregulation of Snail expression in intrahepatic cholangiocarcinoma. Dig Liver Dis 2023; 55: 1133-40.
31. Wang Z, Wang Y, He Y, Zhang N, Chang W, Niu Y. Aquaporin-1 facilitates proliferation and invasion of gastric cancer cells via GRB7-mediated ERK and Ras activation. Anim Cells Syst (Seoul) 2020; 24: 253-9.
32. Lopes PA, Fonseca E, da Silva IV, Vigia E, Paulino J, Soveral G. Aquaporins transcripts with potential prognostic value in pancreatic cancer. Genes (Basel) 2023; 14: 1694.
33. Pelagalli A, Nardelli A, Fontanella R, Zannetti A. Inhibition of AQP1 hampers osteosarcoma and hepatocellular carcinoma progression mediated by bone marrow-derived mesenchymal stem cells. Int J Mol Sci 2016; 17: 1102.

https://doi.org/10.4132/jptm.2026.01.01

JPTM

ORIGINAL ARTICLE

pISSN 2383-7837 · eISSN 2383-7845

Journal of Pathology and Translational Medicine 2026; 60: 319-330
https://doi.org/10.4132/jptm.2026.01.02

Expression of PD-1/PD-L1 pathway molecules in human cardiac allograft according to acute cellular rejection status: insights from a Korean Heart Transplant Cohort

Jeemin Yim[1,2], Yoon Kyung Jeon[1,3,4], Doo Hyun Chung[1,5,6], Jaemoon Koh[1,3]

[1]Department of Pathology, Seoul National University College of Medicine, Seoul, Korea
[2]Department of Pathology, Seoul Metropolitan Government-Seoul National University Boramae Medical Center, Seoul, Korea
[3]Department of Pathology, Seoul National University Hospital, Seoul, Korea
[4]Cancer Research Institute, Seoul National University College of Medicine, Seoul, Korea
[5]Department of Biomedical Sciences, Seoul National University College of Medicine, Seoul, Korea
[6]Ischemic/Hypoxic Disease Institute, Seoul National University College of Medicine, Seoul, Korea

Graphical abstract

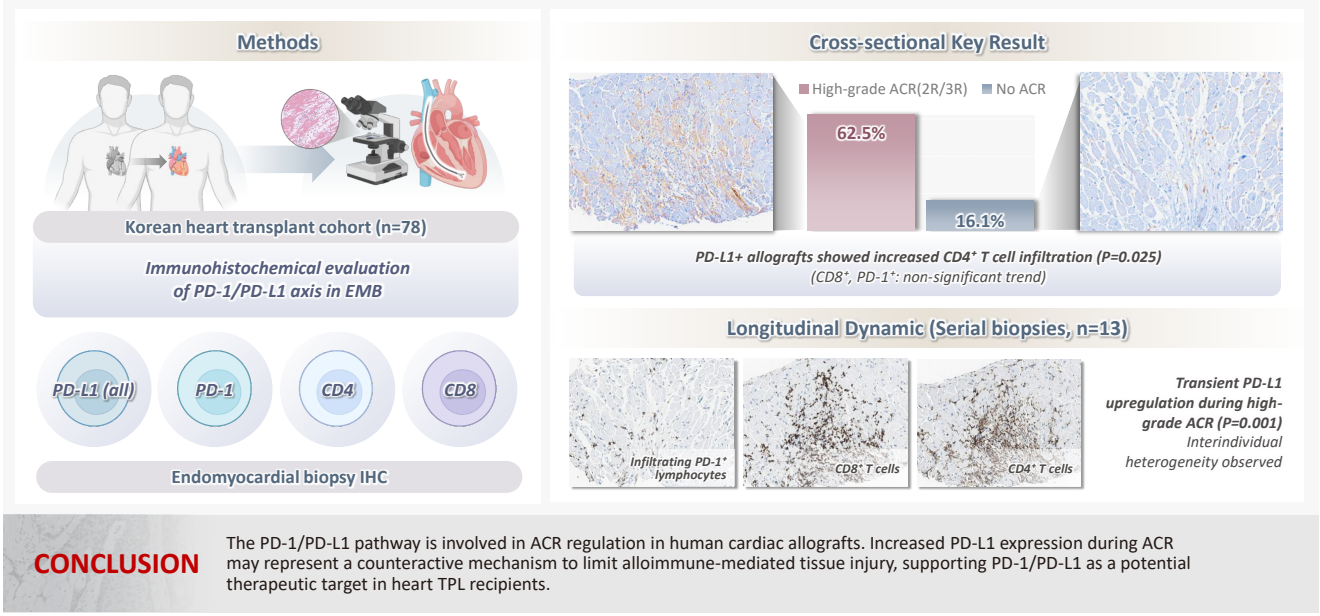

JPTM

ORIGINAL ARTICLE

pISSN 2383-7837 · eISSN 2383-7845

Journal of Pathology and Translational Medicine 2026; 60: 319-330
https://doi.org/10.4132/jptm.2026.01.02

Expression of PD-1/PD-L1 pathway molecules in human cardiac allograft according to acute cellular rejection status: insights from a Korean Heart Transplant Cohort

Jeemin Yim[1,2], Yoon Kyung Jeon[1,3,4], Doo Hyun Chung[1,5,6], Jaemoon Koh[1,3]

[1]Department of Pathology, Seoul National University College of Medicine, Seoul, Korea
[2]Department of Pathology, Seoul Metropolitan Government-Seoul National University Boramae Medical Center, Seoul, Korea
[3]Department of Pathology, Seoul National University Hospital, Seoul, Korea
[4]Cancer Research Institute, Seoul National University College of Medicine, Seoul, Korea
[5]Department of Biomedical Sciences, Seoul National University College of Medicine, Seoul, Korea
[6]Ischemic/Hypoxic Disease Institute, Seoul National University College of Medicine, Seoul, Korea

Background: Acute cellular rejection (ACR) following heart transplantation (TPL) compromises graft function and survival. The programmed cell death-1 (PD-1)/PD-1 ligand-1 (PD-L1) pathway represents an immune checkpoint that maintains peripheral immune tolerance, but its expression and significance in human cardiac allografts with ACR remain unclear. Thus, we investigated PD-1/PD-L1 expression in endomyocardial biopsies from heart TPL recipients to clarify the role of this pathway in the ACR of human cardiac allografts and explore the potential of therapeutic modulation of PD-1/PD-L1 in this setting. **Methods:** Endomyocardial biopsies of 78 patients with heart TPL were subjected to immunohistochemistry for PD-L1, PD-1, CD4, and CD8. PD-L1 expression and quantities of PD-1$^+$, CD4$^+$, and CD8$^+$ infiltrating lymphocytes were evaluated according to clinicopathological features, ACR presence, and clinical outcomes. **Results:** Allografts with high-grade ACR (International Society for Heart and Lung Transplantation grades 2R and 3R) demonstrated markedly higher PD-L1 expression than did those without ACR (62.5% vs. 16.1%, $p < .001$). PD-L1 expression was positively associated with CD4$^+$ lymphocyte infiltration ($p = .025$), whereas CD8 and PD-1$^+$ lymphocyte counts were higher in PD-L1-positive allografts without reaching statistical significance ($p = .059$ and $p = .390$, respectively). Serial biopsies revealed that PD-L1 expression was upregulated in patients with high-grade ACR compared with that in previous non-ACR tissues, and follow-up biopsies were performed after ACR resolution. **Conclusions:** The PD-1/PD-L1 pathway is involved in ACR regulation in human cardiac allografts. Increased PD-L1 expression during ACR may represent a counteractive mechanism to limit alloimmune-mediated tissue injury, supporting PD-1/PD-L1 as a potential therapeutic target in heart TPL recipients.

Keywords: Heart transplantation; Graft rejection; Programmed cell death 1 receptor

INTRODUCTION

Heart transplantation (TPL) is the only treatment of choice for prolonging the survival and quality of life of patients with severe heart failure [1]. Despite advances in immunosuppressive therapy, acute cellular rejection (ACR) continues to impair long-term graft survival. According to the International Society for Heart and Lung Transplantation (ISHLT) registry, ACR accounts for approximately 11% of heart transplant deaths in the first 3 years post-TPL [2], usually occurring within the first year (often in the first 6 months post-TPL) and affecting 20%–40% of recipients, with each episode predisposing to graft dysfunction and failure [3,4]. The gold standard for ACR diagnosis is histopathological grading of endomyocardial biopsy (EMB) for lymphocytic infiltration and myocyte injury. Routine EMB surveillance, as per ISHLT guidelines, enables early detection and

Received: September 30, 2025 **Revised:** December 5, 2025 **Accepted:** December 31, 2025
Corresponding Author: Jaemoon Koh, MD, PhD
Department of Pathology, Seoul National University College of Medicine, 103 Daehak-ro, Jongno-gu, Seoul 03080, Korea
Tel: +82-2-740-0029, Fax: +82-2-743-5530, E-mail: tarda@naver.com

management of rejection [5-8].

ACR arises from the recipient T-cell recognition of donor alloantigens. T-lymphocytes orchestrate allograft injury via antigen-specific activation and costimulatory signaling. Critically, co-inhibitory immune checkpoints temper T-cell activation to maintain peripheral tolerance and prevent excessive tissue damage [9,10]. Among these, the programmed cell death-1 (PD-1) receptor and its ligand programmed death-ligand 1 (PD-L1; also known as B7-H1) constitute a key inhibitory pathway activated during chronic antigen exposure. Engagement of PD-1 on T cells by PD-L1, expressed on antigen-presenting and parenchymal cells, attenuates effector T cell responses and helps preserve transplant tolerance [11,12]. Notably, this pathway is utilized by cancer and chronic viruses to evade immunity. Conversely, PD-1/PD-L1 blockade therapies restore T-cell activity in oncology [11,12]. In TPL models, PD-1/PD-L1 interactions are essential for alloimmune response downregulation and graft survival promotion [13,14]. For instance, PD-L1 expression critically modulates immune responses, contributing to cardiac allograft tolerance in mice and regulating $CD8^+$ T cell–mediated injury in the heart [15,16]. In humans, PD-L1 expression correlates with biopsy-proven ACR severity and rejection risk [17,18]. Moreover, blocking PD-1 and augmenting its signaling (e.g., with PD-L1.Ig fusion proteins) accelerate rejection and prolong allograft survival, respectively [19,20]. PD-1–deficient mice developed severe myocarditis and rapidly rejected cardiac allografts, underscoring the protective role of PD-1 [21]. Notably, patients with solid organ transplants who receive anti–PD-1 cancer therapy manifest acute T cell-mediated graft rejection, highlighting the PD-1/PD-L1 axis as a pivotal mediator of allograft tolerance in humans [22].

Nonetheless, until recently, PD-1/PD-L1 involvement in human cardiac allograft rejection was not well characterized [23]. Emerging clinical evidence indicates that PD-L1 expression is induced in cardiac allografts during ACR [18]. In a recent study on heart transplant recipients, PD-L1 was upregulated in cardiomyocytes in proportion to ACR severity [18], suggesting an intrinsic counter-regulatory mechanism; nevertheless, PD-L1 upregulation alone may not fully prevent allograft damage [24]. While characterization of PD-1/PD-L1 expression in human cardiac allografts has begun in other populations, a comprehensive understanding of PD-1/PD-L1 status and its precise correlation with rejection severity—particularly within specific cohorts such as East Asians—remains largely unknown. Thus, we investigated PD-1 and PD-L1 expression in EMB samples from heart TPL patients, aiming to clarify the role of this checkpoint pathway in the ACR of human cardiac allografts and to explore the potential of therapeutic modulation of PD-1/PD-L1 in this setting.

MATERIALS AND METHODS

Patients

Overall, 78 patients who underwent heart TPL and were followed up at Seoul National University Hospital (SNUH; Seoul, Republic of Korea) between March 2010 and May 2015 were included in this study to evaluate their treatment response and long-term survival. Acute rejection routine surveillance was performed in all patients for at least 1 year by protocol EMBs. Briefly, patients were monitored at the cardiac center for the first 2 weeks following TPL and followed up with routine clinical visits every 3 months for 1-year post-TPL. Protocol EMBs were performed 10 days after TPL with subsequent biopsies, depending on whether the steroids were to be weaned off or reduced to a maintenance dose. Clinical data were obtained from the medical records, and all EMB pathological materials were reviewed.

Histological EMB evaluation

Histology-based rejection grading for cardiac allografts was performed according to the 2004 ISHLT guidelines [8] as follows: (1) grade 0R, no rejection; (2) grade 1R, mild rejection—interstitial and/or perivascular infiltrate with up to 1 focus of myocyte injury; (3) grade 2R, moderate rejection—two or more foci of infiltrate with associated myocyte injury; and (4) grade 3R, severe rejection—a diffuse process of myocyte injury in which distinct foci are difficult to delineate. The most severe grade observed across multiple sections was recorded as the ACR grade of the cardiac allograft. In clinical practice, ISHLT grades 2R and 3R are considered high-grade ACR and require treatment [8]. Thus, in this study, the correlation between ACR and clinicopathological features was compared between patients with grades 0R/1R and those with grades 2R/3R.

Immunohistochemistry

Immunohistochemistry (IHC) was performed using a rabbit anti–PD-L1 (E1L3N) XP monoclonal antibody (mAb) (Cell Signaling Technology, Danvers, MA, USA), a mouse anti–PD-1 mAb (clone MRQ-22, Cell Marque, Rocklin, CA, USA), a mouse anti-CD4 mAb (clone 4B12, Thermo Fisher Scientific,

https://doi.org/10.4132/jptm.2026.01.02

Rockford, IL, USA), and the Benchmark XT autostainer (Ventana Medical Systems, Tucson, AZ, USA). IHC for CD8 (rabbit IgG, clone SP16, Thermo Fisher Scientific) was performed using a Bond-Max automated immunostainer (Leica Microsystems, Melbourne, Australia). All EMB tissues were subjected to PD-L1 expression immunohistochemical analysis. IHC for PD-1, CD4, and CD8 was performed on EMB samples, demonstrating a grade 1R-3R ACR because ACR grade 0 EMB tissues were infiltrated by few or no lymphocytes.

PD-L1 IHC was evaluated based on membranous and/or cytoplasmic staining intensity and proportion in cardiac tissue, including myocardiocytes, endothelial cells, and immune cells, and scored as follows: 0, no staining; 1, weak intensity in any proportion or moderate intensity in ≥5% of total area in EMB tissue; 2, moderate intensity in ≥5% of total area in EMB tissue; and 3, strong intensity in ≥5% of total area in EMB tissue. Patients with PD-L1 IHC scores of 2 or 3 were considered positive for PD-L1 expression. In addition, a PD-L1 H-score was calculated for each biopsy to capture the overall burden of PD-L1 expression. For this purpose, we estimated the percentage of PD-L1–positive cells in the entire biopsy section (0%–100%) and recorded the predominant staining intensity (0–3). The H-score was then derived as intensity × percentage of positive cells, yielding a value between 0 and 300. This continuous H-score was used particularly to evaluate longitudinal changes in PD-L1 expression in serial biopsies.

$CD4^+$, $CD8^+$, and $PD\text{-}1^+$ lymphocyte enumeration

For each specimen, two representative high-power fields (HPFs, 400× magnification) were selected from the areas infiltrated by the highest number of lymphocytes after examination of hematoxylin and eosin–stained slides under a microscope. Identical areas were taken from CD4-, CD8, and PD-1 immunostained slides, and $CD4^+$, $CD8^+$, and $PD\text{-}1^+$ lymphocytes were manually counted. The data are presented as the mean number of cells per HPF.

Statistical analysis

All statistical analyses were performed using the SPSS software ver. 23 (IBM Corp., New York, NY, USA). Comparisons between variables were performed using the χ^2 test, Fisher's exact test, or Student's t-test. Post-transplant survival (PS) was measured from the date of heart TPL to the date of death from any cause. Survival analysis was performed using the Kaplan-Meier method with the log-rank test. Two-sided p-values < .05 were considered statistically significant.

RESULTS

Patient characteristics

The characteristics of the patients with heart TPL are summarized in Table 1. The median patient age was 54 years, ranging from 6 to 76 years. Among others, the underlying diseases leading to cardiac TPL included dilated cardiomyopathy (CMP; n = 43), ischemic CMP (n = 16), congestive heart failure (n =

Table 1. Patient characteristics

Variable	Value
Age (yr)	47.7 (6–76)
Pediatrics	14 (17.9)
Adult	64 (82.1)
Sex	
Male	59 (75.6)
Female	19 (24.4)
Diagnosis	
CHF	7 (9.0)
Dilated CMP	43 (55.1)
Hypertrophic CMP	1 (1.3)
Ischemic CMP	16 (20.5)
Restrictive CMP	2 (2.5)
Valvulopathy	2 (2.5)
Amyloidosis	4 (5.2)
Myocarditis	1 (1.3)
Endocarditis	1 (1.3)
Heart anomaly	1 (1.3)
Smoking	
Never	53 (67.9)
Ever	25 (32.1)
Diabetes mellitus	
Absent	55 (70.5)
Present	23 (29.5)
Ventilator	
Not applied	76 (97.5)
Applied	2 (2.5)
BMI (kg/m^2)	20.9 (11.3–37.8)
Pre-operative EF (%)	25.3 (12–77)
Post-operative EF (%)	63.9 (49–77)
Ischemic time (min)	182.9 (59–283)
Pulmonary artery pressure (mmHg)	47.1 (25–84)

Values are presented as mean (range) or number (%).
CHF, chronic heart failure; CMP, cardiomyopathy; BMI, body mass index; EF, ejection fraction.

7), and amyloidosis (n = 4). The body mass index was 20.9 ± 4.1 (mean ± standard deviation [SD]), and 23 patients (29.5%) exhibited diabetes mellitus. A ventilator was applied to two patients before heart TPL. The ejection fraction measured 25.3 ± 12.1 and 63.9 ± 6.6 before and after heart TPL, respectively. Total ischemic time and the pulmonary artery pressure before heart TPL were 182.9 ± 56.5 minutes and 47.1 ± 14.1 mmHg, respectively. The median follow-up duration for all patients was 124.5 months.

Correlation between ACR and clinical features

EMB histopathological evaluation revealed ACR grade 0R, 1R, 2R, and 3R in 25 (32.0%), 37 (47.4%), 12 (15.5%), and four (5.1%) of the 78 patients with heart TPL, respectively. ACR of ≥grade 2R was observed in 20.6% (16/78) of the patients during the follow-up period. The correlations between the clinical features of the patients and a high-grade ACR are summarized in Table 2. No clinical factors were significantly associated with high-grade ACR in patients with cardiac TPL.

Analysis of PD-L1 expression and PD-1$^+$, CD4$^+$, and CD8$^+$ lymphocytes according to ACR status

Representative IHC images of PD-L1, PD-1, CD4, and CD8 in EMBs are displayed in Fig. 1. PD-L1–expressing cells in cardiac allografts were mostly macrophages or endothelial cells at the immune cell infiltration site in the myocardium. Additionally, PD-L1 expression has been occasionally observed in cardiomyocytes. Overall, PD-L1 expression in cardiac allografts was positive in 25.6% (20/78) of patients with heart TPL. The number of PD-1$^+$, CD4$^+$, and CD8$^+$ cells per HPF, evaluated in 39 of the 78 patients, excluding those with ACR grade 0R, was 18.5 ± 33.3, 116.4 ± 117.8, and 105.2 ± 89.2 (mean ± SD), respectively.

The correlations between high-grade ACR and pathological features, including PD-L1 expression and lymphocyte infiltration, are summarized in Table 2. EMB tissues with high-grade ACR tended to be infiltrated by higher numbers of CD4$^+$ and CD8$^+$ lymphocytes. Notably, patients with high-grade ACR exhibited significantly higher PD-L1 expression than did those without high-grade ACR (62.5% vs. 16.1%, p < .001).

The correlations between PD-L1 expression and the clinicopathological features of patients with heart TPL are summarized in Table 3. There was no significant association between PD-L1 expression and clinical features. Conversely, EMB tissues with PD-L1 positivity were infiltrated with a higher number of CD4$^+$ and CD8$^+$ lymphocytes (p = .025 and p = .059, respectively) (Table 3). Moreover, the number of PD-1$^+$ lymphocytes was higher in the PD-L1–positive group (35.6 ± 58.7) than in the PD-L1–negative group (14.8 ± 24.7), but did not reach statistical significance (p = .390) (Table 3). These findings suggest that the PD-1/PD-L1 pathway may be involved in ACR in human heart transplants.

PD-L1 expression evaluation in serial EMBs with ACR in heart TPL

Serial EMB samples from patients who developed ACR of more than grade 2R on follow-up were available in 13 patients (Table 4). In six patients, the H-score of PD-L1 expression in EMBs increased in cardiac allografts after developing high-grade ACR compared to that in previous EMB tissues without high-grade ACR (Fig. 2). Conversely, five cases demonstrated no PD-L1 H-score differences in EMBs taken at the time without high-grade ACR and at the time of high-grade ACR, and two cases revealed a slight decrease in the PD-L1 H-scores in EMBs with high-grade ACR compared to previous EMBs without ACR. Overall, PD-L1 expression levels significantly increased in EMBs with high-grade ACR compared with previous EMBs without ACR (p =.001) (Fig. 2) and subsequently decreased in follow-up EMBs after ACR subsided (Fig. 2).

Prognostic significance of PD-1/PD-L1 pathway status in heart TPL

Univariate survival analysis revealed that no clinical factors were associated with survival in patients with heart TPL. The episodes of high-grade ACR, PD-L1 expression, and the number of PD-1$^+$, CD4$^+$, or CD8$^+$ lymphocytes in the EMB tissues were not associated with PS (Fig. 3).

DISCUSSION

To the best of our knowledge, this is the first study in East Asia to examine PD-1 and PD-L1 expression in EMBs from heart transplant recipients, including one of the largest cohorts (78 patients) reported to date on this topic [17,18,25]. PD-L1 was significantly upregulated in human cardiac allografts during high-grade ACR, with a concomitant increase in PD-1-positive T lymphocyte infiltration, thereby suggesting that the PD-1/PD-L1 immune checkpoint pathway is actively involved in T-cell-mediated rejection regulation during heart TPL. In addition to prior work conducted primarily in non–East Asian populations [17,18,25], our study provides additional data on

https://doi.org/10.4132/jptm.2026.01.02

Table 2. Correlations between acute cellular rejection and clinical and pathological features including PD-1/PD-L1 status

	High-grade acute cellular rejection[a]		
	Absent (n = 62)	Present (n = 16)	p-value
Age (yr)			
<60	38 (77.6)	11 (22.4)	.773
≥60	24 (82.8)	5 (17.2)	
Sex			
Male	48 (81.4)	11 (18.6)	.520
Female	14 (73.7)	5 (26.3)	
CAD			
Absent	50 (79.4)	13 (20.6)	>.99
Present	12 (80.0)	3 (20.0)	
Diabetes			
Absent	45 (81.8)	10 (18.2)	.540
Present	17 (73.9)	6 (26.1)	
Hypertension			
Absent	45 (76.3)	14 (23.7)	.330
Present	17 (89.5)	2 (10.5)	
Smoking			
Never	43 (81.1)	10 (18.9)	.873
Ever	19 (76.0)	6 (24.0)	
Ventilator			
Not applied	60 (78.9)	16 (21.1)	.334
Applied	2 (100)	0	
Dialysis			
Never	52 (77.6)	15 (22.4)	.273
Ever	10 (90.9)	1 (9.1)	
Body mass index (kg/m^2)	21.0 ± 4.1	20.7 ± 4.2	.828
Preoperative EF (%)	25.5 ± 12.6	24.5 ± 10.3	.764
Postoperative EF (%)	64.1 ± 6.4	62.9 ± 7.5	.548
Ischemic time (min)	184.2 ± 58.7	177.6 ± 48.6	.719
Pulmonary artery pressure (mmHg)	46.4 ± 14.4	50.6 ± 12.8	.379
Post-transplant survival (mo)	32.6 ± 20.0	34.0 ± 19.4	.806
PD-L1 expression			
Negative	52 (89.7)	6 (10.3)	<.001
Positive	10 (50.0)	10 (50.0)	
PD-1+ lymphocytes (number/HPF)	11.3 ± 20.5	31.3 ± 46.7	.148
CD8+ lymphocytes (number/HPF)	89.8 ± 78.3	129.8 ± 102.3	.175
CD4+ lymphocytes (number/HPF)	82.7 ± 72.4	170.5 ± 154.9	.054

Values are presented as number (%) or mean ± SD.
PD-1, programmed cell death-1; PD-L1, programmed death-ligand 1; CAD, coronary artery disease; EF, ejection fraction; HPF, high power field; SD, standard deviation.
[a]Cases with International Society for Heart and Lung Transplantation (ISHLT) grade 2R and 3R were considered to have high-grade acute cellular rejection.

PD-1/PD-L1 expression in an East Asian heart transplant cohort, including recipients with serially evaluated endomyocardial biopsies.

This observation is consistent with evidence from various experimental models demonstrating that the PD-1/PD-L1 axis is crucial for dampening alloimmune injury [13–16]. In murine transplant models, the absence of PD-1 or PD-L1 accelerates cardiac allograft rejection and severe myocarditis, demonstrat-

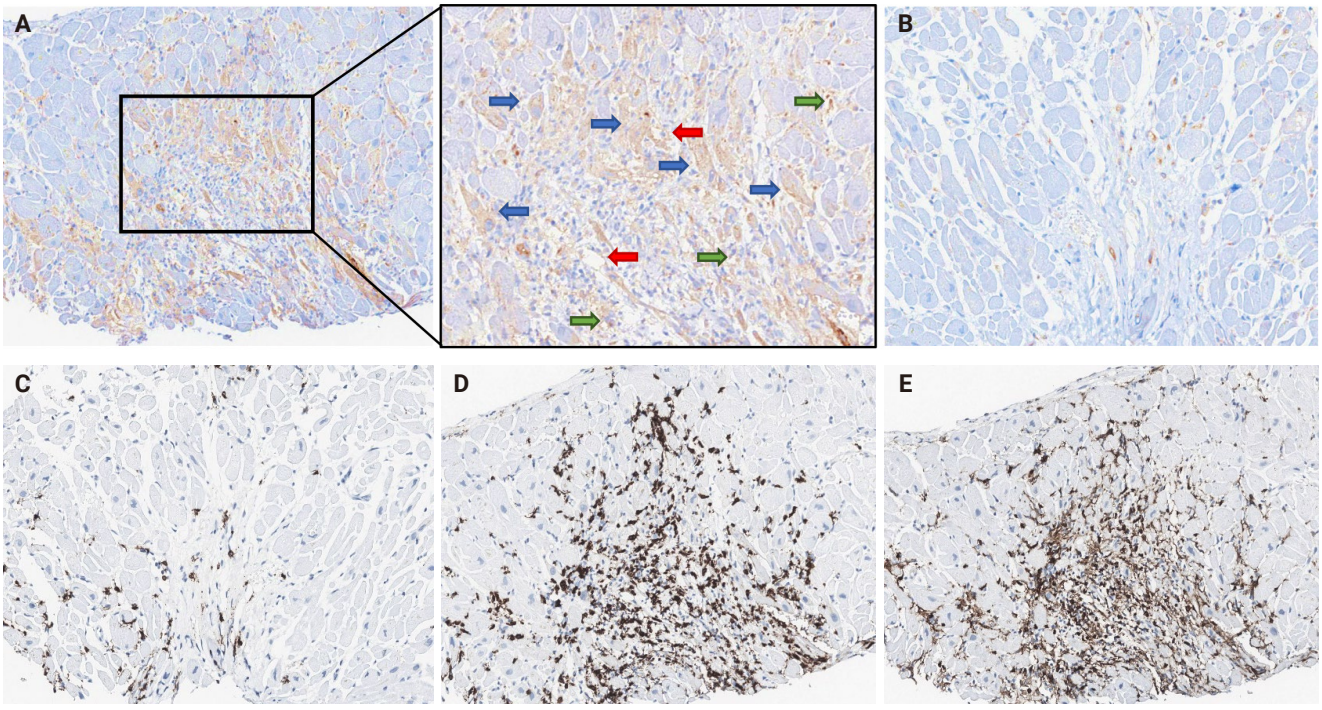

Fig. 1. Representative immunohistochemical staining for programmed death-ligand 1 (PD-L1), programmed cell death-1 (PD-1), CD8, and CD4 in endomyocardial biopsies after heart transplantation. (A) PD-L1–positive allograft showing membranous and cytoplasmic PD-L1 expression in cardiomyocytes (blue arrows), infiltrating immune cells (green arrows), and vascular endothelial cells (red arrows) in a biopsy with acute cellular rejection. The panel on the right is a higher-magnification view of the boxed area. (B) PD-L1–negative allograft with minimal PD-L1 staining. (C–E) Serial sections from a rejection biopsy demonstrating infiltrating PD-1$^+$ lymphocytes (C), CD8$^+$ T cells (D), and CD4$^+$ T cells (E).

ing the important role of this pathway in maintaining peripheral tolerance [15,16,21]. Specifically, donor tissue-derived PD-L1 has been identified as a key mediator of graft acceptance, and cardiac allografts in mice lacking PD-L1 on the parenchymal cells, or specifically on the endothelium, experience more aggressive T-cell infiltration and damage [16,21]. Moreover, pro-inflammatory cytokines, such as interferon-γ, can strongly induce PD-L1 on graft cells, suggesting that the alloimmune response itself induces this protective checkpoint upregulation [16]. Accordingly, PD-1 signaling blockade exacerbates rejection in animal models, while augmenting the pathway (e.g., with PD-L1.Ig fusion proteins) leads to graft protection and prolonged graft survival [19,20]. Collectively, these preclinical findings support our human data and indicate that PD-L1 induction in cardiac allografts functions as a counter-regulatory mechanism to mitigate acute cellular rejection.

Unlike most previous studies that analyzed cross-sectional biopsy samples, our study evaluated serial EMBs from individual patients before, during, and after rejection episodes. This longitudinal approach revealed that PD-L1 expression was dynamically upregulated in allograft tissues early in high-grade ACR development and declined after the rejection resolution, paralleling PD-1 T-cell infiltration changes. Therefore, PD-L1 overexpression may be a transient adaptive mechanism that suppresses T-cell-mediated tissue injury. Consistently, Choudhary et al. [18] reported that PD-L1 expression in transplanted hearts correlated with rejection severity and decreased after successful anti-rejection therapy. Furthermore, Peyster et al. [17] found that patients who never experienced rejection had higher baseline proportions of PD-L1$^+$ and FoxP3$^+$ cells in their allografts than did those who developed ACR. Collectively, these studies support the concept that PD-L1 contributes to an immune-tolerant graft microenvironment, whereas diminished PD-L1 expression may predispose patients to rejection.

Another unique aspect of our study is the compartmental analysis of PD-L1 expression within the allograft and the quantitative assessment of PD-L1 on graft cardiomyocytes, endothelial cells, and infiltrating immune cells. Through this

https://doi.org/10.4132/jptm.2026.01.02

Table 3. Correlations between PD-L1 expression status and clinicopathological features

	PD-L1 expression		
	Absent (n = 58)	Present (n = 20)	p-value
Age (yr)			
<60	35 (71.4)	14 (28.6)	.593
≥60	23 (79.3)	6 (20.7)	
Sex			
Male	47 (79.7)	12 (20.3)	.074
Female	11 (57.9)	8 (42.1)	
CAD			
Absent	49 (77.8)	14 (22.2)	.192
Present	9 (60.0)	6 (40.0)	
Diabetes			
Absent	43 (78.2)	12 (21.8)	.263
Present	15 (65.2)	8 (34.8)	
Hypertension			
Absent	42 (71.2)	17 (28.8)	.369
Present	16 (84.2)	3 (15.8)	
Smoking			
Never	41 (77.4)	12 (22.6)	.488
Ever	17 (68.0)	8 (32.0)	
Ventilator			
Not applied	56 (73.7)	20 (26.3)	.273
Applied	2 (100)	0	
Dialysis			
Never	50 (74.6)	17 (25.4)	.894
Ever	8 (72.7)	3 (27.3)	
Body mass index (kg/m^2)	21.1 ± 4.0	20.1 ± 4.9	.480
Preoperative EF (%)	25.9 ± 12.5	21.4 ± 8.8	.282
Postoperative EF (%)	63.7 ± 6.8	65.3 ± 4.9	.521
Ischemic time (min)	183.9 ± 55.8	176.9 ± 63.7	.733
Pulmonary artery pressure (mmHg)	46.0 ± 13.7	57.2 ± 14.5	.066
Post-transplant survival (mo)	31.5 ± 19.2	42.4 ± 22.1	.104
PD-1+ lymphocytes (number/HPF)	14.8 ± 24.7	35.6 ± 58.7	.390
CD8+ lymphocytes (number/HPF)	91.6 ± 76.4	158.0 ± 119.2	.059
CD4+ lymphocytes (number/HPF)	95.3 ± 105.2	198.4 ± 135.4	.025

Values are presented as number (%) or mean ± SD.
PD-L1, programmed death-ligand 1; CAD, coronary artery disease; EF, ejection fraction; HPF, high power field; SD, standard deviation.

comprehensive approach, we found that all three compartments upregulated PD-L1 during ACR, reflecting a concerted multicellular checkpoint response within the cardiac graft, which is consistent with the findings of Bracamonte-Baran et al. [25], who demonstrated that PD-L1 expression in non-hematopoietic cardiac cells (particularly in the endothelium) is crucial for modulating T cell infiltration in heart transplants. In their study, higher PD-L1 levels in graft endothelial cells were associated with significantly reduced CD8$^+$ T-cell infiltrates, whereas endothelial PD-L1 loss was associated with dense CD8$^+$ T-cell infiltration and more severe rejection. Furthermore, in a mouse model, they demonstrated that the lack of PD-L1 in cardiac endothelial cells led to accelerated rejection, implicating graft-expressed PD-L1 in the protection against alloimmune injury. These results reinforce our human data and earlier murine evidence, underscoring the fact that PD-L1 upregulation

Table 4. Changes of PD-L1 expression and ACR grade in serial biopsies of 13 heart transplant patients

Patient No.	Prior rejection	Rejection	Post-rejection
1			
ACR grade	0R	2R	0R
PD-L1 H-score	0	14	0
2			
ACR grade	1R	2R	1R
PD-L1 H-score	0	0	0
3			
ACR grade	0R	2R	0R
PD-L1 H-score	0	0	0
4			
ACR grade	0R	2R	0R
PD-L1 H-score	0	5	0
5			
ACR grade	0R	2R	0R
PD-L1 H-score	0	5	0
6			
ACR grade	0R	3R	0R
PD-L1 H-score	5	50	0
7			
ACR grade	0R	2R	0R
PD-L1 H-score	2	0	0
8			
ACR grade	0R	2R	0R
PD-L1 H-score	0	6	0
9			
ACR grade	1R	2R	1R
PD-L1 H-score	5	2	0
10			
ACR grade	1R	2R	1R
PD-L1 H-score	0	0	0
11			
ACR grade	2R	3R	0R
PD-L1 H-score	3	15	0
12			
ACR grade	0R	2R	2R
PD-L1 H-score	0	0	0
13			
ACR grade	1R	3R	2R
PD-L1 H-score	0	0	0

PD-L1, programmed death-ligand 1; ACR, acute cellular rejection; H-score, histochemical score.

by grafted parenchymal cells actively suppresses alloreactive T cells. Variability in the dominant site of PD-L1 expression (endothelial vs. parenchymal) may explain differences in graft resilience to immune attacks.

Despite the overall trend of PD-L1 induction in rejection, we observed heterogeneity. Among the 13 patients with serial EMBs available, seven (five with no change and two with a slight decrease) did not exhibit appreciable PD-L1 upregulation at the time of high-grade ACR compared with their prior EMBs. Notably, all these patients still responded to anti-rejection therapy and survived the episode, indicating that the absence of PD-L1 upregulation did not preclude successful rejection control. Therefore, when the PD-1/PD-L1 axis is not engaged, alternative immune-regulatory pathways may compensate; conversely, in some fulminant rejections, the immune response may outpace PD-L1 induction. Indeed, prior transplant biopsy analyses have reported that although PD-L1 is frequently induced during rejection, its presence alone is not always sufficient to prevent ongoing tissue damage [16,18]. Thus, PD-L1 likely functions as a multiple redundant checkpoint that collectively modulates alloimmunity [23], implying that other co-inhibitory receptors (e.g., cytotoxic T-lymphocyte–associated protein 4, T-cell Immunoglobulin and Mucin-domain containing protein 3, and lymphocyte-activation gene 3) may be concurrently involved in restraining rejection, especially in cases where PD-L1 expression remains low [23]. Our results underscore this immune heterogeneity and the need to explore additional inhibitory pathways in transplant rejection, as the therapeutic targeting of PD-1/PD-L1 alone may not uniformly prevent rejection in all settings.

In addition to this heterogeneity within cellular rejection, another important consideration is antibody-mediated rejection (AMR), which was beyond the scope of the present analysis. In the present study, we focused on T cell–mediated acute cellular rejection and did not specifically evaluate pathological or serological features of AMR. To our knowledge, human data directly linking PD-L1 expression to AMR in heart TPL are extremely limited. A small single-center pilot study that analyzed PD-L1 expression in endomyocardial biopsies from patients with AMR, ACR, and no rejection did not find a clear difference in PD-L1 levels between rejection types, although cases with overlapping AMR and ACR showed higher PD-L1 expression and tended to exhibit faster histological resolution of rejection [26]. These preliminary observations, together with prior work mainly focused on cellular rejection and chronic allograft injury, underline the need for future studies that integrate PD-L1 assessment with detailed AMR phenotyping to clarify whether PD-L1 plays a distinct role in humoral rejection.

https://doi.org/10.4132/jptm.2026.01.02

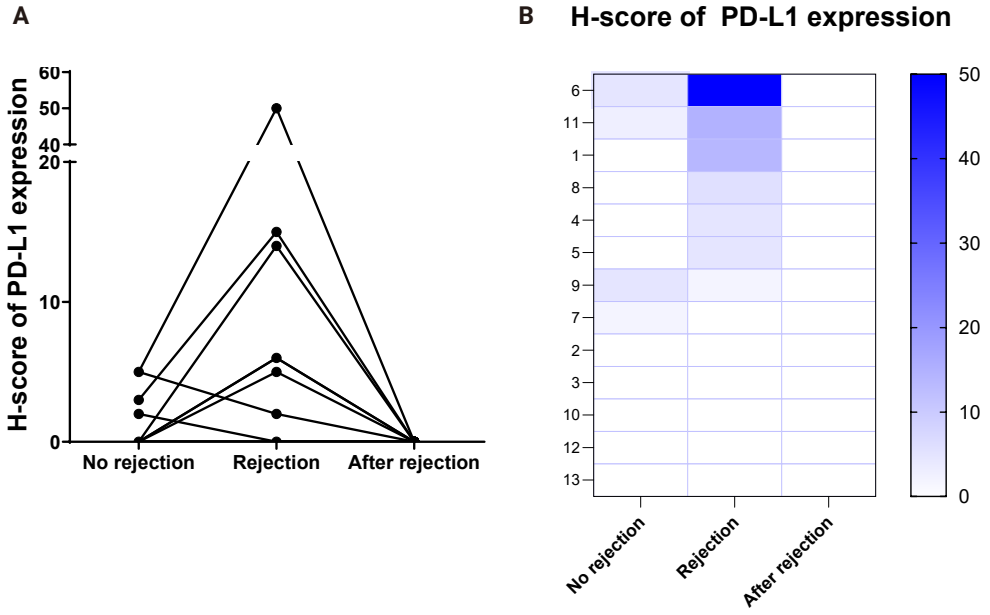

Fig. 2. Changes in programmed death-ligand 1 (PD-L1) expression in serial endomyocardial biopsy samples from heart transplant recipients obtained before rejection, during high-grade acute cellular rejection, and after rejection subsided. (A) Line plot of PD-L1 H-scores in 13 recipients with paired serial biopsies; each line represents an individual patient. (B) Heatmap of PD-L1 H-scores across the same three biopsy categories (no rejection, rejection, and after rejection).

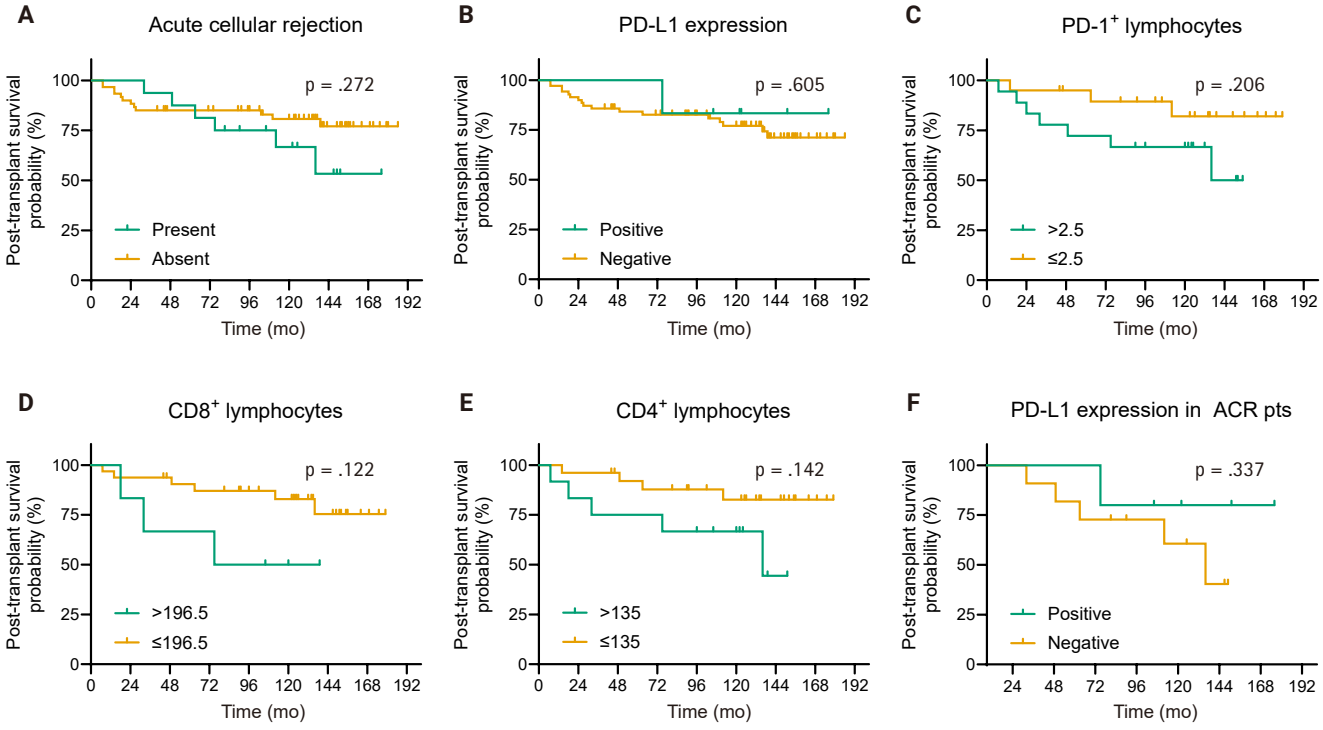

Fig. 3. Kaplan-Meier plots using the log-rank test for post-transplant survival in heart transplant recipients, according to high-grade acute cellular rejection (ACR) (A); programmed death-ligand 1 (PD-L1) expression (B); and the numbers of programmed cell death-1 (PD-1)$^+$ (C), CD8$^+$ (D), or CD4$^+$ (E) lymphocytes. (F) Among patients with high-grade ACR, survival was compared according to PD-L1 expression status.

Additional limitations of our study should be acknowledged. In this study, immunostaining for PD-1, CD4, and CD8 was restricted to EMBs with ACR grade ≥1R. Consequently, we could not systematically quantify low-level baseline immune cell infiltration in grade 0R allografts, and future work incorporating these markers across all rejection grades, including 0R, will be needed to more fully define the spectrum of immune activation within the cardiac allograft.

These findings carry potential clinical implications for graft monitoring and risk stratification. As PD-L1 expression in allografts correlates closely with rejection activity, it could be investigated as a biomarker to aid in ACR diagnosis or prediction. For instance, Novysedlak et al. [27] found that PD-L1 (combined with platelet endothelial cell adhesion molecule-1) was significantly elevated in lung transplant biopsies with ACR and proposed PD-L1 as a useful diagnostic marker for rejection. Similarly, in heart TPL, tracking PD-L1 levels in protocol biopsies or even non-invasively via novel imaging modalities might help identify patients at a higher rejection risk [28,29]. A graft that fails to upregulate PD-L1 in the face of immune stress or exhibits a PD-L1 expression abrupt decline may be more susceptible to uncontrolled T-cell attack. This notion is corroborated by the observation that patients whose allografts eventually experienced rejection tended to have lower baseline PD-L1+ cell fractions and more pronounced $CD8^+$ T cell infiltrates, whereas grafts maintaining high PD-L1 and plentiful regulatory immune cells were more likely to remain quiescent [17]. Incorporating PD-L1 assessment, potentially alongside other immunoregulatory markers such as FoxP3, into post-transplant surveillance may enhance subclinical rejection detection and predict which patients are at the greatest risk for severe ACR. The PD-L1 expression increase observed during ACR may represent a compensatory immunoregulatory response designed to attenuate tissue-damaging lymphocyte activity, highlighting its biological importance.

In our cohort with long-term follow-up (median 124.5 months), neither high-grade ACR, PD-L1 expression status, nor the densities of $PD\text{-}1^+$, $CD8^+$, or $CD4^+$ lymphocytes were significantly associated with all-cause post-TPL survival, indicating that even after more than a decade of observation, these immunological markers did not predict long-term outcomes; specifically, their expression patterns likely reflect active immune regulation during acute rejection rather than survival determinants. The absence of an association may reflect the effective rescue of rejection episodes with immunosuppression, mitigating long-term effects, and the influence of other factors, such as cardiac allograft vasculopathy and infection, may outweigh the contribution of PD-L1–related immune regulation. Taken together, these findings suggest that PD-L1 expression should be interpreted primarily as a marker of ongoing immunological counterresponses rather than as a prognostic biomarker for graft survival.

On the therapeutic front, our data and recent studies provide a rationale for targeting the PD-1/PD-L1 pathway to promote transplant tolerance [23,30]. Augmenting this checkpoint—for example, using PD-1 agonists or strategies to boost PD-L1 expression in the graft—could reinforce the inherent protection of the allograft against T-cell attacks. Experimental approaches, such as PD-L1.Ig fusion proteins (soluble PD-1 agonists), have already prolonged cardiac allograft survival in preclinical models [19], and methods to increase PD-L1 expression in donor tissues via gene therapy or pharmacologic induction are being explored [30]. Any such intervention must be balanced against risks of oversuppression of the immune system (e.g., infection or malignancy). Our findings highlight a cautionary note: therapeutic blockade of the PD-1/PD-L1 axis, as employed in cancer immunotherapy, may precipitate rejection in transplant recipients. Indeed, documented cases demonstrate abrupt acute rejection of transplanted organs in patients receiving PD-1 inhibitors for malignancy [22,31]; moreover, a recent pharmacovigilance analysis further underscored this risk, reporting a high incidence of allograft rejection following checkpoint inhibitor therapy [32]. Collectively, these observations indicate that intact PD-1/PD-L1 signaling is critical for maintaining immune tolerance to transplanted organs in humans, because disrupting this pathway can unleash alloreactive T-cell responses and precipitate rejection [22]. Thus, while modulating the PD-1/PD-L1 pathway offers promising opportunities to improve graft outcomes, caution is warranted in transplant patients.

Ultimately, elucidating the patterns and effects of PD-1/PD-L1 signaling in heart transplantation provides a foundation for improved rejection monitoring and the development of targeted immunotherapies that enhance graft tolerance without undue risk.

Ethics Statement

This study was performed according to the recommendations of the World Medical Association Declaration of Helsinki and was approved by the Institutional Review Board of SNUH (IRB

https://doi.org/10.4132/jptm.2026.01.02

No. H-1412-106-634). Formal written informed consent was not required with a waiver by the appropriate IRB and/or national research ethics committee.

Availability of Data and Material

The datasets generated and analyzed during the current study are not publicly available due to ethical and privacy restrictions (they contain information that could compromise participant confidentiality), but are available from the corresponding author upon reasonable request and with appropriate institutional approval.

Code Availability

Not applicable.

ORCID

Jeemin Yim https://orcid.org/0000-0002-8571-7486
Yoon Kyung Jeon https://orcid.org/0000-0001-8466-9681
Doo Hyun Chung https://orcid.org/0000-0002-9948-8485
Jaemoon Koh https://orcid.org/0000-0002-2824-5080

Author Contributions

Conceptualization: JK, DHC, YKJ. Data curation: JK. Formal analysis: JK, JY. Investigation: JY, JK. Methodology: JK. Project administration: JK. Resources: JK, DHC, YKJ. Supervision: JK, DHC, YKJ. Validation: JY, JK. Visualization: JY, JK. Writing—original draft: JY, JK. Writing—review & editing: JK, JY, YKJ, DHC. Approval of final manuscript: all authors

Conflicts of Interest

The authors declare that they have no potential conflicts of interest.

Funding Statement

This research was supported by grants of the Korea Health Technology R&D Project through the Korea Health Industry Development Institute (KHIDI), funded by the Ministry of Health and Welfare, Republic of Korea (RS-2024-00409089).

REFERENCES

1. de Jonge N, Kirkels JH, Klopping C, et al. Guidelines for heart transplantation. Neth Heart J 2008; 16: 79-87.
2. Lund LH, Edwards LB, Kucheryavaya AY, et al. The registry of the International Society for Heart and Lung Transplantation: thirty-first official adult heart transplant report--2014; focus theme: retransplantation. J Heart Lung Transplant 2014; 33: 996-1008.
3. Soderlund C, Ohman J, Nilsson J, et al. Acute cellular rejection the first year after heart transplantation and its impact on survival: a single-centre retrospective study at Skane University Hospital in Lund 1988-2010. Transpl Int 2014; 27: 482-92.
4. Sinphurmsukskul S, Ariyachaipanich A, Siwamogsatham S, et al. Endomyocardial biopsy and prevalence of acute cellular rejection in heart transplantation. Transplant Proc 2021; 53: 318-23.
5. Velleca A, Shullo MA, Dhital K, et al. The International Society for Heart and Lung Transplantation (ISHLT) guidelines for the care of heart transplant recipients. J Heart Lung Transplant 2023; 42: e1-141.
6. Patel JK, Kobashigawa JA. Should we be doing routine biopsy after heart transplantation in a new era of anti-rejection? Curr Opin Cardiol 2006; 21: 127-31.
7. Billingham ME. Endomyocardial biopsy diagnosis of acute rejection in cardiac allografts. Prog Cardiovasc Dis 1990; 33: 11-8.
8. Stewart S, Winters GL, Fishbein MC, et al. Revision of the 1990 working formulation for the standardization of nomenclature in the diagnosis of heart rejection. J Heart Lung Transplant 2005; 24: 1710-20.
9. Francisco LM, Sage PT, Sharpe AH. The PD-1 pathway in tolerance and autoimmunity. Immunol Rev 2010; 236: 219-42.
10. Li XC, Rothstein DM, Sayegh MH. Costimulatory pathways in transplantation: challenges and new developments. Immunol Rev 2009; 229: 271-93.
11. Ito T, Ueno T, Clarkson MR, et al. Analysis of the role of negative T cell costimulatory pathways in CD4 and CD8 T cell-mediated alloimmune responses in vivo. J Immunol 2005; 174: 6648-56.
12. Zou W, Wolchok JD, Chen L. PD-L1 (B7-H1) and PD-1 pathway blockade for cancer therapy: mechanisms, response biomarkers, and combinations. Sci Transl Med 2016; 8: 328rv4.
13. Sandner SE, Clarkson MR, Salama AD, et al. Role of the programmed death-1 pathway in regulation of alloimmune responses in vivo. J Immunol 2005; 174: 3408-15.
14. Ma D, Duan W, Li Y, et al. PD-L1 deficiency within islets reduces allograft survival in mice. PLoS One 2016; 11: e0152087.
15. Riella LV, Watanabe T, Sage PT, et al. Essential role of PDL1 expression on nonhematopoietic donor cells in acquired tolerance to vascularized cardiac allografts. Am J Transplant 2011; 11: 832-40.
16. Grabie N, Gotsman I, DaCosta R, et al. Endothelial programmed death-1 ligand 1 (PD-L1) regulates $CD8^+$ T-cell mediated injury in the heart. Circulation 2007; 116: 2062-71.

17. Peyster EG, Wang C, Ishola F, et al. In situ immune profiling of heart transplant biopsies improves diagnostic accuracy and rejection risk stratification. JACC Basic Transl Sci 2020; 5: 328-40.
18. Choudhary A, Brinkley DM, Besharati S, et al. PD-L1 (programmed death ligand 1) as a marker of acute cellular rejection after heart transplantation. Circ Heart Fail 2021; 14: e008563.
19. Dudler J, Li J, Pagnotta M, Pascual M, von Segesser LK, Vassalli G. Gene transfer of programmed death ligand-1.Ig prolongs cardiac allograft survival. Transplantation 2006; 82: 1733-7.
20. Ozkaynak E, Wang L, Goodearl A, et al. Programmed death-1 targeting can promote allograft survival. J Immunol 2002; 169: 6546-53.
21. Wang J, Okazaki I, Yoshida T, et al. PD-1 deficiency results in the development of fatal myocarditis in MRL mice. Int Immunol 2010; 22: 443-52.
22. Lipson EJ, Bagnasco SM, Moore JJ, et al. Tumor regression and allograft rejection after administration of anti-PD-1. N Engl J Med 2016; 374: 896-8.
23. Del Bello A, Treiner E. Immune checkpoints in solid organ transplantation. Biology (Basel) 2023; 12: 1358.
24. Riella LV, Paterson AM, Sharpe AH, Chandraker A. Role of the PD-1 pathway in the immune response. Am J Transplant 2012; 12: 2575-87.
25. Bracamonte-Baran W, Gilotra NA, Won T, et al. Endothelial stromal PD-L1 (programmed death ligand 1) modulates CD8(+) T-cell infiltration after heart transplantation. Circ Heart Fail 2021; 14: e007982.
26. Szymanska S, Sobieszczanska-Malek M, Wieckowska-Karkucinska A, Grajkowska W. Tissue expression of ligand to programmed death receptor 1 (PD-L1) in endomyocardial biopsies of patients after heart transplantation: association with allograft rejection, pilot study. World J Surg Surgical Res 2021; 4: 1350.
27. Novysedlak R, Balko J, Tavandzis J, et al. Elevated PD-L1 and PECAM-1 as diagnostic biomarkers of acute rejection in lung transplantation. Transpl Int 2024; 37: 13796.
28. Malih S, Lin W, Tang Z, et al. Noninvasive PET imaging of tumor PD-L1 expression with (64)Cu-labeled Durvalumab. Am J Nucl Med Mol Imaging 2024; 14: 31-40.
29. Niemeijer AN, Leung D, Huisman MC, et al. Whole body PD-1 and PD-L1 positron emission tomography in patients with non-small-cell lung cancer. Nat Commun 2018; 9: 4664.
30. Handelsman S, Overbey J, Chen K, Lee J, Haj D, Li Y. PD-L1's role in preventing alloreactive T cell responses following hematopoietic and organ transplant. Cells 2023; 12: 1609.
31. Owonikoko TK, Kumar M, Yang S, et al. Cardiac allograft rejection as a complication of PD-1 checkpoint blockade for cancer immunotherapy: a case report. Cancer Immunol Immunother 2017; 66: 45-50.
32. Cui X, Yan C, Xu Y, et al. Allograft rejection following immune checkpoint inhibitors in solid organ transplant recipients: a safety analysis from a literature review and a pharmacovigilance system. Cancer Med 2023; 12: 5181-94.

https://doi.org/10.4132/jptm.2026.01.02

JPTM

ORIGINAL ARTICLE

pISSN 2383-7837 · eISSN 2383-7845

Journal of Pathology and Translational Medicine 2026; 60: 331-337
https://doi.org/10.4132/jptm.2026.01.08

HER2-low and ultralow breast cancer: interobserver challenges and lessons from a consensus study

Jiwon Koh[1], Yoon Jin Cha[2], Eun Yoon Cho[3], Ahwon Lee[4], Ja Seung Koo[5], So Yeon Park[6], Min Hwan Kim[7], Jae Ho Jeong[8], Gyungyub Gong[9]

[1]Department of Pathology, Seoul National University Hospital, Seoul National University College of Medicine, Seoul, Korea
[2]Department of Pathology, Gangnam Severance Hospital, Yonsei University College of Medicine, Seoul, Korea
[3]Department of Pathology and Translational Genomics, Samsung Medical Center, Sungkyunkwan University School of Medicine, Seoul, Korea
[4]Department of Hospital Pathology, Seoul St. Mary's Hospital, College of Medicine, The Catholic University of Korea, Seoul, Korea
[5]Department of Pathology, Yonsei University College of Medicine, Seoul, Korea
[6]Department of Pathology, Seoul National University Bundang Hospital, Seoul National University College of Medicine, Seongnam, Korea
[7]Division of Medical Oncology, Department of Internal Medicine, Yonsei Cancer Center, Yonsei University College of Medicine, Seoul, Korea
[8]Department of Oncology, Asan Medical Center, University of Ulsan College of Medicine, Seoul, Korea
[9]Department of Pathology, Asan Medical Center, University of Ulsan College of Medicine, Seoul, Korea

Graphical abstract

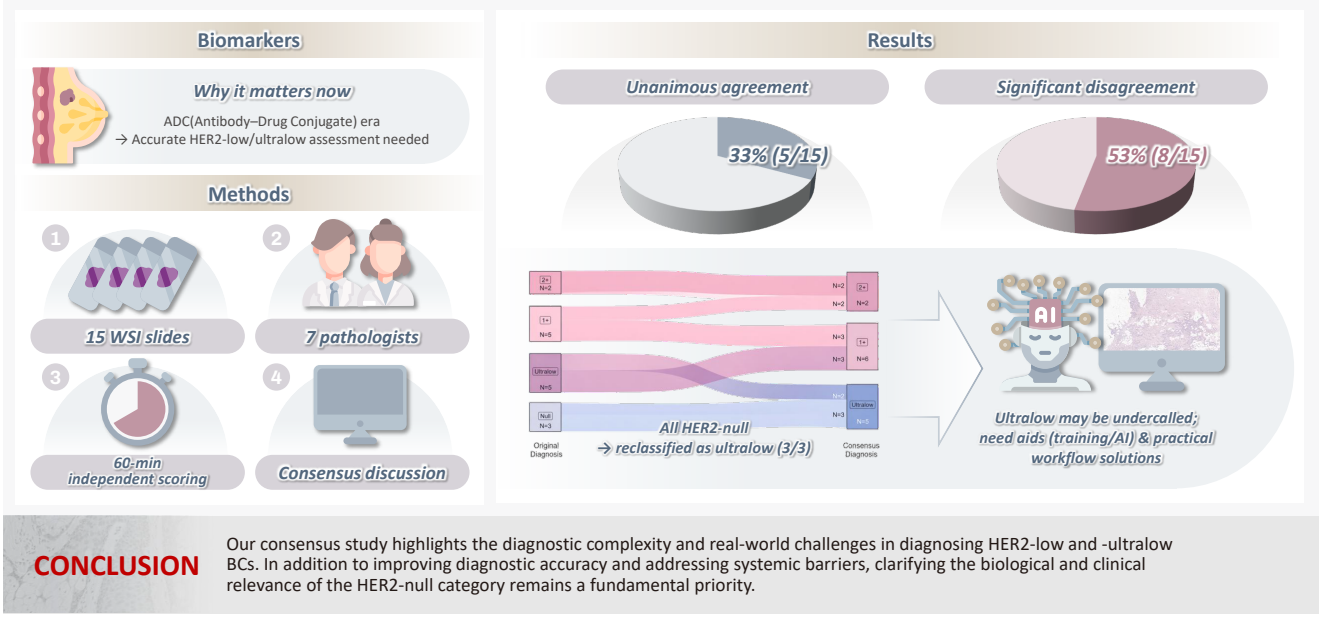

JPTM

ORIGINAL ARTICLE

pISSN 2383-7837 · eISSN 2383-7845

Journal of Pathology and Translational Medicine 2026; 60: 331-337
https://doi.org/10.4132/jptm.2026.01.08

HER2-low and ultralow breast cancer: interobserver challenges and lessons from a consensus study

Jiwon Koh[1], Yoon Jin Cha[2], Eun Yoon Cho[3], Ahwon Lee[4], Ja Seung Koo[5], So Yeon Park[6], Min Hwan Kim[7], Jae Ho Jeong[8], Gyungyub Gong[9]

[1]Department of Pathology, Seoul National University Hospital, Seoul National University College of Medicine, Seoul, Korea
[2]Department of Pathology, Gangnam Severance Hospital, Yonsei University College of Medicine, Seoul, Korea
[3]Department of Pathology and Translational Genomics, Samsung Medical Center, Sungkyunkwan University School of Medicine, Seoul, Korea
[4]Department of Hospital Pathology, Seoul St. Mary's Hospital, College of Medicine, The Catholic University of Korea, Seoul, Korea
[5]Department of Pathology, Yonsei University College of Medicine, Seoul, Korea
[6]Department of Pathology, Seoul National University Bundang Hospital, Seoul National University College of Medicine, Seongnam, Korea
[7]Division of Medical Oncology, Department of Internal Medicine, Yonsei Cancer Center, Yonsei University College of Medicine, Seoul, Korea
[8]Department of Oncology, Asan Medical Center, University of Ulsan College of Medicine, Seoul, Korea
[9]Department of Pathology, Asan Medical Center, University of Ulsan College of Medicine, Seoul, Korea

Background: The recent approval of trastuzumab deruxtecan for human epidermal growth factor receptor 2 (HER2)–low and HER2-ultralow breast cancer mandates an adequate assessment of these categories. **Methods:** Seven breast pathologists from the Breast Pathology Study Group of the Korean Society of Pathologists held an on-site expert consensus meeting. Fifteen sets of virtual whole slide images (WSI) of hematoxylin and eosin stain and HER2 immunohistochemistry were provided. The pathologists were given 60 minutes to submit their diagnosis of HER2 expression into null, ultralow, 1+, 2+, or 3+. Afterwards, in-depth discussion and consensus diagnoses were made by real-time visualization of the WSI. **Results:** After the consensus meeting, unanimous 100% agreements were seen only in five (33.3%) of the examined cases, which consisted of three 1+ cases and two 2+ cases. Two cases (13.3%) had mild disagreement, with only one pathologist's disagreement. Of note, eight cases (53.3%) showed significant disagreement, defined by more than two pathologists' disagreement. All HER2-null cases were reclassified as ultralow after consensus review, suggesting potential widespread underclassification of ultralow cases in clinical practice. **Conclusions:** Experts had significant discrepancies in interpreting HER2-low/ultralow status. It is important to assess if the distinction between HER2-low and ultralow is strictly required and if HER2-null breast cancer exists in reality.

Keywords: Breast neoplasms; HER2; Immunohistochemistry; Trastuzumab deruxtecan

INTRODUCTION

Trastuzumab deruxtecan (T-DXd), an antibody drug conjugate (ADC) using human epidermal growth factor receptor 2 (HER2) as the target antigen and topoisomerase I inhibitor as the payload [1], has started a novel therapeutic era with unprecedented prolongation of progression-free survival and overall survival in patients with metastatic HER2-positive breast cancer (BC) [2]. Furthermore, the DESTINY-Breast 04 study proved its efficacy in patients with HER2-low BC [3], which is defined as HER2 immunohistochemistry (IHC) 1+ or HER2 IHC 2+ with a negative result on *HER2* in situ hybridization (ISH). In response to this, the most recent American Society of Clinical Oncology/College of American Pathologists (ASCO/CAP) guideline, released in 2023, recommended that pathologists be aware of the HER2-low, which became an important trial entry marker [4].

Traditionally, BC has been classified as HER2-positive or

Received: December 17, 2025 **Revised:** January 5, 2026 **Accepted:** January 8, 2026
Corresponding Author: Gyungyub Gong, MD, PhD
Department of Pathology, Asan Medical Center, University of Ulsan College of Medicine, 88 Olympicro-43-gil, Songpa-gu, Seoul 05505, Korea
Tel: +82-2-3010-4554, Fax: +82-2-472-7898, E-mail: gygong@amc.seoul.kr

HER2-negative based on IHC and ISH, with HER2-positive tumors defined as IHC 3+ or IHC 2+ with *HER2* gene amplification [4]. Tumors lacking these features have historically been grouped as HER2-negative. More recently, HER2-low BC has been defined as tumors showing IHC 1+ or IHC 2+ with negative ISH results. An even more refined category, termed HER2-ultralow [5], refers to tumors with faint, incomplete membranous HER2 staining in less than 10% of tumor cells, whereas tumors lacking any convincing membranous staining are classified as HER2-null.

More recently, the DESTINY-Breast 06 study demonstrated similar trends in so-called HER2-ultralow BC, which includes BC with faint or barely perceptible membranous expression of HER2 in less than 10% of the tumor cells [5]. During the screening of DESTINY-Breast 06, it is reported that more than 50% of the locally assessed HER2-null BCs were upgraded into HER2-low or -ultralow after the interpretation by the central lab [6]. In addition, several studies reported significant interobserver variations in determining HER2-low or -ultralow BCs by IHC [7-9].

The Breast Pathology Study Group of the Korean Society of Pathologists previously conducted a nationwide study on the status of HER2-low diagnosis in the Republic of Korea to improve the diagnostic accuracy [10]. In line with this, the group held an expert consensus meeting with seven experienced breast pathologists to evaluate the diagnosis of HER2-low and -ultralow BCs. The meeting aimed to assess (1) the degree of interobserver variability among the breast pathologists, (2) the underlying causes of diagnostic discrepancies, and (3) real-world challenges that may arise in daily practice.

MATERIALS AND METHODS

A breast pathologist (J.K.) reviewed the HER2 IHC slides of BC tissue samples from the Department of Pathology, Seoul National University Hospital (SNUH), and selected 15 cases four weeks prior to the consensus meeting. HER2 IHC was performed on formalin-fixed paraffin-embedded tissue sections of 4-μm thickness using the anti-HER2/neu (4B5) rabbit monoclonal antibody and the BenchMark XT automated IHC platform (Ventana Medical Systems, Tucson, AZ, USA). The whole slide images (WSI) files, including hematoxylin and eosin (H&E) stains and HER2 IHC, were digitally scanned at up to 40× magnification using the Leica Aperio GT450 device (Leica, Wetzlar, Germany). The WSIs were then anonymized and downloaded for use on-site at the consensus meeting. Clinicopathological characteristics were obtained retrospectively from medical records and pathology reports. Categorical variables were compared by Fisher's exact test and continuous variables were compared using the Mann-Whitney test.

Seven breast pathologists from the Breast Pathology Study Group of the Korean Society of Pathologists held an on-site expert consensus meeting. Virtual WSI of H&E and HER2 IHC were reviewed individually by each pathologist during the consensus meeting. To minimize technical variability, all participants used the same model of laptop and the same image viewer software (Aperio ImageScope, Leica) under identical viewing conditions. The pathologists were blinded to the clinicopathological information and given 60 minutes to submit their individual diagnoses of HER2 expression, categorized as null, ultralow, 1+, 2+, and 3+. The original diagnoses and expert submissions were then shared and discussed. Mild disagreement was defined as only one pathologist differing from the consensus, and significant disagreement was defined as more than two pathologists disagreeing. An in-depth discussion was led by the moderator (G.G.), during which HER2 IHC WSIs were displayed in real-time on a shared high-resolution display to facilitate group review.

RESULTS

Study samples

The study set included 15 BC samples, of which 12 cases were invasive ductal carcinomas (IDCs). One sample was obtained from a liver metastasis, while the remaining cases were from the breast. There were five core needle biopsies and 10 surgical resection specimens. The distribution of original HER2 IHC diagnosis was as follows: HER2-null in 20.0% (3/15), ultralow in 33.3% (5/15), 1+ in 33.3% (5/15), and 2+ in 13.3% (2/15). The study set did not include any BCs with HER2 3+. Additional clinicopathological details of the study samples are summarized in Table 1.

Overall diagnostic concordance

After the consensus meeting, unanimous 100% agreement among the seven pathologists was observed in only 5 of the 15 examined cases (33.3%), which consisted of three HER2 1+ cases and two 2+ cases (Fig. 1). Two cases (13.3%) showed mild disagreement, and 8 cases (53.3%) showed significant disagreement. No notable differences in clinicopathological characteristics were observed between cases with concordant versus discor-

https://doi.org/10.4132/jptm.2026.01.08

Table 1. Clinicopathological features of the study set

	Concordant cases	Reclassified cases	Total	p-value
Age (yr)	49 (43–71)	48 (40–70)	49 (40–70)	.524
Site				
Primary	6 (85.7)	8 (100)	14 (93.3)	>.99
Metastasis	1 (14.3)	0	1 (6.7)	
Procedure				
Biopsy	3 (42.9)	2 (25.0)	5 (33.3)	.608
Resection	4 (57.1)	6 (75.0)	10 (66.7)	
Subtype				
IDC	5 (71.4)	7 (87.5)	12 (80.0)	.569[a]
ILC	1 (14.3)	0	1 (6.7)	
IDC + ILC	1 (14.3)	0	1 (6.7)	
IMPaC	0	1 (12.5)	1 (6.7)	
Grade				
I	1 (14.3)	0	1 (6.7)	.467[b]
II	6 (85.7)	6 (75.0)	12 (80.0)	
III	0	2 (25.0)	3 (20.0)	
ER				
Positive	6 (85.7)	5 (62.5)	11 (73.3)	.569
Negative	1 (14.3)	3 (37.5)	4 (26.7)	
PR				
Positive	5 (71.4)	4 (50.0)	9 (60.0)	.608
Negative	2 (28.6)	4 (50.0)	6 (40.0)	
HER2				
0 (null)	0	3 (37.5)	3 (20.0)	.200[c]
0 (ultralow)	2 (28.6)	3 (37.5)	5 (33.3)	
1+ (low)	3 (42.9)	2 (25.0)	5 (33.3)	
2+ (low)	2 (28.6)	0	2 (13.3)	
Ki-67	5 (1–7)	7.5 (1–70)	5 (1–70)	.597
Total	7 (46.7)	8 (53.3)	15 (100)	

Values are presented as median (range) or number (%).
IDC, invasive ductal carcinoma; ILC, invasive lobular carcinoma; IMPaC, invasive micropapillary carcinoma; ER, estrogen receptor; PR, progesterone receptor; HER2, human epidermal growth factor receptor 2.
[a]Compared between IDC and others; [b]Compared between grade III and others; [c]Compared between HER2 2+ (low) and others.

dant diagnoses (Table 1), although cases with revised diagnoses tended to have numerically higher Ki-67 labeling indices.

Among the eight significantly discordant cases, the original diagnoses varied: three were HER2-null, three were ultralow, and two were 1+. Notably, all three HER2-null cases were reclassified as ultralow after consensus review (Fig. 2), suggesting that HER2-ultralow may be underdiagnosed in real-world practice. Additionally, two cases initially called 1+ were upgraded to 2+, and one ultralow case was reclassified as 1+.

Key illustrative cases with significant disagreement

Case 7 was a representative section from a surgically resected breast specimen with IDC, no special type (Fig. 3A). On low-power magnification, no discernible staining by HER2 was observed, and upon closer inspection, the vast majority of tumor cells remained negative; thus, the original diagnosis was HER2-null. During the consensus meeting, however, three pathologists identified tiny foci of cells with faint membranous staining. Their fields of view were shared on the screen in real time, and the panel unanimously agreed that the membrane staining was valid, resulting in a consensus diagnosis of HER2-ultralow. This case highlights the inherent difficulty in differentiating HER2-ultralow BC from HER2-null, as by definition, even a single tumor cell with membranous HER2 staining qualifies the case as HER2-ultralow.

Another case with significant disagreement was caused by the different perceptions of nonspecific cytoplasmic staining. It is well known that valid HER2 staining refers to membranous staining; therefore, cytoplasmic staining should not be interpreted as positive. In this case (case 13) (Fig. 3B), the diagnosis was debatable because some pathologists thought membranous staining was present in more than 10% of tumor cells, while others underestimated the percentage of positive cells as below 10% because they interpreted some stained cells as showing cytoplasmic rather than membranous staining. Coupled with the difficulty of distinguishing membranous from cytoplasmic staining, the semi-quantitative assessment near the 10% cut-off further complicates interpretation.

Next debate on case 15 (Fig. 3C) was related to edge artifacts. Before the emergence of the HER2-ultralow category, peripheral staining like that observed in this case was unequivocally considered HER2-negative, as it was focal and likely attributable to edge artifacts. Given that even a single cell with membranous staining qualifies as HER2-ultralow, it is essential to clarify the approach for identifying and excluding edge artifact to ensure diagnostic accuracy.

Real-world practical challenges

During the consensus discussion, several real-world challenges were identified that impact the consistent and accurate diagnosis of HER2-low and -ultralow BC in routine clinical practice. All participating pathologists emphasized the increasing workload associated with HER2 IHC interpretation, particularly in distinguishing between HER2-null, ultralow, and 1+ categories. The recent clinical emphasis on HER2-low classification has

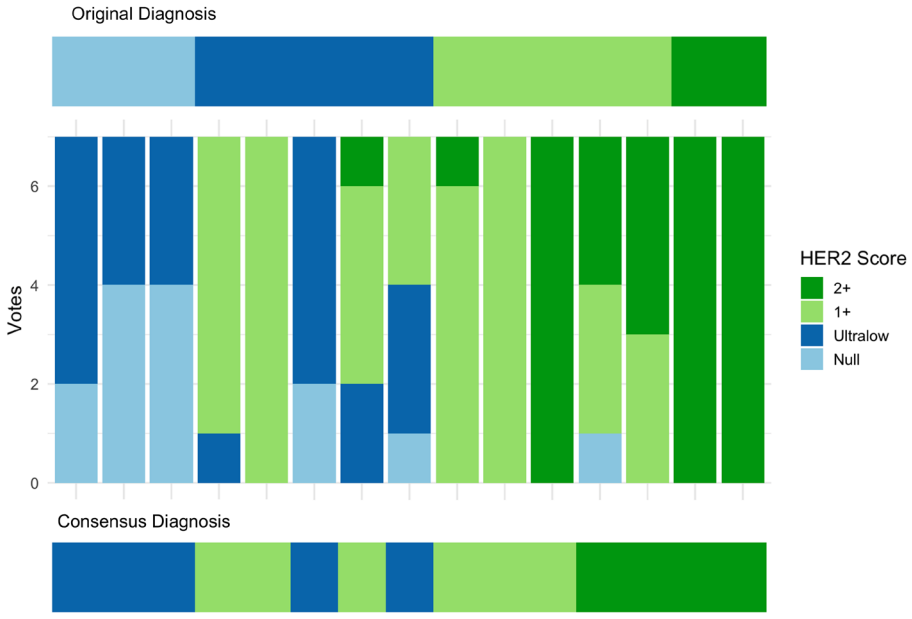

Fig. 1. Individual voting patterns and consensus results for human epidermal growth factor receptor 2 (HER2) immunohistochemistry scoring. Stacked bar plots show the distribution of seven pathologists' scores (null, ultralow, 1+, 2+) for each of the 15 cases. Consensus diagnoses for each case after discussion are shown at the bottom.

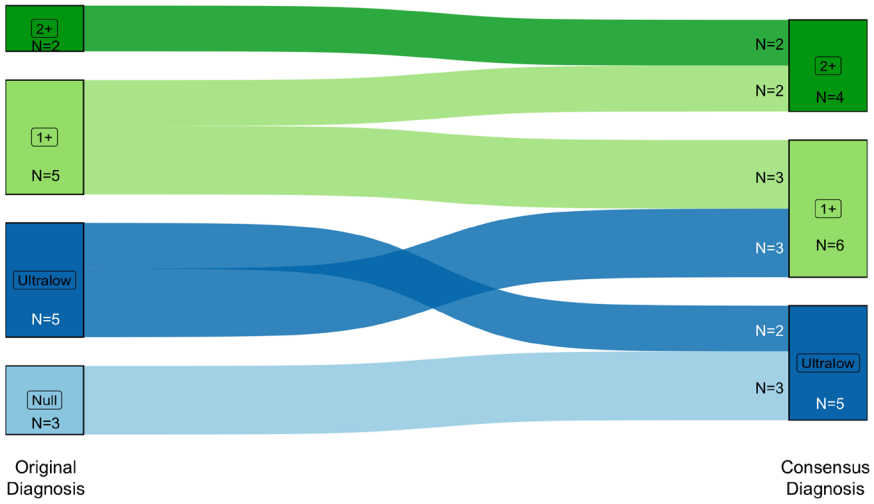

Fig. 2. Sankey diagram showing changes between original human epidermal growth factor receptor 2 (HER2) immunohistochemistry diagnoses and consensus diagnoses. Each stream represents the reclassification of individual cases, with line width proportional to the number of cases. Most reclassification occurred between HER2-null and ultralow groups, while 1+ and 2+ categories were relatively stable.

added further complexity, requiring meticulous examination of cases previously deemed HER2-negative.

In addition, some raised concerns about potential medicolegal consequences arising from diagnostic discrepancies, as variations in interpretation may lead to significant therapeutic implications. Participants even expressed concern about potential pressure to avoid classifying any metastatic BC cases as HER2-null, which may lead to diagnostic inflation. In cases where initial results are equivocal or debated, clinicians may request reevaluation of the immunostain or repeated staining.

https://doi.org/10.4132/jptm.2026.01.08

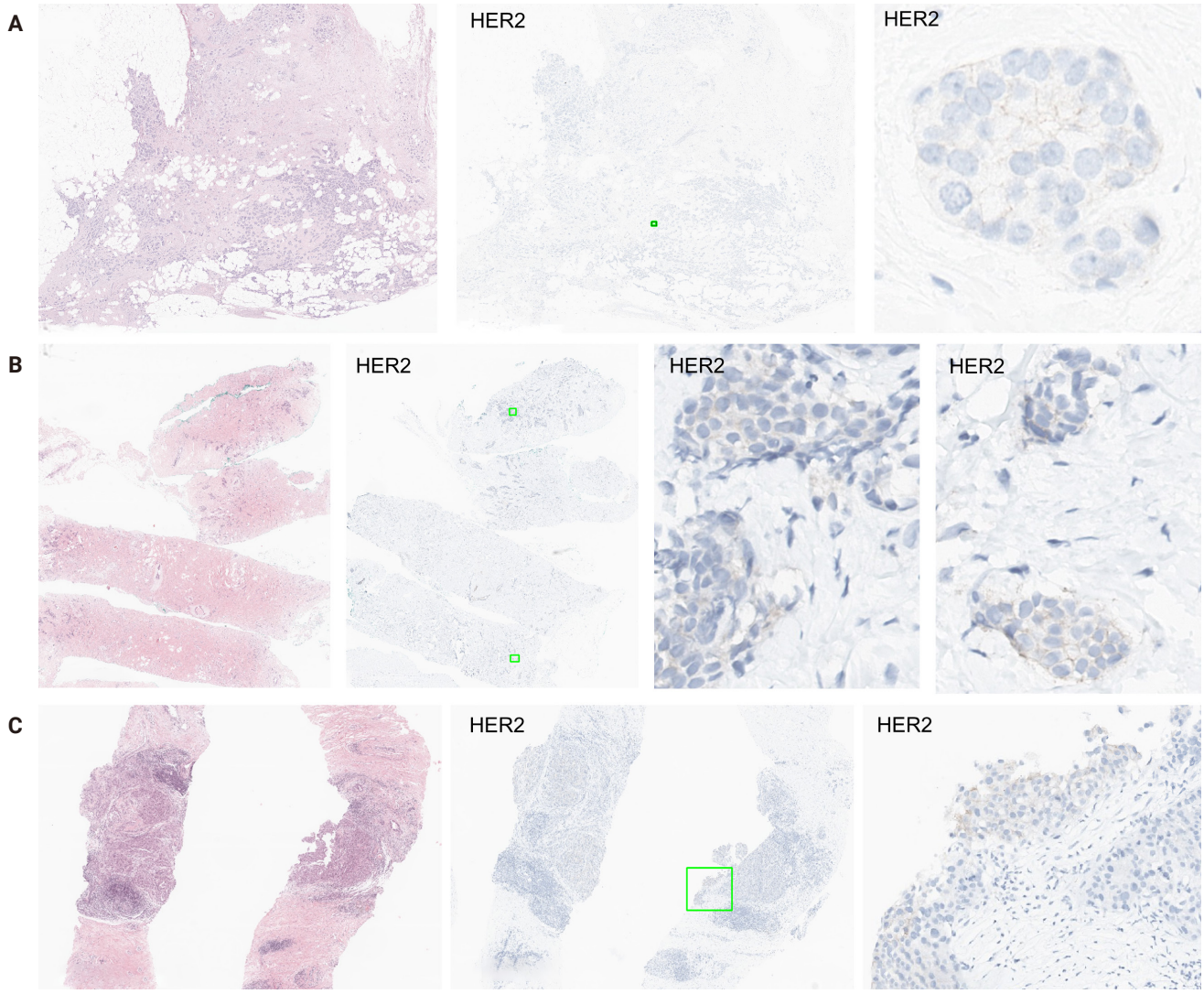

Fig. 3. Representative challenging cases in human epidermal growth factor receptor 2 (HER2)–low/ultralow diagnosis. (A) Case 7: Initially diagnosed as HER2-null, but consensus review revealed small foci of faint membranous staining, leading to reclassification as HER2-ultralow. (B) Case 13: Disagreement due to difficulty distinguishing membranous from nonspecific cytoplasmic staining around the 10% cut-off. (C) Case 15: Debate centered on peripheral staining artifacts; careful distinction between true membranous staining and edge artifact is required for accurate classification.

However, in many countries including the Republic of Korea, such reevaluation or repeated testing is not reimbursed, creating pragmatic barriers.

DISCUSSION

The emergence of HER2-low and -ultralow categories has redefined the landscape of HER2-targeted therapy and placed unprecedented emphasis on diagnostic precision in breast pathology. This distinction has become clinically relevant only recently, in parallel with the expanded eligibility for ADCs, particularly following clinical trials demonstrating therapeutic benefit even in tumors with extremely low HER2 expression. Nevertheless, our findings reveal substantial interobserver variability among experienced breast pathologists, with significant disagreement observed in more than half of the examined cases. Notably, all initially classified HER2-null cases were upgraded to ultralow upon consensus review, raising concern that a substantial proportion of HER2-ultralow BCs may be underrecognized in real-world settings. This diagnostic gap

has critical therapeutic implications, as patients misclassified as HER2-null may be excluded from potentially beneficial T-DXd treatment.

Our study also highlights key diagnostic caveats, including non-specific background or edge staining, ambiguous membranous patterns, and the inherent difficulty of semi-quantitatively estimating HER2 expression with the cut-off value of 10%. These technical challenges, coupled with the rigid—albeit somewhat arbitrary—classification structure of current HER2 diagnosis workflows, limit reproducibility and raise questions about how HER2 diagnosis can be reliably implemented in real-world settings.

From a practical standpoint, these diagnostic challenges translate into a substantial increase in time required for the identification of HER2-ultralow cases, as it necessitates exhaustive slide review to detect rare tumor cells with extremely weak membranous staining. This level of scrutiny may not be feasible in high-volume routine practice.

The challenge is further compounded by the semi-quantitative nature of the 10% cut-off threshold. In this context, artificial intelligence–based image analysis tools may serve as supportive aids for detecting and quantifying weak or focal membranous staining, potentially improving reproducibility, although further validation is required.

Even with such potential supportive tools, the expert panel raised broader systemic concerns. Heavy diagnostic workloads, potential medicolegal conflicts surrounding borderline calls, and the lack of reimbursement for repeat testing were mentioned as significant barriers. Breast pathologists may also feel pressured to avoid classifying any metastatic BC case as HER2-null, due to concerns that the patient might lose access to a therapeutic option. This may contribute to diagnostic inflation and pose ethical concerns.

Several strategies were also suggested to improve diagnostic concordance. These include the development of training programs focused on HER2-low and -ultralow categories, and the integration of artificial intelligence tools to assist in the identification and quantification of weak or focal staining. Policy-level changes, including reimbursement for re-evaluation in borderline cases, are also urgently needed to support pathologists' efforts.

More importantly, a fundamental question lies in whether HER2-null truly exists or not, and whether patients with HER2-null BC would not benefit from T-DXd therapy. The former concern is supported by our finding that all initially HER2-null cases were upgraded after the meeting. Similar phenomena have also been repeatedly reported in other groups [6-9,11]. Regarding the efficacy of T-DXd in HER2-null BCs, although limited in number, there are cases with objective response among HER2-null BC patients in the DAISY trial [12]. Furthermore, the observation that response rates in DB-06 did not linearly correlate with HER2 IHC scores [3] suggests that HER2 expression may serve merely as a trial entry marker, rather than a reliable biomarker for treatment response. Therefore, the true existence of HER2-null BCs should be clarified, and a scientific rationale must be established to justify whether maintaining this distinction between HER2-null and others has any meaningful diagnostic or therapeutic value. We hope the ongoing DESTINY-Breast15 trial will provide clearer answers to these questions [13].

In summary, our consensus study highlights the diagnostic complexity and real-world challenges in diagnosing HER2-low and -ultralow BCs. In addition to improving diagnostic accuracy and addressing systemic barriers, clarifying the biological and clinical relevance of the HER2-null category remains a fundamental priority.

Ethics Statement

This study was approved by the Institutional Review Board (IRB) of SNUH (IRB No. H-2504-142-1635), and formal written informed consent was not required with a waiver by the IRB.

Availability of Data and Material

The datasets generated or analyzed during the study are available from the corresponding author on reasonable request.

Code Availability

Not applicable.

ORCID

Jiwon Koh https://orcid.org/0000-0002-7687-6477
Yoon Jin Cha https://orcid.org/0000-0002-5967-4064
Eun Yoon Cho https://orcid.org/0000-0003-4675-4492
Ahwon Lee https://orcid.org/0000-0002-2523-9531
Ja Seung Koo https://orcid.org/0000-0003-4546-4709
So Yeon Park https://orcid.org/0000-0002-0299-7268
Min Hwan Kim https://orcid.org/0000-0002-1595-6342
Jae Ho Jeong https://orcid.org/0000-0002-8749-2612
Gyungyub Gong https://orcid.org/0000-0001-5743-0712

https://doi.org/10.4132/jptm.2026.01.08

Author Contributions

Conceptualization: GG. Data curation: JK, YJC, EYC, AL, JSK, SYP, MHK, JHJ, GG. Formal analysis: JK. Supervision: GG. Writing—original draft: JK. Writing—review & editing: JK, YJC, EYC, AL, JSK, SYP, MHK, JHJ, GG. Approval of final manuscript: all authors.

Conflicts of Interest

Jiwon Koh has advisory roles for AstraZeneca, Roche, Gilead Korea, and Daiichi Sankyo. S.Y.P., the editor-in-chief of the *Journal of Pathology and Translational Medicine*, was not involved in the editorial evaluation or decision to publish this article. All remaining authors have declared no conflicts of interest.

Funding Statement

No funding to declare.

Acknowledgments

The authors acknowledge the Breast Pathology Study Group of the Korean Society of Pathologists for its academic support and AstraZeneca Korea for their logistical support in organizing the consensus meeting.

REFERENCES

1. Ogitani Y, Aida T, Hagihara K, et al. Ds-8201a, a novel HER2-targeting ADC with a novel DNA topoisomerase I inhibitor, demonstrates a promising antitumor efficacy with differentiation from T-DM1. Clin Cancer Res 2016; 22: 5097-108.
2. Modi S, Saura C, Yamashita T, et al. Trastuzumab deruxtecan in previously treated HER2-positive breast cancer. N Engl J Med 2020; 382: 610-21.
3. Modi S, Jacot W, Yamashita T, et al. Trastuzumab deruxtecan in previously treated HER2-low advanced breast cancer. N Engl J Med 2022; 387: 9-20.
4. Wolff AC, Somerfield MR, Dowsett M, et al. Human epidermal growth factor receptor 2 testing in breast cancer: ASCO-College of American Pathologists guideline update. J Clin Oncol 2023; 41: 3867-72.
5. Bardia A, Hu X, Dent R, et al. Trastuzumab deruxtecan after endocrine therapy in metastatic breast cancer. N Engl J Med 2024; 391: 2110-22.
6. Salgado RF, Bardia A, Curigliano G, et al. LBA21 Human epidermal growth factor receptor 2 (HER2)-low and HER2-ultralow status determination in tumors of patients (pts) with hormone receptor–positive (HR+) metastatic breast cancer (mBC) in DESTINY-Breast06 (DB-06). Ann Oncol 2024; 35(Suppl 2): S1213-4.
7. Zaakouk M, Quinn C, Provenzano E, et al. Concordance of HER2-low scoring in breast carcinoma among expert pathologists in the United Kingdom and the republic of Ireland -on behalf of the UK national coordinating committee for breast pathology. Breast 2023; 70: 82-91.
8. Baez-Navarro X, van Bockstal MR, Nawawi D, et al. Interobserver variation in the assessment of immunohistochemistry expression levels in HER2-negative breast cancer: can we improve the identification of low levels of HER2 expression by adjusting the criteria? An international interobserver study. Mod Pathol 2023; 36: 100009.
9. Wu S, Shang J, Li Z, et al. Interobserver consistency and diagnostic challenges in HER2-ultralow breast cancer: a multicenter study. ESMO Open 2025; 10: 104127.
10. Kim MC, Cho EY, Park SY, et al. A nationwide study on HER2-low breast cancer in South Korea: its incidence of 2022 real world data and the importance of immunohistochemical staining protocols. Cancer Res Treat 2024; 56: 1096-104.
11. Wrobel A, Vandenberghe M, Scott M, et al. Accuracy of human epidermal growth factor receptor 2 (HER2) immunohistochemistry scoring by pathologists in breast cancer, including the HER2-low cutoff : HER2 IHC scoring concordance in breast cancer. Diagn Pathol 2025; 20: 35.
12. Mosele F, Deluche E, Lusque A, et al. Trastuzumab deruxtecan in metastatic breast cancer with variable HER2 expression: the phase 2 DAISY trial. Nat Med 2023; 29: 2110-20.
13. Modi S, Salgado R, Guarneri V, et al. Abstract PO2-19-06: an open-label, interventional, multicenter study of trastuzumab deruxtecan monotherapy in patients with unresectable and/or metastatic HER2-low or HER2 immunohistochemistry 0 breast cancer: DESTINY-Breast15. Cancer Res 2024; 84(9 Suppl):-PO2-19-06.

JPTM

ORIGINAL ARTICLE

pISSN 2383-7837 · eISSN 2383-7845

Journal of Pathology and Translational Medicine 2026; 60: 338-348
https://doi.org/10.4132/jptm.2026.01.15

Clinicopathological profile of high-grade differentiated thyroid carcinoma in an Indonesian tertiary hospital

Novita[1], Agnes Stephanie Harahap[1,2], Maria Francisca Ham[1,2], Alfianto Widiono[3], Chan Kwon Jung[4,5]

[1]Department of Anatomical Pathology, Faculty of Medicine, Universitas Indonesia/Dr. Cipto Mangunkusumo Hospital, Jakarta, Indonesia
[2]Human Cancer Research Center-Indonesian Medical Education and Research Institution, Faculty of Medicine, Universitas Indonesia, Jakarta, Indonesia
[3]Faculty of Medicine, Universitas Indonesia/Dr. Cipto Mangunkusumo Hospital, Jakarta, Indonesia
[4]Department of Hospital Pathology, College of Medicine, The Catholic University of Korea, Seoul, Korea
[5]Cancer Research Institute, College of Medicine, The Catholic University of Korea, Seoul, Korea

Graphical abstract

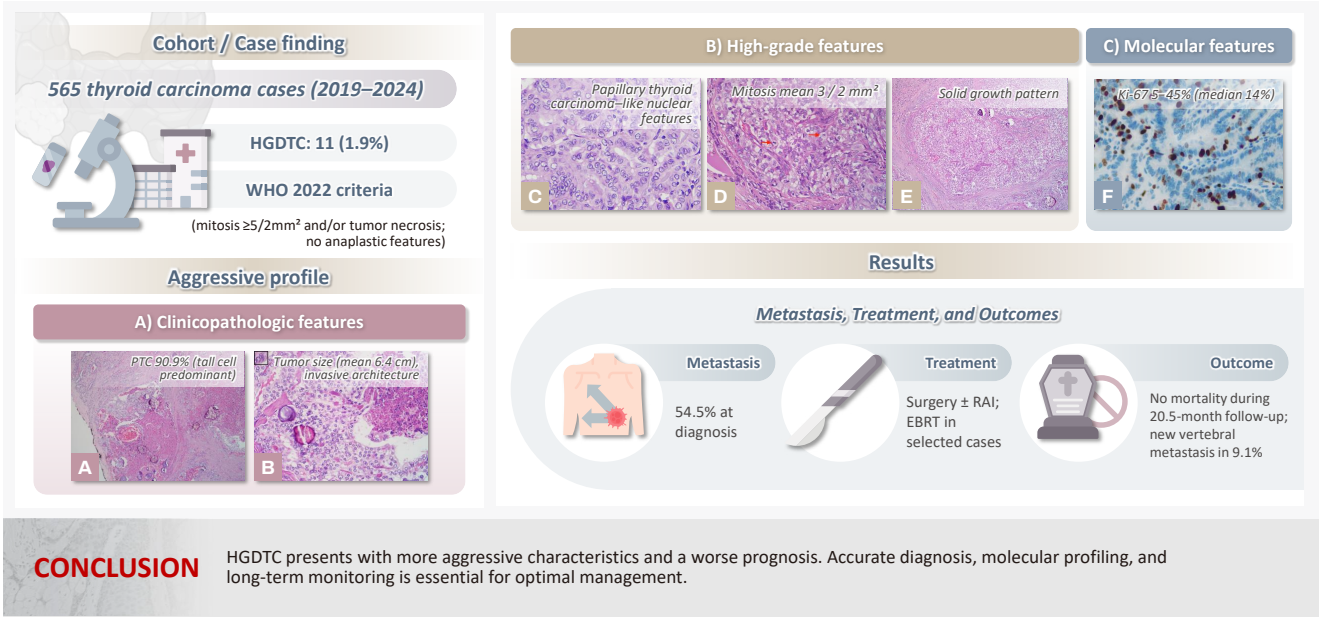

Novita et al. Journal of Pathology and Translational Medicine

JPTM

ORIGINAL ARTICLE

pISSN 2383-7837 · eISSN 2383-7845

Journal of Pathology and Translational Medicine 2026; 60: 338-348
https://doi.org/10.4132/jptm.2026.01.15

Clinicopathological profile of high-grade differentiated thyroid carcinoma in an Indonesian tertiary hospital

Novita[1], Agnes Stephanie Harahap[1,2], Maria Francisca Ham[1,2], Alfianto Widiono[3], Chan Kwon Jung[4,5]

[1]Department of Anatomical Pathology, Faculty of Medicine, Universitas Indonesia/Dr. Cipto Mangunkusumo Hospital, Jakarta, Indonesia
[2]Human Cancer Research Center-Indonesian Medical Education and Research Institution, Faculty of Medicine, Universitas Indonesia, Jakarta, Indonesia
[3]Faculty of Medicine, Universitas Indonesia/Dr. Cipto Mangunkusumo Hospital, Jakarta, Indonesia
[4]Department of Hospital Pathology, College of Medicine, The Catholic University of Korea, Seoul, Korea
[5]Cancer Research Institute, College of Medicine, The Catholic University of Korea, Seoul, Korea

Background: High-grade differentiated thyroid carcinoma (HGDTC) is a recently recognized entity in the 2022 World Health Organization classification, representing a more aggressive subtype of differentiated thyroid carcinoma. Previously, high-grade features such as increased mitotic activity and tumor necrosis were often overlooked, despite being important independent prognostic factors. Although rare, HGDTC carries significant diagnostic, prognostic, and therapeutic implications. Data remain limited in Indonesia. **Methods:** This retrospective descriptive study reviewed 565 thyroid carcinoma cases diagnosed at Cipto Mangunkusumo Hospital from 2019 to 2024. Eleven cases (1.9%) met HGDTC criteria. Clinicopathological characteristics, histologic subtypes, Ki-67 proliferation index, molecular alterations, treatment modalities, and clinical outcomes were analyzed. **Results:** Patients had a mean age of 54.6 years, with a female-to-male ratio of 2.7:1. Papillary thyroid carcinoma was the main type (90.9%), with the tall cell subtype predominating. Mean tumor size was 6.4 cm. Lymphatic invasion, vascular invasion, and extrathyroidal extension were present in 54.5%, 18.2%, and 45.5% of cases, respectively. All tumors showed necrosis. Mean mitotic count was 3 per 2 mm^2. The Ki-67 index ranged from 5% to 45% (median, 14%). *BRAF*V600E and *TERT* promoter mutations were detected in 18.2% and 36.4% of cases, respectively, with co-mutations in 18.2%. Six cases (54.5%) had metastases at time of diagnosis. During a mean follow-up of 20.5 months, one patient (9.1%) developed new vertebral metastases and all patients (100%) remained alive. **Conclusions:** HGDTC presents with more aggressive characteristics and a worse prognosis. Accurate diagnosis, molecular profiling, and long-term monitoring are essential for optimal management.

Keywords: High-grade follicular cell-derived non-anaplastic thyroid carcinoma; High-grade differentiated thyroid carcinoma; Papillary thyroid carcinoma; Thyroid neoplasm

INTRODUCTION

Thyroid carcinoma is one of the most prevalent endocrine malignancies worldwide. According to the Global Cancer Observatory (GLOBOCAN), it ranked seventh in global cancer incidence in 2022, with approximately 821,000 new cases reported [1]. The majority of thyroid carcinomas are classified as differentiated thyroid carcinoma (DTC), which typically exhibits indolent behavior and is associated with a favorable prognosis. However, DTCs that display high-grade features, such as tumor necrosis or an elevated mitotic index, tend to follow a more aggressive clinical course. These cases are linked to a significantly higher risk of extrathyroidal extension and distant metastases compared to DTCs without such features [2]. The 5-year overall survival rate among patients with high-grade features ranges from 50% to 70%, with recurrences most commonly occurring

Received: October 20, 2025 **Revised:** December 22, 2025 **Accepted:** January 15, 2026
Corresponding Author: Agnes Stephanie Harahap, MD, PhD
Department of Anatomical Pathology, Faculty of Medicine, Universitas Indonesia/Dr. Cipto Mangunkusumo Hospital, Jl. Salemba Raya No. 6, Jakarta 14320, Indonesia
Tel: +62-8-18765563, Fax: +62-21-3912477, E-mail: agnes.stephanie01@ui.ac.id

within the first 3 years. Therefore, these features should not be overlooked [3].

The term high-grade differentiated thyroid carcinoma (HGDTC) refers to this specific subset of tumors. In 2022, the World Health Organization (WHO) formally introduced HGDTC as a distinct diagnostic category. It is defined as a follicular cell–derived thyroid carcinoma with a follicular, papillary, or solid growth pattern; invasive architecture; nuclear features resembling either follicular or papillary neoplasms; a mitotic rate of at least five per 2 mm^2; and/or the presence of tumor necrosis, without any features of anaplastic transformation [4,5]. The inclusion of HGDTC in the classification of thyroid malignancies provides pathologists with more precise criteria to identify aggressive lesions that do not meet the Turin criteria for poorly differentiated thyroid carcinoma (PDTC) or the diagnostic threshold for anaplastic carcinoma [2]. Recognition of this entity is clinically important, as it enables more accurate patient triage. HGDTC is associated with more aggressive biological behavior and poorer prognosis than both conventional DTC and PDTC [3]. As such, all patients diagnosed with HGDTC should receive close clinical monitoring [2,5].

Only a limited number of studies have revisited previous DTC diagnoses to identify cases that fulfill the new criteria for HGDTC. In Indonesia, data on HGDTC are lacking. The present study was conducted to investigate the incidence and clinicopathologic profile of HGDTC diagnosed at the Department of Anatomical Pathology, Faculty of Medicine, Universitas Indonesia/Dr. Cipto Mangunkusumo Hospital. The findings are expected to support pathologists in recognizing and diagnosing this entity accurately and to assist clinicians in making informed decisions regarding surveillance and treatment strategies.

MATERIALS AND METHODS

Case selection and histopathologic review

A total of 565 thyroid carcinoma cases diagnosed at our institution between 2019 and 2024 and meeting the inclusion criteria were reviewed. Of these, 516 cases (91.3%) were papillary thyroid carcinomas (PTC), five cases (0.9%) were follicular thyroid carcinomas (FTC), 15 cases (2.6%) were oncocytic carcinomas (OCA), 10 cases (1.8%) were medullary thyroid carcinomas, four cases (0.7%) were PDTC, and 15 cases (2.7%) were anaplastic thyroid carcinomas. Following histopathological re-evaluation, only 11 cases (1.9%) fulfilled the diagnostic criteria for HGDTC.

All thyroid carcinoma cases diagnosed at our institution from 2019 to 2024 were independently reviewed by the primary investigator and confirmed by board-certified endocrine pathologists to ensure diagnostic concordance. Cases were reclassified as HGDTC when they exhibited follicular, papillary, or solid growth patterns with invasive behavior; follicular neoplasm-like or papillary-like nuclear features; and/or oncocytic morphology, with a mitotic rate of ≥5 per 2 mm^2 and/or tumor necrosis in the absence of anaplastic features.

Tumor necrosis referred to geographic or focal necrotic areas showing a sharply abrupt transition from viable to nonviable tumor without intervening granulation tissue, fibrosis, or hyalinization. Necrotic regions displayed cellular debris, cytoplasmic dissolution, nuclear fragmentation with scattered karyorrhectic bodies, irregular chromatin distribution, ghost cell outlines, and apoptotic remnants. Pre-existing vascular structures were often preserved with a peripheral rim of viable tumor cells. Ischemic or infarct-type necrosis attributable to prior fine-needle aspiration (FNA) or core needle biopsy (CNB) typically accompanied by granulation tissue, fibrosis, hemorrhage, histiocytic infiltration, cholesterol clefts, and absence of karyorrhexis—was excluded.

For each case meeting HGDTC criteria, the following clinicopathologic data were retrieved: sex, age, tumor size, tumor focality, laterality, histologic subtype, Ki-67 proliferation index, solid/trabecular (ST) growth pattern, mutational status, lymphatic, vascular, and perineural invasion, extrathyroidal extension, surgical margin status, tumor necrosis, mitotic count, presence of metastases, American Joint Committee on Cancer (AJCC) 8th edition stage, FNA and CNB results, treatment modalities, and follow-up information.

Immunohistochemical analysis

Immunohistochemical staining for Ki-67 was performed using an anti-Ki-67 (SP6) rabbit monoclonal primary antibody (Ventana Medical Systems, Inc., Tucson, AZ, USA). Tumor areas with the highest Ki-67 expression (hot spots) were identified. Photomicrographs were captured from ten high-power fields (40× objective), and 1,000 tumor cells were manually counted using QuPath software to calculate the percentage of positively stained nuclei.

Molecular analysis

Targeted mutation testing was performed using polymerase chain reaction (PCR) followed by Sanger sequencing to evaluate alterations in *BRAF* (codon 600), *NRAS* (codon 61), *HRAS*

(codon 61), *TP53* (codons 208, 220, 241, 277), *PIK3CA* (codon 1047), *PTEN* (codon 130), and *TERT* promoter hotspots (C228T, C250T). Genomic DNA was extracted from 5-μm sections of formalin-fixed paraffin-embedded (FFPE) tumor tissue using the QIAamp DNA FFPE Tissue Kit (Qiagen, Valencia, CA, USA) according to the manufacturer's instructions, and DNA purity and concentration were assessed using a NanoDrop 2000 spectrophotometer (Thermo Fisher Scientific, Waltham, MA, USA). PCR amplification was carried out using KOD One PCR Master Mix (Toyobo, Osaka, Japan), and sequencing was performed with the BigDye Terminator v3.1 Cycle Sequencing Kit on an ABI 3730xl Genetic Analyzer (Applied Biosystems, Carlsbad, CA, USA). Resulting chromatograms were aligned with reference sequences to determine mutational status. The DNA primers of each gene are included in Supplementary Table S1.

Statistical analysis

Statistical analyses were performed using IBM SPSS Statistics ver. 24 (IBM Corp., Armonk, NY, USA). Descriptive statistics were used to summarize clinicopathologic features. Frequencies and percentages were calculated for categorical variables, and means, medians, and ranges were reported for continuous variables as appropriate. Comparative analyses to distinguish clinicopathological features between HGDTC cases with an ST pattern and those without an ST pattern were conducted using Fisher's exact test. A p-value <0.05 was considered statistically significant.

RESULTS

A total of 565 thyroid carcinoma cases were diagnosed at our institution between 2019 and 2024. Following slide re-evaluation, 11 cases (1.9%) were found to fulfill the diagnostic criteria for HGDTC as defined by the 2022 WHO classification. The clinicopathologic profiles of these patients are summarized in Tables 1 and 2.

Among the 11 HGDTC patients, eight were female and three were male, with a mean age of 54.6 (standard deviation [SD], 14.5) years. Four patients (36.4%) were ≥55 years old. Tumor sizes varied, with mean size of 6.4 (SD, 4.2) cm. Among all cases, eight cases (72.7%) were unifocal, and three (27.3%) were multifocal. Seven cases (63.6%) involved both thyroid lobes, and four (36.4%) were confined to a single lobe. Ten cases (90.9%) were originally diagnosed as PTC, five tall cell subtypes (50.0%), two follicular subtypes (20.0%), two classic subtypes (20.0%), and one solid subtype (10.0%). The two follicular-patterned cases in our series were identified as invasive encapsulated follicular variant papillary thyroid carcinoma (IEFVPTC). One case (9.1%) was initially diagnosed as OCA. Tall cell components exceeded 30% in most of the subtype cases.

Lymphatic invasion was observed in six cases (54.5%), vascular invasion in two cases (18.2%), and perineural invasion in one case (9.1%). Extrathyroidal extension was present in five cases (45.5%). All tumors exhibited necrosis: six (54.5%) focal, two (18.2%) multifocal, and three (27.3%) extensive. Mitotic figures ranged from 1 to 6 per 2 mm^2 with a mean of 3 (SD, 1.4) per 2 mm^2 and no significant inter-slide variation across three separate hotspots. The Ki-67 proliferation index ranged from 5% to 45% (median, 14%). Five cases had an index between 5% and 10%, while six cases had an index greater than 10% (Fig. 1).

ST growth pattern was identified in seven cases: six (85.7%) with solid growth patterns and one (14.3%) with trabecular growth. However, none of these cases fulfilled the Turin criteria for PDTC, as the ST areas retained classic PTC-type nuclear features rather than the convoluted nuclei required for a diagnosis of PDTC. No significant differences in clinicopathological profiles or disease outcome were observed between HGDTC cases with an ST pattern and those without an ST pattern.

Six patients (54.5%) had evidence of metastases at the time of diagnosis: all of them (100%) showed lymph node involvement, of whom one (16.7%) had concurrent distant metastases to the lungs and bones. All cases had molecular investigation: two cases with *BRAF*V600E mutations, four cases with *TERT*p mutations, two cases with multiple mutations (*BRAF*V600E and *TERT*p (C228T), *BRAF*V600E and *PIK3CA*), while the remaining cases were negative for mutations in *BRAF*V600E, *NRAS*, *HRAS*, *TP53*, *PIK3CA*, *PTEN*, and *TERT*p.

According to the AJCC 8th edition staging system, eight cases (72.7%) were classified as stage I, two (18.2%) as stage II, and one (9.1%) as stage IVB. FNA cytology was performed in three patients (27.3%): one was categorized as Bethesda IV and the others as Bethesda VI. CNB had been conducted before thyroidectomy in seven patients (63.6%), with results showing one case in category IIIB, three in category IV, one in category V, and two in category VI, based on the Korean Thyroid Association (KTA) classification [6].

Regarding treatment, four patients underwent surgery alone, including lobectomy or total thyroidectomy. Six patients received combined therapy with radioactive iodine (RAI), and

https://doi.org/10.4132/jptm.2026.01.15

https://doi.org/10.4132/jptm.2026.01.15

Table 1. Summary of clinicopathological profile of HGDTC patients

Variable	Case No.										
	1	2	3	4	5	6	7	8	9	10	11
Histologic subtype	PTC (tall cell)	PTC (tall cell)	PTC (solid)	PTC (classic)	PTC (tall cell)	OCA	PTC (classic)	IEFVPTC	IEFVPTC	PTC (tall cell)	PTC (tall cell)
Sex	F	M	M	F	F	M	F	F	F	F	F
Age (yr)	64	47	59	51	52	52	46	72	42	84	32
Tumor size (cm)	5	4.7	12	9	11	12.5	1	3	5	6.5	0.7
Focality	Unifocal	Unifocal	Unifocal	Unifocal	Unifocal	Unifocal	Multifocal	Unifocal	Multifocal	Unifocal	Multifocal
ETE	None	Gross	Microscopic	None	Gross	Gross	None	None	None	Microscopic	None
Tall cell component (%)	>30	>30	0	20	>30	0	0	0	0	>30	>30
Mitosis (/2 mm^2)	3	2	4	3	1	4	2	2	6	4	2
Ki-67 (%)	26	5	8	16	10	30	14	7	31	45	5
Necrosis	Present	Present	Present	Present	Present	Present	Present	Present	Present	Present	Present
ST pattern (% component)	Absent	Absent	Solid (>50%)	Trabecular (<3%)	Absent	Solid (30%)	Solid (30%)	Solid (5%)	Solid (10%)	Absent	Solid (<3%)
pT	3a	4b	3a	3a	4a	4a	1a	2	3a	3a	1a
pN	1b	1b	1b	1a	1b	0	0	x	x	0	1a
LN metastases (at diagnosis)	Present	Present	Present	Present	Present	Absent	Absent	NA	NA	Absent	Present
Distant metastases (at diagnosis)	Absent	Absent	Present (lungs & bones)	Absent	Absent	Absent	Absent	Absent	Absent	Absent	Absent
AJCC stage	II	I	IVB	I	I	I	I	I	I	II	I
Mutation	*BRAF*V600E	*TERT*p	*TERT*p	Unknown[a]	*BRAF*V600E *TERT*p	Unknown[a]	*TERT*p	*TERT*p	*BRAF*V600E	Unknown[a]	*BRAF*V600E, PIK3CA
FNA (Bethesda)	VI	Not performed	IV	Not performed	Not performed	Not performed	Not performed	Not performed	Not performed	Not performed	VI
CNB (KTA)	Not performed	Not performed	Not performed	VI	VI	IV	IIIB	IV	IV	V	Not performed
Treatment	Surgery, RAI	Surgery, RAI	Surgery	Surgery	Surgery	Surgery, RAI, EBRT	Surgery, RAI	Surgery, RAI	Surgery, RAI	Surgery	Surgery, RAI
Follow-up status (duration, mo)	Alive (32)	Alive (33)	Alive (33)	Alive (35)	Alive with disease progression (vertebral metastases) (9)	Alive (12)	Alive (21)	Alive (16)	Alive (12)	Alive (6)	Alive (17)

HGDTC, high-grade differentiated thyroid carcinoma; PTC, papillary thyroid carcinoma; OCA, oncocytic carcinoma; IEFVPTC, invasive encapsulated follicular variant papillary thyroid carcinoma; F, female; M, male; ETE, extrathyroidal extension; ST, solid/trabecular; LN, lymph node; NA, not available; AJCC, American Joint Committee on Cancer; FNA, fine needle aspiration; CNB, core needle biopsy; KTA, Korean Thyroid Association; RAI, radioactive iodine; EBRT, external beam radiation therapy.

[a]Unknown indicates negative results for *BRAF*V600E, *NRAS*, *HRAS*, *TP53*, *PIK3CA*, *PTEN*, and *TERT*p mutations, but the status of other mutations remains undetermined.

Table 2. Clinicopathological profile of HGDTC patients

Parameter	Value (n = 11)
Sex	
Female	8 (72.7)
Male	3 (27.3)
Age (yr)	54.6 ± 14.5
Female	55.4 ± 16.9
Male	52.7 ± 6
No. of patients aged ≥55 years	4 (36.4)
Tumor size (cm)	6.4 ± 4.2
Tumor focality	
Unifocal	8 (72.7)
Multifocal	3 (27.3)
Tumor laterality	
Single lobe	4 (36.4)
Bilateral	7 (63.6)
Histologic subtypes	
Papillary thyroid carcinoma	10 (90.9)
Tall cell	5 (50.0)
IEFVPTC	2 (20.0)
Classic	2 (20.0)
Solid	1 (10.0)
Oncocytic carcinoma	1 (9.1)
Lymphatic invasion	6 (54.5)
Vascular invasion	2 (18.2)
Perineural invasion	1 (9.1)
Extrathyroidal extension	5 (45.5)
Tumor necrosis	
Focal	6 (54.5)
Multifocal	2 (18.2)
Extensive	3 (27.3)
Mitoses per 2 mm^2	3 ± 1.4
Ki-67 proliferation index	14 (5–45)
Metastases (at time of diagnosis)	6 (54.5)
Lymph node	6 (100)
Distant	1 (16.7)
AJCC8 stage	
Stage I	8 (72.7)
Stage II	2 (18.2)
Stage IVB	1 (9.1)
Fine needle aspiration	3 (27.3)
Bethesda IV	1 (33.3)
Bethesda VI	2 (66.7)
Core needle biopsy	7 (63.6)
Category IIIB	1 (14.3)
Category IV	3 (42.9)
Category V	1 (14.3)
Category VI	2 (28.6)
Treatment	
Surgery only	4 (36.4)
Radioactive iodine ablation	6 (54.5)
External beam radiation therapy	1 (9.1)
Follow-up (mo)	20.5 ± 10.8
Alive without disease	10 (90.9)
Alive with disease progression	1 (9.1)

Values are presented as number (%), mean ± SD, or median (range).
HGDTC, high-grade differentiated thyroid carcinoma; IEFVPTC, invasive encapsulated follicular variant of papillary thyroid carcinoma; AJCC, American Joint Committee on Cancer; SD, standard deviation.

one patient received additional external beam radiotherapy (EBRT). The mean follow-up period was 20.5 months (SD, 10.8), during which all patients remained alive. Among the surgery-only group, one patient remained alive with lungs and bones metastases at initial presentation (33 months), one developed vertebral bone metastases nine months postoperatively, and two were alive without evidence of disease (mean follow-up, 20.5 months). Of the six patients who received RAI, all remained disease-free (mean follow-up, 21.8 months). One patient treated with surgery, RAI, and EBRT also remained disease-free (12 months).

DISCUSSION

HGDTC is a newly recognized entity included in the 2022 WHO classification. It is defined as a follicular cell-derived tumor exhibiting follicular, papillary, or solid growth patterns with invasive behavior, follicular or papillary-like nuclear features, a mitotic rate of ≥5 per 2 mm^2, and/or tumor necrosis, in the absence of anaplastic features [2,3,5]. This classification provides pathologists with clearer guidelines for identifying aggressive tumors that do not meet the Turin criteria for PDTC or the criteria for anaplastic thyroid carcinoma. Prior to its recognition as a distinct entity, DTCs with high-grade or aggressive features were often overlooked. However, features such as increased mitotic activity, with or without tumor necrosis, are now understood to be independent prognostic factors. DTC with such features, now termed HGDTC, is associated with worse prognosis than conventional DTC and a significantly higher risk of extrathyroidal extension and distant metastases [7-9].

Our study characterizes the incidence and clinicopathological features of HGDTC, whose data remain limited in Indonesia.

https://doi.org/10.4132/jptm.2026.01.15

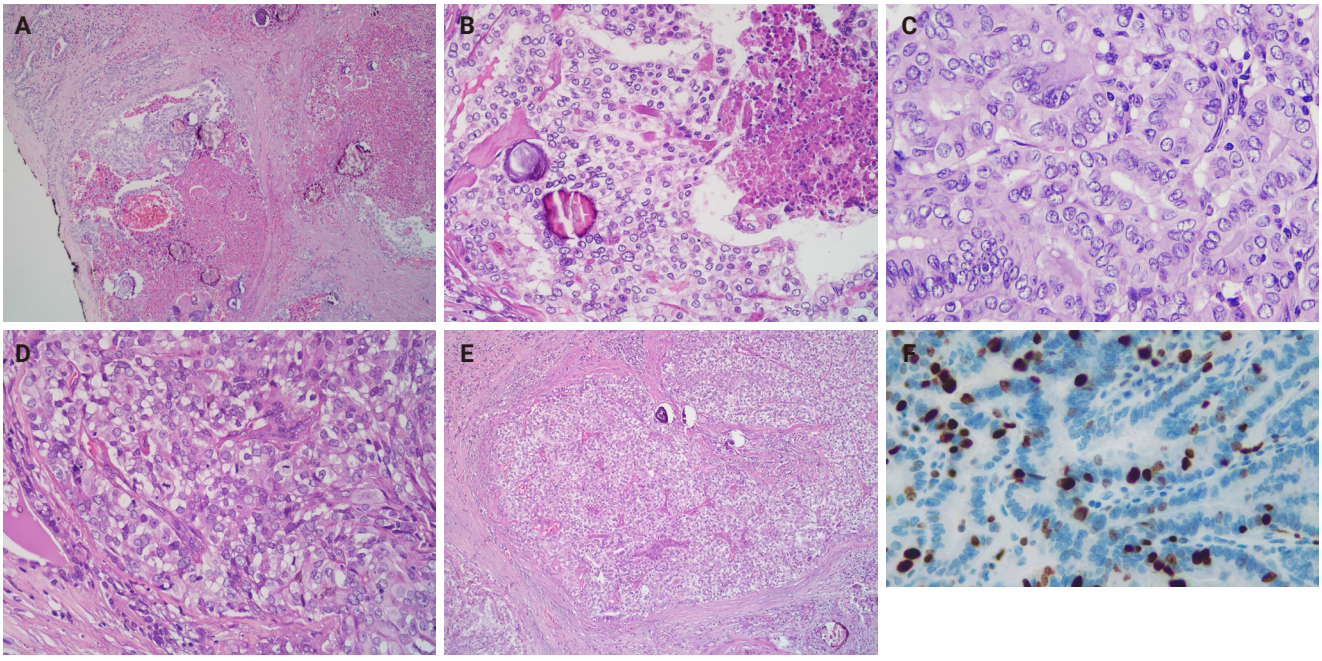

Fig. 1. High-grade differentiated thyroid carcinoma. (A) High-grade papillary thyroid carcinoma (classic subtype) shows tumor necrosis. (B) Area of tumor necrosis adjacent to viable tumor cells. (C) Papillary thyroid carcinoma-like nuclear features. (D) Mitoses (arrows). (E) Solid pattern. (F) The Ki-67 immunostaining demonstrates a proliferation index of 45%.

Of 565 thyroid carcinoma cases diagnosed in our institution, 11 (1.9%) met the criteria for HGDTC, a proportion comparable to that reported in a cohort involving 1,069 PTC and FTC cases (1.3%) [8]. The prevalence of HGDTC varies considerably across studies (0.25%–15.9%) (Table 3) [7-13], largely due to heterogeneity in study populations. A recent meta-analysis reported a 7.2% prevalence among unselected DTC patients, while a study focusing on advanced thyroid carcinoma cases observed a rate of 15.9% [10,14].

Although earlier reports identified a peak incidence of HGDTC and PDTC in patients aged 55–65 years, more recent studies, including the present study, have observed a younger age distribution [3,7,8,12]. In our cohort, the mean patient age was 54.6 years, with most cases occurring in individuals under 55, consistent with findings from more recent series [9,10,13]. These variations may reflect differences in population demographics, genetic backgrounds, environmental exposures, or healthcare access across regions and study settings. A similar observation is also reported for sex distribution across various studies (Table 3).

The mean tumor size in our study was 6.4 (SD, 4.2) cm, slightly larger than displayed in prior studies [7,8,13]. This may support the observation that HGDTC often presents with relatively large tumors (>3 cm), possibly reflecting its more aggressive biological behavior compared to classic DTC. Despite this size-associated trend, the 2022 WHO classification does not mandate a minimum tumor size for defining HGDTC. In principle, high-grade morphology can be diagnosed even in very small lesions (<1 cm). However, the biological and clinical interpretation of such "micro-HGDTCs" requires prudence. While these lesions demonstrate unequivocal high-grade morphology, the prognostic implications of sub-centimeter high-grade tumors remain insufficiently characterized and may not parallel those of conventionally sized counterparts. In the present study, we included one case with a sub-centimeter HGDTC (0.7 cm) because it fully met the WHO diagnostic criteria from a methodological standpoint. This tumor was multifocal, demonstrated tall-cell morphology, and presented with lymph-node metastases. Further studies are required to determine the true clinical relevance of this specific setting.

While limited studies have documented multifocality and laterality status in HGDTC, our study corroborates the findings of Thompson [7], who reported that HGDTC tumors most commonly present as a unifocal lesion, though in some cases it may involve both lobes (bilateral involvement). This pattern may reflect the aggressive behavior of HGDTC, where rapid prolif-

Table 3. Comparison of HGDTC clinicopathological features across studies

Variable	Our study	Hiltzik et al. (2006) [11]	Wong et al. (2021) [8]	Xu et al. (2022) [12]	Thompson (2023) [7]	Jeong et al. (2023) [9]	Tondi Resta et al. (2024) [13]	Caldeira et al. (2025) [10]
No. of total cases (%)	11 (1.9)	11 (0.29)	15	164	17	14 (1.3)	32 (0.25)	22 (15.9)
Age (yr)	54.6 (mean)	Not specified	70 (median)	55 (median)	64 (median)	48.5 (mean)	52.5 (mean)	48 (median)
Sex ratio (F:M)	2.7:1	Not specified	7:8	1.7:1	1:1.1	2.5:1	1:1.3	4.3:1
Tumor size (cm)	6.4 (mean)	Not specified	4.2 (median)	3 (median)	5.4 (median)	3.32 (mean)	5.15 (mean)	3.5 (median)
Histologic type	10 PTCs (5 tall cell, 2 IEFVPTC, 2 classic, 1 solid), 1 OCA	11 PTCs	15 PTCs (2 hobnail, 2 tall cell, 5 columnar cell, 1 solid, 1 classic, 3 mixed tall-cell/hobnail, 1 mixed tall-cell/columnar)	155 PTCs (mostly tall cell, followed by follicular, classic, columnar, diffuse sclerosing, hobnail, and solid) and 9 FTCs	9 PTCs (4 solid, 3 classic, 2 follicular), 8 OCAs	13 PTCs (10 tall cell, 1 classic, 1 encapsulated, 1 diffuse sclerosing), 1 FTC	28 PTCs (10 classic, 6 follicular, 6 tall cell, 2 columnar, 3 oncocytic, 1 diffuse sclerosing), 2 FTCs, 2 OCAs	20 PTCs (5 classic, 1 hobnail, 3 infiltrative follicular, 2 solid, 9 tall cell), 1 OCA, 1 FTC
Necrosis (%)	100	Not specified	33	75.6	100	78	66	19
Mitotic count	3 per 2 mm^2 (mean)	Not specified	9 per 2 mm^2 (median)	≥5 per 10 HPF in 51% patients	5 per 2 mm^2 (median)	3.14 per 2 mm^2 (mean)	3.2 per 2 mm^2 (mean)	6 per 2 mm^2 (median)
Ki-67 index	Median 14% (range, 5 to 45)	Not reported	Median 20%	Not specified	Median 8.3% (mean 9.4%)	Not reported	Mean 5.6%	Not specified
Molecular findings	*TERT*p, *BRAF*V600E, multiple.	Not available	*BRAF*V600E frequent	*BRAF*V600E frequent, *RAS*, *TP53*, *PTEN*, *E1F1AX*	*BRAF*, *RAS*, *PIK3CA*, *TERT*p	*TERT*p *BRAF*V600E	Not specified	*TERT*p, *BRAF*V600E
Outcome	All alive at follow-up (1 AWD, 10 NED)	Poor prognosis, higher mortality vs. conventional DTC	Not specified	DSS was similar to HGTC-PDTC but lower risk for distant metastases	Some mortality reported	All alive at follow-up (2 AWD, 12 NED)	Not specified	Worse disease persistence and survival

HGDTC, high-grade differentiated thyroid carcinoma; F, female; M, male; PTC, papillary thyroid carcinoma; IEFVPTC, invasive encapsulated follicular variant of papillary thyroid carcinoma; OCA, oncocytic carcinoma; FTC, follicular thyroid carcinoma; HPF, high-power field; AWD, alive with disease; NED, no evidence of disease; DTC, differentiated thyroid carcinoma; DSS, disease-specific survival; HGTC, high-grade thyroid carcinoma; PDTC, poorly differentiated thyroid carcinoma.

https://doi.org/10.4132/jptm.2026.01.15

eration results in a dominant tumor mass with limited time for the development of additional distinct foci [12,15,16].

Histologic subtypes observed in our cohort were primarily PTC, including tall cell, IEFVPTC, solid, and classic subtypes, along with one case of OCA. These findings are broadly consistent with those reported in prior studies (Table 3). Most series demonstrate a predominance of aggressive PTC subtypes such as tall cell, hobnail, and columnar cell, though the presence of OCA and FTC has also been variably reported [7-10,12,13]. Although our study did not identify any cases of the diffuse sclerosing subtype of PTC, prior studies have reported a series of HGDTC cases exhibiting this subtype [9,12,13,16,17].

Tumor necrosis and mitotic activity are key diagnostic features of HGDTC. All tumors in our study exhibited necrosis, with 54.5% focal, 18.2% multifocal, and 27.3% extensive necrosis. The mean mitotic count was 3 per 2 mm^2 (SD, 1.4), which is slightly lower than the counts in other studies [7-9]. This discrepancy may reflect the intrinsic heterogeneity of HGDTC. Although studies have shown that aggressive driver mutations such as *TERT*p and *TP53* favor rapid tumor cell proliferation and extensive necrosis, our cohort has found that tumors with those mutations can have extensive necrosis even with low mitotic count. This phenomenon can be explained by some alternative mechanisms. Tumor cells experience metabolic stress caused by hypoxia and nutrient deprivation from insufficient vascularization, leading to increased oxidative stress and cell death pathways. Release of pro-inflammatory cytokines (e.g., tumor necrosis factor-alpha) by immune cells can also induce necrosis through inflammation-related metabolic disruption and a direct cytotoxic effect.

Apart from intrinsic tumor biology, technical factors may also influence mitotic assessment. Mitoses tend to be focal and unevenly distributed, the extent of tissue sampled may result in a different estimation of mitotic number [18-20]. Mitotic figures may also be difficult to distinguish from apoptotic bodies or other morphologic mimics on hematoxylin and eosin (H&E) sections, which may contribute to underestimation. This issue is illustrated by the observation that three of eleven tumors in our cohort had markedly elevated Ki-67 indices (≥30%) despite few identifiable mitoses (range, 4 to 6 mitoses per 2 mm^2). These findings highlight the need for more standardized approaches to mitotic evaluation in HGDTC and support the potential role of ancillary techniques such as digital image analysis or phospho-histone H3 (PHH3) immunostaining for improving mitotic detection.

High-grade necrosis in HGDTC is characterized by geographic or focal necrosis with abrupt borders surrounded by viable tumor cells without stromal changes. Associated features include cellular debris, cytoplasmic degeneration, karyorrhexis, irregular chromatin distribution, ghost cells, and apoptotic bodies. It is essential to distinguish tumor necrosis from infarct-type necrosis, which may result from FNA or CNB and is associated with fibrosis, granulation tissue, histiocytes, hemosiderin, calcification, and cholesterol clefts [2,21].

ST growth pattern was observed in seven cases, including six showing solid growth and one with trabecular architecture. Despite the presence of these patterns, none of the cases met the Turin criteria for PDTC due to retention of PTC-type nuclear features. Similarly, Tondi Resta et al. [13] also identified poorly differentiated features (solid and trabecular patterns) in five of 32 HGDTC cases. In the present study, no significant differences in clinicopathological profiles or outcomes were observed between HGDTC cases with an ST pattern and those without an ST pattern. This may be attributable to the small sample size. Hitherto, the prognostic significance of ST patterns remains unclear in the current literature of HGDTC.

Six patients (54.5%) presented with metastases at diagnosis, all of them found with lymph node involvement (100%) and one patient with concurring distant metastases to the lungs and bones (16.7%). One patient (9.1%) developed vertebral metastases 9 months after diagnosis. These findings are consistent with previous studies and reflect the aggressive clinical behavior of HGDTC [7,12].

Lymphatic invasion was present in 54.5% of cases, vascular invasion in 18.2%, perineural in 9.1%, and extrathyroidal extension in 45.5%. These findings are consistent with prior reports, which noted high rates of invasion and extrathyroidal extension in HGDTC [9,13]. Although lymphatic and vascular invasion are not part of the diagnostic criteria for HGDTC, their presence is linked to aggressive tumor behavior and higher recurrence rates, underscoring their importance in assessing tumor aggressiveness [22,23].

AJCC 8th edition staging classified eight cases (72.7%) as stage I, two (18.2%) as stage II, and one (9.1%) as stage IVB. Similar staging distributions were highlighted by Jeong et al. [9] who found most patients in stage I and II, likely due to the younger age profile of the cohort. Although Thompson [7] reported that 64% of cases occurred in patients ≥55 years, most were staged as AJCC stage I–II, with only a few reaching stages III or IV. As with other thyroid carcinomas, a higher AJCC

stage is associated with worse prognosis [13].

The Ki-67 proliferation index varied across studies, with our median value of 14% (range, 5% to 45%). While some studies did not report or specify Ki-67 values, those that did reported medians ranging from 8.3% to 20%, and means from 5.6% to 9.4% (Table 3). Our findings, however, are consistent with WHO's suggested range (10%–30%) [5]. Despite evidence linking high Ki-67 to metastatic potential, the prognostic significance remains debated, as Thompson [7] observed no clear difference in metastatic risk between low (<5%) and high (>15%) Ki-67 groups.

All cases had molecular investigation; two cases (18.2%) with *BRAF*V600E mutations, four cases (36.4%) with *TERT*p mutations, and two cases (18.2%) with multiple mutations (one with *BRAF*V600E and *TERT*p (C228T) mutation, the other with *BRAF*V600E and *PIK3CA* mutation). The remaining cases showed no detectable mutations in *BRAF*V600E, *NRAS*, *HRAS*, *TP53*, *PIK3CA*, *PTEN*, or the *TERT*p. Further investigation is warranted since the remaining three cases may harbor genetic alterations not assessed in this study. Cracolici and Cipriani [2] and Wong et al. [8] suggested that *BRAF*V600E mutations are more frequently associated with HGDTC. In this series, the molecular profiles align with prior reports across the different tumor types. HGDTC commonly showed driver mutations such as *RAS*, *BRAF*, *PIK3CA*, *PPARγ*, *PTEN*, *CDKN2C*, *ARID1A*, and *PIK3R1*, while *TERT*p mutations were typically observed as a later genetic event [7].

FNA was performed in three patients (27.3%), among these two (66.7%) were classified as Bethesda VI and one (33.3%) as Bethesda IV. Similar results were discovered by Tondi Resta et al. [13] (43.8% Bethesda VI and 31.3% Bethesda IV), reflecting the predominance of PTC subtypes in HGDTC [12,24]. That being said, cytologic diagnosis of HGDTC remains challenging. The presence of DTC components may obscure high-grade features and evaluation of necrosis along with mitotic activity is limited on cytologic preparations. FNA has low sensitivity for detecting high-grade features. Necrosis may appear nonspecific and mitotic figures are rarely seen. Even when present, they can be difficult to distinguish from apoptotic or degenerative cells. Additionally, mitotic index cannot be reliably quantified in cytology specimens due to a lack of standardized field size [24-26].

CNB was conducted in seven (63.6%) cases prior to thyroidectomy, with one (14.3%) case categorized as KTA IIIB, three (42.9%) as KTA IV, one (14.3%) as KTA V, and two (28.5%) as KTA VI. No prior studies have included CNB classification as a variable, and discrepancies between CNB and final histopathology were observed. These may be due to inadequate sampling or poor representation of nuclear features in follicular cells, where nuclei may appear smaller and hyperchromatic, limiting detection of PTC features [27]. In daily practice, HGDTC is rarely encountered and difficult to diagnose using small CNB specimens. Harahap et al. [27] reported only 3 HGDTC cases among 338 thyroid nodules sampled by CNB between July 2022 and July 2024 in our institution.

In terms of treatment, four patients underwent surgery alone, six received combined RAI therapy, and one with additional EBRT. All of our patients were still alive at follow-up. Thompson [7] also reported a mortality rate of three out of 17 HGDTC cases, with a median survival of 12.1 months following diagnosis [7,9,12].

There are several limitations to our study. The follow-up duration was relatively short, even though some of the reviewed cases dated back to 2019. A proper assessment of disease-specific survival and overall survival generally requires a minimum follow-up period of 5 years. In addition, the limited number of genes examined may have failed to reveal the underlying molecular alterations in some cases. Another limitation relates to mitotic quantification. Although all slides were re-reviewed and the mitotic counts remained largely consistent, some degree of measurement imprecision is still possible when relying solely on H&E sections. Our institution lacks PHH3 immunostaining, a technique that improves the accuracy of counting cell division (mitoses). This absence may have reduced the precision of our proliferative assessment.

This study provides a comprehensive overview of our institutional experience with HGDTC. We reported 11 cases of HGDTC diagnosed between 2019 and 2024. The mean patient age was 54.6 years, which is similar to those in previous studies. Most cases of HGDTC are dominated by women, with a female-to-male ratio of 2.7:1. The cases in our cohort were consistent with the characteristics described by the WHO, including relatively large tumor size (mean, 6.4 cm), a high frequency of extrathyroidal extension, and the presence of metastases at initial presentation. Six cases (54.5%) had metastases at diagnosis; all involved lymph nodes (100%), and one case (16.7%) showed distant organ metastasis. Most cases (90.9%) were PTC, with the tall cell subtype being the most frequent, followed by the IEFVPTC and classic subtypes. All HGDTC cases showed tumor necrosis, and the mean mitotic count was 3 per 2 mm^2. The median Ki-67 proliferation index was 14% (range, 5% to

https://doi.org/10.4132/jptm.2026.01.15

45%). All of our cases had molecular investigation: *BRAF*V600E mutations in two cases, *TERT*p mutations in four cases, multiple mutations (*BRAF*V600E and *TERT*p (C228T), *BRAF*V600E and *PIK3CA*) were detected in two cases, while three cases showed no detectable mutations in *BRAF*V600E, *NRAS*, *HRAS*, *TP53*, *PIK3CA*, *PTEN*, or the *TERT*p. These findings reflect the aggressive nature of HGDTC, which clearly distinguishes it from DTC without high-grade features. Given its poorer prognosis and more advanced clinical behavior, accurate recognition of HGDTC is essential.

Supplementary Information
The Data Supplement is available with this article at https://doi.org/10.4132/jptm.2026.01.15.

Ethics Statement
This retrospective study has been approved by the Ethics Committee of Universitas Indonesia (No. KET-901/UN2.F1/ETIK/PPM.00.02/2024). The need for informed consent was waived due to the retrospective nature of the study.

Availability of Data and Material
The datasets generated or analyzed during the study are available from the corresponding author on reasonable request.

Code Availability
Not applicable.

ORCID

Novita	https://orcid.org/0009-0006-7717-5919
Agnes Stephanie Harahap	https://orcid.org/0000-0001-8920-7873
Maria Francisca Ham	https://orcid.org/0000-0002-7915-5536
Alfianto Widiono	https://orcid.org/0009-0007-4357-7765
Chan Kwon Jung	https://orcid.org/0000-0001-6843-3708

Author Contributions
Conceptualization: N, ASH, CKJ. Data curation: N, ASH, MFH. Formal analysis: N, ASH, AW. Investigation: N, ASH, MFH, CKJ. Methodology: N, ASH, AW, CKJ. Project administration: N, AW. Resources: N, ASH, MFH. Supervision: MFH, CKJ. Validation: ASH, MFH, CKJ. Visualization: N, ASH. Writing—original draft: N, ASH, AW. Writing—review & editing: all authors. Approval of final manuscript: all authors.

Conflicts of Interest
C.K.J., the editor-in-chief of the *Journal of Pathology and Translational Medicine*, was not involved in the editorial evaluation or decision to publish this article. All remaining authors have declared no conflicts of interest.

Funding Statement
No funding to declare.

REFERENCES

1. Bray F, Laversanne M, Sung H, et al. Global cancer statistics 2022: GLOBOCAN estimates of incidence and mortality worldwide for 36 cancers in 185 countries. CA Cancer J Clin 2024; 74: 229-63.
2. Cracolici V, Cipriani NA. High-grade non-anaplastic thyroid carcinomas of follicular cell origin: a review of poorly differentiated and high-grade differentiated carcinomas. Endocr Pathol 2023; 34: 34-47.
3. Harahap AS, Roren RS, Imtiyaz S. A comprehensive review and insights into the new entity of differentiated high-grade thyroid carcinoma. Curr Oncol 2024; 31: 3311-28.
4. Basolo F, Macerola E, Poma AM, Torregrossa L. The 5th edition of WHO classification of tumors of endocrine organs: changes in the diagnosis of follicular-derived thyroid carcinoma. Endocrine 2023; 80: 470-6.
5. Ghossein RA, Baloch ZW, Erickson LA, et al. High-grade follicular cell-derived non-anaplastic thyroid carcinoma [Internet]. Lyon: International Agency for Research on Cancer, 2022 [cited 2024 Apr 10]. Available from: https://tumourclassification.iarc.who.int/chaptercontent/53/47.
6. Jung CK, Baek JH, Na DG, Oh YL, Yi KH, Kang HC. 2019 Practice guidelines for thyroid core needle biopsy: a report of the Clinical Practice Guidelines Development Committee of the Korean Thyroid Association. J Pathol Transl Med 2020; 54: 64-86.
7. Thompson LD. High grade differentiated follicular cell-derived thyroid carcinoma versus poorly differentiated thyroid carcinoma: a clinicopathologic analysis of 41 cases. Endocr Pathol 2023; 34: 234-46.
8. Wong KS, Dong F, Telatar M, et al. Papillary thyroid carcinoma with high-grade features versus poorly differentiated thyroid carcinoma: an analysis of clinicopathologic and molecular features and outcome. Thyroid 2021; 31: 933-40.
9. Jeong SI, Kim W, Yu HW, et al. Incidence and clinicopathological features of differentiated high-grade thyroid carcinomas: an institutional experience. Endocr Pathol 2023; 34: 287-97.
10. Caldeira M, Canberk S, Macedo S, Melo M, Maximo V, Soares P.

Comparative analysis of follicular cell- derived thyroid carcinoma: assessing the impact of high-grade features in an advanced disease cohort. Virchows Arch 2025; 486: 1305-15.
11. Hiltzik D, Carlson DL, Tuttle RM, et al. Poorly differentiated thyroid carcinomas defined on the basis of mitosis and necrosis: a clinicopathologic study of 58 patients. Cancer 2006; 106: 1286-95.
12. Xu B, David J, Dogan S, et al. Primary high-grade non-anaplastic thyroid carcinoma: a retrospective study of 364 cases. Histopathology 2022; 80: 322-37.
13. Tondi Resta I, Gubbiotti MA, Montone KT, Livolsi VA, Baloch ZW. Differentiated high grade thyroid carcinomas: Diagnostic consideration and clinical features. Hum Pathol 2024; 144: 53-60.
14. Poma AM, Macerola E, Ghossein RA, Tallini G, Basolo F. Prevalence of differentiated high-grade thyroid carcinoma among well-differentiated tumors: a systematic review and meta-analysis. Thyroid 2024; 34: 314-23.
15. Xu B, Ghossein R. Poorly differentiated thyroid carcinoma. Semin Diagn Pathol 2020; 37: 243-7.
16. Ghossein R, Katabi N, Dogan S, et al. Papillary thyroid carcinoma tall cell subtype (PTC-TC) and high-grade differentiated thyroid carcinoma tall cell phenotype (HGDTC-TC) have different clinical behaviour: a retrospective study of 1456 patients. Histopathology 2024; 84: 1130-8.
17. Ghossein RA, Scholfield DW, Qin H, Shaha AR, Ganly I, Xu B. High-grade papillary thyroid carcinoma, diffuse sclerosing subtype: a series of 18 cases detailing the pathologic features, potential for misdiagnosis, and aggressive clinical behavior. Am J Surg Pathol 2025; 49: 481-9.
18. Pyo JY, Cha YJ, Hong S. *TERT* mutations and aggressive histopathologic characteristics of radioiodine-refractory papillary thyroid cancer. J Pathol Transl Med 2024; 58: 310-20.
19. Yee PP, Li W. Tumor necrosis: a synergistic consequence of metabolic stress and inflammation. Bioessays 2021; 43: e2100029.
20. Metovic J, Cabutti F, Osella-Abate S, et al. Clinical and pathological features and gene expression profiles of clinically aggressive papillary thyroid carcinomas. Endocr Pathol 2023; 34: 298-310.
21. Cracolici V. No longer well-differentiated: diagnostic criteria and clinical importance of poorly differentiated/high-grade thyroid carcinoma. Surg Pathol Clin 2023; 16: 45-56.
22. Moon S, Song YS, Jung KY, et al. The initial risk stratification system for differentiated thyroid cancer: key updates in the 2024 Korean Thyroid Association Guideline. Endocrinol Metab (Seoul) 2025; 40: 357-84.
23. Wagner K, Abraham E, Tran B, et al. Lymphovascular invasion and risk of recurrence in papillary thyroid carcinoma. ANZ J Surg 2020; 90: 1727-32.
24. Harahap AS, Jung CK. Cytologic hallmarks and differential diagnosis of papillary thyroid carcinoma subtypes. J Pathol Transl Med 2024; 58: 265-82.
25. Xu B, Ghossein R. Critical prognostic parameters in the anatomic pathology reporting of differentiated follicular cell-derived thyroid carcinoma. Cancers (Basel) 2019; 11: 1100.
26. Torous VF, Jitpasutham T, Baloch Z, et al. Cytologic features of differentiated high-grade thyroid carcinoma: a multi-institutional study of 40 cases. Cancer Cytopathol 2024; 132: 525-36.
27. Harahap AS, Ham MF, Werdhani RA, et al. Lessons learned from the first 2 years of experience with thyroid core needle biopsy at an Indonesian national referral hospital. J Pathol Transl Med 2025; 59: 149-60.

https://doi.org/10.4132/jptm.2026.01.15

JPTM

ORIGINAL ARTICLE

pISSN 2383-7837 · eISSN 2383-7845

Journal of Pathology and Translational Medicine 2026; 60: 349-355
https://doi.org/10.4132/jptm.2026.02.08

Incidental serrated lesions of the appendix: analysis of 2,137 appendectomy specimens

Ömer Atmış, Ecem Dokuzlu Küçük, Hanife Seda Mavili, Fatma Seher Pehlivan, Ayça Tan, Semin Ayhan

Department of Pathology, Faculty of Medicine, Manisa Celal Bayar University, Manisa, Türkiye

Graphical abstract

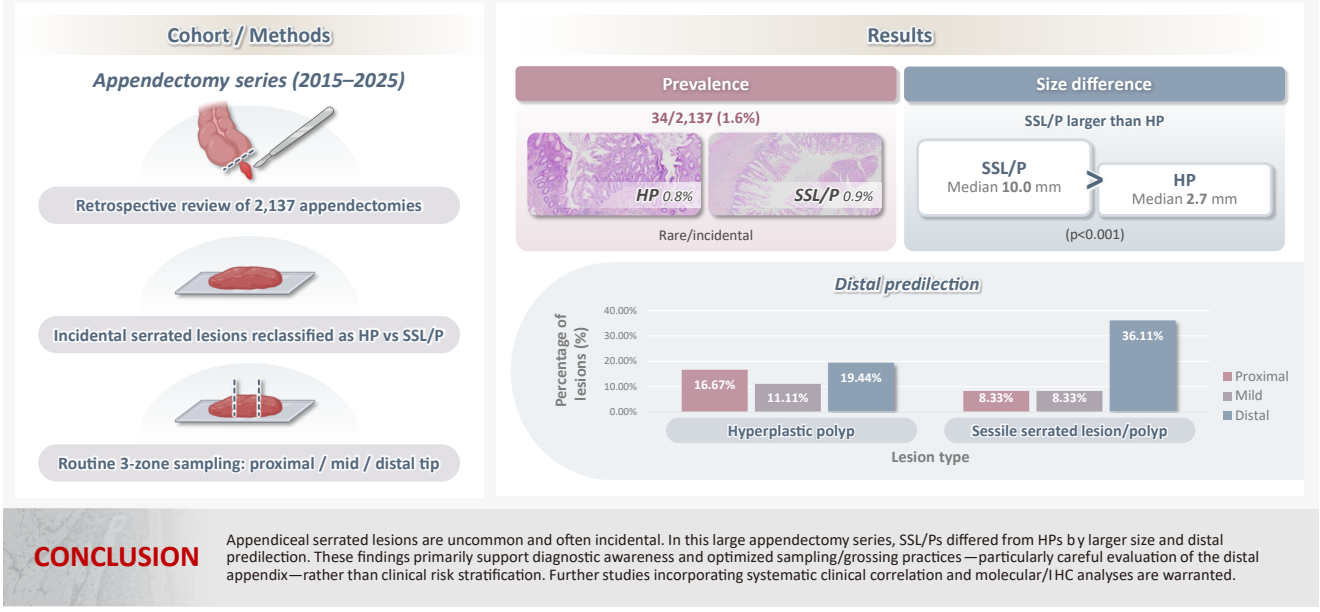

JPTM

ORIGINAL ARTICLE

pISSN 2383-7837 · eISSN 2383-7845

Journal of Pathology and Translational Medicine 2026; 60: 349-355
https://doi.org/10.4132/jptm.2026.02.08

Incidental serrated lesions of the appendix: analysis of 2,137 appendectomy specimens

Ömer Atmış, Ecem Dokuzlu Küçük, Hanife Seda Mavili, Fatma Seher Pehlivan, Ayça Tan, Semin Ayhan

Department of Pathology, Faculty of Medicine, Manisa Celal Bayar University, Manisa, Türkiye

Background: Serrated lesions of the appendix are rare, often incidental findings in routine appendectomy specimens. Their true frequency, histopathologic spectrum, and anatomic distribution remain incompletely characterized, partly due to variability in sampling practices. **Methods:** We retrospectively reviewed 2,137 appendectomy specimens (2015–2025) from a single tertiary pathology center. Cases with histologically confirmed serrated lesions were reexamined, classified as hyperplastic polyp (HP) or sessile serrated lesion/polyp (SSL/P), and assessed for clinicopathologic parameters including lesion size, location, and associated pathologies. Nonparametric tests were used, with statistical significance defined as $p < .05$. **Results:** Serrated lesions were identified in 34 cases (1.6%) with 36 serrated lesions, comprising 17 HPs (0.8%) and 19 SSL/Ps (0.9%). SSL/Ps were significantly larger than HPs (median 10.0 vs. 2.7 mm, $p < .001$) and were more frequently located in the distal appendix (68.4% vs. 33.3%, $p = .045$, one-tailed Fisher's exact test). No dysplasia or traditional serrated adenoma was detected. Acute appendicitis was present in 88% of cases, and associated neoplasms in 9%. **Conclusions:** Appendiceal serrated lesions are uncommon and often incidental. In this large appendectomy series, SSL/Ps differed from HPs by larger size and distal predilection. These findings primarily support diagnostic awareness and optimized sampling/grossing practices—particularly careful evaluation of the distal appendix—rather than clinical risk stratification. Further studies incorporating systematic clinical correlation and molecular/immunohistochemistry analyses are warranted.

Keywords: Appendix; Serrated Polyps; Sessile serrated polyp; Hyperplastic Polyps; Incidental neoplasms

INTRODUCTION

The appendix is one of the most frequently excised gastrointestinal organs due to the clinical suspicion of acute appendicitis, and in a subset of cases, unexpected or incidental lesions are identified during histopathological examination [1]. Recognition of these incidental findings in appendectomy specimens has gained increasing importance in surgical pathology practice [2]. Among these lesions, the serrated polyp family—including hyperplastic polyp (HP), sessile serrated lesion/polyp (SSL/P), and traditional serrated adenoma (TSA)—is classified according to colorectal terminology in most reports of appendiceal serrated lesions [3,4].

Although serrated lesions of the appendix share many morphologic similarities with their colorectal counterparts, certain unique features arise due to the appendix's distinct anatomy and sampling characteristics. For example, a Turkish series reported circumferential involvement in 63.9% of HPs and 74.3% of SSL/Ps [5]. Most of these lesions cannot be detected clinically or radiologically, and diagnosis is usually established during routine histopathological evaluation of the appendectomy specimen [6].

The reported incidence of serrated lesions varies markedly depending on the sampling strategy. In one study, the incidence was 9.3% when the entire appendix was entirely submitted for histologic evaluation, compared with 1.8% in partially sampled specimens [7]. In a Turkish cohort of 960 appendectomy specimens, 71 serrated polyps (7.39%) were identified—36 (50.7%)

Received: December 5, 2025 **Revised:** February 8, 2026 **Accepted:** February 9, 2026
Corresponding Author: Hanife Seda Mavili, MD
Department of Pathology, Hafsa Sultan Hospital, Manisa Celal Bayar University, Manisa 45030, Türkiye
Tel: +90-530-3983544, E-mail: sedaa_ugur@hotmail.com

HPs, 33 (46.5%) SSL/Ps, and two (2.8%) TSAs [5].

Several studies have provided insights into the distribution and size of these lesions. In one series, 45% of 40 serrated lesions were located at the distal tip of the appendix, and 87.5% exhibited a local continuous distribution. Notably, 42.5% of lesions measured ≤6 mm in length, suggesting that appendiceal serrated lesions are typically small and can be easily overlooked both macroscopically and microscopically [7]. Previous studies have shown that extensive and complete sampling of appendectomy specimens increases the detection rate of incidental lesions [8]; however, there is no established consensus regarding the optimal number of blocks required for adequate routine sampling.

From a molecular perspective, *KRAS* mutations are more frequently observed than *BRAF* mutations in appendiceal serrated lesions, supporting the notion that the serrated neoplastic pathway in the appendix may differ from that of the colon [2,4,9].

In summary, the identification of serrated lesions—many of which may be missed in routine practice—depends on the sampling protocol, the level of histologic scrutiny, and the representativeness of the examined tissue. Investigating their true prevalence and clinicopathologic features is therefore warranted. In particular, defining pathological parameters such as anatomic distribution and lesion size may provide valuable contributions to the existing literature.

The present study aims to provide a descriptive analysis of the incidence, histopathologic spectrum, macroscopic/grossing-related sampling characteristics, and anatomic distribution of incidentally detected appendiceal serrated lesions in appendectomy specimens (2015–2025), with a particular focus on the practical utility of a routine zonal sampling approach.

MATERIALS AND METHODS

Study design and cases

This retrospective descriptive study included 2,137 appendectomy specimens evaluated between 2015 and 2025 at the Department of Pathology, Manisa Celal Bayar University Faculty of Medicine. The pathology database was reviewed to identify incidentally detected serrated lesions among appendectomy specimens performed for suspected appendicitis or other indications.

Patient data—including age, sex, diagnosis, presence of associated neoplasms, and macroscopic findings of the appendix—were retrieved from pathology reports. All slides of cases with serrated lesions were re-examined, diagnoses were confirmed, and necessary measurements were performed.

Histopathological examination and sampling protocol

In our department, appendectomy specimens are routinely sampled in three anatomical zones as follows: block 1, proximal surgical margin (en face); block 2, mid-appendiceal segment (2–3 tissue sections); block 3, distal tip of the appendix.

In cases where no definite evidence of acute appendicitis was observed macroscopically or when a suspicious lesion was noted, additional sampling was performed to increase the number of tissue blocks. Serial sections were obtained when necessary to ensure complete morphologic evaluation of the lesion. In cases with suspected neoplasia, additional blocks were taken, and if required, the entire appendix was submitted for histologic examination.

Lesion characterization and measurements

All slides were re-reviewed to confirm the diagnosis and to classify the lesions as HP or SSL/P according to the criteria of the WHO Classification of Digestive System Tumours, 5th Edition (2019) [10].

For each case, the largest diameter of the lesion was measured microscopically using a calibrated micrometer and recorded in millimeters. The anatomic location (zone) of each lesion was determined based on the block in which it was identified—proximal, mid, or distal. In cases where a lesion was present in multiple blocks, the most proximal block was designated as the primary site.

Since additional resampling was performed in some cases and the total number of tissue pieces in the standard three-block protocol varied, the total number of sampled tissue fragments was also recorded for each case.

Statistical analysis

All statistical analyses were performed using IBM SPSS Statistics ver. 25.0 (IBM Corp., Armonk, NY, USA). The normality of data distribution was evaluated using the Kolmogorov-Smirnov and Shapiro–Wilk tests. Descriptive statistics were presented as mean ± standard deviation, median (minimum–maximum), and percentage (%) values. Categorical variables were compared using the chi-square test or Fisher's exact test, while continuous variables were compared using the Mann-Whitney U test or Kruskal-Wallis test as appropriate.

For the analysis of lesion location, a one-tailed Fisher's exact

https://doi.org/10.4132/jptm.2026.02.08

test was applied to test the directional hypothesis that SSL/Ps would show distal predominance, as suggested by previous reports. A p-value < .05 was considered statistically significant.

RESULTS

Among 2,137 appendectomy specimens examined during the study period, 34 cases (1.6%) contained serrated lesions—17 HP (0.8%) and 19 sessile SSL/P (0.9%). One patient had three HPs, while the remaining patients had a single lesion. For case-based analyses, only the most proximal lesion was considered to represent that case, in order to avoid clustering effects. Lesion-based analyses (n = 36 lesions in total) were performed separately where appropriate. No TSA or dysplasia was identified. Table 1 summarizes the main clinical and histologic findings. Representative histopathologic features are shown in Fig. 1.

The patients included 16 men and 18 women (mean age, 52.6 ± 18.4 years). A total of 36 serrated lesions were recorded across these 34 cases. Acute appendicitis was present in most specimens (88.2%), and periappendicitis in 61.8%. Diverticula were noted in 20.6%, and associated neoplasms—two grade I neuroendocrine tumors and one metastatic adenocarcinoma—were identified in 8.8% of cases.

Colonoscopy and upper gastrointestinal endoscopy data were available in three patients (one with SSL/P and two with HP). One patient with an appendiceal HP had multiple tubular adenomas and right-sided colonic adenocarcinoma, along with a gastric hyperplastic polyp. No colorectal or gastric polyps were detected in the remaining two patients. In addition, one patient with appendiceal SSL/P without available colonoscopy data was

Table 1. General characteristics of the cases (n = 34)

Characteristic	No. (%)
Sex	
Male	16 (47.1)
Female	18 (52.9)
Type of lesion	
Hyperplastic polyp	17 (47.2)
Sessile serrated lesion/polyp	19 (52.8)
Acute appendicitis	30 (88.2)
Periappendicitis	21 (61.8)
Diverticulum	7 (20.6)
Associated neoplasm	3 (8.8)
Location (lesion-based, n = 36)	
Proximal	9 (25.0)
Middle segment	7 (19.4)
Distal	20 (55.6)
Perforation	1 (2.9)

A total of 34 cases (patients) were included, comprising a total of 36 lesions. One patient harbored three hyperplastic polyps. Case-based analyses were performed using the most proximal lesion of each case.

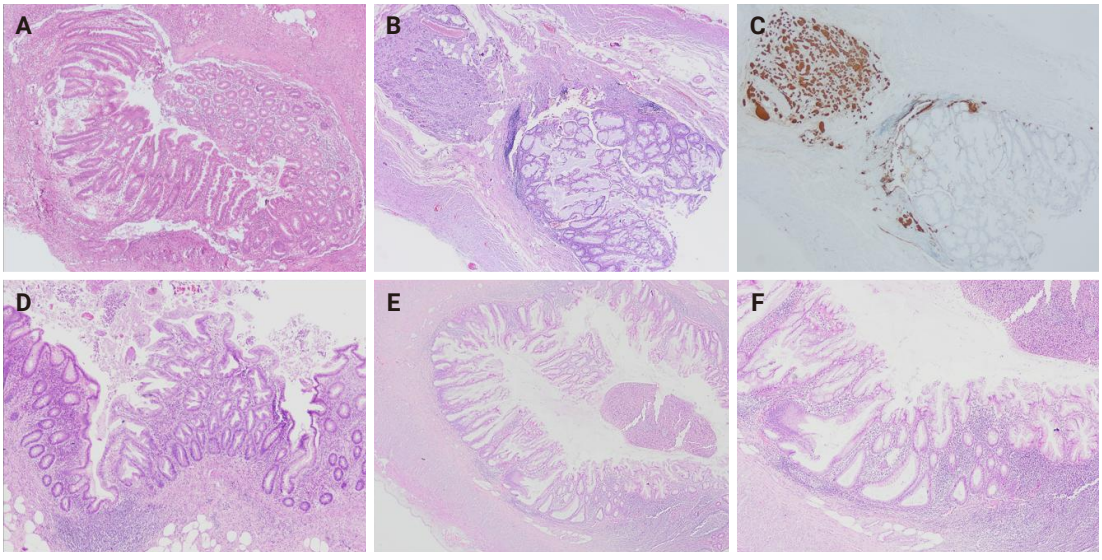

Fig. 1. Representative histopathologic features of appendiceal serrated lesions, including a case coexisting with a neuroendocrine tumor. (A) Proximally located hyperplastic polyp. (B) Distal-type neuroendocrine tumor adjacent to a sessile serrated lesion/polyp (SSL/P). (C) Synaptophysin immunoreactivity in the neuroendocrine tumor. (D) Distally located hyperplastic polyp. (E) Distally located SSL/P. (F) The same SSL/P showing dilated, asymmetric crypt bases.

diagnosed with left-sided colonic adenocarcinoma.

Lesions were predominantly located in the distal appendix (55.6%), followed by the proximal (25.0%) and mid segments (19.4%) (Table 1). The mean lesion diameter was 6.5 ± 5.0 mm (median, 4.0 mm; range, 1.5 to 17.9 mm). No significant differences were found between HP and SSL/P groups with respect to age, appendix length, or diameter ($p > .05$). However, SSL/Ps were significantly larger than HPs in case-based analysis ($p < .001$) (Table 2, Fig. 2A). Lesion-based analysis yielded similar results, with SSL/Ps showing significantly larger sizes than HPs ($p < .001$) and a tendency for distal predominance ($p = .242$). The number of sampled tissue fragments was slightly higher in SSL/Ps, showing a near-significant trend ($p = .079$).

Clinicopathologic variables—including sex, presence of acute appendicitis, periappendicitis, diverticulum, and perforation—did not differ significantly between the two groups (all $p > .05$). Although associated neoplasms were more frequent among SSL/Ps (15.8%) than HPs (0%), this difference did not reach statistical significance ($p = .238$). These comparative data are detailed in Table 3.

SSL/Ps demonstrated a distal predilection (68.4% vs. 33.3% in HPs), which was statistically supported by a one-tailed Fisher's exact test ($p = .045$) and a linear-trend analysis ($p = .047$) (Fig. 2B). Lesion size did not vary significantly by anatomic zone ($p = .520$, Kruskal-Wallis test).

DISCUSSION

This single-center study evaluated the prevalence and histopathologic characteristics of incidentally detected serrated

Table 2. Comparison of HP and SSL/P cases

Variable	Median [IQR] (min–max)		Mann-Whitney U	Z	p-value (2-tailed)
	HP (n = 15)	SSL/P (n = 19)			
Age (yr)	59 [33–67] (26–82)	60 [37–66] (21–81)	139.0	–0.12	.903
Lesion size (mm)	2.7 [2.0–3.8] (1.5–9.0)	10.0 [5.8–13.3] (2.0–17.9)	36.0	–3.70	<.001
No. of sampled tissue fragments	6 [5–7] (4–11)	7 [5.5–9] (4–15)	92.5	–1.76	.079
Appendix length (cm)	5.7 [5.0–8.0] (4.5–8.7)	6.0 [4.3–6.8] (3.0–9.0)	110.0	–1.13	.258
Appendix diameter (cm)	0.9 [0.75–1.0] (0.5–2.0)	0.8 [0.7–1.15] (0.6–3.5)	142.0	–0.02	.986

HP, hyperplastic polyp; SSL/P, sessile serrated lesion/polyp; IQR, interquartile range.

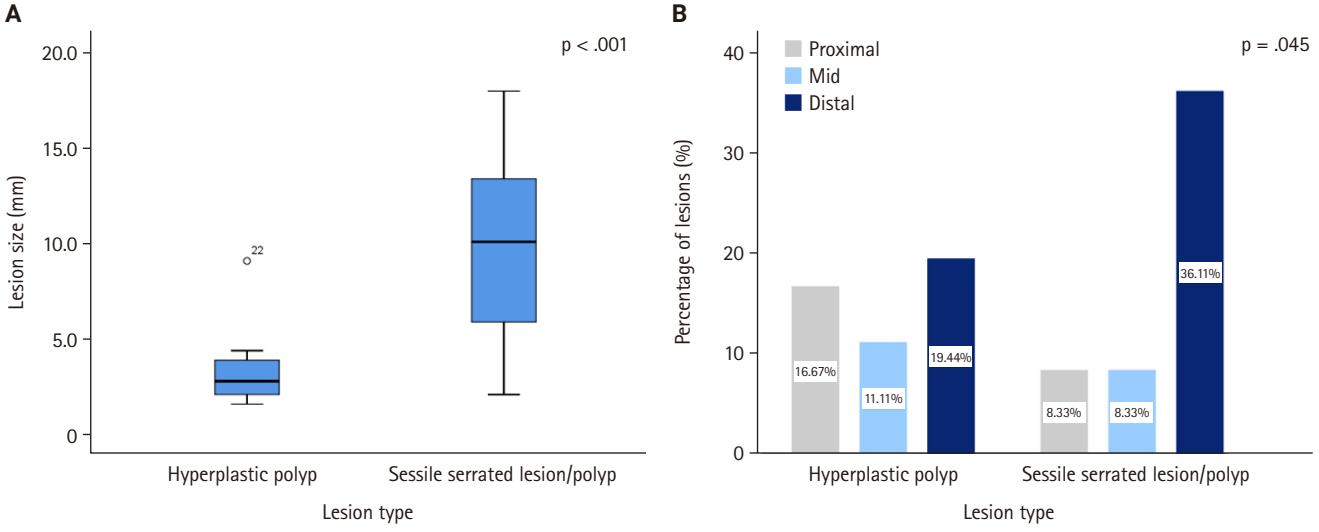

Fig. 2. Comparison of lesion size and anatomic distribution between hyperplastic polyps (HP) and sessile serrated lesions/polyps (SSL/P). (A) Boxplot showing lesion size by lesion type. SSL/Ps were significantly larger than HPs ($p < .001$, Mann-Whitney U test). (B) Bar chart illustrating the anatomic distribution of HP and SSL/P within the appendix. SSL/Ps were significantly more frequent in the distal segment ($p = .045$, Fisher's exact test, one-tailed).

https://doi.org/10.4132/jptm.2026.02.08

Table 3. Comparison of clinical and histopathologic features between HP and SSL/P cases

Variable	HP (n = 15)	SSL/P (n = 19)	p-value
Sex (male/female)	6/9	10/9	.464
Presence of acute appendicitis	14 (93.3)	16 (84.2)	.613[a]
Presence of periappendicitis	11 (73.3)	10 (52.6)	.296[a]
Presence of diverticulum	3 (20.0)	4 (21.1)	>.99[a]
Associated neoplasm	0	3 (15.8)	.238[a]
Location zone			
Proximal	6 (40.0)	3 (15.8)	
Middle segment	4 (26.7)	3 (15.8)	
Distal segment	5 (33.3)	13 (68.4)	.117[b]
Perforation	1 (6.7)	0	.441[a]

Values are presented as number (%).
HP, hyperplastic polyp; SSL/P, sessile serrated lesion/polyp.
[a]Fisher's exact test; [b]Pearson χ^2 test (linear-trend p = .047).

lesions (HP and SSL/P) in appendectomy specimens. The observed rate of 1.6% aligns with previously reported frequencies of incidental appendiceal neoplasms (1.5%–2.1%) [11,12], indicating methodological comparability with prior series. Differences in reported prevalence across institutions are largely attributable to sampling strategy: complete submission of the entire appendix substantially increases detection compared with partial sampling (9.3% vs. 1.8%) [7], and intensified block submission similarly improves the yield of otherwise rare or subtle lesions [8].

Morphologically, SSL/Ps slightly outnumbered HPs (52.8% vs. 47.2%), were significantly larger, and showed a distal predilection in our cohort. This distal tendency is in line with previous studies describing a tip-dominant distribution of appendiceal serrated lesions, particularly for SSL/Ps [3,5,7]. Because many lesions are small (≤6 mm in fully submitted specimens), limited or non-representative sectioning may miss focal serrated changes, underscoring the need for careful microscopic scrutiny and appropriate block selection, particularly in the distal segment [7,8].

Although colonoscopy was not routinely performed, endoscopic data were available only in a very small subset of patients; therefore, the present cohort does not allow any inference regarding synchronous or metachronous colorectal lesions. Accordingly, any potential clinical association should be explored in future studies with systematic colonoscopic correlation.

From a molecular standpoint, appendiceal serrated lesions preferentially harbor *KRAS* rather than *BRAF* mutations, suggesting divergence from the colonic serrated pathway [9]. Broader profiling further supports the dominant role of *KRAS* across appendiceal serrated and mucinous neoplasia, suggesting site-specific biological features, as reported in prior studies, with potential diagnostic relevance [13,14]. However, molecular or immunohistochemical analyses were not performed in the present study, and the molecular characteristics discussed herein are based on previously published data. Accordingly, molecular considerations in this study are intended to provide contextual background rather than direct evidence.

Historically, the taxonomy of appendiceal epithelial proliferations was heterogeneous. The adaptation of colorectal serrated classifications to the appendix—since the seminal works of Longacre and Fenoglio-Preiser [15], Williams et al. [16], and Carr et al. [17]—and the demonstration of outcome associations have shaped contemporary diagnostic and reporting practices. Clinically, SSL/Ps may occasionally present with acute appendicitis and, rarely, with complications such as pyogenic liver abscesses, implying potential mechanical effects (e.g., luminal obstruction) even for small, focal lesions [18]. In parallel, growing interest in non-operative (antibiotic-based) management of appendicitis raises concerns about delayed recognition of incidental tumors, a consideration supported by our detection rate [19].

Current recommendations emphasize complete submission in suspicious or neoplastic settings; however, no universal consensus exists regarding a fixed number of blocks for routine appendectomies. Institutional variation in sampling intensity likely contributes to incidence variability across studies [7,8]. The distribution of HP versus SSL/P and the spectrum of concomitant lesions in our series (e.g., neuroendocrine tumors, metastasis) broadly mirror prior reports, including a Turkish series with a 7.39% serrated polyp rate, near-equal HP/SSL/P proportions, and frequent circumferential involvement [5].

In summary, although uncommon, appendiceal serrated lesions show distinct subtype-specific features: SSL/Ps are significantly larger than HPs and tend to occur distally. These observations reinforce the importance of vigilant morphologic assessment and adequate sampling—particularly of the distal portion—for accurate detection and classification. Recognition and accurate classification of these lesions may provide a framework for future studies addressing whether appendiceal serrated neoplasia follows a molecular trajectory distinct from the colorectal serrated pathway, as suggested by prior literature.

Our study has several limitations. The retrospective design, the absence of routine colonoscopic evaluation in patients with incidentally detected appendiceal serrated lesions, and the lack of molecular or immunohistochemical analyses represent major constraints. These limitations preclude meaningful clinicopathologic correlation and restrict the interpretation of our findings primarily to diagnostic and sampling-related implications. Because the majority of specimens were obtained for acute appendicitis, the low number of advanced appendiceal neoplasms may also reflect inherent selection bias. Importantly, given its retrospective and primarily descriptive design, the study was not intended to establish biological mechanisms or clinically meaningful risk estimates.

In conclusion, incidentally detected serrated lesions of the appendix are uncommon but may be underrecognized in routine practice. In our series, the prevalence was 1.6%, with SSL/Ps being significantly larger and showing a distal predilection compared with HPs. No dysplasia or TSA was observed. These findings primarily reinforce diagnostic awareness and the importance of adequate sampling and careful microscopic evaluation—particularly of the distal appendix—for the detection and classification of incidental serrated lesions. In the absence of systematic clinical correlation and molecular/immunohistochemical validation, our results should be interpreted as descriptive observations with practical implications for routine pathology practice. Prospective studies integrating standardized submission protocols with systematic clinical correlation and molecular/immunohistochemical analyses are warranted.

Ethics Statement
All procedures performed in the current study were approved by the Ethics Committee of Manisa Celal Bayar University Faculty of Medicine (approval number: 20.478.486-3609, date: 03.12.2025) in accordance with the 1964 Helsinki declaration and its later amendments. Formal written informed consent was not required, with a waiver granted by the appropriate Institutional Review Board (IRB) of Manisa Celal Bayar University Faculty of Medicine.

Availability of Data and Material
The datasets generated or analyzed during the study are available from the corresponding author on reasonable request.

Code Availability
Not applicable.

ORCID
Ömer Atmış https://orcid.org/0000-0003-4789-0875
Ecem Dokuzlu Küçük https://orcid.org/0009-0005-5389-1825
Hanife Seda Mavili https://orcid.org/0000-0003-3741-8489
Fatma Seher Pehlivan https://orcid.org/0000-0002-7702-855X
Ayça Tan https://orcid.org/0000-0003-4450-5425
Semin Ayhan https://orcid.org/0000-0002-8546-0705

Author Contributions
Conceptualization: ÖA, SA. Methodology: ÖA, AT. Data curation: EDK, FSP. Formal analysis: ÖA, AT. Investigation: ÖA, HSM. Supervision: AT, SA. Writing—original draft: ÖA. Writing—review & editing: ÖA, HSM. Approval of final manuscript: all authors.

Conflicts of Interest
The authors declare that they have no potential conflicts of interest.

Funding Statement
No funding to declare.

REFERENCES

1. Cakar E, Sevinc MM, Colak S, Demir M, Yarikkaya E, Idiz UO. Status of appendiceal neoplasms in acute appendicitis cases. Istanbul Med J 2023; 24: 241-5.
2. Constantin M, Petrescu L, Matanie C, et al. The vermiform appendix and its pathologies. Cancers (Basel) 2023; 15: 3872.
3. Bellizzi AM, Rock J, Marsh WL, Frankel WL. Serrated lesions of the appendix: a morphologic and immunohistochemical appraisal. Am J Clin Pathol 2010; 133: 623-32.
4. Requena DO, Yantiss RK. A practical guide to serrated appendiceal lesions. Semin Diagn Pathol 2024; 41: 243-9.
5. Yuyucu Karabulut Y, Savas B, Kursun N, Ensar A. Serrated lesions of the appendix: do they differ from their colorectal counterparts? Turk J Gastroenterol 2014; 25: 29-34.
6. Kaya T, Atici SD. Sessile serrated adenoma of appendix. Aegean J Med Sci 2021; 4: 105-9.
7. Li F, Lu Y, Hou F, Ma R, Wang D, Qi C. Significance of the entire appendiceal evaluation in the diagnosis of serrated lesions, low-grade appendiceal mucinous neoplasm, and appendiceal diverticulosis disease. Front Oncol 2021; 11: 812794.
8. Kepil N, Batur S, Akinci O, Pekmezci S. Incidental lesions in appendectomy specimens: rare or rarely sampled? North Clin

https://doi.org/10.4132/jptm.2026.02.08

Istanb 2021; 8: 71-5.
9. Pai RK, Hartman DJ, Gonzalo DH, et al. Serrated lesions of the appendix frequently harbor *KRAS* mutations and not *BRAF* mutations indicating a distinctly different serrated neoplastic pathway in the appendix. Hum Pathol 2014; 45: 227-35.
10. WHO Classification of Tumours Editorial Board. Digestive system tumours. 5th ed. Lyon: International Agency for Research on Cancer, 2019.
11. Nunez-Rocha RE, Giron F, Rodriguez L, et al. Incidence of appendiceal neoplasms in appendectomy patients. BMC Surg 2023; 23: 287.
12. Solis-Pazmino P, Oka K, La K, et al. Incidence rate and histology of appendiceal neoplasms in complicated versus uncomplicated appendicitis: a meta-analysis and systematic review. Langenbecks Arch Surg 2023; 408: 432.
13. Munari G, Businello G, Mattiolo P, et al. Molecular profiling of appendiceal serrated lesions, polyps and mucinous neoplasms: a single-centre experience. J Cancer Res Clin Oncol 2021; 147: 1897-904.
14. Satorres C, Garcia-Campos M, Bustamante-Balen M. Molecular features of the serrated pathway to colorectal cancer: current knowledge and future directions. Gut Liver 2021; 15: 31-43.
15. Longacre TA, Fenoglio-Preiser CM. Mixed hyperplastic adenomatous polyps/serrated adenomas: a distinct form of colorectal neoplasia. Am J Surg Pathol 1990; 14: 524-37.
16. Williams GR, du Boulay CE, Roche WR. Benign epithelial neoplasms of the appendix: classification and clinical associations. Histopathology 1992; 21: 447-51.
17. Carr NJ, McCarthy WF, Sobin LH. Epithelial noncarcinoid tumors and tumor-like lesions of the appendix: a clinicopathologic study of 184 patients with a multivariate analysis of prognostic factors. Cancer 1995; 75: 757-68.
18. Sato K, Banshodani M, Nishihara M, et al. Sessile serrated adenoma/polyp leading to acute appendicitis with multiple pyogenic liver abscesses: a case report. Int J Surg Case Rep 2018; 42: 38-43.
19. Doita S, Taniguchi F, Mouri K, et al. Retrospective analysis of risk factors associated with incidental appendiceal neoplasms in patients with acute appendicitis. Dig Surg 2025; 42: 213-9.

JPTM

CASE STUDY

pISSN 2383-7837 · eISSN 2383-7845

Journal of Pathology and Translational Medicine 2026; 60: 356-363
https://doi.org/10.4132/jptm.2025.12.31

Multidimensional analysis of concurrent proximal bronchiolar adenoma and lung carcinoma

Lu-Yao Li[1*], Gong-Ming Dong[2*], Yun-Peng Zhang[1], Ting-Ting Wang[1], Fu-Quan Jia[3], Guan-Jun Zhang[1]

[1]Department of Pathology, The First Affiliated Hospital of Xi'an Jiaotong University, Xi'an, China
[2]Health Science Center of Xi'an Jiaotong University, Xi'an, China
[3]College of Basic Medical Science, Inner Mongolia Medical University, Hohhot, China

Bronchiolar adenoma (BA) is a rare type of lung tumor characterized by bilayered epithelial cells having a continuous basal layer and a luminal layer. It resembles mucinous adenocarcinoma (MA) on frozen section, with difficulty in distinguishing the basal layer. Immunohistochemistry is the best choice for verifying the diagnosis. This study aimed to comprehensively characterize three cases of BA-combined carcinoma using clinical, histopathological, and genetic features. BA and carcinoma sections were subjected to next-generation sequencing, respectively. It was hypothesized that while different mutation forms matched different regions, BA and lung adenocarcinoma shared the same gene mutation when they co-occurred in the same location. BA with extensive carcinoma is extremely rare and presents diagnostic challenges due to its overlap with conditions such as MA. Because of its distinctive morphological characteristics, BA may be regarded as a low-grade malignancy, particularly during a confusing evaluation. A multifaceted examination of clinical, radiological, immunohistochemical, and genetic data is necessary for an accurate diagnosis.

Keywords: Adenoma; Lung neoplasms; Immunohistochemistry; Pathology, molecular; Case report

INTRODUCTION

Bronchiolar adenomas (BAs) have recently been recognized as a group of apparently benign neoplasms arising from the epithelial cell components of pulmonary bronchioles [1]. In 2021, BA or ciliated muconodular papillary tumor was defined in the 5th World Health Organization based on the characteristic bilayered architecture and a continuous basal cell layer [2]. Based on the degree of similarity to the cell proportion of bronchioles, BA was divided into proximal and distal types [2]. The continuous basal layer is a reliable histological characteristic for differentiating BA from carcinoma. Additionally, the presence of ciliated cells in frozen tissue sections consistently indicates BA rather than carcinoma [3]. During subsequent follow-ups, given its favorable prognosis, including the absence of lymph node or distant metastases in earlier studies, researchers believe that BA should be a benign tumor [4]. The possibility of BA turning into a malignant tumor could not be ruled out yet. Rapid and accurate postoperative discrimination of BA based on our proposal is crucial and will help prevent needless treatment. Additionally, no report has yet confirmed whether BA and carcinoma were accidentally mixed or had a common origin when they coex-

Received: August 29, 2025 **Revised:** November 12, 2025 **Accepted:** December 31, 2025
Corresponding Author: Guan-Jun Zhang, PhD
Department of Pathology, The First Affiliated Hospital of Xi'an Jiaotong University, No. 277 Yanta West Road, 710061, Xi'an, China
Tel, Fax: +86-029-85323251, E-mail: zgjxjtu@163.com

Fu-Quan Jia, PhD
College of Basic Medical Science, Inner Mongolia Medical University, No. 5 Xinhua Street, 010059, Hohhot, China
Tel, Fax: +86-0471-6636017, E-mail: jiafuquan915@163.com

*Lu-Yao Li and Gong-Ming Dong contributed equally to this work.

isted in the same patient. In practice, pathologists frequently misdiagnose and underdiagnose BA [5]. Different morphological characteristics of lung tumors may be identified using histologic and genetic features to presumably reveal biological behavior, transformation, and prognosis [6]. In this study, we recruited three bilayered BA cases combined with carcinoma, all of which had continuous basal cells. To determine whether the coexistence of BA and lung carcinoma suggests the potential for malignant differentiation of BA and the formation of a new specific subtype, we seek to identify the multifaceted similarities and differences between BA and carcinoma components. Investigation of molecular features, in particular, is a prerequisite for examining the relationship between BA and carcinoma, as well as possible mechanisms of tumor progression. Comprehensive evaluation of clinical, morphologic, immunohistochemical, and molecular characteristics was conducted (Fig. 1A).

CASE REPORT

Case 1

A 63-year-old male was asymptomatic and diagnosed incidentally with nodules during physical examination. The patient had a smoking history of 30 years with no family history of lung cancer. Radiologically, computed tomography (CT) revealed mixed density of nodules in the lower lobe of the right lung and the upper lobe of the left lung. No pleural effusion was observed. Complete blood count and serum tumor markers were normal. However, pulmonary function tests revealed a drop in the oxygenation index to 249 mmHg (reference range, 400–500 mmHg). Echocardiography, head CT scan, and abdominal ultrasound displayed no abnormalities. The patient underwent thoracoscopic resection of the right lung's lower lobe and frozen section analysis following the completion of preoperative evaluations.

The dimensions of the removed specimen were 10 × 8 × 3 cm. In the lung's periphery, a gray-white nodular mass (2.7 × 2.5 × 1.6 cm) was observed, invading the local pleura. A gray-red nodule (5 mm) was inadvertently found near the mass during sampling. The distance between the two was 1.5 cm. Lung adenocarcinoma or BA was first suggested based on intraoperative frozen-section analysis. The postoperative pathological findings revealed the coexistence of BA and invasive adenocarcinoma. BA was mainly flat with a few papillary structures, according to histological analysis. Under a microscope, BA displayed two distinct epithelial layers with distinct cell component ratios. Prominent mucinous cells comprised the luminal cell layer (Fig. 1B). Notably, the tumor depicted significant destruction of alveolar structure, and interstitial fibrous tissue proliferation was observed. B-Raf proto-oncogene, serine/threonine kinase (BRAF) and mucin 5AC (MUC5AC) were not expressed, according to immunohistochemistry (IHC) staining. In this instance, the invasive adenocarcinoma region displayed structures with 50% acinar (Fig. 1C), 40% papillary (Fig. 1D), and 10% micropapillary (Fig. 1E).

To identify molecular characteristics, we compared the genetic changes between the concurrent primary carcinoma and BA. Supplementary Tables S1–S3 present the genetic alterations that were discussed. Out of 15 changes found in this study, 13 were unique (Supplementary Table S4). The most common mutations found in BA and invasive adenocarcinoma were Kirsten rat sarcoma viral oncogene homolog (KRAS) G12C and Axin family member 2 (AXIN2). Furthermore, only invasive adenocarcinoma harbored a *TP53* mutation. To some extent, tumor mutation burden (TMB) was accurately reflected by single-nucleotide mutations and insertions or deletions (Indels). TMB was 9.3 in carcinoma and 4.1 in BA (Fig. 1F). The patient was diagnosed with invasive adenocarcinoma without pleural invasion after undergoing a thoracoscopic resection of the upper lobe of the right lung more than four months later. After 23 months, the patient exhibited no signs of metastasis or postsurgical recurrence.

Case 2

A 58-year-old male was admitted with abnormal lung CT manifestations. The patient had smoked for 40 years without experiencing any respiratory problems. Neuron-specific enolase (NSE) and cytokeratin 19-fragments (CYFRA21-1), two serum tumor markers, were marginally elevated. There was a slight decrease in the oxygenation index (377 mmHg). A chest CT scan revealed a fibrous rope band in the left upper lung lobe and a 14 × 18 mm nodular shadow with a spicule sign in the right upper lung lobe. He had a bilateral pulmonary wedge resection after evaluation.

The left upper lung lobe of the wedge-resected specimen had a gray nodule (10 × 6 × 5 mm). In comparison, the right upper lung lobe had a mass (17 × 14 × 10 mm). The 60% acinar (Fig. 2A), 20% papillary (Fig. 2B), and 20% adherent subtype (Fig. 2C) were found in the invasive adenocarcinoma region. The absence of cilia and basal cells, cell atypia, and an infiltrating interstitial reaction characterize invasive adenocarcinoma. The luminal epithelium inside the bilayered BA was positive for thyroid transcription factor-1 (TTF-1) (Fig. 2E), napsin A (Fig. 2F),

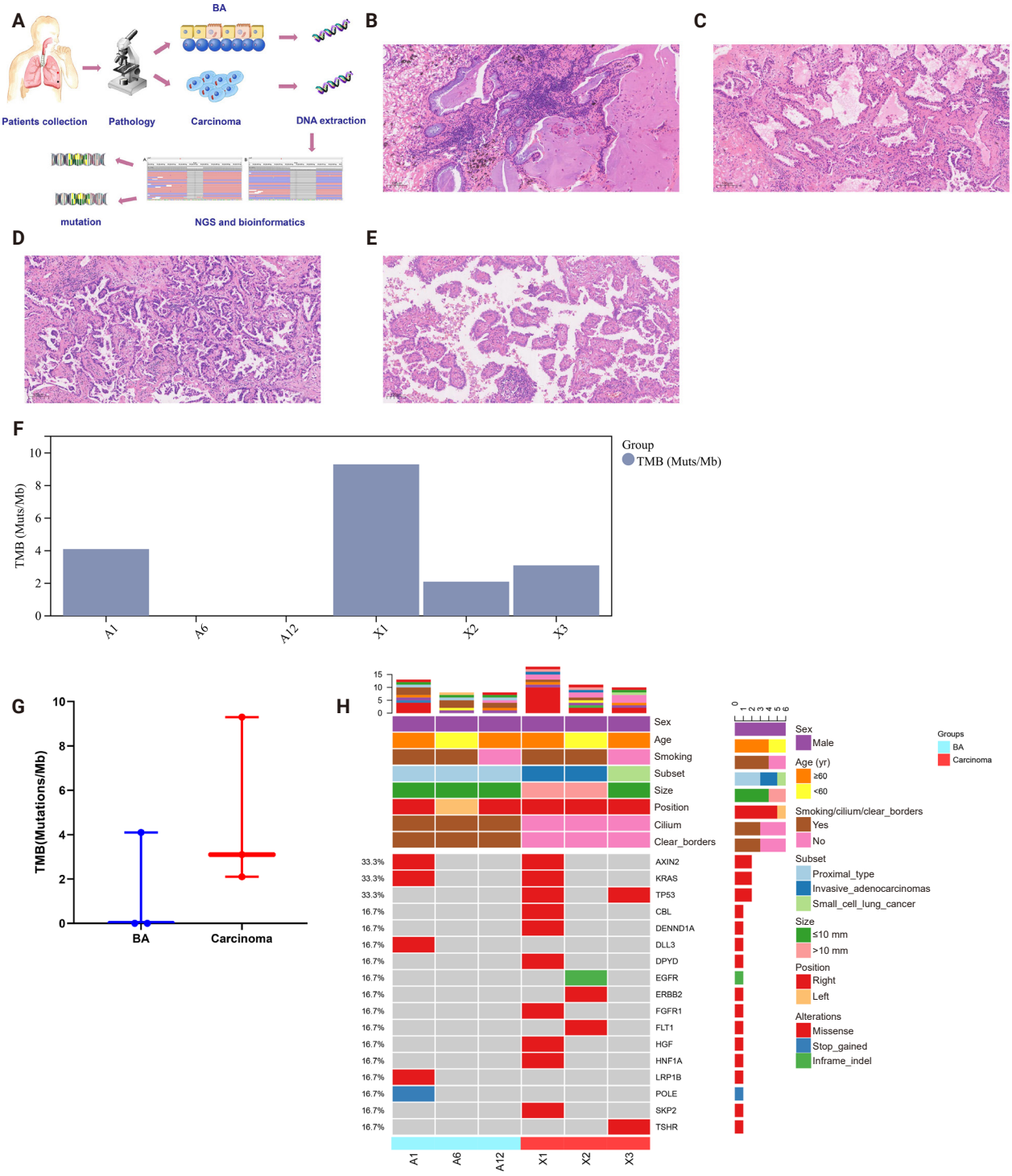

Fig. 1. Schematic diagrams and histological features of case 1. (A) Diagram illustrating the analysis process of three cases in this study. (B) Bronchial lumen filled with mucin of bronchiolar adenoma (BA) in case 1. (C) Acinar structures of adenocarcinoma in case 1. (D) Papillary structures of adenocarcinoma in case 1. (E) Micropapillary structures of adenocarcinoma in case 1. (F) Tumor mutation burden (TMB) displayed in each tumor. (G) Scatter plot comparing TMB between bilayered BAs and lung carcinomas. (H) Co-mutation plot displaying all mutations detected in each tumor. The axis on the right side of the landscape lists clinical characteristics, morphological features, and detected gene mutations. The axis on the left side reveals the percentage of cases with the corresponding mutations. NGS, next-generation sequencing.

https://doi.org/10.4132/jptm.2025.12.31

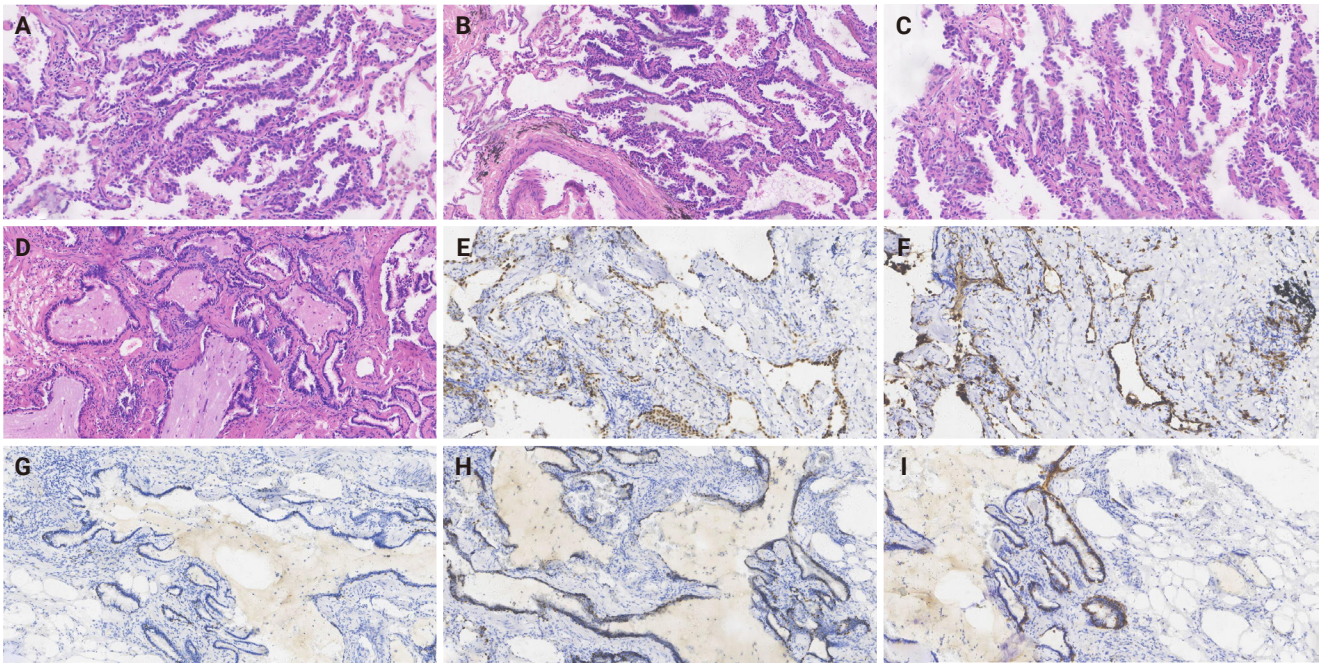

Fig. 2. Histological and immunohistochemical findings in case 2. (A) Acinar structures of invasive adenocarcinoma. (B) Papillary structures of invasive adenocarcinoma. (C) Adherent subtype of invasive adenocarcinoma. (D) The tumor with abundant mucus in the alveoli of bronchiolar adenoma (BA). (E) Luminal cells expressing thyroid transcription factor-1 in BA. (F) Luminal cells expressing napsin A in BA. (G) p40 expressed in basal cells of BA. (H) p63 expressed in basal cells of BA. (I) Cytokeratin 5/6 expressed in basal cells of BA.

p40 (Fig. 2G), p63 (Fig. 2H), and cytokeratin (CK) 5/6 (Fig. 2I) expressed in basal cells. BA was discovered by accident and lined with a spot of mucinous cells with abundant mucus in alveoli (Fig. 2D). MUC5AC and BRAF were negative. A pathology diagnosis of proximal-type BA was made based on the presence of numerous ciliated columnar cells and fragments of mucus cells in the luminal cell layer, as well as positivity for p63, p40, and CK5/6 in the basal cells, which verifies the preservation of the continuous basal cell architecture. KRAS, epidermal growth factor receptor (EGFR), anaplastic lymphoma kinase (ALK), c-ros oncogene 1, receptor tyrosine kinase (ROS1), BRAF, and other genes were not mutated or fused in BA. Only the invasive adenocarcinoma component contained EGFR (exon 19 deletion), Fms-like tyrosine kinase 1 (FLT1), and Erb-B2 receptor tyrosine kinase 2 (ERBB2). TMB was 2.1 in invasive adenocarcinoma and 0 in BA (Fig. 1F). After a 24-month follow-up, the patient made a full recovery with no distant metastases or recurrence.

Case 3

A 71-year-old male was admitted for chest tightness. Other clinical symptoms, such as cough or chest pain, were absent. The patient had no prior history of cancer or smoking. A routine CT scan revealed multiple fiber rope bands in both lungs and a 10 mm × 10 mm anterior basal segment nodule in the right lower lung lobe. No anomalies were found in the remaining tests, except for CYFRA21-1 and NSE, which were marginally elevated. He underwent surgery without frozen section pathology following laboratory testing and other preoperative examinations.

The removed specimen consisted of right middle and lower lobes of the lung, measuring 90 × 80 × 30 mm. A calcified nodule (10 mm) and a gray-red solid area (10 mm × 10 mm × 3 mm) were noted grossly, and the microscopic examination revealed the tumor to be composed of flat luminal and basal cell. The cellular constituents of the luminal epithlium were mucinous cells and ciliated columnar cells. Some BA foci displayed central fibrosis and focal lymphocyte infiltration (Fig. 3A). Notably, the tumor cells displayed no signs of necrosis, mitosis, or atypia. IHC revealed that luminal cells were negative for CK5/6, p40, and p63 but positive for CK7 (Fig. 3B), TTF-1 (Fig. 3C), and napsin A (Fig. 3D). Basal cells were negative for BRAF and MUC5AC and expressed CK5/6 (Fig. 3E) and p40 (Fig. 3F). Small cell lung cancer (SCLC) was identified and elaborated in Fig. 3G, which invaded the peripheral lung tissue and the entire bronchial wall layer without invading the lung pleura. Strong

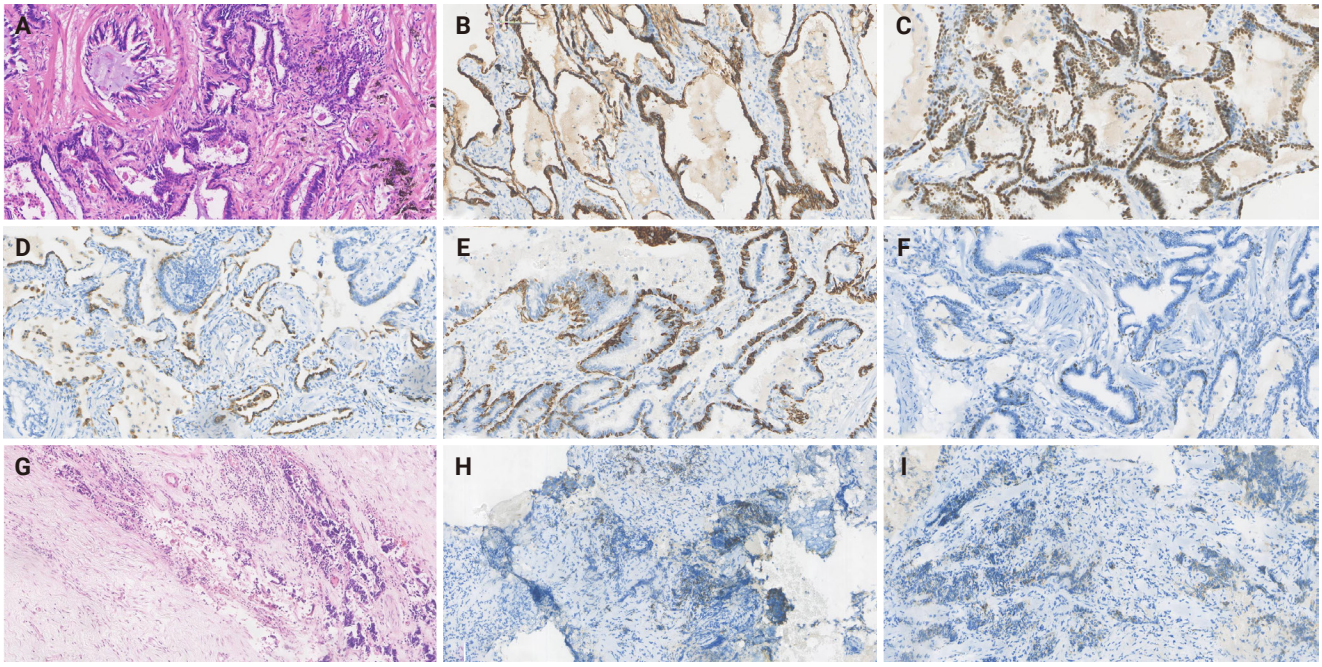

Fig. 3. Histological and immunohistochemical findings in case 3. (A) Flat structures in bronchiolar adenoma (BA), displaying central fibrosis and focal infiltration of lymphocytes. (B) Luminal cells express cytokeratin (CK) 7 in BA. (C) Luminal cells express thyroid transcription factor-1 in BA. (D) Luminal cells express napsin A in BA. (E) Basal cells express CK5/6 in BA. (F) Basal cells express p40 in BA. (G) Lymphoid cells with large nuclei and deep staining typical of small cell lung cancer. (H) Chromogranin A expression in small cell lung cancer. (I) Synaptophysin expression in small cell lung cancer.

and widespread positive expression of tumor cells in SCLC was demonstrated by CgA (Fig. 3H) and Syn (Fig. 3I). Next-generation sequencing also depicts that TP53 and TSHR were detected in BA, but no mutations or fusions were found. TMB was 3.3 in SCLC and 0 in BA (Fig. 1F). These patients' carcinoma components clearly had comparatively higher TMB, but there was no statistically significant difference (p = .259) (Fig. 1G).Overall description of the mutations were provided in Fig. 1H. The patient was lost to follow-up after 61 months of survival without metastasis or recurrence.

DISCUSSION

The characteristic double-layered epithelial cells and a continuous layer of basal cells are the main features of BA, a recently identified benign or potentially malignant lung tumor [7]. Lately, BA has been recognized as a distinct entity, setting it apart from other pulmonary lesions and lung carcinoma [8]. According to earlier research, the most reliable histological indicator for distinguishing BA from carcinoma is a continuous layer of basal cells [1,5]. Pathogenesis analysis has not yet revealed a clear correlation between BA and a specific histological subtype of lung carcinoma [9]. Case reports of BA are still uncommon in the current study, and BA coexisting with lung carcinoma are even less common. The current report provides a thorough analysis of radiological, morphological, and molecular features in patients with BA combined with lung carcinoma, based on the compared studies.

Accurate differential diagnosis and thorough and methodical understanding of BA are essential. Pathology has been the primary focus of research on BA, and its clinical and imaging features still remain poorly understood. Most elderly, lethargic individuals with BA do not exhibit symptoms like coughing, expectoration, or chest pain. Therefore, regular follow-up is crucial. BA shows various imaging features, most of which are irregular peripheral solitary nodules (≤2 cm) with distinct boundaries [10]. They can occasionally be misdiagnosed as adenocarcinoma *in situ* due to shallow lobulation or ground-glass components, features that overlap with the early signs of lung adenocarcinoma [10,11]. Additionally, thin-slice CT examinations frequently depict BA with pseudocavity formation; therefore, imaging observations must be closely monitored for

https://doi.org/10.4132/jptm.2025.12.31

early warning signs of malignant transformation, such as pleural traction or necrosis [11].

The well-known histologic characteristics of BA are flat, glandular, or papillary. To confirm the basal layer by IHC, a bilayered structure consisting of a continuous basal cell layer and a luminal cell layer is often required. The basal layer displays positive expression of common basal cell markers, including CK5/6, p40, and p63. Interestingly, lung carcinomas had a relatively high Ki-67 proliferating index (10%–40%), whereas BAs had a low Ki-67 proliferating index (5%–10%). However, Ki-67 could not be used as a criterion to distinguish between benign and malignant tumors. IHC is therefore an essential tool for differential diagnosis [12]. When cilia are clearly visible, even diagnosis on frozen section can be straightforward. It is very uncommon for a malignant tumor to show cilia in the lung. Histologically, the presence of cilia and a basal cell layer is the main distinguishing feature of BA from carcinoma, and the luminal cells in BA typically consist of varying proportions of mucinous and ciliated cells. Based on the aforementioned features, BA was artificially separated into proximal and distal types [5]. A portion of distal-type BAs may develop into adenocarcinoma, according to several studies [5,6]. In contrast, BA, mixed-type BAs with monolayered lesions, and monolayered BA-like lesions displayed progressive loss of a continuous basal layer, morphologically approaching adenocarcinoma, suggesting the possibility of a malignant transition from BA to carcinoma [10,13]. The morphology of bilayered BA in these three proximal cases with carcinoma components suggests a potential for malignant transformation. While basal cells and mild cell morphology indicated that bilayered BA is probably benign [14], low-grade malignant features, such as central fibrosis and focal lymphocyte infiltration, were somewhat similar to those of lung adenocarcinoma. Intriguingly, BA and SCLC exhibit few histological similarities, suggesting that their tissue origins differ. The histological origin of BA may be closer to that of invasive adenocarcinoma, and the co-occurrence of SCLC and BA is thought to be coincidental.

We are now considering whether the bilayered structures represent adenocarcinoma extending to bronchiolar epithelium without total loss of basal cells in light of the two cases of bilayered BA with malignant transformation. Consequently, it is not possible to classify classical bilayered BA as benign tumors. The genetic changes in BA were first identified and described by Liu et al. [15]. The most prevalent mutational feature in BA (38%) is the *BRAF* V600E mutation. *EGFR* mutation [10,16], *KRAS* mutation [10,17], *AKT1* mutation [17], *ALK* gene rearrangement [18,19], and other molecular profiles have also been reported. They are all relatively common in lung cancer, suggesting that there are some genetic similarities between BA and lung cancer. The same *KRAS* G12C and *AXIN2* mutations, which are frequently found in invasive adenocarcinomas [19], were identified in both sections of case 1, suggesting that the adenocarcinomas and BAs may have shared a similar genetic background. The aforementioned findings might lend credence to BA's malignant transformation. Simultaneously, one of the current cases revealed EGFR 19del in the carcinoma component to be distinct from the BA, suggesting that the pathogenesis of BA and adenocarcinoma may differ (case 2). Based on the molecular analysis, we hypothesized that if lung adenocarcinoma and BA are found in the same focus, they might share a driver gene mutation (case 1) [9]; on the other hand, if BA and adenocarcinoma co-occur at different locations, they might have different forms (case 2). We hypothesize that the inconsistent genetic detection of BA and adenocarcinoma in distinct foci can be attributed to two factors. First, gene mutations may accompany tumor cells of the same origin during development and metastasis, which encourages the formation of cells with different histological manifestations. The same genetic mutation was found in both bilayered BA and adenocarcinoma, confirming the same cell origin and the potential for BA to undergo malignant transformation. Second, distinct cell types are produced by the unique genetic profiles of tissue cells from various sources. In terms of non-fixed loci, it is hypothesized that mutations may have occurred in BA linked to lung carcinoma in the two cases (cases 2 and 3). Variant allele frequencies between the two components were *AXIN2* (33.3% in BA, 33.3% in carcinoma), *KRAS* (33.3% in BA, 33.3% in carcinoma), *TP53* (0% in BA, 66.7% in carcinoma), *CBL* (0% in BA, 33.3% in carcinoma), *DENND1A* (0% in BA, 33.3% in carcinoma), *DLL3* (33.3% in BA, 0% in carcinoma), *DPYD* (0% in BA, 33.3% in carcinoma), *EGFR* (0% in BA, 33.3% in carcinoma), *ERBB2* (0% in BA, 33.3% in carcinoma), *FGFR1* (0% in BA, 33.3% in carcinoma), *FLT1* (0% in BA, 33.3% in carcinoma), *HGF* (0% in BA, 33.3% in carcinoma), *HNF1A* (0% in BA, 33.3% in carcinoma), *LRP1B* (33.3% in BA, 0% in carcinoma), *POLE* (33.3% in BA, 0% in carcinoma), *SKP2* (0% in BA, 33.3% in carcinoma), and *TSHR* (0% in BA, 33.3% in carcinoma).

As in our study, BA can be found coincidentally in lung carcinomas. Treatment guidelines for carcinoma can serve as a starting point. Nevertheless, during long-term follow-ups, none of the three cases under study has experienced metastasis or postsurgical recurrence. BA with carcinoma appeared to be low-

grade malignant. Therefore, unlike classical bilayered BA and lung adenocarcinoma, the case with BA and malignant components may be an independent variant with unique histological and molecular variation. The invasiveness and malignancy of carcinoma may be diminished as the tumor progresses due to the addition of BA components in this particular variant. Notably, due to sample limitations, no comparison between proximal and distal types was performed, and all BAs with carcinoma in the current study were proximal.

In conclusion, histological and genetic evidence for the possible malignant transformation of BAs was presented by both this study and recent case reports [20]. The findings in our study indicate that BA is associated with malignant differentiation, particularly when co-occurring with carcinoma. Genetics and histopathology remain essential diagnostic methods. Future research on the clinical and biological significance of specific alterations and related changes is necessary, given the small sample size. To determine whether BA is a possible precursor to carcinoma based on its long-term prognosis, further research is required.

Supplementary Information
The Data Supplement is available with this article at https://doi.org/10.4132/jptm.2025.12.31.

Ethics Statement
The study was conducted in accordance with the Declaration of Helsinki, and approved by the Ethics Committee at the First Affiliated Hospital of Xi'an Jiaotong University (No. XJTU1AF2024LSYY-472 and date of approval is December 6, 2024). Informed consent was obtained from the individuals for the publication of any potentially identifiable data included in this article.

Availability of Data and Material
The original contributions presented in the study are included in the article/supplementary material. Further inquiries can be directed to the corresponding author.

Code Availability
Not applicable.

ORCID
Lu-Yao Li https://orcid.org/0009-0009-2239-3574
Gong-Ming Dong https://orcid.org/0009-0009-8287-4441
Yun-Peng Zhang https://orcid.org/0009-0003-0363-8536
Ting-Ting Wang https://orcid.org/0009-0009-0339-1258
Fu-Quan Jia https://orcid.org/0009-0006-2900-8761
Guan-Jun Zhang https://orcid.org/0009-0003-3107-2656

Author Contributions
Conceptualization: GJZ. Data curation: LYL, GMD, TTW. Supervision: GJZ, FQJ. Writing—original draft: LYL, GMD, YPZ. Writing—review & editing: all authors. Approval of final manuscript: all authors.

Conflicts of Interest
The authors declare that they have no potential conflicts of interest.

Funding Statement
This study was supported by the Xi'an Jiaotong University Medical Development Fund (No. XJYG2025-SFJJ011).

REFERENCES
1. Kao T, Yeh Y. Ciliated muconodular papillary tumor/bronchiolar adenoma of the lung. Semin Diagn Pathol 2021; 38: 62-71.
2. Nicholson AG, Tsao MS, Beasley MB, et al. The 2021 WHO classification of lung tumors: impact of advances since 2015. J Thorac Oncol 2022; 17: 362-87.
3. Kamata T, Yoshida A, Kosuge T, Watanabe S, Asamura H, Tsuta K. Ciliated muconodular papillary tumors of the lung: a clinicopathologic analysis of 10 cases. Am J Surg Pathol 2015; 39: 753-60.
4. Yang C, Wang X, Da J, Ma K. Distal-type bronchiolar adenoma of the lung harboring an EGFR exon 21 p.L858R mutation: a case report. Thorac Cancer 2020; 11: 3596-8.
5. Chang JC, Montecalvo J, Borsu L, et al. Bronchiolar adenoma: expansion of the concept of ciliated muconodular papillary tumors with proposal for revised terminology based on morphologic, immunophenotypic, and genomic analysis of 25 cases. Am J Surg Pathol 2018; 42: 1010-26.
6. Chen F, Ren F, Zhao H, Xu X, Chen J. Mucinous adenocarcinoma caused by cancerization from a ciliated multinodular papilloma tumor: a case report. Thorac Cancer 2021; 12: 1629-33.
7. Shao K, Wang Y, Xue Q, et al. Clinicopathological features and prognosis of ciliated muconodular papillary tumor. J Cardiothorac Surg 2019; 14: 143.
8. Shao J, Yin JC, Bao H, et al. Morphological, immunohistochemical, and genetic analyses of bronchiolar adenoma and its putative

variants. J Pathol Clin Res 2021; 7: 287-300.
9. Han X, Hao J, Ding S, Wang E, Wang L. Bronchiolar adenoma transforming to invasive mucinous adenocarcinoma: a case report. Onco Targets Ther 2021; 14: 2241-6.
10. Cao L, Wang Z, Gong T, et al. Discriminating between bronchiolar adenoma, adenocarcinoma in situ and minimally invasive adenocarcinoma of the lung with CT. Diagn Interv Imaging 2020; 101: 831-7.
11. Li F, He Y, Yang H, et al. Pseudocavity on thin-slice CT can be a suggestion of bronchiolar adenoma: a preliminary study on 80 cases with bronchiolar adenoma of the lung. J Comput Assist Tomogr 2025; 49: 934-42.
12. Gao Z, Feng Q, Wang Y, Jiang Y, Han D, Xu W. Case report: two cases of bronchiolar adenoma/ciliated muconodular papillary tumor characterized by significant basal cell hyperplasia and squamous metaplasia. Front Oncol 2025; 15: 1617720.
13. Zhu M, Yang Q, Zhan S, Liu W, Guo L, Huang S. Clinicopathological analysis of bronchiolar adenoma combined with lung adenocarcinoma: report of eight cases and literature review. Histol Histopathol 2024; 39: 783-94.
14. Cheung FM, Guan J, Luo QG, Sihoe AD, Shen XP. Ciliated muconodular papillary tumour of the lung mimicking mucinous adenocarcinoma: a case report and literature review. Hong Kong Med J 2019; 25: 71-3.
15. Liu L, Aesif SW, Kipp BR, et al. Ciliated muconodular papillary tumors of the lung can occur in Western patients and show mutations in BRAF and AKT1. Am J Surg Pathol 2016; 40: 1631-6.
16. Zheng Q, Hou L, Shang G, et al. Frequent EGFR exon 20 insertion in the so-called peripheral-type squamous cell neoplasm of uncertain malignant potential: a variant of bronchiolar adenoma or under-recognised entity? Histopathology 2023; 83: 178-92.
17. Udo E, Furusato B, Sakai K, et al. Ciliated muconodular papillary tumors of the lung with *KRAS/BRAF/AKT1* mutation. Diagn Pathol 2017; 12: 62.
18. Jin Y, Shen X, Shen L, Sun Y, Chen H, Li Y. Ciliated muconodular papillary tumor of the lung harboring *ALK* gene rearrangement: case report and review of the literature. Pathol Int 2017; 67: 171-5.
19. Di Federico A, Hong L, Elkrief A, et al. Lung adenocarcinomas with mucinous histology: clinical, genomic, and immune microenvironment characterization and outcomes to immunotherapy-based treatments and KRAS(G12C) inhibitors. Ann Oncol 2025; 36: 297-308.
20. Li X, Wu Y, Hui D, et al. Multiple bronchiolar adenomas with malignant transformation and *CCNE1* mutation: a case report and literature review. J Cardiothorac Surg 2021; 16: 307.

JPTM
Journal of Pathology and Translational Medicine 2026; 60: 364-370
https://doi.org/10.4132/jptm.2026.04.27

NEWSLETTER

pISSN 2383-7837 / eISSN 2383-7845

PathologyOutlines.com

What's new in digital and computational pathology 2026: advances in adoption, standards, AI technologies, and clinical integration

Selim Sevim[1], Chadi Hajar[2], Snehal Sonawane[3]

[1]Cancer Early Detection Advanced Research Center (CEDAR), Knight Cancer Institute, Oregon Health and Science University, Portland, OR, USA
[2]Department of Pathology and Laboratory Medicine, Medical University of South Carolina, Charleston, SC, USA
[3]Department of Pathology and Laboratory Medicine, University of Illinois at Chicago, Chicago, IL, USA

Received: March 27, 2026
Accepted: April 27, 2026

Corresponding Author:
Snehal Sonawane, MD
Department of Pathology and Laboratory Medicine, University of Illinois at Chicago, Chicago, IL, USA
E-mail: snehal@uic.edu

ORCID
Selim Sevim
https://orcid.org/0000-0002-3436-0464
Chadi Hajar
https://orcid.org/0009-0007-0420-4050
Snehal Sonawane
https://orcid.org/0000-0003-3384-7702

This article has been published jointly, with consent, in both Journal of Pathology and Translational Medicine and PathologyOutlines.com.

ABSTRACT

Digital and computational pathology are expanding rapidly worldwide, driven by advances in whole-slide imaging, AI algorithms, multimodal data integration, and improved digital infrastructure. Adoption continues to accelerate in the United States and internationally, supported by professional guidelines, emerging reimbursement pathways, and the growing need for remote workflows and collaborative diagnostics. Progress in interoperability standards, regulatory frameworks, and FDA approvals has strengthened the foundation for clinical deployment, while large-scale data repositories and federated learning approaches enable more robust and privacy-preserving model development. Foundation models, multimodal AI systems, and LLM-based copilots are reshaping diagnostic support, prognostication, workflow efficiency, clinical trials and drug discovery.

DIGITAL PATHOLOGY INFRASTRUCTURE – UNITED STATES AND GLOBAL

- The implementation of computational and digital pathology in the United States continues to develop despite the problems related to financial investment, data storage, reimbursement uncertainties, and regulatory constraints.
- The digital pathology market is projected to exceed $2 billion by 2032 [1-3]. This increase is supported by new applications, such as biomarker quantification, large-scale image archiving, inter-institutional slide consultation, and telepathology [1].
- Broader implementation and standardization are encouraged by guidelines and recommendations issued by entities like the College of American Pathologists (CAP) and other professional bodies, such as the Digital Pathology Association (DPA), the European Society of Digital and Integrative Pathology (ESDIP), and others.
- On par with the United States, the primary factors that drive international adoption are based on the growing burden of cancer worldwide, understaffing, the need for personalized medicine, and collaborative diagnostic processes [3,4].
- International adoption of digital and computational pathology remains uneven. A higher pace of adoption is mentioned in high-income countries. In contrast, developing countries face technical, financial, and workforce challenges when implementing digital initiatives [3,4].
- A growing need for professional awareness, domain-specific education, and broader advocacy for digital pathology is reflected in the recent establishment of several continental societies, including the Asian Society of Digital Pathology (ASDP), the African Society of Digital Pathology (AFSDP), and the Latin American Society of Digital Pathology (LASDP), alongside

https://doi.org/10.4132/jptm.2026.04.27

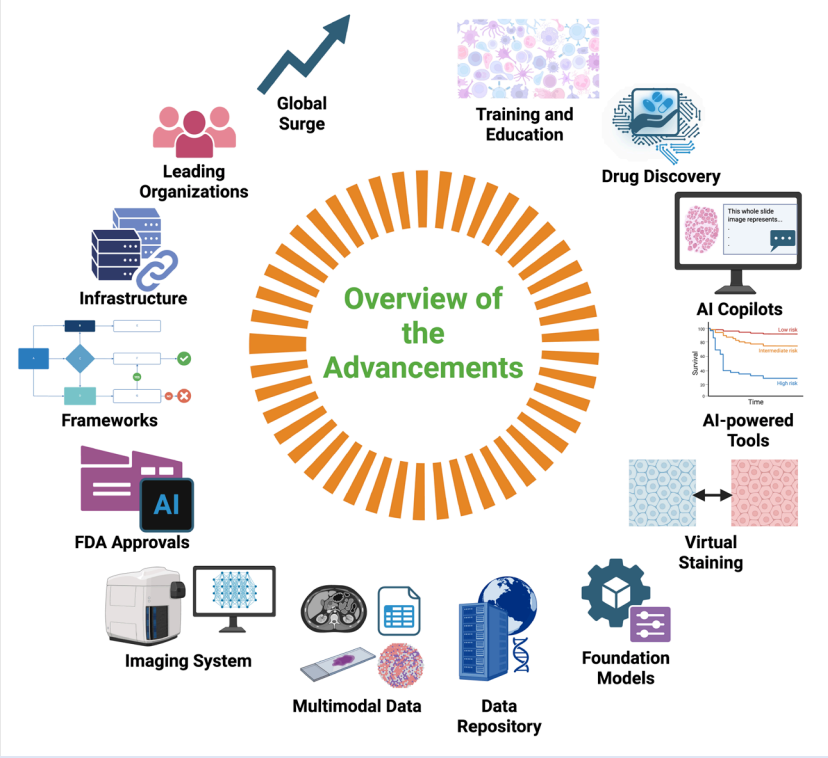

Fig. 1. Brief overview of the advancements in digital and computational pathology.

the longer-standing ESDIP and DPA.

SURGE IN DIGITAL PATHOLOGY ADOPTION

- A global surge in adoption of digital pathology has been driven primarily by advances in scanning technology and speed, the expansion of AI tools, and the growing need for remote workflows (Fig. 1).
- An international survey conducted in 2023 across 127 laboratories reported that 57% of these laboratories had implemented digital pathology for research or clinical purposes. This implementation works to improve turnaround time, case traceability within departments, and multi-site collaboration. The survey also reported challenges with laboratory information systems (LIS) integration and a lack of workforce training [5].
- In 2024, CAP estimated that digital pathology adoption is approximately 10% in U.S. labs [6].
- In 2023, the American Society of Cytopathology (ASC) conducted a large-scale international survey about the use of scanners in cytology, with 327 participants. The results indicated that most respondents do not routinely scan cytology slides, highlighting concerns of image quality and the cost of implementation; however, pathologists also indicated interest in the implementation of the technology for screening liquid-based Papanicolaou tests, rapid onsite evaluation, and AI-assisted screening [7].

LATEST GUIDELINES AND RECOMMENDATIONS

- CAP recommends using a validation set of at least 60 cases, with consistency between whole-slide images (WSI) and glass slide reads greater than 95%, for implementation of digital pathology workflow [8].
- CAP also advocated for the implementation of 30 new Category 3 CPT codes in 2024 to highlight the additional work involved in digitizing surgical pathology slides for primary diagnosis [9].
- The Center for Medicare & Medicaid Services (CMS) has released their newest recommendation in 2025, which indicates that all remote review of digital cytology specimens requires a remote location with a separate CLIA certificate [10].
- ASC proposed a structured validation process for telecytology, including training, retrospective slide review, and hardware/software testing [11].
- Consensus-based recommendations released by the Royal College of Pathologists (RCP) (UK) [12], ESDIP [13], and European Society of Pathology (ESP) [14] reflect European approaches to the implementation of digital pathology.

INTEROPERABILITY AND STANDARDIZED FRAMEWORKS

- Interoperability remains hindered by technical issues, such as proprietary image file formats, diverse data types, and legacy systems.
- Economic barriers to interoperability and standardized frameworks include high costs, vendor lock-in, and limited reimbursement incentives.
- Regulatory and organizational challenges primarily arise from a fragmented health IT ecosystem, workflow variability, compliance complexities, and resistance to change.
- Due to these reasons, standardization has accelerated through the adoption and implementation of key interoperability standards.
    - o IHE Digital Pathology Image Acquisition (DPIA) profile, Health Level 7 (HL7) for metadata exchange, and Digital Imaging and Communications in Medicine (DICOM) for image encoding are the main standardization efforts.
- These frameworks enable consistent communication between slide scanners, viewers, the LIS, and analytics systems.
- While progress has been made and continues, substantial improvement remains necessary, requiring collaboration among governmental agencies, medical organizations, and the private sector [15-17].

REGULATORY PROGRESS AND FDA APPROVALS

- The key criteria for the approval of AI and digital pathology in medical devices are based on safety and effectiveness through valid scientific evidence, and these should prove that the benefit outweighs the risk for the intended use in the target

population.
- FDA approvals have spanned all the domains of digital and computational pathology, including scanners, image management systems (IMS), and AI algorithms for clinical use [18].
- Examples of the latest FDA approvals:
  - o AISight Dx (PathAI): cloud-based digital viewing and management platform, which supports integration with several slide scanners [19].
  - o PathPresenter Clinical Viewer: digital pathology image management and viewer platform used for primary diagnosis, assisting in case tracking, image archiving, and collaboration features [20].
  - o Roche Digital Pathology Dx (VENTANA DP 200): automated digital slide creation, viewing, and management system intended for in vitro diagnostic use as an aid to the pathologist to review and interpret WSIs [21].

MULTIMODAL DATA INTEGRATION

- Progress in multimodal data integration can be seen in devices and techniques that fuse histopathological images with clinical and molecular data.
  - o Rapid optical-genomic screening system DeepGlioma combines stimulated Raman histology with deep learning-based genomics to predict key glioma molecular alterations with 93% accuracy in < 90 seconds, demonstrating the potential of real-time histology and genomics integration in pathology [22].
- Federated learning methods tailored to pathology enable multi-institutional model training by learning from local healthcare datasets and aggregating updates to build more robust and generalizable AI models while preserving data privacy (e.g., federated frameworks for WSI analysis).
- Innovative approaches, like FedMM, address modality gaps across hospitals by training separate single-modality feature extractors, resulting in superior classification accuracy and area under the curve (AUC) on multi-institutional datasets [23].
- To address heterogeneity across multiple pathology labs and medical institutions, PathFL recently introduced multi-level alignment strategies.
  - o Those strategies are applied at three distinct levels: "style, feature, and model aggregation."
  - o This alignment involves slide scanners, organs, modalities, and sources to improve validity in pathology image segmentation [24].

BIG DATA REPOSITORIES

- High-throughput scanners revolutionized the digital pathology field due to rapid scanning of glass slides with file sizes ranging from hundreds of megabytes to gigabytes. Traditional databases are inadequate to hold this large amount of data [25].
- In recent years, structured data repositories have been developed to enable standardized storage, metadata annotation, and efficient data sharing. The aim is to support foundation model development, biomarker discovery, drug research, and education while accelerating AI innovation through access to large and

Fig. 2. Interface of the World Tumor Registry public platform showing WSI viewer, multiple slides representing a single case, descriptive case notes, diagnostic features annotated directly on the slides, and accompanying case details.

https://doi.org/10.4132/jptm.2026.04.27

diverse cohorts [26].
  - Examples of some big data repositories are: BIGPICTURE [26], BD4BO [27], eTOX [28], eTRANSAFE [29], MELLODDY [30], OPTIMA [31], VICT3R [32].

DIGITAL PATHOLOGY IN TRAINING AND EDUCATION

- Digital and computational pathology innovation has expanded its benefits in pathology education and training. It has enabled the creation of web-based image collections/libraries of various diseases. These libraries are accompanied by annotations, which may highlight the various features on WSIs.
  - Institutional and academic-society WSI collections range from open access to closed and vary in curation rigor.
  - PathologyOutlines.com continues to expand its virtual-slide content on textbook pages.
  - World Tumor Registry (WTR) is a web-based open-access collection of WSIs of tumors from every region of the world, annotated by subspecialty experts (Fig. 2). It removes geographic boundaries and serves as an educational and practical resource for cancer care and research [33].
- The innovative integration of a web-based pathology image collection with organ-based text can be supported by QR codes. These codes link each topic to its corresponding virtual slide. This approach combines the traditional hard-copy reading experience with immediate access to virtual slides, providing a dynamic and interactive learning environment for the next generation of pathologists (Fig. 3) [34].

AI-POWERED TOOLS FOR CLINICAL USE

- In recent years, various AI-based tools and related technologies have demonstrated strong diagnostic and predictive/prognostic capabilities. In different studies, the effectiveness of those beneficial tools has been repeatedly verified [35].
- Expert panels predicted that many tasks in digitized pathology laboratories could be delegated to AI by the next decade [36]. The most promising applications include cancer detection and grading in histopathology (e.g. prostate, breast, gastrointestinal) and cervical cytology screening [37].
- AI algorithms evaluate various tissue compartments and predict disease outcomes in breast, oropharyngeal, bladder, prostate, and non-small-cell lung cancers. Results from those algorithms showed great promise to shape treatment modality choice and patient-specific approaches instead of tumor/disease-specific management by emphasizing risk scores of individuals [38].
  - Diagnostic tools: FDA clearance of AI-powered applications reflects their diagnostic capability [39,40], as demonstrated by the approvals of Paige Prostate and Ibex Prostate Detect for prostate cancer diagnostics [41,42].
  - Predictive/prognostic tools: predictive tools nourished by multimodal datasets, such as H&E, clinical data (age, PSA, grading, Ki67 status, etc.), and molecular data, to create a digital biomarker of indolence/aggressiveness of tumor. These algorithms can also predict treatment response. In recent years, AI-powered tools that combine clinical data and H&E images have demonstrated their potential in the field [43-45].
- Artera AI app uses multimodal AI to predict 5- and 10-year risk of distant metastasis and biochemical failure, as well as prostate cancer-specific and overall survival [46]. In addition, the potential benefit of androgen deprivation therapy, radiotherapy, and castration resistance prediction for patients has been effectively estimated in clinical trials [47,48].
- RlapsRisk BC predicts 5-year metastasis-free survival in early, ER-positive, HER2-negative breast cancer [44].
- Computational histology and AI (CHAI) is an algorithm that works on high-risk non-muscle invasive bladder cancer to predict BCG response [45]. It creates an AI-based signature to stratify these patient groups as high- and low-risk in terms of recurrence-free and progression-free survival.

VIRTUAL STAINING

- The concept of virtual staining has emerged in recent years as a valuable complement to the diagnostic process, driven by the increasing use of high-throughput digital pathology and deep learning methods. Virtual staining refers to the synthetic generation of images that replicate routine diagnostic stains. When properly validated and integrated into the digital pathology workflow, virtual staining can offer meaningful gains in cost-effectiveness and time efficiency [49].

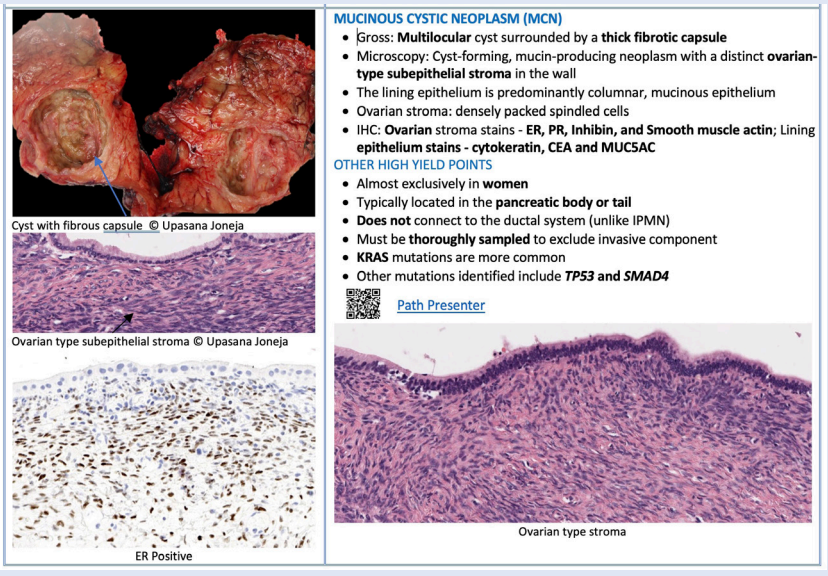

Fig. 3. Image demonstrating a surgical pathology book with web-based pathology image collection and organ-based text. This book uses QR codes to link each topic to the corresponding virtual slide. Gupta, Akanksha. Ace the Boards: Surgical Pathology Reimagined. 2022 (used with permission).

FOUNDATION MODELS

- Foundation models (FMs) are large-scale AI models trained on vast and diverse datasets that can be adapted to a wide range of downstream tasks with minimal fine-tuning.
- FMs can be applied to a wide range of downstream tasks, including cancer subtyping, mutation prediction, biomarker detection, spatial proteomics analysis, and pan-cancer detection independent of tissue type.
  - o Prov-GigaPath is a whole-slide pathology FM trained on 1.3 billion tiles [50]. It demonstrated robust performance in cancer subtyping and pathomics tasks.
  - o Virchow model achieved a 0.95 AUC in detecting 16 types of cancers, both rare and common, using nearly 1.5 million H&E slides [51].
  - o CytoFM, the first cytology FM, demonstrated the adaptability of FMs to cytology specimens and was trained on 1.4 million cytology patches [52].
  - o KRONOS, a spatial proteomics FM, was trained on 8 fluorescence-based imaging platforms, 16 tissue types, 175 protein markers, and 47 million image patches [53].
- Studies have shown that FMs can help guide computational pathology to tailor patient-specific approaches.

AI COPILOTS

- Large-language models (LLMs) are AI systems trained on massive amounts of text data to understand, generate, and respond to human language in a way that mimics human communication. The input and output of these models can be unimodal or multimodal, spanning text, images, audio, and other data types.
- The interactive nature of LLMs and generative AI is driving the emergence of specialized AI assistants in human-integrated workflows.
- In pathology, generative AI has a revolutionary potential to improve diagnostic accuracy, workflow efficiency, education, and research [54].
  - o PathChat is a vision-language generalist AI tool to assist pathologists in diagnostic tasks [55]. This multimodal AI copilot was generated on approximately one million pathology-related answers and questions. The performance of that algorithm was evaluated by both multiple-choice and open-ended questions.
  - o Alba AI copilot has the potential to aggregate multi-sourced data, help with routine diagnostics, perform image analysis for cancer detection, screen biomarkers, and generate pathology reports with the help of voice and chat assistance [56].
  - o PathAsst multimodal LLM was designed to overcome the lack of high-quality data and specialized models [57]. Experimental results showed that it outperformed existing models in visual question answering tasks in pathology.
  - o TeamPath algorithm was designed to enhance multimodal pathology diagnosis with the help of reasoning AI copilots [58]. TeamPath's framework was shaped by human-AI collaboration and showcases the power of an algorithm to correct and verify pathologist-provided answers and reasoning paths.
- General-purpose LLMs such as ChatGPT and Gemini are widely used by pathologists for administrative, educational, and other tasks [59]. Because they are not trained on domain-rich pathology datasets and lack clinical-grade validation or approval, their use for diagnostic purposes is discouraged due to limited performance and privacy risks [60].

DIGITAL AND COMPUTATIONAL PATHOLOGY IN CLINICAL TRIALS AND DRUG DISCOVERY

- Digital and computational pathology provide multidimensional benefits in clinical trials and drug discovery by enabling centralized slide review, improving accuracy and efficiency, and supporting standardized and reproducible interpretation across participating centers. Various integrated data analytics tools allow efficient patient enrollment, randomization, stratification, and endpoint evaluation in clinical trials.
- Improved digital pathology platforms streamline study protocols and enable real-time result evaluation, enhancing toxicopathology workflows, which involve evaluating tissue changes in non-clinical models to assess drug safety. Digitization also facilitates navigation of complex regulatory requirements, including specimen handling, data safety, integrity, and compliance.
- Lately, the integration of molecular/genomic data has enabled complex tissue-based experiments and strengthened global collaboration among pharmaceutical companies, technology vendors, and clinical researchers. These advances are helping to drive the continued development of precision medicine [61].

REFERENCES

1. Bessen JL, Alexander M, Foroughi O, et al. Perspectives on reducing barriers to the adoption of digital and computational pathology technology by clinical labs. Diagnostics (Basel) 2025; 15: 794.
2. Ardon O, Klein E, Manzo A, et al. Digital pathology operations at a tertiary cancer center: Infrastructure requirements and operational cost. J Pathol Inform 2023; 14: 100318.
3. Ahmed MI, Spooner B, Isherwood J, Lane M, Orrock E, Dennison A. A systematic review of the barriers to the implementation of artificial intelligence in healthcare. Cureus 2023; 15: e46454.
4. Coudry RA, Assis EACP, Frassetto FP, et al. Crossing the andes: challenges and opportunities for digital pathology in Latin America. J Pathol Inform 2024; 15: 100369.
5. Pinto DG, Bychkov A, Tsuyama N, Fukuoka J, Eloy C. Real-world implementation of digital pathology: results from an intercontinental survey. Lab Invest 2023; 103: 100261.
6. Digital pathology at 10% adoption and in-lab plans [Internet]. Northfield: CAP Today, 2025 [cited 2025 Dec 20]. Available from: https://www.captodayonline.com/digital-pathology-at-10-adoption-and-in-lab-plans/.
7. Kim D, Thrall MJ, Michelow P, et al. The current state of digital cytology and artificial intelligence (AI): global survey results from the American Society of Cytopathology Digital Cytology Task Force. J Am Soc Cytopathol 2024; 13: 319-28.
8. Evans AJ, Brown RW, Bui MM, et al.

https://doi.org/10.4132/jptm.2026.04.27

Validating whole slide imaging systems for diagnostic purposes in pathology. Arch Pathol Lab Med 2022; 146: 440-50.
9. Advocacy update: July 11, 2023 [Internet]. Northfield: College of American Pathologists, 2023 [cited 2025 Dec 20]. Available from: https://www.cap.org/advocacy/latest-news-and-practice-data/july-11-2023.
10. Current CAP guidelines [Internet]. Northfield: College of American Pathologists, 2025 [cited 2025 Dec 20]. Available from: https://www.cap.org/protocols-and-guidelines.
11. Lin O, Alperstein S, Barkan GA, et al. American Society of Cytopathology Telecytology validation recommendations for rapid on-site evaluation (ROSE). J Am Soc Cytopathol 2024; 13: 111-21.
12. Cross S, Furness P, Igali L, Snead D, Treanor D. Best practice recommendations for implementing digital pathology January 2018. London: The Royal College of Pathologists, 2018.
13. Fraggetta F, L'Imperio V, Ameisen D, et al. Best practice recommendations for the implementation of a digital pathology workflow in the anatomic pathology laboratory by the European Society of Digital and Integrative Pathology (ESDIP). Diagnostics (Basel) 2021; 11: 2167.
14. Eloy C, Fraggetta F, van Diest PJ, et al. Digital transformation of pathology: the European Society of Pathology expert opinion paper. Virchows Arch 2025; 487: 971-81.
15. Dash RC, Jones N, Merrick R, et al. Integrating the health-care enterprise pathology and laboratory medicine guideline for digital pathology interoperability. J Pathol Inform 2021; 12: 16.
16. Mantri M, Taran S, Sunder G. DICOM integration libraries for medical image interoperability: a technical review. IEEE Rev Biomed Eng 2022; 15: 247-59.
17. Abels E, Pantanowitz L, Aeffner F, et al. Computational pathology definitions, best practices, and recommendations for regulatory guidance: a white paper from the Digital Pathology Association. J Pathol 2019; 249: 286-94.
18. Zhang DY, Venkat A, Khasawneh H, Sali R, Zhang V, Pei Z. Implementation of digital pathology and artificial intelligence in routine pathology practice. Lab Invest 2024; 104: 102111.
19. 510(k) Premarket notification K243391 [Internet]. Silver Spring: U.S. Food and Drug Administration, 2024 [cited 2025 Jan 12]. Available from: https://www.accessdata.fda.gov/scripts/cdrh/cfdocs/cfpmn/pmn.cfm?ID=K243391.
20. 510(k) Premarket notification K250968 [Internet]. Silver Spring: U.S. Food and Drug Administration, 2025 [cited 2025 Jan 12]. Available from: https://www.accessdata.fda.gov/scripts/cdrh/cfdocs/cfpmn/pmn.cfm?ID=K250968.
21. 510(k) Premarket notification K232879 [Internet]. Silver Spring: U.S. Food and Drug Administration, 2024 [cited 2026 Mar 6]. Available from: https://www.accessdata.fda.gov/cdrh_docs/reviews/K232879.pdf.
22. Hollon T, Jiang C, Chowdury A, et al. Artificial-intelligence-based molecular classification of diffuse gliomas using rapid, label-free optical imaging. Nat Med 2023; 29: 828-32.
23. Peng Y, Bian J, Xu J. FedMM: federated multi-modal learning with modality heterogeneity in computational pathology. In: ICASSP 2024-2024 IEEE International Conference on Acoustics, Speech and Signal Processing (ICASSP); 2024 Apr 14-19; Seoul, Korea.
24. Lu MY, Chen RJ, Kong D, et al. Federated learning for computational pathology on gigapixel whole slide images. Med Image Anal 2022; 76: 102298.
25. Zarella MD, Rivera Alvarez K. High-throughput whole-slide scanning to enable large-scale data repository building. J Pathol 2022; 257: 383-90.
26. Moulin P, Grunberg K, Barale-Thomas E, der Laak JV. IMI-Bigpicture: a central repository for digital pathology. Toxicol Pathol 2021; 49: 711-3.
27. Szocska M, Jayawardana S, Smand C, Salimullah T, Reed C, Hanif S. Big data for better outcomes: supporting health care system transformation in Europe. Eurohealth 2017; 23: 7-9.
28. Sanz F, Pognan F, Steger-Hartmann T, et al. Legacy data sharing to improve drug safety assessment: the eTOX project. Nat Rev Drug Discov 2017; 16: 811-2.
29. Sanz F, Pognan F, Steger-Hartmann T, et al. eTRANSAFE: data science to empower translational safety assessment. Nat Rev Drug Discov 2023; 22: 605-6.
30. Heyndrickx W, Mervin L, Morawietz T, et al. MELLODDY: cross-pharma federated learning at unprecedented scale unlocks benefits in QSAR without compromising proprietary information. J Chem Inf Model 2024; 64: 2331-44.
31. N'Dow J, Smith EJ, Polychronopoulos K, et al. 917P OPTIMA: improve care for patients with prostate, breast, and lung cancer through artificial intelligence. Ann Oncol 2022; 33(Suppl 7): S966.
32. Steger-Hartmann T, Sanz F, Bringezu F, Soininen I. IHI VICT3R: developing and implementing virtual control groups to reduce animal use in toxicology research. Toxicol Pathol 2025; 53: 230-3.
33. The World Tumor Registry: tell all your friends [Internet]. London: The Pathologist, 2025 [cited 2025 Dec 20]. Available from: https://thepathologist.com/issues/2025/articles/june/the-world-tumor-registry-tell-all-your-friends/.
34. Gupta A, Sonawane S. Pathology visions 2023 overview. The path to unprecedented excellence: redefining pathology education through Ace My Path surgical pathology reimagined. J Pathol Inform 2024; 15: 100362.
35. McGenity C, Clarke EL, Jennings C, et al. Artificial intelligence in digital pathology: a systematic review and meta-analysis of diagnostic test accuracy. NPJ Digit Med 2024; 7: 114.
36. Berbis MA, McClintock DS, Bychkov A, et al. Computational pathology in 2030: a Delphi study forecasting the role of AI in pathology within the next decade. EBioMedicine 2023; 88: 104427.
37. Chong Y, Bychkov A. Commercially available artificial intelligence solutions for gynaecologic cytology screening and their integration into clinical workflow. Cytopathology 2026; 37: 24-44.
38. Bera K, Schalper KA, Rimm DL, Velcheti V, Madabhushi A. Artificial intelligence in digital pathology: new tools for diagnosis and precision oncology. Nat Rev Clin Oncol 2019; 16: 703-15.
39. Pantanowitz L, Quiroga-Garza GM, Bien L, et al. An artificial intelligence algorithm for prostate cancer diagnosis in whole slide images of core needle

biopsies: a blinded clinical validation and deployment study. Lancet Digit Health 2020; 2: e407-16.
40. Raciti P, Sue J, Ceballos R, et al. Novel artificial intelligence system increases the detection of prostate cancer in whole slide images of core needle biopsies. Mod Pathol 2020; 33: 2058-66.
41. Evaluation of automatic class III designation for Paige Prostate (DEN200080) [Internet]. Silver Spring: U.S. Food and Drug Administration (FDA), 2021 [cited 2025 Dec 20]. Available from: https://www.accessdata.fda.gov/cdrh_docs/reviews/DEN200080.pdf.
42. Ibex Medical Analytics receives first FDA 510(k) clearance [Internet]. Tel Aviv: Ibex Medical Analytics, 2025 [cited 2025 Dec 13]. Available from: https://ibex-ai.com/fda-510k-clearance/.
43. Esteva A, Feng J, van der Wal D, et al. Prostate cancer therapy personalization via multi-modal deep learning on randomized phase III clinical trials. NPJ Digit Med 2022; 5: 71.
44. Garberis I, Gaury V, Saillard C, et al. Deep learning assessment of metastatic relapse risk from digitized breast cancer histological slides. Nat Commun 2025; 16: 5876.
45. Lotan Y, Krishna V, Abuzeid WM, et al. Predicting response to intravesical bacillus Calmette-Guérin in high-risk nonmuscle-invasive bladder cancer using an artificial intelligence-powered pathology assay: development and validation in an international 12-center cohort. J Urol 2025; 213: 192-204.
46. De Novo Classification Request for DEN240068 [Internet]. Silver Spring: U.S. Food and Drug Administration, 2025 [cited 2025 Dec 13]. Available from: https://www.accessdata.fda.gov/scripts/cdrh/cfdocs/cfpmn/denovo.cfm?id=DEN240068.
47. Armstrong AJ, Liu VY, Selvaraju RR, et al. Development and validation of an artificial intelligence digital pathology biomarker to predict benefit of long-term hormonal therapy and radiotherapy in men with high-risk prostate cancer across multiple phase III trials. J Clin Oncol 2025; 43: 3494-504.
48. Feng FY, Smith MR, Saad F, et al. Digital pathology-based multimodal artificial intelligence scores and outcomes in a randomized phase III trial in men with nonmetastatic castration-resistant prostate cancer. JCO Precis Oncol 2025; 9: e2400653.
49. Bai B, Yang X, Li Y, Zhang Y, Pillar N, Ozcan A. Deep learning-enabled virtual histological staining of biological samples. Light Sci Appl 2023; 12: 57.
50. Xu H, Usuyama N, Bagga J, et al. A whole-slide foundation model for digital pathology from real-world data. Nature 2024; 630: 181-8.
51. Vorontsov E, Bozkurt A, Casson A, et al. A foundation model for clinical-grade computational pathology and rare cancers detection. Nat Med 2024; 30: 2924-35.
52. Ivezic V, Radhachandran A, Redekop E, et al. CytoFM: the first cytology foundation model. In: 2025 IEEE/CVF Conference on Computer Vision and Pattern Recognition Workshops; 2025 Jun 11-12; Nashville, TN, USA.
53. Shaban M, Chang Y, Qiu H, et al. A foundation model for spatial proteomics. Preprint arXiv: 250603373. https://doi.org/10.48550/arXiv.2506.03373 (2025).
54. Brodsky V, Ullah E, Bychkov A, et al. Generative artificial intelligence in anatomic pathology. Arch Pathol Lab Med 2025; 149: 298-318.
55. Lu MY, Chen B, Williamson DFK, et al. A multimodal generative AI copilot for human pathology. Nature 2024; 634: 466-73.
56. ALBA: generalist foundation model for computational pathology [Internet]. New York: Paige, 2025 [cited 2025 Dec 13]. Available from: https://www.paige.ai/al/alba.
57. Sun Y, Zhu C, Zheng S, et al. PathAsst: a generative foundation AI assistant towards artificial general intelligence of pathology. In: Proceedings of the 38th AAAI Conference on Artificial Intelligence; 2024 Feb 20-27; Vancouver, Canada.
58. Liu T, Xuan W, Wu H, et al. TeamPath: building multimodal pathology experts with reasoning AI copilots. Preprint arXiv: 251117652. https://doi.org/10.48550/arXiv.2511.17652 (2025).
59. Laohawetwanit T, Pinto DG, Bychkov A. A survey analysis of the adoption of large language models among pathologists. Am J Clin Pathol 2025; 163: 52-9.
60. Laohawetwanit T, Apornvirat S, Asaturova A, Li H, Lami K, Bychkov A. Evaluation of general-purpose large language models as diagnostic support tools in cervical cytology. Pathol Res Pract 2025; 274: 156159.
61. Sebastian M, Batra H, Saini ML, et al. Applications and challenges of utilizing digital pathology and AI-enabled workflows in clinical trials. J Pathol Inform 2026; 20: 100542.

Meet the Authors

Dr. Selim Sevim is a pathologist with a background in digital pathology, artificial intelligence, and 3D tissue imaging. After completing his pathology residency at the Department of Pathology, Ankara University (Türkiye), he joined the Cancer Early Detection Advanced Research Center (CEDAR) at Oregon Health and Science University. His work focuses on AI-assisted histopathological analysis and novel computational tools for cancer diagnosis.

Dr. Chadi Hajar has received his medical degree from the Lebanese University School of Medicine. He completed his Anatomic and Clinical Pathology Residency in Colorado at Penrose-Saint Francis Medical Center, followed by a Fellowship in Surgical, Gastrointestinal & Liver Pathology at the Medical University of South Carolina. In addition, he completed his MBA in Health Administration at the University of Colorado, Denver, and has an interest in digital and computational pathology. He is currently an Assistant Professor in Surgical, Gastrointestinal & Liver Pathology in the Department of Pathology and Laboratory Medicine at the Medical University of South Carolina.

Dr. Snehal Sonawane has been an author for PathologyOutlines since 2016. She has completed an Anatomic and Clinical Pathology Residency at the University of Illinois College of Medicine in Chicago, followed by a Fellowship in Surgical/GI Pathology at Loyola University Medical Center. She has also completed a Master's in Health Informatics and has an interest in digital and computational pathology. She works as an Assistant Professor at the Department of Pathology, College of Medicine, University of Illinois at Chicago.

https://doi.org/10.4132/jptm.2026.04.27